APPLICATION OF ^{13}C FLUX ANALYSIS TO INCREASE METABOLIC EFFICIENCY OF INDUSTRIAL CHINESE HAMSTER OVARY CELL LINES

By

Sarah Anne Sacco

Dissertation

Submitted to the Faculty of the

Graduate School of Vanderbilt University

in partial fulfillment of the requirements

for the degree of

DOCTOR OF PHILOSOPHY

in

Chemical and Biomolecular Engineering

May 31, 2022

Nashville, Tennessee

Approved:

Jamey D. Young, Ph.D.

Ethan Lippmann, Ph.D.

Richard O'Brien, Ph.D.

Marjan Rafat Ph.D.

“If I have seen further, it is by standing upon the shoulders of giants”
— Sir Isaac Newton

ACKNOWLEDGMENTS

Usually when someone says “it takes a village”, they’re referring to raising a child. But now, as I’m almost to the other side of the crazy journey that has been grad school, I’d amend that proverb to say “it takes a village to get a Ph.D.”. Truly, without everyone in my life that has led me to this point and everyone that has been a part of these last five and a half years, I don’t think I’d be at this point.

First, I want to thank Jamey Young, my advisor, for taking on a shy, nervous first year and somehow guiding her to becoming a confident scientist. Jamey has made this entire journey the most challenging and rewarding experience of my life, and I would not have made it to the finish line without his mentorship and guidance. I would also like to thank the other members of my committee, Ethan Lippmann, Richard O’Brien, and Marjan Rafat for their support and guidance over the years. As Jamey has said at nearly every committee meeting, you guys are the bio experts, and so much of the work in this dissertation would have never been possible without your creative suggestions.

To the rest of my collaborators, at Vanderbilt and beyond, a lot of this work would not have been possible without your input and efforts. At Johns Hopkins, Michael Betenbaugh, Anne Le, and the various Betenbaugh lab members I’ve met throughout our GOALI collaboration have helped immensely with troubleshooting and brainstorming. At Merck, Xiaolin Zhang and Xiaowen Wang provided excellent feedback and ideas throughout our collaboration. And finally, to everyone at Janssen who has helped with these projects, either through our GOALI collaboration calls or when I was on-site running my MFA study (or both!), I can’t thank you enough. Particularly Angela Tuckowski, Ryan Neff, and Dennis Powell, who helped immensely with showing me the ropes and helping with the bioreactors when I was on site, and Lauren Kraft, who had some big shoes to fill but has been wonderful to work with this past year and a half. I would especially like to thank Kevin Smith, who was an integral part of many of the studies described here and has remained an incredible

mentor.

I was not expecting to find the wonderful, nerdy, loving group of people who make up the Young lab, both past and present. My experience in grad school would not have felt complete without you all. I cannot thank enough Ali McAtee, Mohsin Rahim, Ian Cheah, and Clint Hasenour for being such a welcoming presence when I first joined the lab; you all taught me so much, and I'm so incredibly grateful for that. I will truly miss the office chats about lab work, science, and life that I've had with Amy Zheng, Javier Gomez, Baltazar Zuniga, Deveena Banerjee, Rachel Moen, Miles Crockett, and Bo Wang, but I'm so glad that I get to call all of you not just my labmates, but my friends.

To say that I probably wouldn't have made it through the first year of grad school without the rest of my cohort would not be too much of an exaggeration. So I definitely need to thank Alex Yang, Greg Lowen, Kyle Garland, Ray Matsumoto, and Dustin Groff. And, in need of a special shout-out, Christian Palmer, who has become one of my best friends and has been someone I can always go to, whether it's to rant or to celebrate a success. Even though we all ended up all over the place, I know that I made some life long friends.

I also need to thank the other people who have made my time in Nashville special: Mat Miletich, Veronica Groff, Felisha Bacquera, the rest of the ChBE department, the Vanderbilt Water Polo team (especially my fellow Grannies, Eileen Schwann, Mariana Jimenez, and Justine Sinnaeve), the Vanderbilt Master's Swim Team, and so many others.

I'd also like to thank the wonderful people who've supported me since long before I moved to Nashville, and have remained such a huge part of my life. To Haley Wight and Jamie Simpson, who I've known for over 16 years at this point and I've watched grow into some of the most amazing women I know, I've always loved sharing my ups and downs with you, and I can't thank you enough for all of your support and encouragement. To Morgan Karetnick and Michael Casper, who've stuck with me through some of the craziest parts of my life, I will always appreciate your silliness and the joy you've brought and I

can't thank you enough for the support you've given me. To the DND crew - Jon Drake, Charlie Kelman, Lauren Philips, Nate Batchell, and Taylor Eisenhauer - I'm so glad that we've had such fun and amazing adventures (in real life too!), hanging out with you guys is always a bright spot in my week. To all of the mentors who helped me achieve more than I ever thought possible - Sarah Stocking, Andy Sinkleris, Sarah Jane White, Mark Brynildsen, and Kristen Adolfsen - I never would have pushed myself this far without you believing in me. And to all of the friends and family - Lynzie Worth, Conor Burns, Cam Richardson, Liam Federico, and so many more - who've been a part of this journey, I can't thank you enough for asking me about my research, letting me vent, and letting me celebrate with you.

I also need a separate section to thank my amazing fiancé, Zach Jenkins, who honestly deserves some sort of award for sticking through all of this with me. Our time at Vandy started as classmates and, through some crazy twists and turns, ended as labmates, but I'm not sure I'll ever be able to thank you enough for your support through all of this. You've listened to my practice talks enough that you could give them, you are always the first person to celebrate any success, and you've been a shoulder to cry on when nothing is working. Truly, this Ph.D. is as much yours as it is mine.

Finally, I need to thank my family. Ever since I was a preschooler who, when asked what they wanted to be when they grew up, would answer "a paleontologist", my parents have always supported my dreams. I can't thank them enough for instilling a love of science into me ever since I was a young child and for encouraging my inquisitiveness. I don't think I would have chosen this path if not for them. My sisters, Jessica and Emily, have always been so supportive and interested in hearing about what I'm doing, even if it's inane. My grandparents, whose pride and excitement every time we talk reminds me why I'm passionate about what I do. And the rest of my extended family, who have always encouraged me.

I would also like to thank the National Science Foundation (NSF) for providing the

funding for the work presented here, both through an NSF GOALI grant to fund our collaboration with Janssen and Johns Hopkins and for funding me through an NSF GRFP award.

Like I said, it takes a village.

TABLE OF CONTENTS

LIST OF TABLES

LIST OF FIGURES

Figure Page

CHAPTER 1

Introduction

Since the first approval of Orthoclone OKT3 in 1986, the monoclonal antibody (mAb) market has grown rapidly, currently accounting for nearly half of all biopharmaceutical sales [1]. Today, mAbs can be used as life-altering treatments for a wide range of maladies, such as (but not limited to) cancers, autoimmune disorders, and inflammatory diseases [2]. Due to their complex nature, mAbs are unable to be chemically synthesized and require the use of mammalian host cell lines for production. The current process used to bring mAb-producing cell lines to production scale is highly resource and time intensive, typically taking over a year [3]. Most optimization in the process of developing high-producing cell lines has focused on media formulations which allow for high viable cell densities (VCDs) and high final product titer. However, little change has been made to the cell specific production rate [4]. With nearly 600 new mAbs in development [5], there is an *urgent need* for reduced timelines in bringing high-producing cell lines to manufacturing scale.

Chinese hamster ovary (CHO) cells are one of the most commonly used mammalian host cell lines in industry. Their widespread adaptation stems from their ability to grow in suspension [6], to survive in media without serum supplementation [7], and to perform post-translational modifications necessary for the efficacy of the final product [8]. However, CHO cells are not naturally metabolically efficient; they produce lactate and ammonia as byproducts of growth, inhibiting maximal cell growth and product quality [9]. In this dissertation, carbon-13 metabolic flux analysis (^{13}C MFA), a technique that allows for the quantification of intracellular metabolism, has been applied to industrial CHO cells in order to understand desirable metabolic characteristics and provide targets for the rational design of metabolically efficient CHO cell lines.

The long term goal of the work presented herein is to develop novel strategies to allow

for the systematic engineering of host cell metabolism to enhance recombinant protein production. This work builds upon previous studies which have identified high flux through oxidative metabolism as a hallmark of high-producing cell lines [10, 11]. The overall objectives were to apply metabolic engineering concepts to cell lines to enhance productivity, to utilize ^{13}C MFA to elucidate metabolic phenotypes, and to develop tools to aid in the identification of desirable characteristics of production cell lines. This dissertation attempts to address the following questions:

- Which metabolic phenotypes correlate with high specific productivity (qP)?
- How does cellular metabolism change under different bioprocess conditions?
- Can metabolic engineering be applied to systematically generate high producing CHO cell lines?
- What tools and techniques can be developed to aid in answering these questions?

Ideally, this work can provide a fundamental understanding of how metabolism can be manipulated to increase productivity in such a way that could eventually be applied to reduce the costs associated with biopharmaceutical development. It is expected that these reduced costs will lead to savings at the patient level, increasing access to these life-altering therapies.

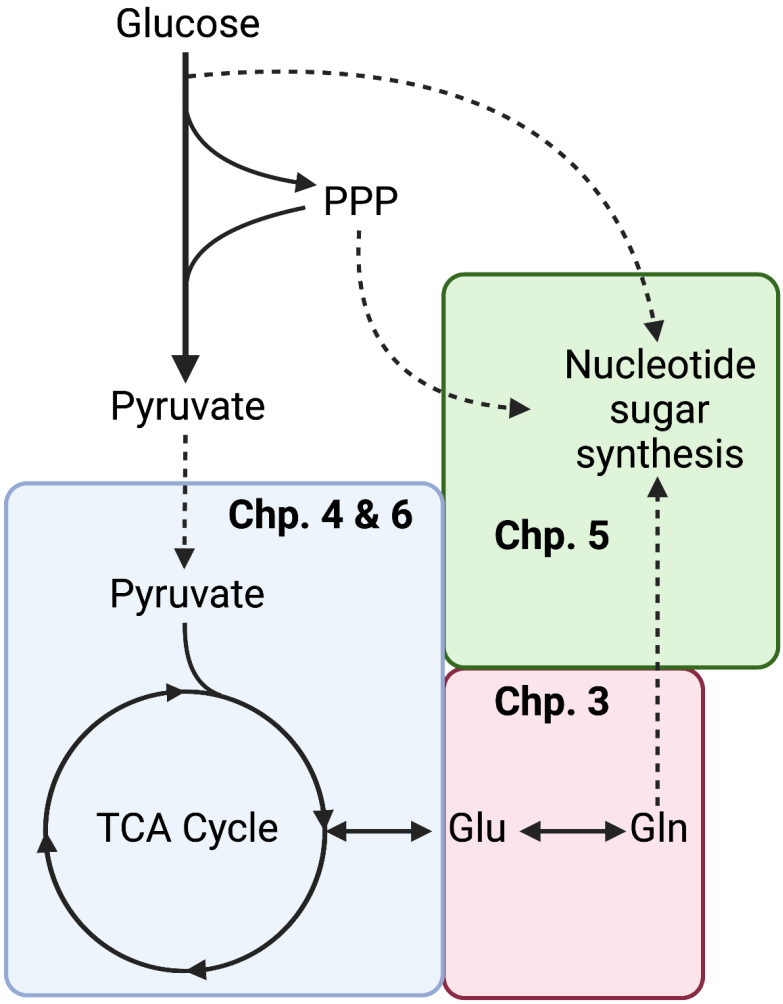

Figure 1.1: **The different parts of metabolism covered in this dissertation.** Each chapter focuses on a different part of metabolism. Chapter 3 explores the glutamine synthetase reaction. Chapters 4 and 6 focus on the tricarboxylic acid (TCA) cycle. Chapter 5 focuses on nucleotide sugar synthesis pathways. Each of these distinct pathways are intricately related; one cannot be addressed without considering the others. PPP, pentose phosphate pathway; Glu, glutamate; Gln, glutamine. Created with Biorender.com.

The metabolic engineering paradigm of "design-build-test-learn" (DBTL) acts as an overarching guide to the studies presented herein, by using ^{13}C MFA as a "test" to guide the "learn" and "design" phases [12, 13]. This dissertation explores a number of different and interrelated portions of metabolism (Figure 1.1) and is presented as follows:

Chapter 2 provides the foundational knowledge upon which chapters 3, 4, 5, and 6 are

built upon. The history, economic aspects, and current state-of-the-art production methods for biopharmaceuticals are discussed. Additionally, an overview of CHO cells is provided. Finally, ^{13}C MFA, a powerful technique to quantify metabolism used throughout the later chapters, is described.

Chapter 3 explores the attenuation of the promoter region of the glutamine synthetase selection system, one of the most commonly used selection systems used throughout the biopharmceutical industry. The effects of promoter attenuation on glutamine overflow, IgG production, and host metabolism were explored. An attenuated glutamine synthetase promoter was found to reduce wasteful glutamine production and increase IgG production while central carbon metabolism was unchanged.

Chapter 4 delves into the characterization of an industrial, IgG-producing CHO cell line which had been engineered to overexpress PGC-1α, a global regulator of mitochondrial metabolism. The phenotypic changes upon PGC-1α expression as well as various techniques to determine protein expression are considered. Overexpression of PGC-1α was found to increase metabolism at a global level and increase qP.

Chapter 5 details the development of a metabolic model of glycosylation precursor production. The validation of this model through a study comparing glucose fed cultures to galactose fed cultures is described. Additionally, an LC-MS/MS method was developed to measure isotope enrichment in nucleotide sugars.

Chapter 6 describes a ^{13}C MFA study exploring the effects of feeding TCA cycle intermediates during a fed-batch culture. TCA cycle intermediate feeding was found to increase TCA cycle flux, reduce ammonia and lactate production, and modestly increase titer.

Chapter 7 provides concluding remarks describing the overarching significant findings of this work and outlines possible future directions based on these findings.

References

[1] Gary Walsh. Biopharmaceutical benchmarks 2018. *Nature Biotechnology*, 36(12):1136–1145, 2018.

[2] Malgorzata Kesik-Brodacka. Progress in biopharmaceutical development. *Biotechnology and Applied Biochemistry*, 65(3):306–322, 2018.

[3] F M Wurm. Production of recombinant protein therapeutics in cultivated mammalian cells. *Nat Biotechnol*, 22(11):1393–1398, 2004.

[4] Chih Chung Kuo, Austin WT Chiang, Isaac Shamie, Mojtaba Samoudi, Jahir M. Gutierrez, and Nathan E. Lewis. The emerging role of systems biology for engineering protein production in CHO cells. *Current Opinion in Biotechnology*, 51:64–69, 2018.

[5] Ruei Min Lu, Yu Chyi Hwang, I. Ju Liu, Chi Chiu Lee, Han Zen Tsai, Hsin Jung Li, and Han Chung Wu. Development of therapeutic antibodies for the treatment of diseases. *Journal of Biomedical Science*, 27(1):1–30, 2020.

[6] Simon Fischer, René Handrick, and Kerstin Otte. The art of CHO cell engineering : A comprehensive retrospect and future perspectives. *Biotechnology Advances*, 33(8):1878–1896, 2015.

[7] Smriti Shridhar, Gerald Klanert, Norbert Auer, Inmaculada Hernandez-Lopez, Maciej M. Kańduła, Matthias Hackl, Johannes Grillari, Nancy Stralis-Pavese, David P. Kreil, and Nicole Borth. Transcriptomic changes in CHO cells after adaptation to suspension growth in protein-free medium analysed by a species-specific microarray. *Journal of Biotechnology*, 257:13–21, 2017.

[8] Allison G. McAtee Pereira, Jason L. Walther, Myles Hollenbach, Jamey D. Young, Allison G. McAtee Pereira, Jason L. Walther, Myles Hollenbach, and Jamey D. Young. 13C Flux Analysis Reveals that Rebalancing Medium Amino Acid Composition can Reduce Ammonia Production while Preserving Central Carbon Metabolism of CHO Cell Cultures. *Biotechnology Journal*, 13(10):1–7, 2018.

[9] Woo Suk Ahn and Maciek R Antoniewicz. Towards dynamic metabolic flux analysis in CHO cell cultures. *Biotechnology Journal*, 7:61–74, 2012.

[10] Neil Templeton, Kevin D Smith, Allison G Mcatee-pereira, Haimanti Dorai, J Betenbaugh, Steven E Lang, and Jamey D Young. Application of 13C flux analysis to identify high-productivity CHO metabolic phenotypes. *Metabolic Engineering*, 43(B):218–225, 2017.

[11] Neil Templeton, Jason Dean, Pranhitha Reddy, and Jamey D. Young. Peak antibody production is associated with increased oxidative metabolism in an industrially relevant fed-batch CHO cell culture. *Biotechnology and Bioengineering*, 110(7):2013–2024, 2013.

[12] Paul Opgenorth, Zak Costello, Takuya Okada, Garima Goyal, Yan Chen, Jennifer Gin, Veronica Benites, Markus De Raad, Trent R. Northen, Kai Deng, Samuel Deutsch, Edward E.K. Baidoo, Christopher J. Petzold, Nathan J. Hillson, Hector Garcia Martin, and Harry R. Beller. Lessons from Two Design-Build-Test-Learn Cycles of Dodecanol Production in Escherichia coli Aided by Machine Learning. *ACS Synthetic Biology*, 8(6):1337–1351, 2019.

[13] Christopher M. Whitford, Pablo Cruz-Morales, Jay D. Keasling, and Tilmann Weber. The design-build-test-learn cycle for metabolic engineering of streptomycetes. *Essays in Biochemistry*, 65(2):261–275, 2021.

CHAPTER 2

Background and Significance

Portions of this chapter are adapted from ^{13}C metabolic flux analysis in cell line and bioprocess development *published in* Current Opinion in Chemical Engineering *and has been reproduced with the permission of the publisher and my co-author, Jamey Young* [1]

2.1 Biopharmaceuticals

2.1.1 The Emergence of Biopharmaceuticals: from 1982 to the present

Biopharmaceuticals are a class of drugs consisting of therapeutics derived from biological sources, either extracted from native sources or, most commonly, produced recombinantly by a host organism [2]. Defined as any pharmaceutical manufactured in or extracted from a biological source, biopharmaceuticals encompass therapeutics such as monoclonal antibodies, vaccines, nucleic acids, and more. The first United States Food and Drug Administration (FDA) approved biopharmaceutical was human insulin, produced using recombinant DNA technologies, in 1982 [3]. As of 2018, 374 biopharmaceuticals have been approved in the United States and Europe; 155 of these approvals happened in the span of 2014-2018 [4]. Biopharmaceuticals can be delineated based on their functional class; an overview of these functional classes can be found in Table 2.1. A number of protein therapeutics can be used to treat cancer or endocrine disorders, such as diabetes. With current projections estimating a 50% increase in cancer incidence [5] and a 300% increase in diabetes diagnoses [6] by 2050, the demand for drugs to treat these diseases will continue to rise. Additionally, highlighted by the recent (and ongoing) COVID-19 pandemic, a shorter time from discovery to production is necessary in times of public health crises [7]. Challenges for biopharmaceuticals are not just due to demand and development time; some of the most expensive drugs per dose are biopharmaceuticals [8], making these life-altering treatments cost prohibitive for some, particularly in underdeveloped countries. Overall, with the in-

creasing demand for more biopharmaceuticals, on a faster time scale and in large enough quantities to drive down costs, more efficient means of production are urgently needed.

Functional Class	Purpose	Examples of clinical use
Enzymatic or regulatory activity	Replace deficient or abnormal protein	Endocrine disorders Hemostasis and thrombosis Metabolic enzyme deficiencies Pulmonary and gastrointestinal-tract disorders Immunodeficiences
	Increase activity of existing pathway	Hematopoiesis Fertility Immunoregulation Hemostasis and thrombosis Endocrine disorders
	Provide non-native activity/function	Enzymatic degradation of macromolecules Enzymatic degradation of small-molecule metabolites Hemostasis and thrombosis
Protein therapeutics with special targeting activity	Interfering with a molecule or organism	Cancer Immunoregulation Transplantation Pulmonary disorders Infectious diseases Hemostasis and thrombosis Endocrine disorders
	Delivering other compounds or proteins	Cancer
Protein vaccines	Protection against a virus	Hepatitis B Human papillomavirus Lyme disease
	Treating an autoimmune disease Treating cancer	
Protein Diagnostics	Infectious diseases Endocrine disorders Cancer	

Table 2.1: **Functional Classes of Protein Therapeutics.** Adapted from Leader et al.[2]

A major class of biopharmaceuticals are monoclonal antibodies (mAbs), which accounted for over 65% of global biopharmaceutical sales in 2018 [4]. MAbs function by binding to an antigen and tagging it for immune system clearance or blocking the effects

of the antigen. The first mAbs were murine-derived, causing immunogenicity and limiting their use as long-term treatments [9]. Advances in protein engineering allowed for the development of chimeric (typically mouse-human) antibodies in the 1990s, ushering in the "age of antibodies" [10]. Fully human mAbs entered the market with the approval of Humira (adalimumab) in 2002, and now comprise over 40% of all approved mAbs [10]. As of 2020, six of the top ten selling drugs worldwide are mAbs [11]. Due to the wide-ranging scope of biopharmaceuticals, the remainder of this chapter will focus on mAbs.

2.1.2 Advantages and disadvantages of monoclonal antibodies

MAbs are highly desirable as therapeutics for a number of reasons; however, there are still many opportunities to improve upon not only the mAbs themselves but also the processes used to produce them. First, and possibly most importantly, mAbs are highly specific for the intended target, which not only increases the efficacy of the treatment but also greatly reduces the chances of undesirable side-effects [12]. High specificity is an inherent trait of antibodies; taking advantage of this evolutionary perk for therapeutic benefit is no surprise. Second, advances in protein engineering have allowed for the creation of mAbs targeting a number of antigens, consistently increasing the range of diseases that can be treated with mAbs.

As the number of disease targets and possible patients increases, the disadvantages of mAbs become more of an issue. Due to their complexity, mAbs cannot be chemically synthesized at a feasible scale and must be produced in cell lines. The development of production cell lines is currently a time and resource intensive process [13], and will be described in more detail in section 2.1.4. Additionally, doses can be high, sometimes exceeding 500 mg; producing hundreds of thousands of doses would require hundreds of kilograms [7]. While yields have greatly improved over the years to over 10 g/L in some cases [14], some "difficult-to-express" mAbs achieve titers below 1 g/L [15, 16]. The combination of high necessary doses and relatively low yields results in high prices for the end-user. While

mAbs present a promising class of drugs for a wide range of diseases, improvements in production methods can help to make mAbs more widely accessible.

2.1.3 Economics

Total mAb sales amounted to $115 billion in 2018 and are projected to reach $300 billion by 2025 [17]. There are currently 79 mAbs approved by the FDA and an estimated 570 mAbs are in clinical trials around the world [17]. In 2018, each of the top 10 best-selling mAbs generated revenue above $3 billion [17]. It is estimated that the cost to develop a new drug, including expenditures on drugs that never even see the market, is typically between $1 and $2 billion, with biologics trending towards, or exceeding, the high end of this range [18, 19]. Especially with the growing market of off-patent biosimilars, reducing the cost to bring a drug to production is critical for these highly competitive products. While the reward for a successful mAb product can be high, the risk is substantial.

It stands to reason that reducing the total time and effort required to bring a new mAb to market, or even to phase I clinical trials, can improve nearly every aspect of the drug development pipeline. In terms of the length of time it takes to bring a drug from discovery to market, a huge investment for mAbs occurs in the pre-clinical phase; yet these drugs have a less than 10% chance of actually making it to market [18]. Meanwhile, the process to produce enough of a therapeutic to even attempt clinical trials is time and resource intensive, typically taking at least a year and requiring the screening of hundreds, if not thousands, of clones [13]. Additionally, the process developed during the pre-clinical phase will undergo most optimization only after the mAb has passed phase II clinical trials.

Cost, both to pharmaceutical companies and to consumers, is a huge motivator of research attempts to increase the production of protein therapeutics. The goal of this research is typically to reduce the time and, by extension, cost it takes to bring a drug to market. To best achieve this goal, a stronger understanding of the entire production process is necessary. Overall, by reducing the timespan of bringing a drug from discovery to market,

upfront costs can be reduced, which is expected to reduce costs for the consumer.

2.1.4 Current production methods

The current process used to bring mAb-producing cell lines to production scale is very resource and time-intensive, typically taking over a year [13].

First, the gene of the protein of interest (GOI) must be stably transferred into the host cell line. The GOI can enter the cell by way of physical transfection (e.g. electroporation), chemical transfection (e.g. polyethylenimine), or viral transduction. This GOI can then be stably integrated into the genome of the cell through random integration, site-specific integration, viral infection, or transposon-mediated integration. Next, clones that have successfully integrated the GOI must be selected for. These clones will undergo a lengthy screening process to determine which clones possess desirable characteristics, such as high productivity or high final viable cell densities. Eventually, a "lead" clone will be chosen and further process development will be carried out, such as media formulation and bioprocess parameter optimization [13].

Most process optimization will focus on maximizing the final product titer. This can be achieved by increasing two characteristics: the integrated viable cell density (VCD) (i.e. the total number of cells in the culture) or the specific productivity (i.e. the amount of product produced by each individual cell.) Up to this point, most process development has focused on increasing VCDs since this can be achieved through media and bioprocess optimization. In 1986, fed-batch processes were able to achieve 4 x 10^6 cells/mL [15]. Now, VCDs on the order of 60 x 10^6 cells/mL are not unheard of in perfusion style reactors [20]. Culture lengths are also able to reach nearly 30 days in perfusion reactors, further increasing final titers by allowing cells longer time spans to be in production phase [21]. Typically, in order to increase specific productivity beyond what is achieved through natural clonal variation, the host cell line needs to be engineered in some manner.

Due to the complexity and necessary post-translational modifications, mAbs are pro-

duced in mammalian cell lines. Initially, mouse hybridomas were used, but they are labor intensive, provide low product yields, and can cause immunogenicity issues [22]. Now, Chinese Hamster Ovary (CHO) cells are one of the most popular choices in industry, producing nearly 70% of all protein therapeutics [13].

2.2 Chinese Hamster Ovary Cells

CHO cells are considered the workhorse of the biopharmaceutical industry for a number of reasons. First, because they have been used so extensively, they are considered to be a proven safe host cell line [13]. They are also able to grow in serum-free media, which limits batch-to-batch variations in media composition [23]. Additionally, CHO cells can be cultured in suspension, which allows for easier scale-up to production bioreactors [24]. CHO cells are also capable of creating human-like post-translational modifications, which allow for the proper efficacy of the drug in the body [25]. All of these characteristics make the FDA approval process easier [26, 12]. However, CHO cells are not naturally metabolically efficient [27]. They produce lactate and ammonia as byproducts of growth, both of which can inhibit cell growth and affect product quality [28]. Additionally, CHO cells are genetically and transcriptomically diverse; even within phenotypically similar CHO cell lines (e.g., adherent CHOK1, suspension CHOS) there can be a wide range of reported transcriptomic profiles [29]. This genetic diversity can help to create the clonal differences, positive or negative, that drive the current cell line development workflow, but it can cause issues in developing stable genetically engineered clones [30, 31, 32, 33, 34]

2.2.1 CHO cell metabolism

MAbs are energy intensive for the cell to produce, requiring three ATP molecules per peptide bond.[35] During times of high production, mAbs can represent up to 20% of the total cellular protein.[36] Even though large amounts of energy and biosynthetic precursors are needed to maximize mAb production, CHO cells are not naturally metabolically efficient. Lactate, ammonia, and other byproducts accumulate in the culture during cell

growth, and can inhibit cell growth and affect final product quality.[25] Interestingly, high-producing industrial cultures switch from lactate production during growth phases to lactate consumption during the stationary phase, when most of the mAb production occurs.[36] These inefficiencies pose a challenge for achieving the maximum production potential of CHO cells. Previous studies have attempted to identify the metabolic phenotypes of high-producing cell lines. In a small scale study of industrial high-producing clones, it was found that peak antibody production occurs during stationary phase.[36] While glycolytic flux is at its highest during exponential phase, there is a marked shift to increased oxidative metabolism and lactate consumption that coincides with increased antibody production. In another study of industrial clones at a larger scale, it was found that when comparing high-producing clones to non-producing clones, the flux through the TCA cycle is significantly increased in the high-producing strains.[28] Together, these studies provide a general idea of the metabolism of high-producing clones. During exponential phase, glycolytic flux is at a maximum as well as biomass production. Once the cell culture has reached its peak VCD in stationary phase, the energy of the cell is switched from growth to mAb production. At this point, we see maximal mAb production, a switch from lactate production to lactate consumption occurs, and a significant increase in flux through oxidative metabolism, which provides much of the energy and biosynthetic precursors for the cell. Overall, high-producing clones require energy to produce large amounts of mAbs and the upregulation of oxidative metabolism appears to provide the necessary energy.

2.2.2 Previous efforts to improve CHO cell productivity

Volumetric titer is one of the main parameters used to define CHO cell productivity. There are two ways to increase volumetric titer, (i) increase the number of cells in the reactor or (ii) increase the amount an individual cell can produce (i.e., specific productivity, qP). Improvements can be made to the production process itself, the media composition, or the host cell line.

One major development in bioprocessing has been the increased usage of perfusion reactors for production. Perfusion reactors have a continuous input feed, which provides nutrients, as well as a continuous output bleed, which removes spent media, limiting byproduct buildup. Perfusion reactors are able to reach much higher cell densities than batch or fed-batch setups and can be run for much longer culture times [20]. Walther et al. showed that while volumetric titers are higher in a fed-batch process, productivity (defined as g/L produced per day, not normalized to cell density) and cell density was higher in a perfusion process [37]. Templeton et al. also showed higher volumetric titers in a fed-batch process and higher VCDs in a perfusion reactor, but cell specific productivity was reduced in a perfusion reactor [21].

Media formulation optimization has been a major focus of improving CHO cell productivity. The limitation of glucose, the main carbon source throughout the culture length, has been found to reduce lactate accumulation [38]. Glucose limitation can also lead to slower culture growth, which can be remedied through the supplementation of amino acid metabolism byproducts and intermediates [39]. Fouladiha et al. applied a genome-scale model to identify metabolites, such as threonine and arachidonate, to supplement into cell culture media and were able to achieve a two-fold increase in total mAb production [40]. Zhang et al. hypothesized that supplementing TCA cycle intermediates would allow for sustained high oxidative metabolism and found that feeding TCA cycle intermediates during the stationary phase increased productivity [41]. Media composition can also be altered to reduce undesirable phenotypes, such as ammonia production, without significantly altering other culture characteristics such as growth, titer, or metabolism, as shown by McAtee Pereira et al. [42].

While bioprocess optimization and media manipulation can increase VCD and volumetric titers, typically improvements in specific productivity require engineering of the host cell line [43]. Lasorsa et al. found that the expression of a mitochondrial Ca^{2+} sensitive aspartate/glutamate transporter in CHO cells increased ATP levels, which could help

to increase qP by increasing the availability of ATP [44]. Recombinant expression of pyruvate carboxylase, which directs pyruvate into the TCA cycle, was shown to increase lactate consumption, prolong growth, increase peak VCD, and increase volumetric titers [45, 46]. Mulukutla et al. overexpressed genes in the phenylalanine-tyrosine catabolism pathway and knocked out branched chain aminotransferase 1 (BCAT1), which decreased production of small molecule growth inhibitors derived from BCAA catabolism, such as 3-phenyllactate, isovalerate, and isobutyrate [47]. Ley et al. applied CRISPR/Cas9 to engineer nine genes in seven different amino acid catabolic pathways and showed reduced lactate and ammonia secretion in the engineered clones [48].

Engineering host CHO cell lines requires the development of efficient genetic engineering tools. Lentiviral vector based gene transfer systems have been shown to create stable recombinant CHO lines in just a few days [49]. Meanwhile, cumate-inducible gene expression systems have been developed to allow for recombinant gene expression to be easily turned on and off, dependent on when the inducer is added [50]. Shin and Lee optimized a CRISPR/Cas9 based strategy to allow for site-specific gene integration [51]. Xiong et al. applied CRISPR intereference (CRISPRi) to reduce the expression of apoptotic genes in CHO, leading to reduced apoptosis and increased mitochondrial membrane integrity [52]. Transposase based systems can increase production beyond that achieved by random integration, with the added benefit of reduced time to generate stable pools [53, 54, 55].

Overall, while significant improvements have been made to CHO cell cultures over the past three decades, there are still inefficiencies in the metabolic phenotype of CHO cells. In order to understand the causes of these inefficiencies, an in-depth understanding of metabolism is necessary. The following section will discuss Carbon-13 metabolic flux analysis (^{13}C MFA), a technique that allows for a quantitative analysis of metabolism.

2.3 ^{13}C Metabolic Flux Analysis

2.3.1 Overview of ^{13}C MFA

In brief, ^{13}C MFA utilizes labeled carbon sources to trace the flow of carbon through the metabolism of the cell, providing a quantitative map of reaction fluxes [56]. The workflow consists of both experimental and computational components (Figure 2.1). The large number of independent measurements provided by the ^{13}C labeling experiment ensures that net fluxes can be estimated with high precision and accuracy; this data richness also enables the estimation of some parallel and reversible reactions. Without the use of stable isotope tracers, the number of independent extracellular measurements represents the maximum number of independent intracellular fluxes that can be discerned [56]. To ensure a unique flux solution, an appropriate tracer (or mix of tracers) must be selected. There are typically tradeoffs for different tracers, in that some tracers will have improved flux resolution for some pathways with reduced resolution for others [57]. However, parallel labeling experiments can be used to increase the resolution of fluxes throughout several overlapping metabolic pathways [58]. In addition to the measurement of labeling patterns of free metabolites, the inclusion of labeling data from hydrolyzed glycogen or RNA monomers can greatly increase flux resolution, particularly in the pentose phosphate pathway (PPP) [59, 60]. Software has been developed to aid in the computational aspects of ^{13}C MFA that is user-friendly and available to the scientific community, such as INCA[61], Metran[62], and OpenFLUX[63], among others.

Using just extracellular flux rates, the nutrient demands and mass balance for the cell can be determined. However, in this case the cell is effectively treated as a black box; carbon sources, such as glucose and amino acids, act as inputs and are converted into outputs such as biomass, wasteful byproducts, and desired products. With ^{13}C MFA, the dynamics of intracellular metabolism can be elucidated by quantifying nutrient fluxes inside of living cells. The final results of ^{13}C MFA can be used to characterize cell lines, identify wasteful pathways, and identify metabolic bottlenecks, allowing for fundamental insights

into metabolic networks and, ultimately, guiding metabolic engineering efforts.

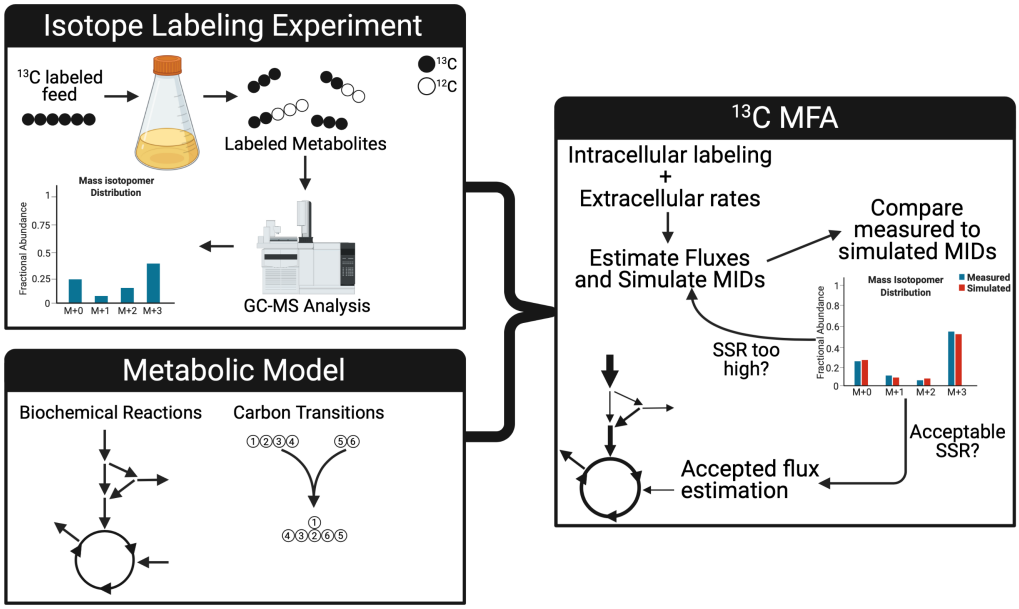

Figure 2.1: **Overview of the ^{13}C MFA workflow.** In an isotope labeling experiment (ILE), a ^{13}C labeled tracer is fed to the cell culture of interest. As labeled substrate is consumed by the cells, specific atomic positions of downstream metabolites will be enriched by the tracer. Samples are removed to measure extracellular metabolite concentrations and to extract intracellular metabolites. The extracted samples can be analyzed by mass spectrometry (MS) or nuclear magnetic resonance (NMR). MS data provides the mass isotopomer distribution (MID) of labeled metabolites, which quantifies the relative abundance of each mass isotopomer (i.e., species with increasing numbers of heavy atoms: denoted M+0, M+1, M+2, etc.). The ILE provides two types of measurements: intracellular labeling data and extracellular rates of metabolite production and consumption. While extracellular rates provide boundary conditions that constrain the flux solution, they are not sufficient to determine intracellular fluxes, particularly in the case of parallel pathways or metabolic cycles. In addition to the experimental data, a metabolic model is also needed for ^{13}C MFA. The metabolic model consists of the biochemical reactions that describe the relevant metabolism of the cell as well as known carbon transitions of the reactions included in the model. At its core, ^{13}C MFA requires solving a non-linear optimization problem to minimize the mismatch between model-predicted measurements and experimentally determined measurements. Using the data from the ILE and the metabolic model, fluxes are adjusted until the sum of squared residuals (SSR) is minimized. The fit is either accepted or rejected based on statistical tests. If rejected, the model can be adjusted and the estimation process repeated until an acceptable fit is obtained. Created with BioRender.com.

2.3.2 Inputs for ^{13}C MFA

As summarized in Figure 2.1, there are two major requirements for ^{13}C MFA: the experimental data and the metabolic model. For the experimental side of ^{13}C MFA, isotope labeling experiments (ILEs) are carried out by feeding a cell culture a substrate, the "tracer", that is labeled with the stable isotope ^{13}C. Dependent on the pathways of interest, this substrate can be glucose, an amino acid, or any other carbon source consumed by the cells. This substrate is metabolized by the cell, producing labeled metabolites throughout metabolism. The labeling patterns of these metabolites can be measured via nuclear magnetic resonance (NMR) or mass spectrometry (MS). MS based methods can provide information about the relative abundance of mass isotopomers, but cannot provide positional information. Fragmentation of metabolites, either in the ion source (e.g., typical of gas chromatography (GC)-MS instruments) or in a collision cell (e.g., typical of tandem liquid chromatography (LC)-MS/MS instruments), can provide some positional information. NMR can monitor ^{13}C enrichment at specific atom positions in the molecule, but requires significantly more sample material. For all of the experiments reported in this dissertation, MS based methods were used.

In addition to the intracellular labeling patterns, extracellular flux rates provide boundary conditions for the model. Growth rates can be calculated based on the measured viable cell densities and represent the flux through the defined biomass equation in the metabolic model. The coefficients for the biomass equation can be calculated based on a measured dry cell weight for the culture and known cellular compositions [64]. The concentration of metabolites in the media can be measured by high-performance liquid chromatography (HPLC) based methods, colorimetric assay kits, or MS based methods. Using the measured concentrations of metabolites and the viable cell density, per-cell consumption or production rates can be calculated using softwares such as ETA [60] or equations such as those reported in Walther et al [37].

The computational side of ^{13}C MFA requires a metabolic model. This model consists

of the biochemical reactions that comprise cellular metabolism and the carbon transitions that occur in these reactions. The choice of reactions that can be included in the metabolic model is dependent on (i) the metabolic pathways of interest and (ii) the availability of measurements to resolve the fluxes in those pathways. Any pathways of interest can be included in the metabolic model, as long as some metabolites in those pathways or their downstream products can be measured. Typically, metabolic models consist of central carbon metabolism (e.g., glycolysis, the pentose phosphate pathway, the tricarboxylic acid cycle, etc.), amino acid metabolism, and other biosynthetic pathways of interest. Compartmentation within the cell, such as between the cytosol and mitochondria, can also be taken into consideration when constructing the metabolic model [65].

As with any attempt to model a natural system mathematically, certain criteria must be met for the model to be applied. ^{13}C MFA, in its most basic form, assumes that both metabolic and isotopic steady state have been reached. Metabolic steady state is defined as the state in which the system has constant intracellular pool sizes of metabolites and metabolic fluxes (both extracellular and intracellular) are constant. Isotopic steady state is defined as the state in which the intracellular labeling patterns have reached a constant state. If isotopic steady state is not achieved, isotopically non-stationary MFA (INST-MFA) can be used. While INST-MFA is computationally more demanding, the analysis of dynamic labeling at multiple time points allows for greater accuracy in flux estimation [66, 67].

Figure 2.2 summarizes the different types of MFA that can be performed, dependent on whether metabolic and/or isotopic steady state has been achieved. ^{13}C-MFA requires that both metabolic and isotopic steady state have been achieved. ^{13}C-INST-MFA can be used to regress fluxes in systems that have achieved metabolic steady state, but not isotopic steady state. Dynamic ^{13}C MFA (^{13}C-D-MFA) can be used when neither metabolic or isotopic steady state has been achieved [56].

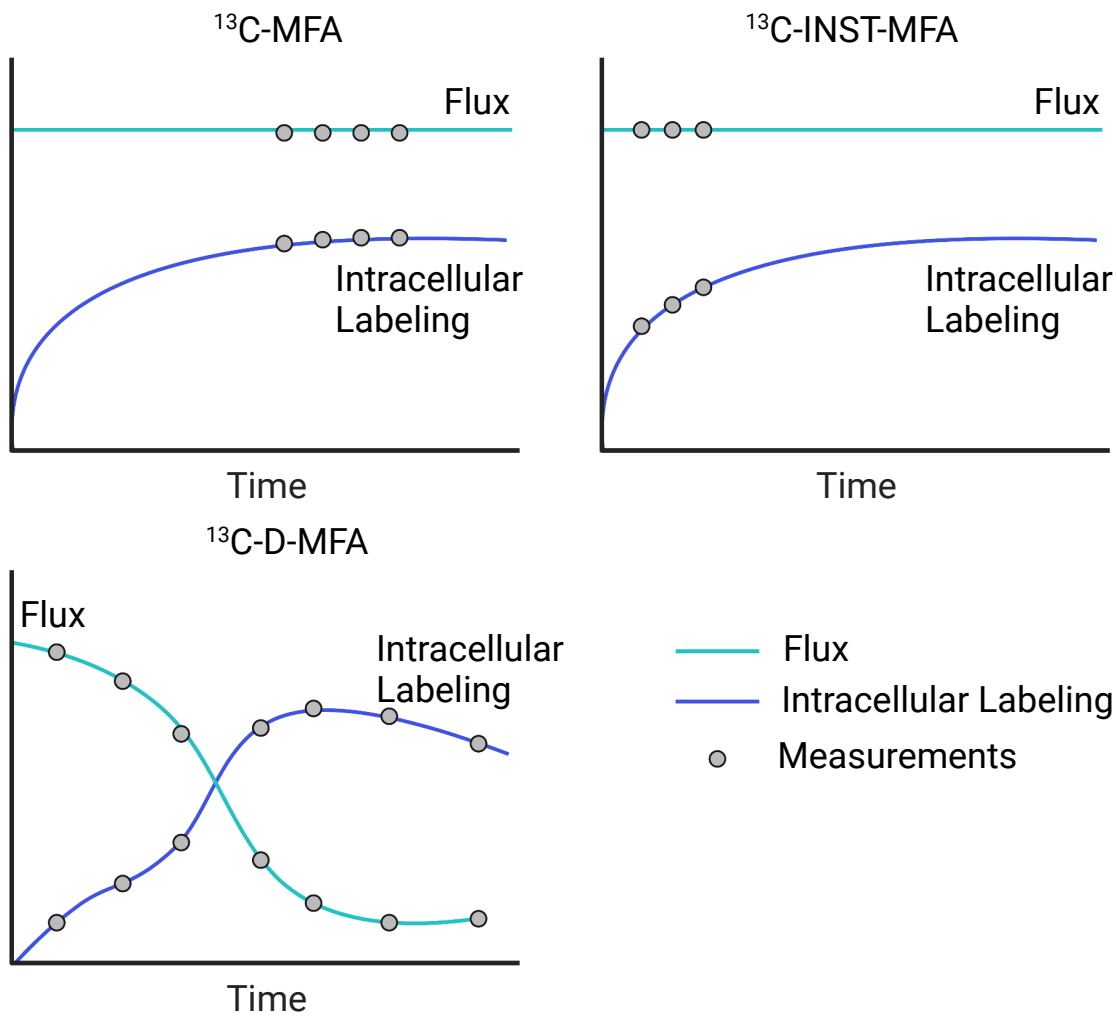

Figure 2.2: **The different types of MFA that can be used.** The type and complexity of MFA that can be performed is dependent on the steady states that are achieved in the system. In ^{13}C-MFA, both metabolic and isotopic steady state have been achieved, as shown by the measurements taken once both flux and intracellular labeling are constant. ^{13}C-INST-MFA can be used to regress fluxes in systems that have not yet achieved a constant state of intracellular labeling. Meanwhile, ^{13}C-D-MFA must be applied when both flux rates and intracellular labeling are changing. Adapted from Antoniewicz [56]. Created with BioRender.com.

A final important aspect of ^{13}C MFA to consider before carrying out an ILE is the choice of tracer. The choice of tracer can determine which fluxes can be well-resolved, dependent on how the labeled carbons in the tracer are incorporated. One example that highlights this is the use of a [1,2-$^{13}C_2$] glucose tracer to elucidate the percentage of flux through glycolysis vs the PPP via pyruvate labeling (Figure 2.3). If a fully labeled glucose

tracer were used, all pyruvate resulting from either glycolysis or the PPP would be fully labeled as well. However, if [1,2-$^{13}C_2$] glucose is used, the pyruvate pool will contain M0, M1, and M2 pyruvate. If all incoming glucose is metabolized via glycolysis, pyruvate will have a mass isotopomer distribution (MID) containing 50% M0 and 50% M2. Meanwhile, if all incoming glucose is metabolized via the PPP, the MID would have 60% M0, 20% M1, and 20% M2. Since glucose will realistically be metabolized by a combination of glycolysis and PPP, the true MID will be a linear combination of these two.

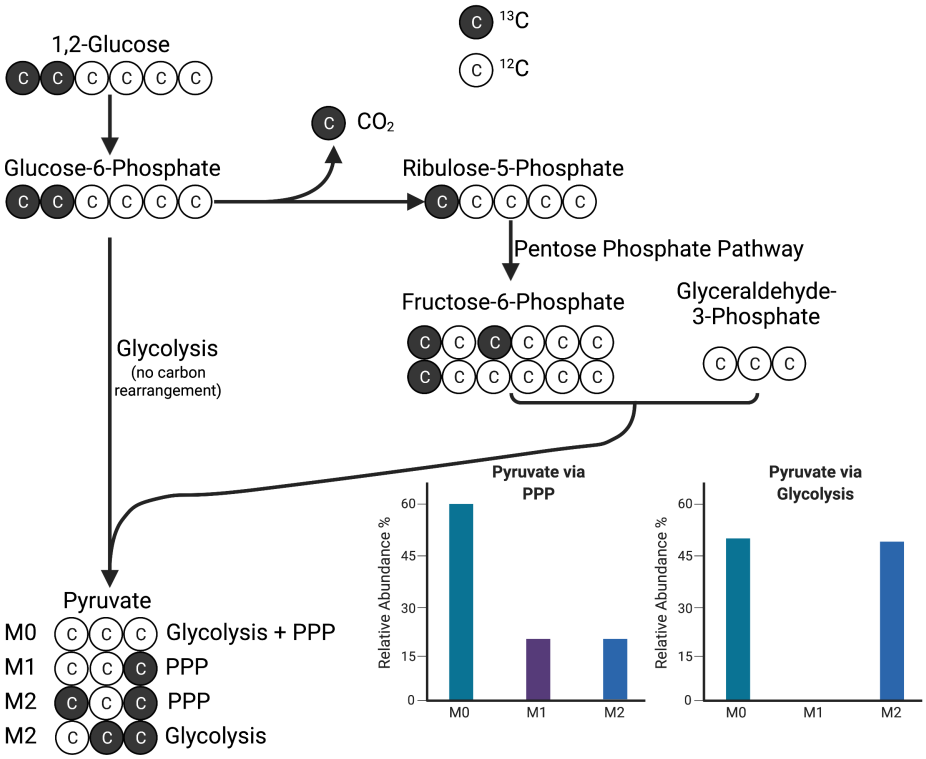

Figure 2.3: **The labeling pattern of pyruvate can be used to discern the split between glycolysis and the pentose phosphate pathway (PPP).** If pyruvate were to be produced purely from glycolysis or the PPP, the mass isotopomer distribution (MID) would be as shown. In a typical cell, both pathways will be utilized resulting in a linear combination of these two MIDs. The ratio of carbon that traverses through glycolysis versus the PPP can be determined based on the resulting MID measurement.

Typically, multiple pathways will be of interest, which would lead to a desire to use multiple tracers. This can be achieved through parallel labeling studies [68]. In a paral-

lel labeling study, multiple tracers can be fed to reactors in parallel and then the data from these reactors will be regressed simultaneously. Parallel labeling studies can be particularly useful if a single tracer will result in reduced flux resolution in somepathways of interest. For example, if both the PPP and the TCA cycle are studied simultaneously, the combination of a [1,2-$^{13}C_2$]glucose tracer and a [U-$^{13}C_5$]glutamate or glutamine tracer will provide higher resolution than a [U-$^{13}C_6$]glucose tracer alone. The use of a parallel labeling study is highlighted in Chapter 3 of this dissertation.

2.3.3 The mathematics of ^{13}C MFA

At its core, ^{13}C MFA is a nonlinear optimization problem, meaning that it aims to satisfy some sort of objective function while taking constraints into consideration. After the metabolic model has been defined, it can be converted into a stoichiometric matrix, S, and a flux vector, v. The model is governed by the equation:

$$S \cdot v = 0 \tag{2.1}$$

which defines that metabolism is at steady-state. In the case of systems that are not at metabolic steady-state, dynamic ^{13}C MFA must be used, and is subject to different governing equations. The stoichiometric matrix S will have dimensions of $m\,x\,n$, where m is the number of metabolites and n is the number of reaction fluxes. Therefore, the degrees of freedom (DOF) can be calculated using:

$$DOF = n - m \tag{2.2}$$

If the number of input measurements (e.g., isotopomer abundances, extracellular fluxes, etc.) exceeds the DOF, the system is considered overdetermined. Typically, ^{13}C MFA is nearly always overdetermined, which allows for the calculation of statistical goodness-of-fit metrics and 95% confidence intervals for each flux [69].

Because of the constraints imposed by equation 2.1, the only flux solutions that satisfy this equation reside in the null space of S. This reduces the dimensions of the feasible flux space, allowing the model to be parametrized in terms of its free fluxes, which are determined by the equation:

$$v = N \cdot u \tag{2.3}$$

where N is the null space matrix of the stoichiometric matrix S, and u is the vector of free fluxes. These free fluxes are included in the constraint definition of the objective function, described below.

In ^{13}C MFA, the objective is to minimize the difference between measured and simulated data and can be described by the following problem statement:

$$min\Phi = (x(u) - x^{obs})^T \cdot \Sigma_x^{-1} \cdot (x(u) - x^{obs}) \tag{2.4}$$

Such that:

$$N \cdot u \geq 0,\ c \geq 0,\ h \geq 0$$

where Φ is the objective function to minimize the sum of squared residuals, $x(u)$ is the simulated measurements vector, and x^{obs} is the experimental measurements vector. $\sum_x$ is the covariance of all the experimental measurements, and allows for the incorporation of experimental errors; based on this definition, measurements with lower errors will be weighted more than those with higher errors. The objective function is minimized by application of a minimization routine such as the Levenberg-Marquardt gradient-based algorithm [70]. The non-negativity constraint defines that the free fluxes ($v = N \cdot u$), pool sizes (c), and scaling factors (h) must be greater than 0. Non-negative fluxes ensure reactions proceed in the correct direction, as separate forward and reverse reactions are defined for

reversible reactions. Pool sizes, which are effectively the "amount" of a metabolite present in the compartment defined in the model, cannot be negative by definition. Scaling factors are used by the model to renormalize measured MIDs, which helps to account for truncated or missing data as well as noisy values. Based on this mathematical definition of ^{13}C MFA, if a model does not fit well, there are three possible issues: (i) a measurement or measurements are inaccurate, (ii) the metabolic model is poorly defined, or (iii) the measurements are inappropriately weighted (i.e., the measurement errors are poorly defined).

2.3.4 Limitations of ^{13}C MFA

While ^{13}C MFA is a powerful technology that has allowed for the quantitative study of intracellular metabolism, there are limitations to the applicability of ^{13}C MFA that need to be considered. Pathways included in the metabolic model for ^{13}C MFA are typically in central carbon metabolism, such as glycolysis, PPP, TCA cycle, and anaplerotic reactions. While secondary pathways can be included in the metabolic model, an appropriate tracer that will allow for labeling in those pathways must be used, and labeling patterns of metabolites within that pathway must be measured to attain an acceptable resolution of fluxes. Additionally, the output of ^{13}C MFA is highly dependent on the inputs; poor flux resolution can occur if the model is inadequate or if measurements contain large errors[56]. Incorrect assumptions can also hinder the use of ^{13}C MFA, as the proper type of analysis is dependent on the experimental assumptions. Detailed descriptions of the various methodologies of ^{13}C MFA are outside of the scope of this chapter, but these different methodologies are well described in the literature [56, 71, 66]. It should also be emphasized that though the fluxes estimated by ^{13}C MFA can be used to determine possible pathway bottlenecks or targets for metabolic engineering, flux values should not be used as direct measurements or proxies of gene expression levels. The biological network within a cell is highly complex and any engineering efforts can have off-target effects that need to be considered.

2.3.5 Application of ^{13}C MFA to cell culture

^{13}C MFA can be applied to identify the metabolic phenotypes of cell cultures under conditions of interest. This iterative process is shown and described in Figure 2.4. By understanding the metabolism of desirable clones, engineering targets can be identified, and genetic engineering can be applied to induce these metabolic phenotypes. Experimental details for referenced studies in this section are described in Table 2.2.

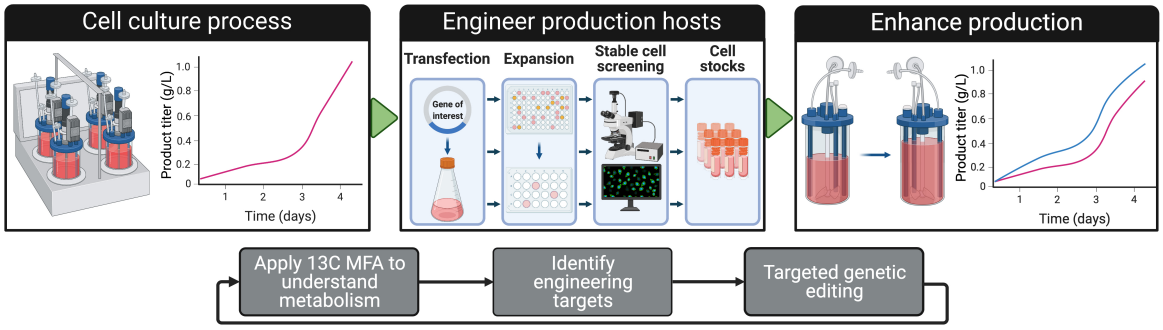

Figure 2.4: **The use of ^{13}C MFA in engineering industrial cell lines.** A typical workflow for engineering a cell line involves examining the parental host line, transfecting it with a gene of interest, and then selecting and expanding the resulting cell population to obtain stable clones. This cell line will then be analyzed to determine if the desired phenotype, such as enhanced production, has been achieved. ^{13}C MFA can be used to guide this process. By applying ^{13}C MFA to industrial cell lines, targets for engineering can be identified. In addition, ^{13}C MFA can help to characterize the engineered clones to determine how their cellular metabolism has been altered. Created with BioRender.com

2.3.5.1 Increased understanding of production cell line metabolism

Identifying metabolic hallmarks of high-producing cells can provide insight into the most important pathways to target for future engineering efforts. Templeton et al. [21] compared a non-producing and a high-IgG producing industrial CHO cell line using flux maps determined by ^{13}C MFA. They identified a marked increase in TCA cycle flux in the high-producing cell line during stationary phase. In addition, high producers were found to have lower lactate production, higher NADH production, and a greater percentage of pyruvate

entering mitochondrial metabolism. In a later study comparing fed-batch and perfusion cultures of IgG1-producing CHO cells, similar TCA cycle flux was observed in both culture modes, even though specific productivity was significantly higher in the fed-batch culture. Upon accounting for cell growth during the study, it was found that the total protein burden of biomass and IgG was similar, leading to the similar levels of TCA cycle flux [72]. Together, these studies indicate that recombinant protein and biomass production are the main sinks of energy metabolism in the cell, highlighting the TCA cycle as a possible metabolic engineering target for enhancing cellular biosynthesis and energetics.

Increased energy and biosynthetic demand were also identified in cell lines producing adenoviral (AV) vectors. AV vector production is of interest due to AV use in vaccine and gene delivery applications. Carinhas et al. [73] studied metabolic changes in MDCK cells during canine AV production. Canine AV infection increased fluxes through nearly all of central carbon metabolism. The flux from citrate to cytosolic AcCoA in the infected condition was more than double that of non-infected cells, likely indicating increased lipogenesis. These findings were corroborated in a later study of human AV infection, where AV production during the stages of exponential growth and growth arrest were compared [74]. ^{13}C MFA revealed increased glycolytic and PPP flux during exponential growth, while infection during growth arrest increased overall carbon flux, except PPP flux. In both conditions, flux from citrate to cytosolic AcCoA was similarly increased, identifying AcCoA production as a potential target to increase AV production.

Due to eukaryotic cells having inherently compartmentalized metabolism, the transport of metabolites across membranes can greatly affect cellular metabolism. Junghans et al. [75] utilized ^{13}C MFA to study compartment-specific metabolism in IgG-producing CHO cells under different nutrient levels. They identified mitochondrial shuttle systems as key enablers of high TCA cycle flux during periods of high cell growth and high production. A switch in mitochondrial malate flux from net export to net import coincided with reduced glutamine availability, lower NADPH formation, and a marked decrease in IgG production.

In addition, a Michealis-Menten type correlation between qP and cytosolic malic enzyme activity was noted, suggesting that production can be further improved by maintaining high flux through cytosolic malic enzyme. ^{13}C MFA can be used to quantify the transport of metabolites across intracellular membranes, identifying possible engineering targets to optimize transport.

In addition to quantifying fluxes through already known metabolic pathways, ^{13}C MFA can be used to identify previously unknown reactions that are active in host cells. Since ^{13}C MFA is typically based on a simplified core model that assumes negligible activity of some reactions, the introduction of new reactions to the model can sometimes reconcile apparently inconsistent experimental data. Through the use of parallel ^{13}C MFA tracer experiments, Ahn et al. [76] identified the presence of a transketolase-like protein 1 (TKTL1) reaction in the PPP. Slade et al. [77] found that flux from mannose to mannose-1-phosphate could explain the reduction in lactate production that was observed in CHO cells fed mannose rather than glucose as a primary carbon source. These studies highlight the use of ^{13}C MFA to discover new metabolic activities and deepen our understanding of metabolic regulation in mammalian hosts.

2.3.5.2 Characterization of altered culture conditions

While altered phenotypes may appear under varying culture conditions, the mechanism underlying these changes may not always be obvious. Media optimization has been a main driver of improved bioprocesses, and ^{13}C MFA has been used to study the intracellular changes caused by different media compositions. Sheikholeslami et al. [78] compared flux maps generated from CHO cell cultures that were fed either a high or low glutamine feed. They observed higher TCA cycle flux, higher specific productivity, and lower peak VCDs in the low-glutamine condition, while the high-glutamine condition achieved high lactate production and higher PPP flux. This study highlights the need to optimize the amino acid composition of culture media to achieve desired metabolic phenotypes. McAtee Pereira

Cell Line & Product	Tracer(s) Used	Culture Mode and Scale	Reference
IgG-producing and non-producing CHOK1SV	[1,2-$^{13}C_2$] and [U-$^{13}C_6$] Glucose	3L fed-batch bioreactors	[21]
IgG1-producing GS-CGO	[1,2-$^{13}C_2$] and [U-$^{13}C_6$] Glucose	3L perfusion and fed-batch bioreactors	[72]
AV-producing MDCK	[1,2-$^{13}C_2$] and [U-$^{13}C_6$] Glucose	6-well culture plates	[73]
AV-producing 1G3	[1,2-$^{13}C_2$] and [U-$^{13}C_6$] Glucose	6-well culture plates	[74]
IgG-producing CHO DP-12	[U-$^{13}C_6$] Glucose	3.5L fed-batch bioreactors	[75]
CHO-K1	[1-$^{13}C_1$], [2-$^{13}C_1$], [3-$^{13}C_1$], and [4,5,6-$^{13}C_3$] Glucose	T-25 culture flasks	[76]
IgG producing CHO	[1,2-$^{13}C_2$] and [U-$^{13}C_6$] Glucose; [1,2-$^{13}C_2$] Mannose	24 deep-well plates	[77]
Cumate-inducible IgG producing CHO	[1-$^{13}C_2$], [6-$^{13}C_2$], and [U-$^{13}C_6$] Glucose; [U-$^{13}C_5$] Glutamine	125 mL shake flasks	[78]
mAb-producing CHO	[1,2-$^{13}C_2$] Glucose and [U-$^{13}C_5$] Glutamine	250 mL shake flasks	[79]
Recombinant protein-producing CHO	[U-$^{13}C_6$] Glucose	3L fed-batch bioreactors	[80]
Cumate-inducible mAb producing CHO	[1-$^{13}C_1$], [6-$^{13}C_1$], and [U-$^{13}C_6$] Glucose; [U-$^{13}C_5$] Glutamine	Semi-continuous, 10 mL working volume shake flasks	[81]
High-producing dihydrofolate reductase-deficient CHO	[1-$^{13}C_1$], [1,2-$^{13}C_2$], and [U-$^{13}C_6$] Glucose	125 mL shake flasks or 24-deep well plates	[36]
Interferon-α2b-producing HEK293	[1-$^{13}C_1$], [6-$^{13}C_1$], and [U-$^{13}C_6$] Glucose; [U-$^{13}C_5$] Glutamine	Semi-continuous 50 mL spin-tubes	[82]

Table 2.2: **Summary of experimental parameters of the studies highlighted in this chapter.**

et al. [79] used parallel ^{13}C MFA experiments to determine metabolic changes caused by a media developed to lower ammonia production in industrial CHO cells. Central carbon metabolism, growth, and specific productivity were unaffected by the media alterations, likely because amino acids in the media were replaced with complementary nutrients. ^{13}C MFA was able to confirm that rebalancing of amino acid metabolism was accomplished without impacting key metabolic branch points.

In addition to sugars and amino acids, micronutrients can impact cellular metabolism. Nargund et al. [80] used ^{13}C MFA to study the role copper plays in CHO cell metabolism. Copper deficiency disrupts the electron transport complex, limiting energy production. By comparing high-copper cultures to low-copper cultures, the authors found that low-copper conditions led to an elimination of flux through the PPP and decreased TCA cycle flux, indicative of a dysfunctional ETC and a need for aerobic glycolysis to produce ATP and NAD^+. Although final titer was not affected by copper concentration in the media, this study highlights how intracellular metabolism can be modulated by adjusting micronutrient availability.

2.3.5.3 Characterization of metabolically engineered clones

^{13}C MFA can help to identify bottlenecks in pathways and hallmarks of desirable phenotypes that may not be readily observable through other methods. Upon identification of possible metabolic engineering targets, characterization of engineered clones is necessary to test the validity of the hypothesized alterations and to iteratively improve cell culture performance (Fig. 2.4).

Due to the increased burden of recombinant protein production, there is interest in inducible expression systems to begin protein production after cells have reached stationary phase. Sheikholeslami et al. [81] used ^{13}C MFA to study a CHO cell line that had been engineered with a cumate-inducible expression system, allowing the expression of the recombinant protein to be controlled in order to decouple cell growth from product formation.

This study highlighted the metabolic changes that occur following induction of product expression. An increase in TCA cycle flux was observed post-induction, likely due to an increased need for energy and biosynthetic precursors for recombinant protein production. Even though the onset of protein production did not occur until stationary phase, the increased energy demand observed in other studies was still observed [28, 36].

A major focus of host cell engineering has been lactate metabolism. Lactate is a major byproduct of growth, due to the "Warburg Effect" that is commonly observed in CHO cells during exponential phase. This excess production of lactate is important for maintaining redox balance, producing NAD^+ that is required for glycolysis [83]. Lactate metabolism often switches from production to consumption during stationary phase, and high lactate consumption has been found to correlate with high mAb production [36]. The switch from lactate production to lactate consumption has also been observed in HEK293 cells [84].

Lactate is produced from pyruvate via lactate dehydrogenase, so redirecting pyruvate flux into the TCA cycle is a possible strategy to draw carbon away from lactate production. In HEK293 cells engineered to express pyruvate carboxylase (PC) from yeast, Henry et al. [82] found PC-expressing cells to be more metabolically efficient than the parental cells. This increased efficiency was highlighted by a decrease in glucose and glutamine consumption as well as lower lactate production. Interestingly, qP was unchanged in PC-expressing cells, but volumetric titer was increased due to increased VCD.

In addition to PC, pyruvate dehydrogenase (PDH) is a major enzyme responsible for the entry of pyruvate into the TCA cycle. Buchsteiner et al. [85] found that the treatment of CHO cells with a PDH kinase inhibitor caused a reduction in lactate production and glycolytic fluxes, while TCA cycle flux and qP were maintained when compared to an untreated control. Higher volumetric titer was achieved alongside a higher VCD, likely due to the reduced lactate concentration and delayed glucose depletion in the inhibitor-treated cultures. These studies highlight the use of metabolic engineering to create clones that exhibit desirable metabolic phenotypes.

References

[1] Sarah A Sacco and Jamey D Young. 13C metabolic flux analysis in cell line and bioprocess development. *Current Opinion in Chemical Engineering*, 34, 2021.

[2] Benjamin Leader, Quentin J. Baca, and David E. Golan. Protein therapeutics: A summary and pharmacological classification. *Nature Reviews Drug Discovery*, 7(1):21–39, 2008.

[3] Nabih A. Baeshen, Mohammed N. Baeshen, Abdullah Sheikh, Roop S. Bora, Mohamed Morsi M. Ahmed, Hassan A.I. Ramadan, Kulvinder Singh Saini, and Elrashdy M. Redwan. Cell factories for insulin production. *Microbial Cell Factories*, 13(1):1–9, 2014.

[4] Gary Walsh. Biopharmaceutical benchmarks 2018. *Nature Biotechnology*, 36(12):1136–1145, 2018.

[5] Hannah K Weir, Trevor D Thompson, Sherri L Stewart, and Mary C White. Cancer Incidence Projections in the United. pages 1–8, 2021.

[6] Ji Lin, Theodore J. Thompson, Yiling J. Cheng, Xiaohui Zhuo, Ping Zhang, Edward Gregg, and Deborah B. Rolka. Projection of the future diabetes burden in the United States through 2060. *Population Health Metrics*, 16(1):1–9, 2018.

[7] Brian Kelley. Developing therapeutic monoclonal antibodies at pandemic pace. *Nature Biotechnology*, 38(5):540–545, 2020.

[8] Neil Templeton and Jamey D. Young. Biochemical and metabolic engineering approaches to enhance production of therapeutic proteins in animal cell cultures. *Biochemical Engineering Journal*, 136:40–50, 2018.

[9] H. Michael Shepard, Gail Lewis Phillips, Christopher D. Thanos, and Marc Feldmann. Developments in therapy with monoclonal antibodies and related proteins. *Clinical Medicine, Journal of the Royal College of Physicians of London*, 17(3):220–232, 2017.

[10] Malgorzata Kesik-Brodacka. Progress in biopharmaceutical development. *Biotechnology and Applied Biochemistry*, 65(3):306–322, 2018.

[11] Brian Buntz. 50 of 2020's best-selling pharmaceuticals.

[12] Christopher L. Gaughan. The present state of the art in expression, production and characterization of monoclonal antibodies. *Molecular Diversity*, 20(1):255–270, 2016.

[13] F M Wurm. Production of recombinant protein therapeutics in cultivated mammalian cells. *Nat Biotechnol*, 22(11):1393–1398, 2004.

[14] Kenji Masuda, Kazuhiko Watanabe, Tomonori Ueno, Yuto Nakazawa, Yumiko Tanabe, Yuko Ushiki-Kaku, Kiyoko Ogawa-Goto, Yukikazu Ehara, Hisashi Saeki, Takeshi Okumura, Koichi Nonaka, and Masamichi Kamihira. Novel cell line development strategy for monoclonal antibody manufacturing using translational enhancing technology. *Journal of Bioscience and Bioengineering*, xxx(xxx), 2021.

[15] Karthik P. Jayapal, Katie F. Wlaschin, Wei Shou Hu, and Miranda G.S. Yap. Recombinant protein therapeutics from CHO Cells - 20 years and counting. *Chemical Engineering Progress*, 103(10):40–47, 2007.

[16] Sven Mathias, Anna Wippermann, Nadja Raab, Nikolas Zeh, René Handrick, Ingo Gorr, Patrick Schulz, Simon Fischer, Martin Gamer, and Kerstin Otte. Unraveling what makes a monoclonal antibody difficult-to-express: From intracellular accumulation to incomplete folding and degradation via ERAD. *Biotechnology and Bioengineering*, 117(1):5–16, 2020.

[17] Ruei Min Lu, Yu Chyi Hwang, I. Ju Liu, Chi Chiu Lee, Han Zen Tsai, Hsin Jung Li, and Han Chung Wu. Development of therapeutic antibodies for the treatment of diseases. *Journal of Biomedical Science*, 27(1):1–30, 2020.

[18] Helen Dowden and Jamie Munro. Trends in clinical success rates and therapeutic focus. *Nature reviews. Drug discovery*, 18(7):495–496, 2019.

[19] Olivier J. Wouters, Martin McKee, and Jeroen Luyten. Estimated Research and Development Investment Needed to Bring a New Medicine to Market, 2009-2018. *JAMA - Journal of the American Medical Association*, 323(9):844–853, 2020.

[20] Jean Marc Bielser, Moritz Wolf, Jonathan Souquet, Hervé Broly, and Massimo Morbidelli. Perfusion mammalian cell culture for recombinant protein manufacturing – A critical review. *Biotechnology Advances*, 36(4):1328–1340, 2018.

[21] Neil Templeton, Sen Xu, David J Roush, and Hao Chen. 13C metabolic flux analysis identifies limitations to increasing specific productivity in fed-batch and perfusion. *Metabolic Engineering*, 44(September):126–133, 2017.

[22] Zehra Elgundi, Mouhamad Reslan, Esteban Cruz, Vicki Sifniotis, and Veysel Kayser. The state-of-play and future of antibody therapeutics. *Advanced Drug Delivery Reviews*, 122:2–19, 2017.

[23] Smriti Shridhar, Gerald Klanert, Norbert Auer, Inmaculada Hernandez-Lopez, Maciej M. Kańduła, Matthias Hackl, Johannes Grillari, Nancy Stralis-Pavese, David P. Kreil, and Nicole Borth. Transcriptomic changes in CHO cells after adaptation to suspension growth in protein-free medium analysed by a species-specific microarray. *Journal of Biotechnology*, 257:13–21, 2017.

[24] Simon Fischer, René Handrick, and Kerstin Otte. The art of CHO cell engineering : A comprehensive retrospect and future perspectives. *Biotechnology Advances*, 33(8):1878–1896, 2015.

[25] Sara Pereira, Helene Faustrup Kildegaard, and Mikael Rørdam Andersen. Impact of CHO Metabolism on Cell Growth and Protein Production: An Overview of Toxic and Inhibiting Metabolites and Nutrients. *Biotechnology Journal*, 13(3):1–13, 2018.

[26] Valerie Le Fourn, Pierre-alain Girod, Montse Buceta, Alexandre Regamey, and Nicolas Mermod. CHO cell engineering to prevent polypeptide aggregation and improve therapeutic protein secretion. *Metabolic Engineering*, 21:91–102, 2014.

[27] Woo Suk Ahn and Maciek R Antoniewicz. Towards dynamic metabolic flux analysis in CHO cell cultures. *Biotechnology Journal*, 7:61–74, 2012.

[28] Neil Templeton, Kevin D Smith, Allison G Mcatee-pereira, Haimanti Dorai, J Betenbaugh, Steven E Lang, and Jamey D Young. Application of 13C flux analysis to identify high-productivity CHO metabolic phenotypes. *Metabolic Engineering*, 43(B):218–225, 2017.

[29] Ankita Singh, Helene F. Kildegaard, and Mikael R. Andersen. An Online Compendium of CHO RNA-Seq Data Allows Identification of CHO Cell Line-Specific Transcriptomic Signatures. *Biotechnology Journal*, 1800070:1–11, 2018.

[30] Peggy Ko, Shahram Misaghi, Zhilan Hu, Dejin Zhan, Joni Tsukuda, Mandy Yim, Mark Sanford, David Shaw, Masaru Shiratori, Brad Snedecor, Michael Laird, and Amy Shen. Probing the importance of clonality: Single cell subcloning of clonally derived CHO cell lines yields widely diverse clones differing in growth, productivity, and product quality. *Biotechnology Progress*, 34(3):624–634, 2018.

[31] Hussain Dahodwala and Kelvin H. Lee. The fickle CHO: a review of the causes, implications, and potential alleviation of the CHO cell line instability problem. *Current Opinion in Biotechnology*, 60(August 2018):128–137, 2019.

[32] Florian M. Wurm. CHO quasispecies-Implications for manufacturing processes. *Processes*, 1(3):296–311, 2013.

[33] Florian M. Wurm and Maria João Wurm. Cloning of CHO Cells, productivity and genetic stability-a discussion. *Processes*, 5(2), 2017.

[34] Gino Stolfa, Matthew T. Smonskey, Ryan Boniface, Anna Barbara Hachmann, Paul Gulde, Atul D. Joshi, Anson P. Pierce, Scott J. Jacobia, and Andrew Campbell. CHO-Omics Review: The Impact of Current and Emerging Technologies on Chinese Hamster Ovary Based Bioproduction. *Biotechnology Journal*, 13(3):1–14, 2018.

[35] Gargi Seth, Patrick Hossler, Joon Chong Yee, and Wei-Shou Hu. Engineering Cells for Cell Culture Bioprocessing- Physiological Fundamentals. *Adv Biochem Eng Biotechnol*, 101:119–164, 2006.

[36] Neil Templeton, Jason Dean, Pranhitha Reddy, and Jamey D. Young. Peak antibody production is associated with increased oxidative metabolism in an industrially relevant fed-batch CHO cell culture. *Biotechnology and Bioengineering*, 110(7):2013–2024, 2013.

[37] Jason Walther, Jiuyi Lu, Myles Hollenbach, Marcella Yu, Chris Hwang, Jean Mclarty, and Kevin Brower. Perfusion Cell Culture Decreases Process and Product Heterogeneity in a Head-to-Head Comparison With. *Biotechnology Journal*, 14(1700733):1–10, 2019.

[38] Jason Dean and Pranhitha Reddy. Metabolic analysis of antibody producing CHO cells in fed-batch production. *Biotechnology and Bioengineering*, 110(6):1735–1747, 2013.

[39] Bhanu Chandra Mulukutla, Jaitashree Kale, Taylor Kalomeris, Michaela Jacobs, and Gregory W. Hiller. Identification and control of novel growth inhibitors in fed-batch cultures of Chinese hamster ovary cells. *Biotechnology and Bioengineering*, 114(8):1779–1790, 2017.

[40] Hamideh Fouladiha, Sayed-Amir Marashi, Fatemeh Torkashvand, Fereidoun Mahboudi, Nathan E Lewis, and Behrouz Vaziri. A metabolic network-based approach for developing feeding strategies for CHO cells to increase monoclonal antibody production. *bioRxiv*, page 751347, 2020.

[41] Xiaolin Zhang, Rubin Jiang, Henry Lin, and Sen Xu. Feeding tricarboxylic acid cycle intermediates improves lactate consumption and antibody production in Chinese hamster ovary cell cultures. *Biotechnology Progress*, (January):1–9, 2020.

[42] Allison G. McAtee Pereira, Jason L. Walther, Myles Hollenbach, Jamey D. Young, Allison G. McAtee Pereira, Jason L. Walther, Myles Hollenbach, and Jamey D. Young. 13C Flux Analysis Reveals that Rebalancing Medium Amino Acid Composition can Reduce Ammonia Production while Preserving Central Carbon Metabolism of CHO Cell Cultures. *Biotechnology Journal*, 13(10):1–7, 2018.

[43] Chih Chung Kuo, Austin WT Chiang, Isaac Shamie, Mojtaba Samoudi, Jahir M. Gutierrez, and Nathan E. Lewis. The emerging role of systems biology for engineering protein production in CHO cells. *Current Opinion in Biotechnology*, 51:64–69, 2018.

[44] Francesco Massimo Lasorsa, Paolo Pinton, Luigi Palmieri, Giuseppe Fiermonte, Rosario Rizzuto, and Ferdinando Palmieri. Recombinant expression of the Ca(2+)-sensitive aspartate/glutamate carrier increases mitochondrial ATP production in agonist-stimulated Chinese hamster ovary cells. *The Journal of biological chemistry*, 278(40):38686–38692, 2003.

[45] Cécile Toussaint, Olivier Henry, and Yves Durocher. Metabolic engineering of CHO cells to alter lactate metabolism during fed-batch cultures. *Journal of Biotechnology*, 217:122–131, 2016.

[46] Sanjeev Kumar Gupta, Santosh K. Srivastava, Ankit Sharma, Vaibhav H. H. Nalage, Darshita Salvi, Hiralal Kushwaha, Nikhil B. Chitnis, and Pratyoosh Shukla. Metabolic engineering of CHO cells for the development of a robust protein production platform. *Plos One*, 12(8):e0181455, 2017.

[47] Bhanu Chandra Mulukutla, Jeffrey Mitchell, Pauline Geoffroy, Cameron Harrington, Manisha Krishnan, Taylor Kalomeris, Caitlin Morris, Lin Zhang, Pamela Pegman, Gregory W. Hiller, Jeffrey Mitchell, Cameron Harrington, Manisha Krishnan, Taylor Kalomeris, Caitlin Morris, Lin Zhang, Pamela Pegman, and Gregory W. Hiller. Metabolic engineering of Chinese hamster ovary cells towards reduced biosynthesis and accumulation of novel growth inhibitors in fed-batch cultures. *Metabolic Engineering*, 54(March):54–68, 2019.

[48] Daniel Ley, Sara Pereira, Lasse Ebdrup Pedersen, Johnny Arnsdorf, Hooman Hefzi, Anne Mathilde Davy, Tae Kwang Ha, Tune Wulff, Helene Faustrup Kildegaard, and Mikael Rørdam Andersen. Reprogramming AA catabolism in CHO cells with CRISPR/Cas9 genome editing improves cell growth and reduces byproduct secretion. *Metabolic Engineering*, 56(August):120–129, 2019.

[49] Agata Oberbek, Mattia Matasci, David L. Hacker, and Florian M. Wurm. Generation of stable, high-producing cho cell lines by lentiviral vector-mediated gene transfer in serum-free suspension culture. *Biotechnology and Bioengineering*, 108(3):600–610, 2011.

[50] Bruno Gaillet, Rénald Gilbert, Sophie Broussau, Amélie Pilotte, Félix Malenfant, Alaka Mullick, Alain Garnier, and Bernard Massie. High-level recombinant protein production in CHO cells using lentiviral vectors and the cumate gene-switch. *Biotechnology and Bioengineering*, 106(2):203–215, 2010.

[51] Sung Wook Shin and Jae Seong Lee. Optimized CRISPR/Cas9 strategy for homology-directed multiple targeted integration of transgenes in CHO cells. *Biotechnology and Bioengineering*, 117(February):1–9, 2020.

[52] Kai Xiong, Kim Fabiano Marquart, Karen Julie la Cour Karottki, Shangzhong Li, Isaac Shamie, Jae Seong Lee, Signe Gerling, Nan Cher Yeo, Alejandro Chavez, Gyun Min Lee, Nathan E. Lewis, and Helene Faustrup Kildegaard. Reduced Apoptosis in Chinese Hamster Ovary Cells via Optimized CRISPR Interference. *Biotechnology and Bioengineering*, page bit.26969, 2019.

[53] Sowmya Balasubramanian, Robert B. Peery, Jeremy Minshull, Maggie Lee, Regina White, Ronan M. Kelly, and Gavin C. Barnard. Generation of High Expressing Chinese Hamster Ovary Cell Pools Using the Leap-In Transposon System. *Biotechnology Journal*, 13(10):1–8, 2018.

[54] Samira Ahmadi, Fatemeh Davami, Noushin Davoudi, Fatemeh Nematpour, Maryam Ahmadi, Saeedeh Ebadat, Kayhan Azadmanesh, Farzaneh Barkhordari, and Fereidoun Mahboudi. Monoclonal antibodies expression improvement in CHO cells by PiggyBac transposition regarding vectors ratios and design. *PLoS ONE*, 12(6):1–16, 2017.

[55] Sowmya Balasubramanian, Yashas Rajendra, Lucia Baldi, David L. Hacker, and Florian M. Wurm. Comparison of three transposons for the generation of highly produc-

tive recombinant CHO cell pools and cell lines. *Biotechnology and Bioengineering*, 113(6):1234–1243, 2016.

[56] Maciek R. Antoniewicz. A guide to metabolic flux analysis in metabolic engineering: Methods, tools and applications. *Metabolic Engineering*, 63:2–12, 2020.

[57] Scott B. Crown, Christopher P. Long, and Maciek R. Antoniewicz. Optimal tracers for parallel labeling experiments and 13C metabolic flux analysis: A new precision and synergy scoring system. *Metabolic Engineering*, 38:10–18, 2016.

[58] Maciek R. Antoniewicz. Parallel labeling experiments for pathway elucidation and 13C metabolic flux analysis. *Current Opinion in Biotechnology*, 36:91–97, 2015.

[59] Christopher P. Long, Jennifer Au, Jacqueline E. Gonzalez, and Maciek R. Antoniewicz. 13C metabolic flux analysis of microbial and mammalian systems is enhanced with GC-MS measurements of glycogen and RNA labeling. *Metabolic Engineering*, 38:65–72, 2016.

[60] Taylor A. Murphy and Jamey D. Young. ETA: Robust software for determination of cell specific rates from extracellular time courses. *Biotechnology and Bioengineering*, 110(6):1748–1758, 2013.

[61] Jamey D Young, Douglas K Allen, and John A Morgan. Chapter 7 Isotopomer Measurement Techniques in Metabolic Flux Analysis II : Mass Spectrometry. *Plant Metabolism: Methods and Protocols*, 1083:85–108, 2014.

[62] Maciek R. Antoniewicz, David F. Kraynie, Lisa A. Laffend, Joanna González-Lergier, Joanne K. Kelleher, and Gregory Stephanopoulos. Metabolic flux analysis in a nonstationary system: Fed-batch fermentation of a high yielding strain of E. coli producing 1,3-propanediol. *Metabolic Engineering*, 9(3):277–292, 2007.

[63] Lake Ee Quek, Christoph Wittmann, Lars K. Nielsen, and Jens O. Krömer. OpenFLUX: Efficient modelling software for 13C-based metabolic flux analysis. *Microbial Cell Factories*, 8, 2009.

[64] Kashif Sheikh, Jochen Förster, and Lars K. Nielsen. Modeling hybridoma cell metabolism using a generic genome-scale metabolic model of Mus musculus. *Biotechnology Progress*, 21(1):112–121, 2005.

[65] Averina Nicolae, Judith Wahrheit, Janina Bahnemann, An Ping Zeng, and Elmar Heinzle. Non-stationary 13C metabolic flux analysis of Chinese hamster ovary cells in batch culture using extracellular labeling highlights metabolic reversibility and compartmentation. *BMC Systems Biology*, 8(1):1–15, 2014.

[66] Yi Ern Cheah and Jamey D. Young. Isotopically nonstationary metabolic flux analysis (INST-MFA): putting theory into practice. *Current Opinion in Biotechnology*, 54:80–87, 2018.

[67] Wolfgang Wiechert and Katharina Nöh. Isotopically non-stationary metabolic flux analysis: Complex yet highly informative. *Current Opinion in Biotechnology*, 24(6):979–986, 2013.

[68] Ahn Woo Suk and Maciek R. Antoniewicz. Parallel labeling experiments with [1,2-13C]glucose and [U-13C]glutamine provide new insights into CHO cell metabolism. *Metabolic Engineering*, 15(1):34–47, 2013.

[69] Maciek R. Antoniewicz, Joanne K. Kelleher, and Gregory Stephanopoulos. Determination of confidence intervals of metabolic fluxes estimated from stable isotope measurements. *Metabolic Engineering*, 8(4):324–337, 2006.

[70] Jamey D. Young. INCA: A computational platform for isotopically non-stationary metabolic flux analysis. *Bioinformatics*, 30(9):1333–1335, 2014.

[71] Maciek R. Antoniewicz. A guide to 13C metabolic flux analysis for the cancer biologist. *Experimental Molecular Medicine*, 50(4):19, 2018.

[72] Neil Templeton, Sen Xu, David J. Roush, and Hao Chen. 13C metabolic flux analysis identifies limitations to increasing specific productivity in fed-batch and perfusion. *Metabolic Engineering*, 44(August):126–133, 2017.

[73] Nuno Carinhas, Daniel A M Pais, Alexey Koshkin, and Paulo Fernandes. Metabolic flux profiling of MDCK cells during growth and canine adenovirus vector production. *Nature Publishing Group*, (March):1–11, 2016.

[74] Nuno Carinhas, Alexey Koshkin, Daniel A.M. Pais, Paula M. Alves, and Ana P. Teixeira. 13C-metabolic flux analysis of human adenovirus infection: Implications for viral vector production. *Biotechnology and Bioengineering*, 114(1):195–207, 2017.

[75] Lisa Junghans, Attila Teleki, Andy Wiranata Wijaya, Max Becker, Michael Schweikert, and Ralf Takors. From nutritional wealth to autophagy: In vivo metabolic dynamics in the cytosol, mitochondrion and shuttles of IgG producing CHO cells. *Metabolic Engineering*, 54(January):145–159, 2019.

[76] Woo Suk Ahn, Scott B. Crown, and Maciek R. Antoniewicz. Evidence for transketolase-like TKTL1 flux in CHO cells based on parallel labeling experiments and 13C-metabolic flux analysis. *Metabolic Engineering*, 37:72–78, 2016.

[77] Peter G. Slade, R. Guy Caspary, Shilpa Nargund, and Chung Jr Huang. Mannose metabolism in recombinant CHO cells and its effect on IgG glycosylation. *Biotechnology and Bioengineering*, 113(7):1468–1480, 2016.

[78] Zahra Sheikholeslami, Mario Jolicoeur, and Olivier Henry. Elucidating the effects of postinduction glutamine feeding on the growth and productivity of CHO cells. *Biotechnology Progress*, 30(3):535–546, 2014.

[79] A.G. Mcatee Pereira, J.L. Walther, M. Hollenbach, and J.D. Young. ¡sup¿13¡/sup¿C Flux Analysis Reveals that Rebalancing Medium Amino Acid Composition can Reduce Ammonia Production while Preserving Central Carbon Metabolism of CHO Cell Cultures. *Biotechnology Journal*, 2018.

[80] Shilpa Nargund, Jinshu Qiu, and Chetan T. Goudar. Elucidating the role of copper in CHO cell energy metabolism using 13C metabolic flux analysis. *Biotechnology Progress*, 31(5):1179–1186, 2015.

[81] Zahra Sheikholeslami, Mario Jolicoeur, and Olivier Henry. Probing the metabolism of an inducible mammalian expression system using extracellular isotopomer analysis. *Journal of Biotechnology*, 164(4):469–478, 2013.

[82] Olivier Henry, Mario Jolicoeur, and Amine Kamen. Unraveling the metabolism of HEK-293 cells using lactate isotopomer analysis. *Bioprocess and Biosystems Engineering*, 34(3):263–273, 2011.

[83] Fiona Hartley, Tracy Walker, Vicky Chung, and Karl Morten. Mechanisms driving the lactate switch in Chinese hamster ovary cells. *Biotechnology and Bioengineering*, 115(8):1890–1903, 2018.

[84] Iván Martínez-Monge, Joan Albiol, Martí Lecina, Leticia Liste-Calleja, Joan Miret, Carles Solà, and Jordi J. Cairó. Metabolic flux balance analysis during lactate and glucose concomitant consumption in HEK293 cell cultures. *Biotechnology and Bioengineering*, 116(2):388–404, 2019.

[85] Maria Buchsteiner, Lake Ee Quek, Peter Gray, and Lars K. Nielsen. Improving culture performance and antibody production in CHO cell culture processes by reducing the Warburg effect. *Biotechnology and Bioengineering*, 115(9):2315–2327, 2018.

CHAPTER 3

Attenuation of glutamine synthetase selection marker improves product titer and reduces glutamine overflow in Chinese hamster ovary cells

This chapter is adapted from Attenuation of glutamine synthetase selection marker improves product titer and reduces glutamine overflow in Chinese hamster ovary cells *published in* Biotechnology and Bioengineering *and has been reproduced with the permission of the publisher and my co-authors, Angela Tuckowski, Irina Trenary, Lauren Kraft, Michael Betenbaugh, Jamey Young, and Kevin Smith.* [1]

Abstract

Chinese hamster ovary (CHO) cells are used extensively throughout the biopharmaceutical industry, producing nearly 70% of all protein therapeutics. The glutamine synthetase (GS) selection system is commonly used to ensure stable transgene integration and amplification in CHO host lines. Transfected cell populations are typically grown in the presence of the GS inhibitor, methionine sulfoximine (MSX), to further select for increased transgene copy number. However, high levels of GS activity produce excess glutamine. We hypothesized that attenuating the GS promoter while keeping the strong IgG promoter on the GS-IgG expression vector would result in a more efficient cellular metabolic phenotype. Herein, we characterized CHO cell lines expressing GS from either an attenuated promoter or an SV40 promoter and selected either with or without MSX. CHO cells with the attenuated GS promoter had higher IgG specific productivity and lower glutamine production compared to cells with SV40-driven GS expression. Selection with MSX increased both specific productivity and glutamine production, regardless of GS promoter strength. ^{13}C metabolic flux analysis (MFA) was performed to further assess metabolic differences between these cell lines. Interestingly, central carbon metabolism was unaltered by the attenuated GS promoter while the fate of glutamate and glutamine varied depending on promoter strength and MSX selection. This study highlights the ability to optimize the

GS selection system to improve IgG production and reduce wasteful glutamine overflow, without significantly altering central metabolism. Additionally, we provide a detailed supplementary analysis of two "lactate runaway" reactors that provides insight into the poorly understood phenomenon of excess lactate production by some CHO cell cultures.

3.1 Introduction

The biopharmaceuticals market has grown rapidly since the approval of the first recombinant protein therapeutic, tissue plasminogen activator, in 1986 [2]. Biopharmaceuticals consist of cellular components or macromolecules, such as monoclonal antibodies (mAbs), and are among the most expensive drug compounds on the market [3, 4]. Due to their complexity, biopharmaceuticals are typically produced in mammalian cells; in particular, Chinese hamster ovary (CHO) cells are considered the "workhorse" of the biopharma industry, as they are used to produce nearly 70% of all protein therapeutics [2, 5]. CHO cells are a preferred host for a number of reasons, including their ability to perform post-translational modifications that are necessary for the efficacy of many therapeutic proteins [6, 7], ability to grow in serum-free media [8, 9, 10], and the development of suspension CHO lines that facilitate process scale-up [11, 12].

Media and bioprocess optimization efforts have resulted in dramatic improvements in viable cell densities (VCDs) and final product titers over the past 30 years [13, 14]. However, comparatively little progress has been achieved in enhancing cell-specific production rate (qP), which represents an untapped opportunity to further increase product yield [15]. Additionally, the high VCDs attained in modern bioprocesses are associated with accumulation of toxic byproducts, specifically lactate and ammonia, which introduce unwanted variability into cell culture bioprocesses [16], impact the glycosylation profile of recombinant proteins, and have been linked to drastic declines in cell viability during production phase of fed-batch cultures [17, 18]. As a result, there is a pressing need to develop improved host cell lines and expression systems that can effectively balance the competing

metabolic requirements for cell growth and product biosynthesis in order to meet the increasing demand for biopharmaceuticals manufacturing.

The glutamine synthetase (GS) selection system is widely used in industrial CHO lines to achieve stable transgene integration and amplification [19]. The GS enzyme catalyzes direct glutamine synthesis from glutamate, ammonia, and ATP [19]. Because most immortalized cell lines express low endogenous levels of GS, glutamine is an "essential" nutrient in CHO cell cultures. Transfecting CHO cells with a recombinant vector that expresses GS cDNA in addition to the transgene(s) of interest enables stable clone selection through growth of cells in glutamine-free medium. Parental CHO lines with deletion of the endogenous GS gene have been developed to further increase selection stringency [20]. The GS inhibitor methionine sulfoximine (MSX) is typically supplemented into the culture medium to promote gene amplification during clone selection [21, 22]. As a result, clones that do not integrate multiple copies of the GS expression vector will not grow in glutamine-free medium containing MSX since they will be incapable of synthesizing enough glutamine to support protein synthesis. MSX has also been shown to inhibit glutathione synthesis, which has been found to further increase mAb titer [23].

The typical GS-CHO system utilizes a single plasmid with strong promoters (e.g., CMV, SV40) driving expression of the GS enzyme and the biopharmaceutical product protein. The system was designed to select clones that could survive in glutamine-free medium with just 1-2 copies of the transgenes integrated. However, modern MSX selection strategies often result in clones with 10+ integrated copies. Because of excess GS expression, clones selected on MSX will often excrete glutamine into the culture medium as a waste product. Additionally, excess GS expression could create a potential metabolic burden fur to the energy and amino acid requirements for transcription and translation of the GS enzyme. Prior studies have shown that attenuating GS activity by either (i) mutating the viral promoter driving GS expression [24] or (ii) mutating the coding region of the GS gene itself [25] can lead to higher bulk culture productivity, greater prevalence of high-titer clones,

and improved production stability in the absence of MSX. However, these studies did not examine the impacts of attenuating GS activity on host metabolism or whether increases in productivity were associated with improved metabolic efficiency of the CHO host line.

The overall objective of the current study is to assess the metabolism of GS-CHO lines that express GS from an attenuated SV40 promoter to determine how reducing wasteful glutamine biosynthesis contributes to increased mAb production. We hypothesized that attenuating the GS selection marker, while keeping the same strong CMV promoters for the mAb light-chain and heavy-chain genes, would improve mAb production through redirecting host metabolism to a more efficient phenotype. We applied ^{13}C metabolic flux analysis (MFA) to examine the metabolic impacts of attenuating GS activity as well as selecting cells in the presence or absence of MSX. Weakening the SV40 promoter driving GS expression increased product qP of stable pools and decreased excess glutamine production; selection with MSX further increased productivity but also accelerated glutamine overflow. These effects were not associated with major flux alterations within central carbon metabolism. This study reveals that attenuating the GS selection marker can reduce wasteful amino acid metabolism while boosting product titers, suggesting that optimization of GS expression systems can lead to more efficient CHO cell lines.

3.2 Materials and Methods

3.2.1 Cell lines, transfection, and culture conditions

Cell lines were generated in a manner similar to that described by Dhiman et al. [26], with some alterations. Suspension-adapted Horizon Discovery CHO-K1 (HD-BIOP3) glutamine synthetase knockout cells were cultured in CDFortiCHO (Gibco/ThermoFisher) + 4 mM L-glutamine (Gibco/ThermoFisher) with 50 mL culture volume in 125 mL shake flasks at 130 rpm with a 25-mm orbit in a humidity controlled 37°C incubator with 5% CO2 and passaged every 3–4 days at $3x10^5$ viable cells/mL. Proprietary expression plasmids were licensed from ATUM (Newark, CA) conferring a functional GS gene driven by standard

Simian Virus 40 (SV40) or a weaker engineered promoter, unrelated to SV40, as well as IgG heavy and light chain genes driven by human cytomegalovirus (hCMV-MIE) promoters, Fifteen micrograms of each vector was transfected by electroporation (Bio-Rad Gene Pulser) into 1x10^6 cells in 1 mL Ex-Cell CD-CHO Fusion media (SAFC) by exponential decay at voltage of 300 V and capacitance of 950μF, either with or without supplemental MSX. Transfected cells were transferred to a T25 flask with 4 mL CDFortiCHO + 4 mM L-glutamine to recover for one day in a humidity controlled static incubator at 37°C with 5% CO2. Twenty-four hours post transfection, cells were centrifuged for media exchange for selection in 10 mL CD-OptiCHO without glutamine (Gibco/ThermoFisher) in a T75 flask for 7–12 days to generate non-clonal cell pools, maintaining the MSX concentration from transfection (Table 3.1). Cell bank vials were created with 2x10^6 cells in 1 mL CD OptiCHO selection media with 10% dimethyl sulfoxide (DMSO) and stored in liquid nitrogen.

Cell Pool	[MSX] Selection	HC Copy Number	LC Copy Number	Avg. Dry Cell Weight (pg)	Initial Lag Phase (days)
ATT(+)	10 μM	23	24	730 ± 0	1.16
ATT(-)	-	10	10	715 ± 35	0.90
SV40(+)	25 μM	14	14	680 ± 20	1.31
SV40(-)	-	3	3	635 ± 95	1.16

Table 3.1: **Key characteritics of cell lines used in this study.** Cell pools with the attenuated (ATT) or SV40 promoter driving GS expression were generated either with (+) or without (-) MSX selection. Copy numbers have been averaged over the entire non-clonal sample population, which is expected to contain a diverse set of random integrations. Dry cell weight measurements are the average of two experimental replicates. Lag phase duration was calculated as the time-intercept of the best-fit trendline of growth during exponential phase. HC=heavy chain, LC=light chain.

3.2.2 Isotope labeling experiments (ILES)

An ambr250 automated bioreactor system (Sartorius) with pH, temperature, agitation, and dissolved oxygen (DO) controls was used for cell culture. Culture pH was maintained between 6.7 and 7.3 by sodium carbonate additions or carbon dioxide sparging. Temper-

ature was held at 36.5°C. Agitation was set to 584 rpm using dual pitched blade impeller. Oxygen was set to sparge when DO reached 40% of saturation, maintaining DO levels between 40% and 100% of saturation. Prior to inoculation of bioreactors, cell bank vials were thawed, and cultures were passaged every 3–4 days and adapted to Janssen R&D proprietary medium without glutamine. These pre-cultures were grown in shake flasks under the same conditions described in Section 3.2.1. Bioreactor cultures were inoculated by seeding pre-cultures into a 220mL working volume of Janssen R&D proprietary medium followed by growth in batch mode for the first 3 days. Bioreactors were fed with glucose, amino acids, vitamins, and minerals daily using a Janssen R&D proprietary feed until the end of the run.

On day 6 of culture, a bolus feed containing glucose (unlabeled or [1,2-$^{13}C_2$]-labeled) was added to reactors to achieve a sufficient concentration such that glucose would not be fully consumed by the end of the experiment. The amount of glucose fed to each reactor was calculated based on the average glucose consumption rates of each cell line during days 6-9 of culture, which were determined from a pilot experiment. In addition, a complex feed containing amino acids and glutamate (unlabeled or [U-$^{13}C_5$]-labeled) was fed as a bolus; the amount fed was sufficient such that no amino acids were completely consumed by the end of the experiment. All conditions were repeated in at least duplicate reactors. The complete timeline of ILEs is provided in Table 3.2.

Samples consisting of media and quenched cell pellets were collected at 1, 24, 48, and 72 hours after the bolus feed. For media samples, 1 mL of culture was removed and centrifuged to remove cells. Media supernatant was removed and stored at -80°C until further analysis. Cold-quenching of cell pellets was performed as previously described [27]. In brief, a quenching solution consisting of 60% methanol and 40% AMBIC (0.85% w/v solution in water) was pre-chilled to at least -40°C in a 4.5 M $CaCl_2$ ice bath. An aliquot of culture was drawn from each bioreactor containing approximately 5x10^6 cells; this aliquot was quickly mixed with quenching solution at a ratio of 1 volume culture media to 5 vol-

	Day:	0	1	2	3	4	5	6	7	8	9
Experimental condition	**Feed type**										
Labeled glucose (n=2)	Unlabeled glucose				+	+	+				
	Unlabeled glutamate				+	+	+	Bolus			
	[1,2-$^{13}C_2$] glucose							Bolus			
Labeled glutamate (n=2)	Unlabeled glucose				+	+	+	Bolus			
	Unlabeled glutamate				+	+	+				
	[U-$^{13}C_5$] glutamate										
Unlabeled control (n=2)	unlabeled glucose				+	+	+	Bolus			
	unlabeled glutamate				+	+	+	Bolus			
ALL reactors	Amino Acids				+	+	+	Bolus			
	Tyrosine & Cysteine				+	+	+	+	+	+	+
Samples collected	Quenched cell pellet							X	X	X	X
	Extracellular media							X	X	X	X

Table 3.2: **Fed-batch schedule for isotope labeling experiments.** '+' indicates when the designated feed was added. Glucose was fed at volumes calculated to achieve a predetermined final concentration; all amino acids, including glutamate, tyrosine, and cysteine, were fed at a volume based on a fixed percentage of the total reactor volume. The bolus feeds on day 6 contained sufficient amounts of nutrients such that no metabolite would be depleted prior to the end of the experiment, as described in Section 3.2.2. The gray shaded area indicates the time span of the isotope labeling experiment.

umes quenching solution. Samples were centrifuged at 0°C at 1000 RCF for 1 minute. Supernatant was removed and cell pellets were stored at -80°C until further analysis.

3.2.3 Evaluation of heavy and light chain copy number

Gene copy number was determined by Digital Droplet PCR (ddPCR) on a QX200 (Bio-Rad), as previously described by Dhiman et al. [26]. In brief, a pellet of $1x10^6$ cells was harvested and frozen 17 days post thaw from the ambr250 bioreactor during exponential growth phase. Denomic DNA was isolated from the frozen pellet using a DNeasy Blood & Tissue Kit (Qiagen). Genomic DNA samples were fragmented by restriction digest with an enzyme that did not cut in the coding regions. Primer probe sets were designed with primers to specifically amplify heavy chain and light chain coding sequences of the transgene flanking a fluorescein (FAM) labelled probe that binds the amplicon. Analysis included a glucagon receptor (GcgR) housekeeping gene primer and hexachlorofluorescein (HEX) labelled probe set for normalization. Genomic DNA of the CHO host was fragmented with the same restriction enzyme as a negative control sample to ensure primer specificity of the transgene FAM labelled probe set and confirm the housekeeper HEX labelled probe set. A template-free water negative control and a transgene expression plasmid positive control were also included.

3.2.4 Extraction and derivatization of intracellular metabolites from quenched cell pellets

Extraction and derivatization of metabolites were performed as previously described [27]. In brief, 6 mL of a 2:1 mixture of ice-cold chloroform and ice-cold methanol was added to each cell pellet. This solution was vortexed for 30 min at 4°C. Then, 1.5 mL of ice-cold water and 6 μL of a 10-mM norvaline internal standard solution were added, and samples were vortexed for 5 minutes at 4°C. Samples were then centrifuged at 4000 RCF for 20 minutes at 4°C. The aqueous phase was collected and dried under air flow overnight. The dried sample was dissolved in 50 μL of methoxyamine reagent (MOX; Pierce, Rockford,

IL), sonicated for 30 min at room temperature, and incubated at 40°C for 90 minutes. Seventy μL of MTBSTFA + 1% TBDMCS in pyridine (Pierce) was added, and the sample was incubated for 30 min at 70°C.

3.2.5 Extraction and derivatization of extracellular metabolites

For media samples containing [1,2-$^{13}C_2$]glucose, tracer enrichment was measured using GC-MS after conversion of glucose to its di-O-isopropylidene propionate (DIO) derivative as described previously [28]. In brief, 300 μL of cold acetone was added to 20 μL of media. After centrifugation to remove debris, the supernatant was moved to a glass tube and dried under air flow at 60°C. 500 μL of a 1:46 v/v mixture of 96% sulfuric acid and acetone was added to the dried sample. After incubation for 60 min at room temperature, 400 μL of 0.44 mM sodium carbonate was added to neutralize the reaction; additionally, 1.5 mL of saturated sodium chloride solution and 1 mL of ethyl acetate were added. Tubes were vortexed and allowed to incubate until complete separation. The organic layer was removed and evaporated to dryness under air flow at room temperature. Then, 150 μL of a 2:1 propionic anhydride and pyridine mixture was added to the dried sample. After incubation for 30 min at 60°C, samples were evaporated to dryness under air flow at 60°C. Finally, samples were redissolved in 100 μL ethyl acetate prior to GC-MS analysis.

For media samples containing [U-$^{13}C_5$]glutamate, tracer enrichment was measured using GC-MS after conversion of glutamate to its tert-butyldimethylsilyl (TBDMS) derivative. Thirty μL of media was mixed with 360 μL of a 2:1 mixture of ice-cold methanol and chloroform. Samples were vortexed at -20°C for 10 min. After vortexing, 120 μL of ice-cold chloroform and 210 μL of ice-cold water were added to each sample. After centrifugation at 0°C for 10 min at 14,000 RPM, the aqueous phase was transferred to a new tube and the sample was dried under air flow overnight at room temperature. The dried samples were then derivatized as described in Section 3.2.4.

3.2.6 Gas chromatography-mass spectrometry (GC-MS) analysis of metabolites

As described previously [13], derivatized extracts were injected into an Agilent 7890A gas chromatogram with an Agilent HP-5ms column (30 m x 0.25 mm i.d. x 0.25 μm) connected to an Agilent 5977B GC/MSD. For TBDMS-derivatized cell pellet samples, the oven program was as follows: held at 80°C for 1 min, increased to 140°C at a rate of 20°C/min, then increased from 140°C to 234°C at 4°C/min, held at 234°C for 5 min, and finally increased from 234°C to 285°C at a rate of 20°C/min. A sample volume of 1 μL was injected at a 5:1 split ratio and column flow rate of 1 mL/min. Due to a wide range of metabolite concentrations in the cell pellets, the gain factor was dynamically adjusted using timed event mode. TBDMS-derivatized media samples were run using the same parameters as the cell pellets, but with a 15:1 split ratio. DIO-derivatized media samples were run using the following oven program: held at 80°C for 1 min, increased from 80°C to 220°C at a rate of 40°C/min, then increased from 220°C to 240°C at a rate of 10°C/min. The injection volume and flow rate were as described above, but a 30:1 split ratio was used.

3.2.7 Calculation of specific growth rate and extracellular exchange rates

Certain metabolites (glucose, lactate, glutamate, glutamine) and IgG were monitored using a Cedex BioHT (Roche), and cell density and viability were measured using a ViCell XR (Beckman Coulter). Cell viability was maintained at or above 90% throughout the experiments. Concentrations of all other amino acids were measured using an Agilent 1200 series high performance liquid chromatograph (HPLC) as described previously [29]. Specific growth rate and cell specific consumption and production rates were determined using the ETA software package [30], as previously described [29].

3.2.8 Cell dry weight and biomass composition

Dry cell weight was measured as described previously [27]. In brief, a known number of cells was transferred to a previously weighed bottle-top filter. After media was removed by vacuum filtration, the filters were left to dry in a non-humidified 37°C oven. Filters were

weighed after drying, and dry cell weight was calculated based on the change in mass. Cell biomass composition was estimated based on previously published values for hybridoma cells [31].

3.2.9 Metabolic network model

A metabolic model of CHO central carbon metabolism was developed to enable flux estimation by ^{13}C MFA. This metabolic network was based on previously published models [13, 32]. However, due to the inherent compartmentalization of metabolism in eukaryotic cells [33], the model included separate pools of metabolites present in both the mitochondria and cytosol; this compartmentalization was necessary to accurately describe the experimental measurements. The model contained reaction equations representing glycolysis, the pentose phosphate pathway (PPP), the TCA cycle, amino acid catabolism, cell growth, and IgG biosynthesis (84 reactions). Coefficients for the cell growth equation were determined based on the measured dry weight of each cell line and the cell biomass composition. A schematic depiction of the reaction network is shown in Fig. 3.1.

3.2.10 ^{13}C metabolic flux analysis (MFA)

The INCA software package [34] (publicly available at http://mfa.vueinnovations.com) was used to fit the experimental data to the metabolic model, as previously described [29]. While metabolic steady state was achieved, as confirmed by constant changes in concentrations of extracellular metabolites, isotopic steady state was not. Therefore, isotopically nonstationary MFA (INST-MFA) was applied to estimate fluxes [35]. Fluxes were regressed using the Levenberg-Marquardt optimization algorithm to simultaneously fit isotope labeling data from parallel [1,2-$^{13}C_2$]glucose and [U-$^{13}C_5$]glutamate tracer experiments. A minimum of 50 random restarts were used for each flux estimation to ensure a global minimum was found. To assess goodness-of-fit, flux results were subjected to a chi-square statistical test. 95% confidence intervals were calculated for each flux value using parameter continuation. Goodness-of-fit metrics for each flux solution are provided in

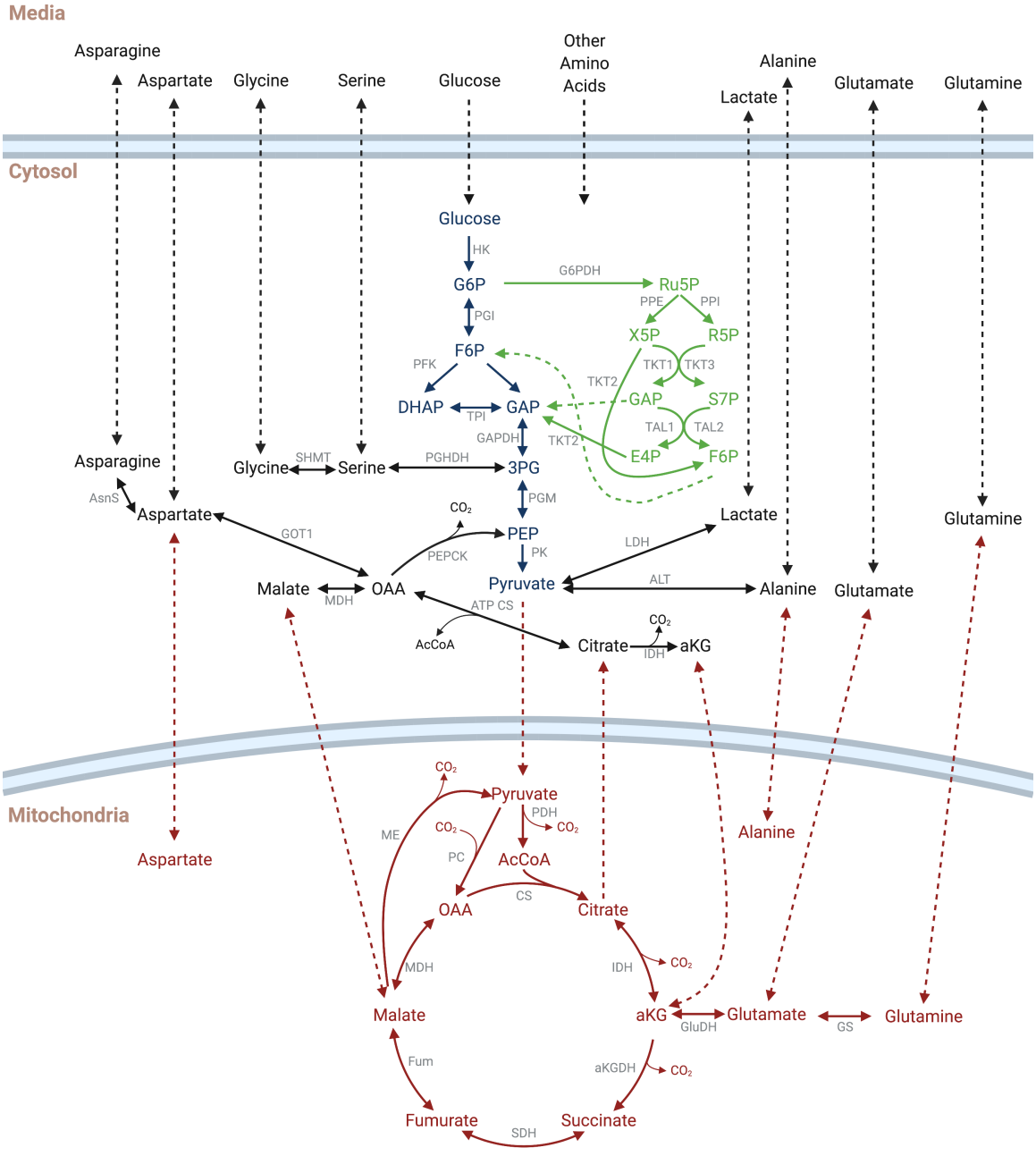

Figure 3.1: **Schematic of metabolic model used for ^{13}C MFA.** Media, cytosolic, and mitochondrial compartments are indicated. Metabolites and reactions are shown for glycolysis in blue font, the pentose phosphate pathway in green font, the TCA cycle in red font, and amino acid metabolism in black font. Solid arrows indicate reactions, with enzymes indicated in gray font. Dashed arrows indicate exchange of a metabolite between different compartments. Created with BioRender.com

Table 6.A1, and the full list of best-fit flux values and 95% confidence intervals are shown in Tables 3.A2, 3.A3, 3.A4, and 3.A5.

3.2.11 Statistical analysis

One-way ANOVA was used to determine statistically significant differences between cell lines (α = 0.05). A Tukey multiple comparison test was applied if significant differences were detected. The standard error of the mean (SEM) was estimated for intracellular fluxes using the formula SEM = (UB-LB)/3.92, where UB and LB represent the upper and lower bounds of the 95% confidence intervals, respectively, and 3.92 is the number of standard errors that span the 95% confidence interval of a normally distributed random variable.

3.3 Results

3.3.1 GS attenuation and MSX selection lead to increased transgene copy number

We adapted the standard GS system by partially crippling the SV40 promoter driving expression of the GS gene while maintaining the same strong CMV promoters for the IgG light-chain and heavy-chain genes. CHO cell lines were engineered to produce IgG from either the attenuated GS system (ATT) or the standard SV40-based system (SV40). Stable pools were isolated by selection in glutamine-free media either with (+) or without (-) MSX selection. The copy numbers of both the heavy- and light-chains of the IgG were evaluated via ddPCR. Cell lines containing the same GS promoter had higher copy numbers after selection with MSX, while ATT cell lines had higher copy numbers compared to SV40 lines of the same MSX selection condition. Note that the addition of MSX could have potentially selected for a modified genotype compared to cell lines obtained without MSX selection pressure [36, 37]. Key characteristics of each cell line are summarized in Table 3.1.

3.3.2 Attenuated GS system improves IgG titer and reduces glutamine overflow

Each of the ATT and SV40 cell lines were characterized in 6 different 250-mL AMBR mini-bioreactors: two labeled with [1,2-$^{13}C_2$]glucose, two labeled with [U-$^{13}C_5$]glutamate,

and two unlabeled controls (Table 3.2). The concentration of glutamine (Fig. 3.2A) and volumetric IgG titer (Fig. 3.2B) were monitored throughout each 9-day fed-batch experiment. All cell lines excreted glutamine into the media, due to excess glutamine production from the GS selection system. Cell lines with the attenuated GS selection marker exhibited higher titers compared to control SV40 lines (Fig. 3.2B). Glutamine production (Fig. 3.2A,D) was significantly reduced in ATT lines compared to SV40 lines isolated under the same MSX selection condition; glutamine production was also significantly higher in cell lines derived from MSX selection compared to cell lines incorporating the same GS promoter but selected without MSX. ATT lines exhibited slightly higher concentrations of ammonia in culture media, likely due to lower GS activity (Fig. 3.A1). Conversely, qP was significantly higher in ATT lines when compared to SV40 lines isolated under the same MSX selection condition, while MSX selection further increased qP of cell lines with either GS promoter (Fig. 3.2E). ATT cell lines had significantly higher IgG/Gln ratios compared to SV40 cell lines, while MSX selection did not affect this ratio (Fig. 3.2C). Similar to the ratio of the volumetric titer to the concentration of glutamine, the ratio of specific productivity to specific glutamine production was higher in ATT lines (Fig. 3.2F). This increase was particularly apparent in the ATT(-) line, due to such low levels of specific glutamine production paired with moderate levels of specific productivity. These data indicate that the IgG/Gln ratio is controlled by the relative strength of IgG versus GS promoters, while MSX selection amplifies the expression level of both GS and IgG genes without altering the relative production rate of IgG to glutamine.

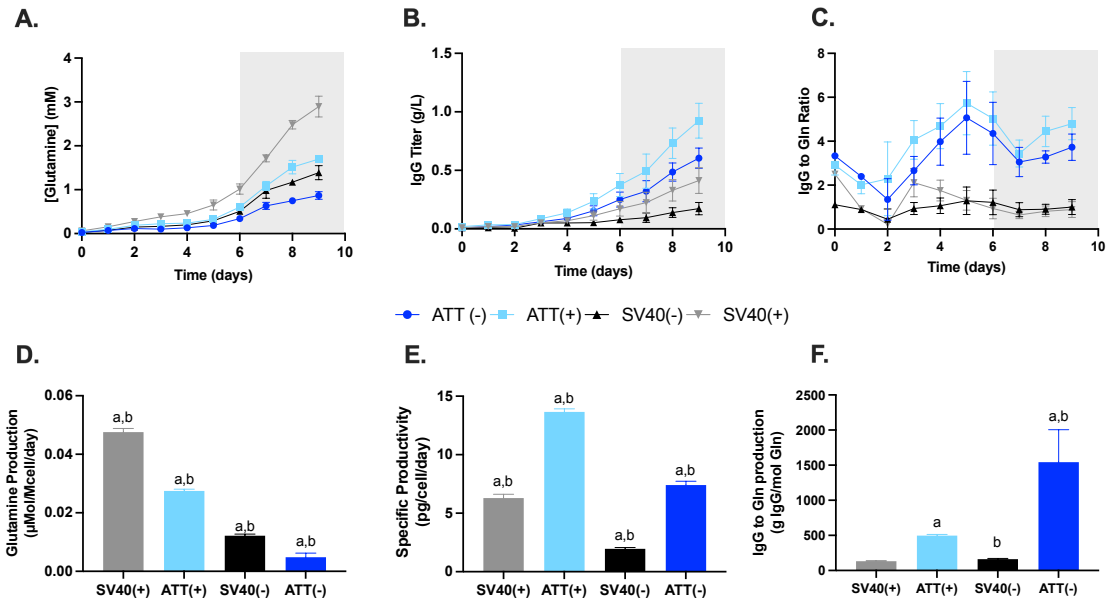

Figure 3.2: **Glutamine and IgG production.** (A) Glutamine concentration over time. (B) Volumetric IgG titer over time. (C) IgG to glutamine ratio over time. The measured IgG titer was divided by the measured glutamine concentration at each time point. (D) Specific glutamine production during stationary phase. (E) Specific productivity of IgG (qP) during stationary phase. (F) Ratio of specific productivity to specific glutamine production during stationary phase. Gray boxes indicate the time span of the isotope labeling study. Data indicate mean value ± SEM. a indicates significant differences ($p<0.05$) between cell lines with matched promoter type. b indicates significant differences ($p<0.05$) between cell lines with matched MSX condition.

3.3.3 qP is dependent on transgene copy number, while glutamine production is dependent on both copy number and GS promoter strength

Since expression levels of the IgG and GS transgenes varied with copy number, we examined how IgG and glutamine productivity correlated with the number of plasmid copies integrated in each cell line. Correlation analysis revealed that specific IgG productivity was directly related to copy number ($r^2 = 0.92$), suggesting that higher transgene copy number leads to higher qP (Fig. 3.3A). Conversely, production of glutamine was dependent on both copy number and GS promoter strength. Increasing copy number without changing promoter strength led to higher production of glutamine. However, attenuating the GS selection marker had a negative impact on glutamine production, resulting in a rightward

shift and a partial flattening of the Gln vs. copy number response curve (Fig. 3.3B). Multiple linear regression analysis revealed that promoter strength was the major determinant of glutamine production rate (Table 3.3).

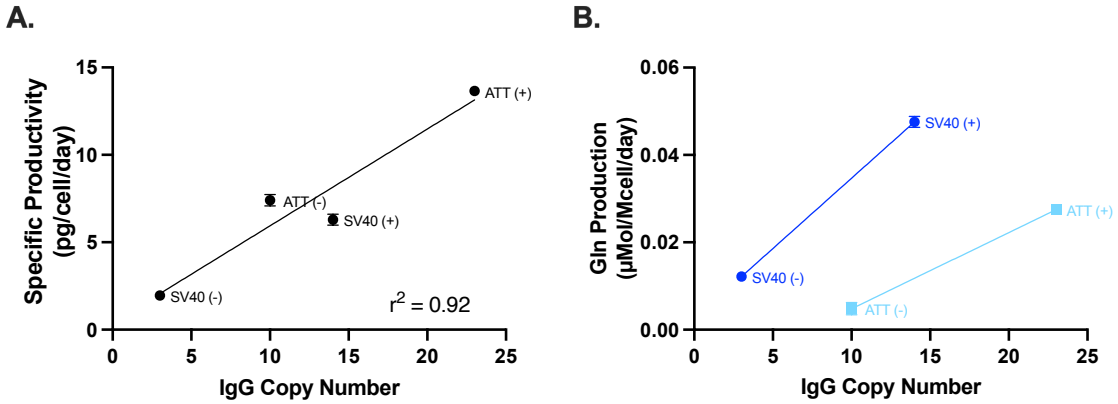

Figure 3.3: **Correlation of copy number with IgG and glutamine production.** (A) Correlation between specific productivity (qP) and IgG copy number. (B) Correlation between specific glutamine production during stationary phase and IgG copy number. Data indicate mean value ± SEM.

Coefficient	qP model	Gln production model
β_0	0.1899	-0.2655
β_1	0.8101	0.8428
β_2	-0.1340	0.3180
β_3	-0.1438	0.7139

Table 3.3: **Multiple regression analysis of qP and glutamine production.** A multiple linear regression analysis was used to determine how qP and glutamine production were affected by promoter type and copy number. Data was normalized to the range of [0,1] to account for varying magnitudes. Due to only two data points per promoter type, a perfect fit was found. Summarized in the table below are the coefficients for the following model: Dependent variable $\sim \beta_0 + \beta_1$[Copy Number] + β_2[Promoter Type] + β_3[Copy Number:Promoter Type]. QP, glutamine production, and copy number were continuous variables, while promoter type was a categorical variable with a value of either 0 (ATT) or 1 (SV40).

3.3.4 Glucose and glutamate consumption are unaffected by GS promoter strength

Cultures were fed glucose and amino acids once per day from day 3 to 6, except tyrosine and cysteine, which were fed daily throughout the duration of the 9-day culture. On day 6, a large bolus of glucose, glutamate, and other amino acids was added to achieve concentrations that were sufficient to prevent nutrient depletion during the final 3 days of culture. These concentrations were calculated based on nutrient consumption rates determined from an earlier pilot study. Glucose consumption after the bolus feed was consistent across all cell lines (Fig. 3.4A,D). Lactate production appears to have been stimulated by the nutrient bolus, likely due to the resulting spike in medium glucose concentration (Fig. 3.4B); however, lactate production after the bolus feed did not significantly differ across the cell lines (Fig. 3.4E). Glutamate consumption after the bolus feed, while not significantly different, trended higher in cell lines isolated without MSX, but did not show a correlation with GS promoter strength (Fig. 3.4C,F).

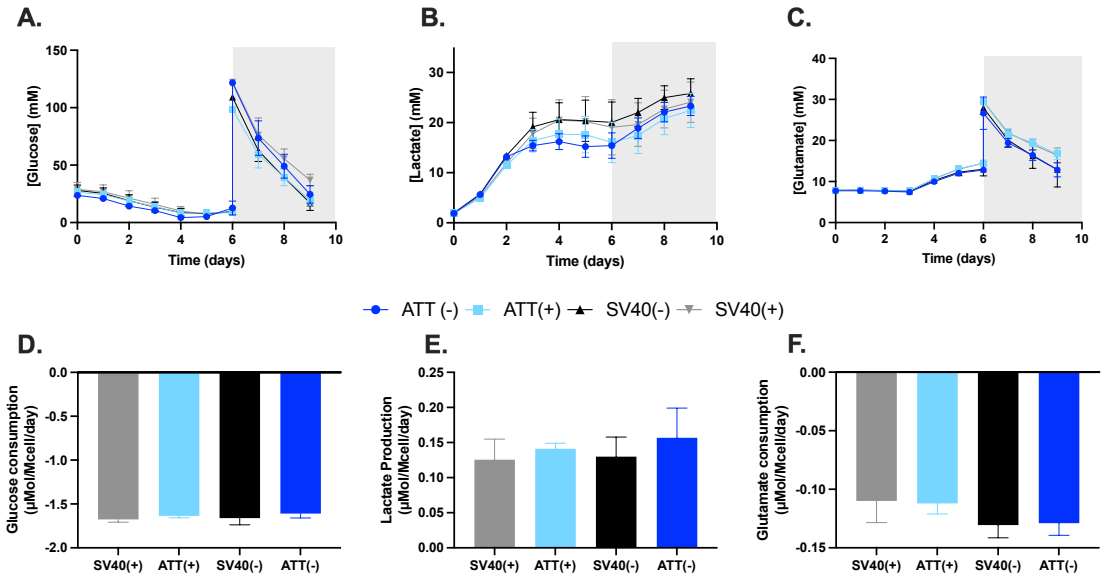

Figure 3.4: **Glucose, lactate, and glutamate exchange rates.** (A) Glucose concentration over time. A bolus of glucose was fed on day 6. (B) Lactate concentration over time. (C) Glutamate concentration over time. A bolus of glutamate was fed on day 6. (D) Specific glucose consumption after bolus feed. (E) Specific lactate production after bolus feed. (F) Specific glutamate consumption after bolus feed. Gray box indicates the time span of the isotope labeling study. Data indicate mean value ± SEM.

3.3.5 MSX selection reduced peak VCD and IVCD, while growth rates were unaffected

Cell lines selected without MSX achieved slightly higher peak VCDs as well as higher integrated viable cell density (IVCD), regardless of GS promoter strength (Fig. 6.1A, D). All cell lines maintained viability above 90% throughout the entire culture, and viability did not differ significantly between the lines (Fig. 6.1B). Growth rates during exponential phase did not vary across cell lines (Fig. 6.1C). While all cell lines were seeded at approximately the same density, lag phases were slightly longer in SV40(+) and ATT(+) lines (Table 3.1). Therefore, the differences in peak VCDs and IVCDs are likely due to a slightly prolonged lag phase in cultures selected on MSX. Cell size was not significantly altered, but trended higher in ATT lines, reflected in the slightly higher average per-cell dry weight of ATT lines compared to SV40 lines (Table 3.1).

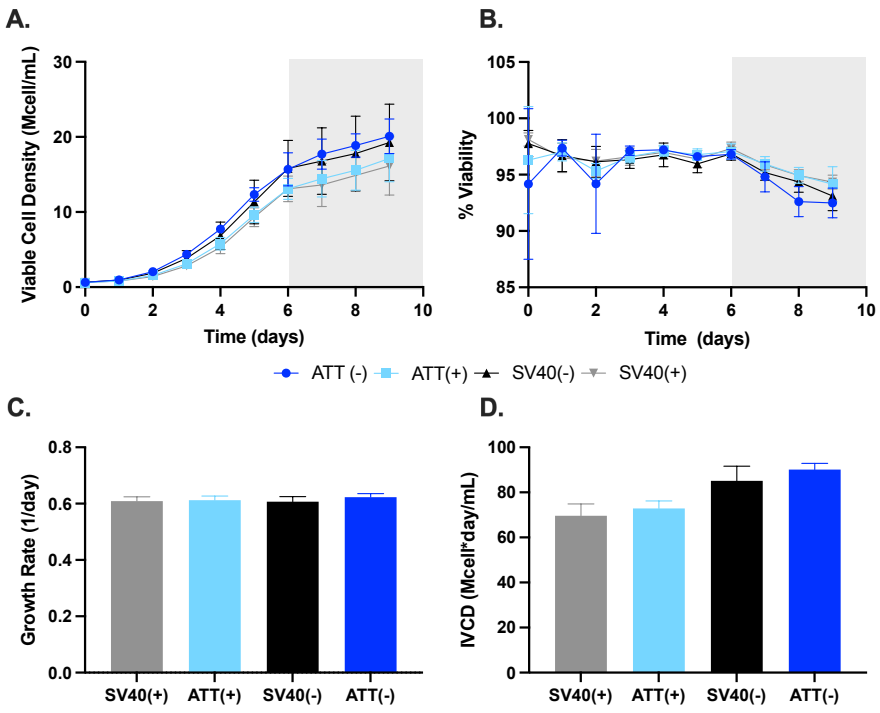

Figure 3.5: **Growth characteristics of cell lines.** (A) viable cell density (VCD) over time. (B) Percent viability over time. (C) Growth rate during exponential phase. (D) Integrated viable cell density (IVCD) calculated over the entire culture length. Gray boxes indicate the time span of the isotope labeling study. Data indicate mean value ± SEM.

3.3.6 ^{13}C metabolic flux analysis reveals repartitioning of glutamate and glutamine fluxes without significant changes in central carbon metabolism dur to varying GS activity

^{13}C INST-MFA was applied to assess intracellular metabolic fluxes of ATT and SV40 cell lines by fitting a CHO metabolic model to isotope enrichment datasets obtained from parallel labeling experiments with [1,2-$^{13}C_2$]glucose and [U-$^{13}C_5$]glutamate tracers. Overall, fluxes through central carbon metabolism were not significantly different across the four cell lines examined. Glycolytic fluxes downstream of phosphofructokinase (PFK) trended higher in the SV40 cell lines (Fig. 3.6A, 3.1). TCA cycle fluxes also trended higher in the SV40 lines (Fig. 3.6B). In contrast, PPP fluxes (Fig. 3.6C) were highest in ATT lines and varied linearly (r^2 = 0.95) with specific productivity (Fig. 3.6D). Previous studies [27, 33, 38, 39] have hypothesized that PPP flux increases in response to increased productivity; this hypothesis is further supported by our findings.

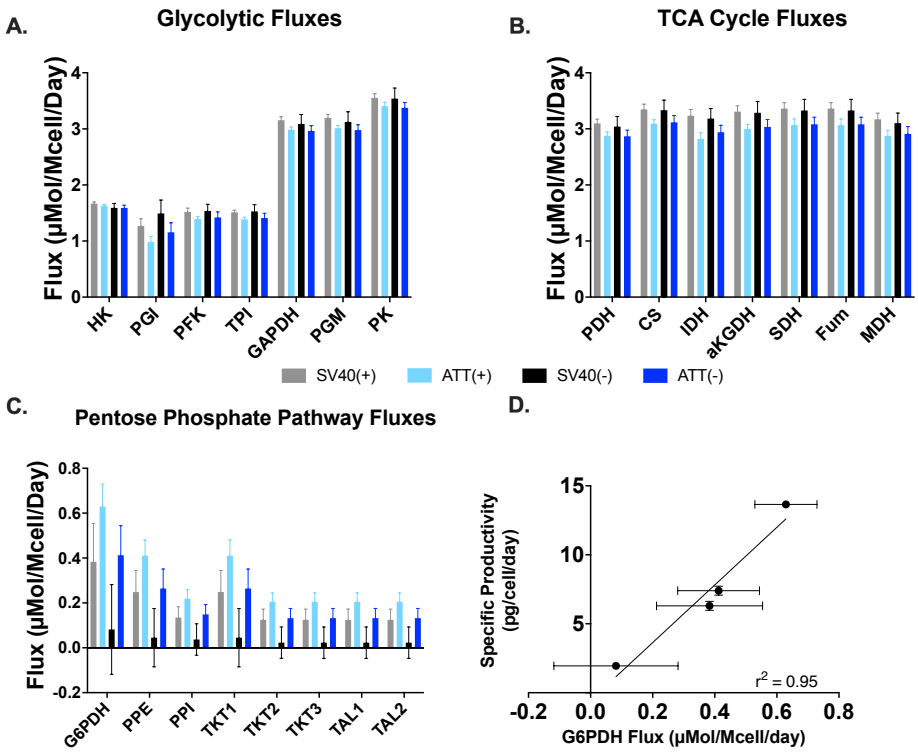

Figure 3.6: **Fluxes determined by ^{13}C MFA.** (A) Glycolytic fluxes. (B) TCA cycle fluxes. (C) Pentose phosphate pathway fluxes. (D) Correlation of specific productivity and G6PDH flux, the rate controlling enzyme of the pentose phosphate pathway. Data indicate mean value $\pm$ SEM, calculated as described in Section 3.2.11.

The largest metabolic changes occurred in the relative partitioning of glutamate and glutamine fluxes. While media provided the major source of glutamate for all cell lines, histidine catabolism made a higher contribution to glutamate production in the SV40 lines relative to ATT lines (Fig. 3.7A). Histidase activity was not impacted by MSX selection, but the contribution from arginase was elevated in the MSX-selected lines. Despite this repartitioning of glutamate sources, the total glutamate consumption flux was similar across all four cell lines (Fig. 3.7B). The intracellular fate of glutamate also varied with GS promoter strength and MSX selection. A larger percentage of glutamate was used for IgG and cell biomass production in the ATT lines compared to the SV40 lines (Fig. 3.7C). Selection with MSX decreased the relative flux of glutamate toward the TCA cycle and biomass synthesis, and proportionately increased flux toward IgG biosynthesis and glutamine excretion.

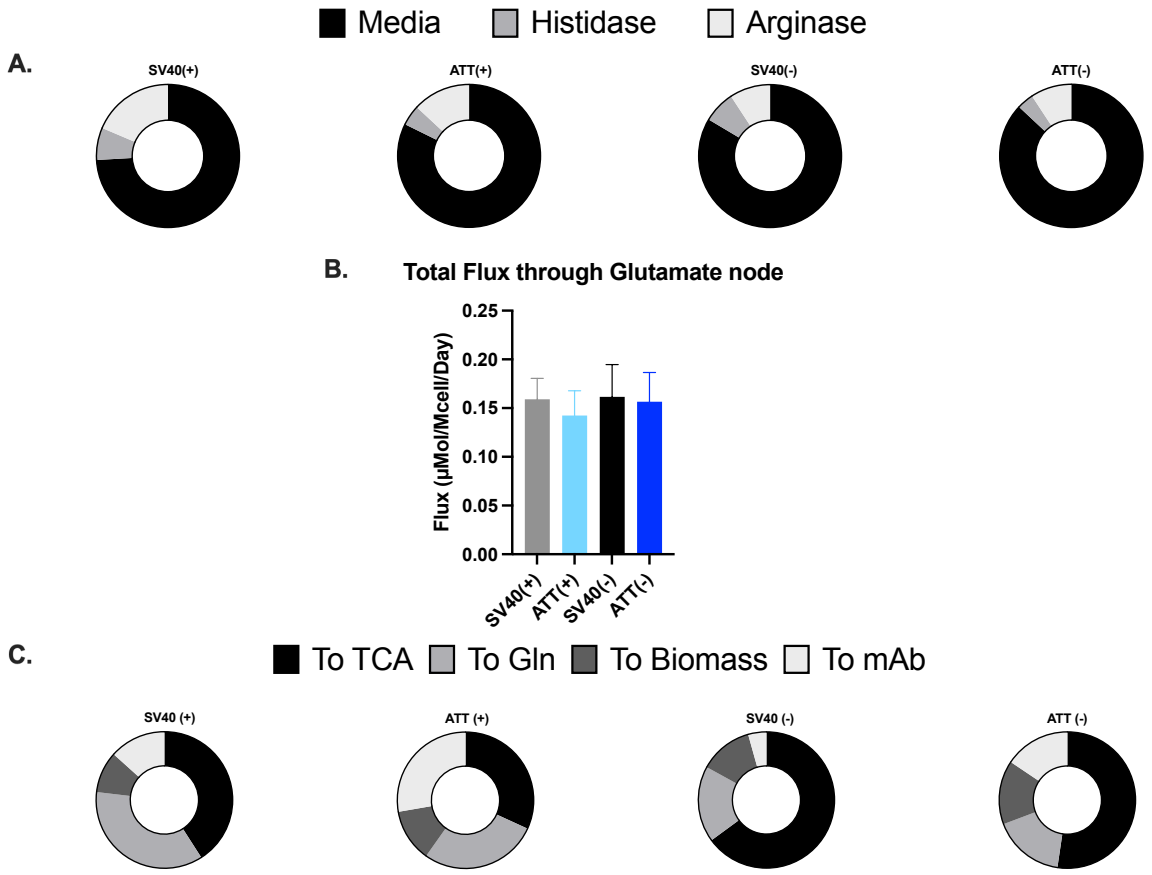

Figure 3.7: **Variation in glutamate fluxes across different cell lines.** (A) Relative contributions of different sources to intracellular glutamate. (B) Total flux leading to/from glutamate. (C) Relative contribution of glutamate toward different metabolic sinks. The flux to glutamine is the total flux through the GS reaction, which ultimately contributes to media glutamine, biomass synthesis, or mAb production. The proportion of glutamine directed to each of these fates is shown in Figure 3.8.

The only source of glutamine in the model was from the GS reaction. The total flux to glutamine biosynthesis was significantly higher in MSX-selected cells (Fig. 3.8A). The percentage of glutamine directed toward IgG production was substantially higher in the ATT lines but was not impacted by MSX selection (Fig. 3.8B). For both ATT and SV40 lines, cells selected without MSX partitioned the majority of glutamine flux toward biomass synthesis, whereas cells selected with MSX excreted more than half of their glutamine flux to the media. Overall, this rewiring of glutamate and glutamine metabolism occurred without major readjustments to central carbon metabolism or differences in fluxes of other

amino acids.

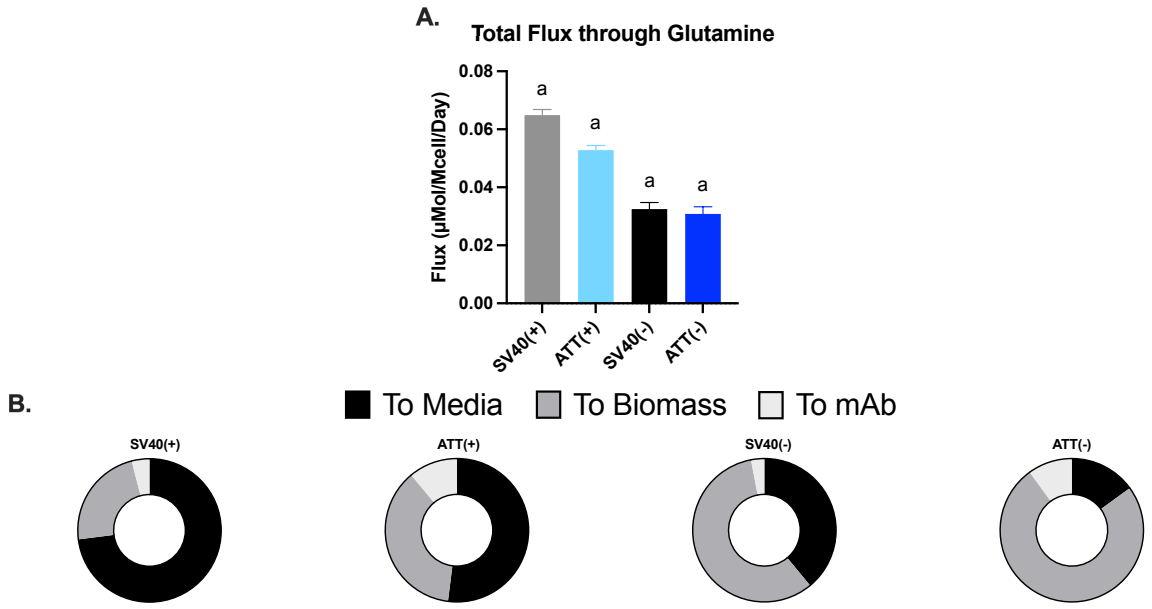

Figure 3.8: **Variation of glutamine fluxes across different cell lines.** (A) Total glutamine biosynthetic flux. (GS provides the only source of glutamine in the model.) (B) Relative contribution of glutamine toward different metabolic sinks. a indicates significant differences ($p<0.05$) between cell lines with matched promoter type.

3.3.7 Runaway reactors provide clues to understand variability in lactate production by CHO cells

During the isotope labeling studies, two separate cultures produced lactate at an excessive rate, a phenomenon referred to as "lactate runaway" (Fig. 3.9A). These were unplanned, spontaneous behaviors that were not exhibited by other replicate cultures grown under the same experimental conditions. The data from these runaway reactors were excluded from the analyses presented previously to avoid biasing the results. However, we decided to perform separate analyses of these two runaway reactors to further characterize their lactate production phenotypes. One runaway reactor contained the ATT(+) line and achieved a peak lactate concentration of 98.2 mM, compared to an average peak lactate concentration of 22.5 mM in the other ATT(+) reactors. The second runaway reactor contained the SV40(-) cell line and reached a peak lactate concentration of 36.6 mM, while the average

peak lactate concentration in other SV40(-) reactors was 25.8 mM. Therefore, the ATT(+) runaway reactor exhibited an extreme lactate production phenotype and the SV40(-) runaway reactor exhibited a moderate lactate production phenotype.

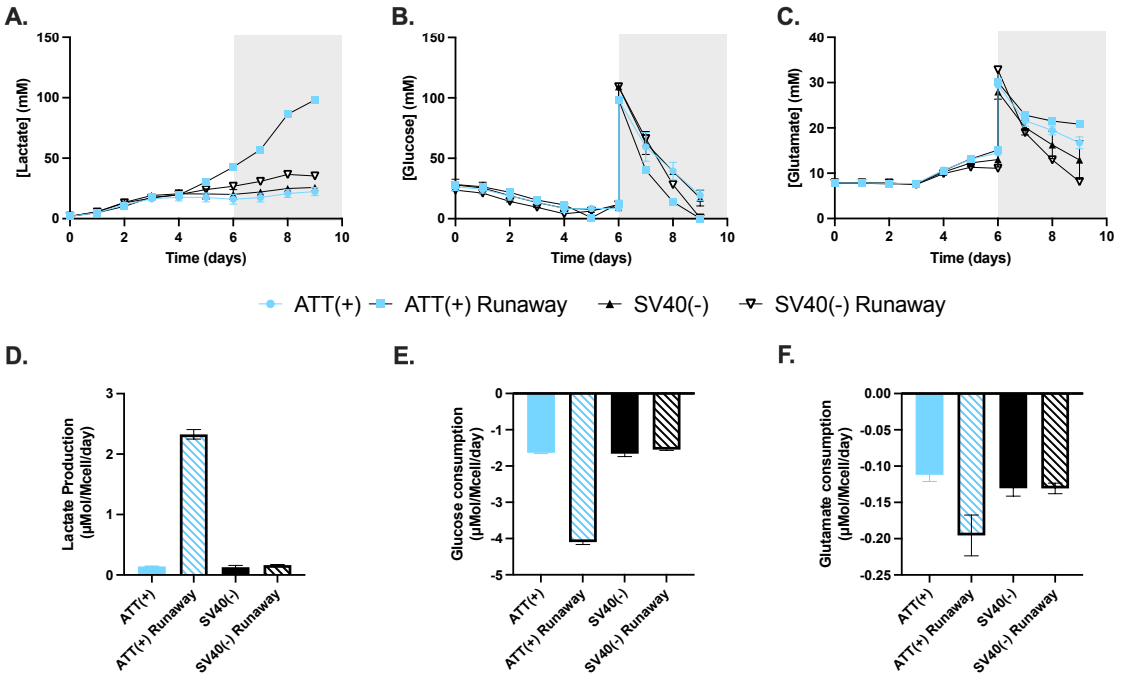

Figure 3.9: **Nutrient metabolism of runaway reactors compared to average behavior of replicate reactors.** (A) Lactate profiles. (B) Glucose profiles. A bolus of glucose was fed on day 6. (C) Glutamate profiles. A bolus of glutamate was fed on day 6. (D) Specific lactate production after bolus feed. (E) Specific glucose consumption after bolus feed. (F) Specific glutamate consumption after bolus feed. Data indicate mean value $\pm$ SEM.

For both runaway reactors, lactate concentration began to rise above their matched replicate cultures starting on day 5 (Fig. 3.9A). The extreme runaway culture depleted glucose completely before it was fed on day 5 (Fig. 3.9B). The moderate runaway culture did not completely deplete glucose, but the concentration of glucose trended slightly lower during the early exponential phase of culture. Both reactors completely depleted glucose by day 9, three days after the bolus feed on day 6. During stationary phase, the ATT(+) runaway reactor consumed glucose at a nearly three-fold higher rate than the other reactors (Fig. 3.9E). Glutamate consumption in the ATT(+) runaway reactor was nearly two-fold higher than the other ATT(+) reactors as well (Fig. 3.9F).

Likely due to the extreme lactate levels present in the ATT(+) runaway reactor, VCD was greatly reduced (Fig. 3.10A). While volumetric titer for the ATT(+) runaway reactor was slightly reduced compared to the ATT(+) average, the specific productivity of the ATT(+) runaway reactor was significantly elevated due to the marked reduction in VCD during stationary phase (Fig. 3.10B,C). The SV40(-) runaway reactor had a similar volumetric titer and specific productivity to the SV40(-) average. Interestingly, glutamine production during stationary phase was significantly lower in both runaway reactors (Fig. 3.10D,E). However, the IgG/Gln ratio was not altered in either of the runaway reactors compared to matched replicates (Fig. 3.10F). This result provides further evidence that the relative production rate of IgG and glutamine is controlled primarily by the relative strength of the promoters driving IgG and GS expression and is independent of alterations in central carbon metabolism.

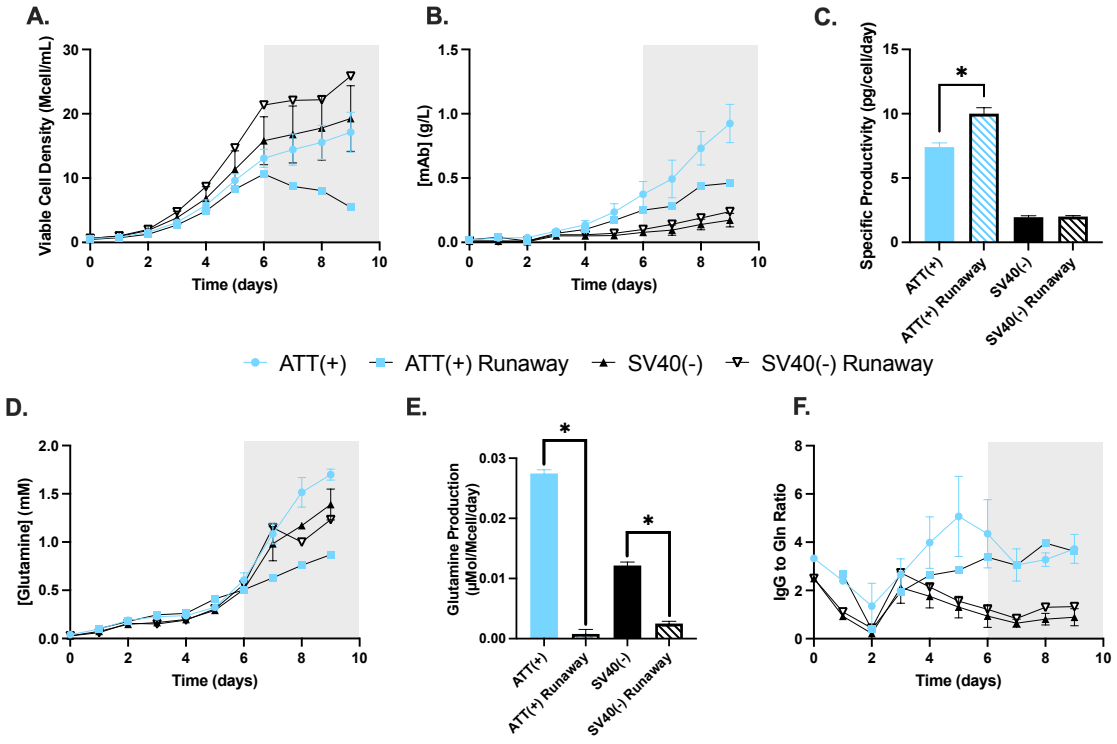

Figure 3.10: **Growth and productivity of runaway reactors compared to average behavior of replicate reactors.** (A) VCD over time. (B) Volumetric mAb titer over time. (C) Specific productivity. (D) Glutamine profiles. (E) Specific glutamine production. (F) IgG to glutamine ratio over time. Gray box indicates the time span of the isotope labeling study. Data indicate mean value ± SEM. * indicates significant differences ($p<0.05$).

Both runaway reactors were labeled with a ^{13}C tracer, so we attempted to estimate metabolic fluxes using ^{13}C MFA. The ATT(+) runaway reactor was labeled with [1,2-$^{13}C_2$]glucose, which enabled fluxes to be precisely determined throughout central carbon metabolism. In contrast, the SV40(-) runaway reactor received [U-$^{13}C_5$]glutamate; because of this, no labeling occurred outside of TCA cycle metabolites and fluxes in other pathways could not be resolved. Therefore, only fluxes for the ATT(+) runaway reactor were further assessed and compared to the average of the other ATT(+) reactors.

Consistent with a three-fold increase in glucose consumption, glycolytic fluxes in the ATT(+) runaway reactor were more than double the average of the other ATT(+) replicates (Fig. 3.11A). Flux through lactate dehydrogenase (LDH) was also substantially higher in the ATT(+) runaway culture (Fig. 3.11B). However, PPP fluxes were unchanged in

the runaway reactor (Fig. 3.11C). In addition to the increased flux through LDH, TCA cycle fluxes were more than doubled in the ATT(+) runaway reactor as a consequence of elevated substrate influx from glucose and glutamate (Fig. 3.11D). In particular, flux through GS was nearly 10-fold lower in the runaway reactor, while conversion of glutamate to alpha-ketoglutarate (modeled as GluDH flux) increased 5-fold (Fig. 3.11B). These data indicate that the runaway ATT(+) reactor shifted to a hyperactive metabolic state, involving upregulation of flux throughout central carbon metabolism, rather than simply diverting the elevated substrate influx to waste products (e.g., lactate and glutamine).

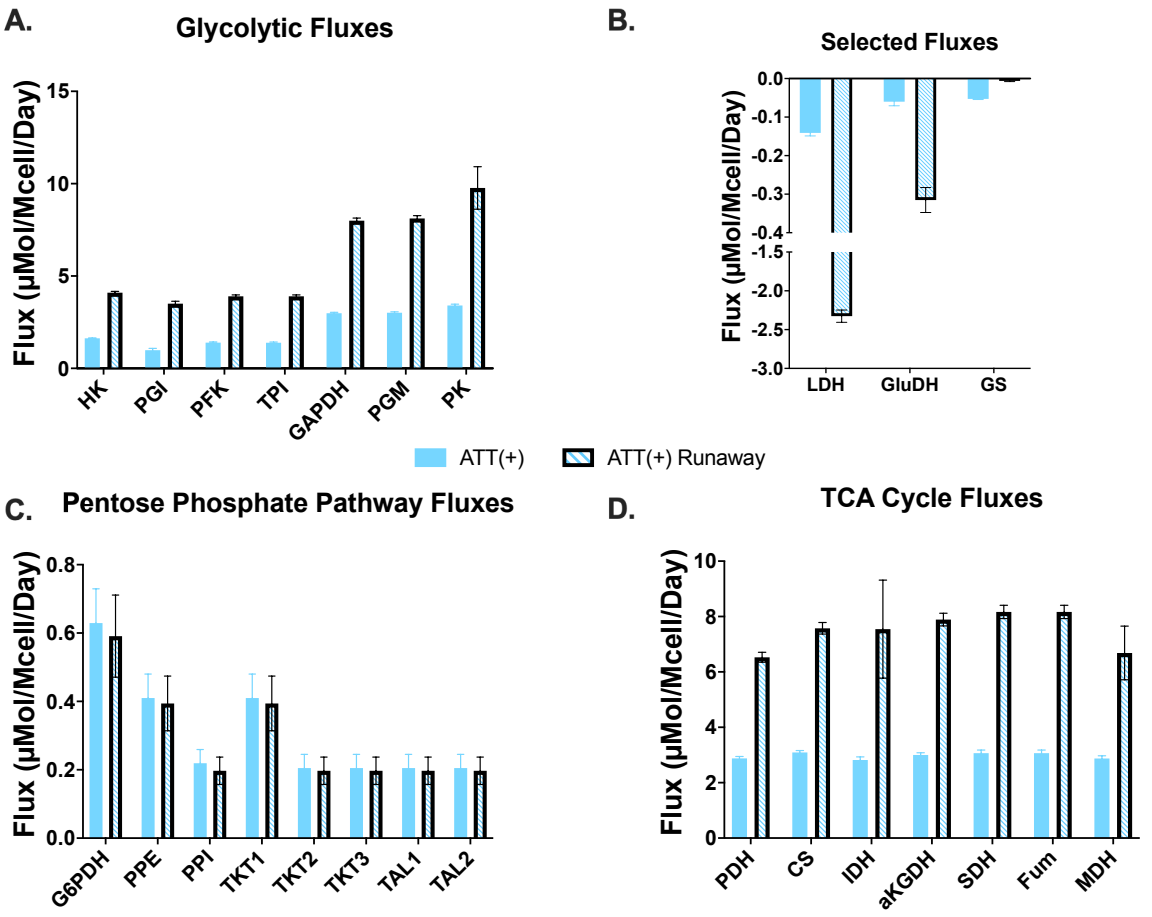

Figure 3.11: **Intermediary fluxes of ATT(+) runaway reactor compared to average behavior of replicate reactors.** (A) Glycolytic fluxes. (B) Lactate dehydrogenase (LDH), glutamate dehydrogenase (GluDH), and glutamine synthetase (GS) fluxes. (C) Pentose phosphate pathway fluxes. (D) TCA cycle fluxes. Data indicate mean value ± SEM, calculated as described in Section 3.2.11.

3.4 Discussion

This study aimed to characterize the metabolic alterations that result from attenuation of the GS selection marker in stable GS-CHO cell lines. A weaker SV40 promoter driving GS gene expression has previously been shown to increase stringency of selection and mAb titer [24]. It has also been shown that using a mutant GS gene that causes GS deficiency in humans increases titer and allows for greater stability of transgene integration [25]. Our study builds upon this previous work by investigating how an attenuated GS selection marker affects the metabolism of the host cell. Overall, weakening the GS promoter increased IgG production and decreased wasteful glutamine production, while leaving central carbon metabolism largely unchanged. Although the cell lines used in this study were derived from the same parental CHO line, the number and location of GS vector integration sites as well as the genetic background of the host lines could have varied during the selection process; as a result, the resulting phenotypes represent the average behavior of non-clonal GS CHO pools.

A previous study found that amino acid metabolism could be manipulated to reduce ammonium production (through the use of different media formulations) without altering central carbon metabolism [32]; the current study further validates this finding for genetic manipulations of amino acid metabolism. The attenuated GS selection marker led to integration of additional copies of the recombinant vector that were necessary to survive selection in glutamine-free medium. These higher copy numbers were directly related to increases in qP of the resulting cell lines (Fig. 3.3A). In addition, glutamine production was lower in ATT lines as compared to SV40 lines, even at similar copy number levels (Fig. 3.3B). These observations also held true in two runaway reactors exhibiting aberrant metabolic phenotypes characterized by excess lactate accumulation.

In addition to being a metabolically wasteful process that diverts carbon and ATP away from other biosynthetic pathways, excess glutamine production could enable "hitchhiker" cells to circumvent the selection process. Non-clonal pools selected by growth on

glutamine-free media could still contain individual cells that have not successfully integrated the GS-transgene cassette and survive by consuming glutamine secreted by other cells in the population. Ideally, GS activity should not exceed the glutamine demand of each individual cell, thereby minimizing excess glutamine accumulation in the culture media. Our study confirms that improved balancing of glutamine and mAb production can be achieved by attenuating the promoter driving expression of the GS selection marker, resulting in increased mAb production by GS-CHO cells. We hypothesized that these changes would correlate with more efficient energy metabolism of high-producing cultures. To test this hypothesis, we applied ^{13}C MFA to examine how the metabolism of GS-CHO cell lines were altered by attenuating GS promoter strength.

^{13}C MFA utilizes stable isotope tracers and mathematical modeling to determine intracellular metabolic fluxes of live cell cultures [40, 41, 42]. Interestingly, we found that host central carbon metabolism was not significantly altered by attenuating GS promoter strength or selection with MSX. Glycolytic fluxes were similar in all four cell lines, trending slightly (3%) higher in SV40 lines (Fig. 3.6A). TCA cycle fluxes also trended higher in SV40 lines, but only by about 6% (Fig. 3.6B). The most dramatic differences appeared in PPP fluxes, where higher fluxes correlated with increased qP (Fig. 3.6C). However, these differences were not significant and were similar in magnitude to differences in glycolysis. Overall, significant changes occurred in the production of IgG and the metabolism of glutamate (Fig. 3.7) and glutamine (Fig. 3.8) but not in other metabolic pathways. These results were surprising since they did not support our hypothesis that decreasing glutamine overflow and increasing qP would correlate with more efficient energy metabolism.

Previous ^{13}C MFA studies in CHO cells have identified metabolic responses to different culture growth stages [27, 39, 43], varying feeding or growth strategies [44, 45, 46], and metabolic engineering of host cell lines [29]. Several reports have identified increased oxidative metabolism, particularly through the TCA cycle, as a hallmark of high mAb productivity [13, 27, 47]. While this correlation between TCA cycle flux and IgG production

was not observed in the current study, we hypothesize that our findings provide an extension, rather than a contradiction, of prior results. Specific productivities in studies that have observed variation in TCA cycle flux ranged from approximately 20 to 60 pcd, with elevated TCA cycle fluxes observed near the top of that range [13, 27]. At such high production rates, ATP could become a major limiting factor, causing cells to upregulate TCA cycle flux to meet energetic demands for growth and mAb secretion. In contrast, specific productivities reported in the current study ranged from 2 to 14 pcd. Therefore, energy supply may not have been a major factor limiting mAb production; in fact, since qP was so closely correlated with the number of chromosomally integrated plasmid copies, it is likely that gene expression was the major limiting factor in these cell lines.

Finally, the observation of "runaway" lactate production in two reactors during the ^{13}C labeling study provided a unique opportunity to assess cellular metabolic alterations during this phenomenon. Other replicate reactors did not exhibit lactate runaway despite being seeded with identical cell lines and grown under the same experimental conditions. While it is possible that a distinct subpopulation of the non-clonal cell lines became dominant in the runaway reactors or a variable process condition caused epigenetic or physiological alterations to the cells, the ultimate cause of this divergent behavior is unclear. The excessive production of lactate in the runaway reactors appears to have occurred by random chance. Due to this, all data for the two runaway reactors is based on a single replicate, which is a major limitation of the conclusions drawn here. Although the phenomenon is not well understood, some mechanisms have been previously hypothesized to explain the runaway lactate production.[48] Steady-state multiplicity in the glycolysis pathway has been proposed as a mechanism to explain bistable switching between high-lactate and low-lactate producing states [49, 50, 51]. In contrast to the generally accepted hypothesis that high glucose levels promote high lactate production[48, 52, 53], the two runaway reactors depleted glucose more rapidly than the other replicate reactors prior to the nutrient bolus on day 6 of culture. Since measurements were taken only daily, it is unclear whether glucose

was depleted prior to the onset of lactate overproduction, or if the high-lactate phenotype caused glucose to be depleted.

It is also unclear what led the runaway cultures to shift to an aberrant metabolic phenotype in the first place. One possibility is that faulty pH control could have been to blame. The pH controllers were set to add base whenever the culture pH ventured outside the range of 6.7 to 7.3. Unlike the other reactors, the runaway reactors received nearly continuous additions of base throughout the culture to counteract the decrease in pH caused by high lactate production. However, it is again unclear if a possibly faulty pH sensor began to call for unnecessary base additions, which caused the cultures to respond by producing excess lactate, or if the base additions were actually necessary to combat the decrease in pH caused by lactate accumulation. Due to the unexpected nature of these runaway lactate reactors, the ability to draw definitive conclusions is somewhat limited.

Regardless of its ultimate cause, the upregulation of fluxes throughout central carbon metabolism observed in the ATT(+) runaway reactor is an intriguing observation. Instead of directing the elevated influx of glucose and amino acids exclusively to waste products, the entire metabolism shifted to a hyperactive state. This would imply an increased demand for energy by the cells, but it is unclear what the fate of that additional energy was. The upregulation of TCA cycle flux is surprising as well; with such a drastic increase in lactate production, the availability of pyruvate to enter the TCA cycle would be expected to decrease rather than increase. Further study of this runaway lactate phenomenon in a more controlled setting could provide insight into the hyperactive metabolic phenotype observed here.

In summary, we hypothesized that an attenuated GS promoter would decrease glutamine production, resulting in a more efficient metabolism and increased production of mAb. GS promoter attenuation and MSX selection both increased transgene copy numbers, which led to proportional changes in qP. Glutamine overflow was also reduced by GS promoter attenuation, while MSX selection increased glutamine production. These

changes in cell culture performance occurred without any major disruptions to central carbon metabolism. Additionally, the observation of extensive upregulation of cellular metabolism during lactate runaway provides new insights into this poorly understood metabolic phenotype. Overall, this study shows the possibility of optimizing the GS selection system to improve mAb titer and qP while reducing wasteful glutamine overflow, but without altering central carbon metabolism. These improvements in vector design can be combined with other host cell engineering strategies to achieve optimal growth and productivity of GS-CHO cultures.

Acknowledgements

This work was supported by the National Science Foundation (NSF) GOALI Program [grant numbers CBET-1604426, CBET-2035085] and NSF Graduate Research Fellowship Program [grant numbers 1445197, 1937963]. Any opinions, findings, and conclusions or recommendations expressed in this material are those of the author(s) and do not necessarily reflect the views of the National Science Foundation.

Nomenclature

.c: Cytosolic

.e: Extracellular

.m : Mitochondrial

3PG: 3-phosphoglyceric acid

AA: Amino acid

AASS: Alpha-aminoadipic semialdehyde synthase

AcCoA: Acetyl-CoA

aKG: Alpha-ketoglutarate

aKGDH: Alpha-ketoglutarate dehydrogenase

Ala: Alanine

ALT: Alanine transaminase

AMBIC: Ammonium bicarbonate

Arg: Arginine

ARGS: Arginase

Asn : Asparagine

AsnS: Asparagine synthase

Asp: Aspartate

ATP: Adenosine triphosphate

ATP CS: ATP Citrate lyase

ATT: Attenuated

CHO: Chinese hamster ovary

Cit: Citrate

CMV: Cytomegalovirus

CS: Citrate synthase

Cys: Cystine

DHAP: Dihydroxyacetone phosphate

E4P: Erythrose-4-phosphate

F6P: Fructose-6-phosphate

Fum: Fumarate

FUS: Fumarase

G6P: Glucose-6-phosphate

G6PDH: Glucose-6-phosphate dehydrogenase

GAP: Glyceraldehyde-3-phosphate

GAPDH: Glyceraldehyde-3-phosphate dehydrogenase

Glc: Glucose

Gln: Glutamine

Glu: Glutamate

GluDH: Glutamate dehydrogenase

Gly: Glycine

GlyS: Glycine synthase

GOT1: Glutamine-oxaloacetic transaminase 1

GS: Glutamine synthetase

His: Histidine

HK: Hexokinase

IBD: Isobutyryl-CoA dehydrogenase

IDH: Isocitrate dehydrogenase

Ile: Isoleuicine

IVCD: Integrated viable cell density

IVD: Isovaleryl-coA dehydrogenase

Lac: Lactate

LDH: Lactate Dehydrogenase

Leu: Leucine

Lys: Lysine

mAb: Monoclonal antibody

Mal: Malate

MAT: Methionine adenosyltransferase

MDH : Malate dehydrogenase

ME: Malic Enzyme

Met: Methionine

MFA: Metabolic flux analysis

MSX: Methionine Sulfoximine

OAA: Oxaloacetate

PAH: Phenylalanine Hydroxylase

PC: Pyruvate Carboxylase

PDH: Pyruvate Dehydrogenase

PEP: Phosphoenolpyruvate

PEPCK: Phosphoenolpyruvate Carboxykinase

PFK: Phosphofructokinase

PGHDH: Phosphoglycerate dehydrogenase

PGI: Phosphoglucoisomerase

PGM: Phosphoglycerate mutase

Phe: Phenylalanine

PK: Pyruvate kinase

PPE: Ribulose-5-phosphate 3-epimerase

PPI: Ribulose-5-phosphate isomerase

Pro: Proline

PYR: Pyruvate

qP: Specific productivity

R5P: Ribose-5-phosphate

Ru5P: Ribulose-5-phosphate

S7P: Sedoheptulose-7-phosphate

SBCAD: Short/branched chain acyl-coA dehydrogenase

SDH: Succinate dehydrogenase

Ser: Serine

SHMT: Serine hydroxymethyltransferase

Suc: Succinate

SV40: Simian virus 40

TAL: Transaldolase

TCA cycle: Tricarboxylic acid cycle

TDO: Tryptophan dioxygenase

Thr: Threonine

TKT: Transketolase

TPI: Trisephosphate isomerase

Trp: Tryptophan

Tyr: Tyrosine

Val: Valine

VCD: Viable Cell Density

X5P: Xylulose-5-phosphate

3.5 Appendix

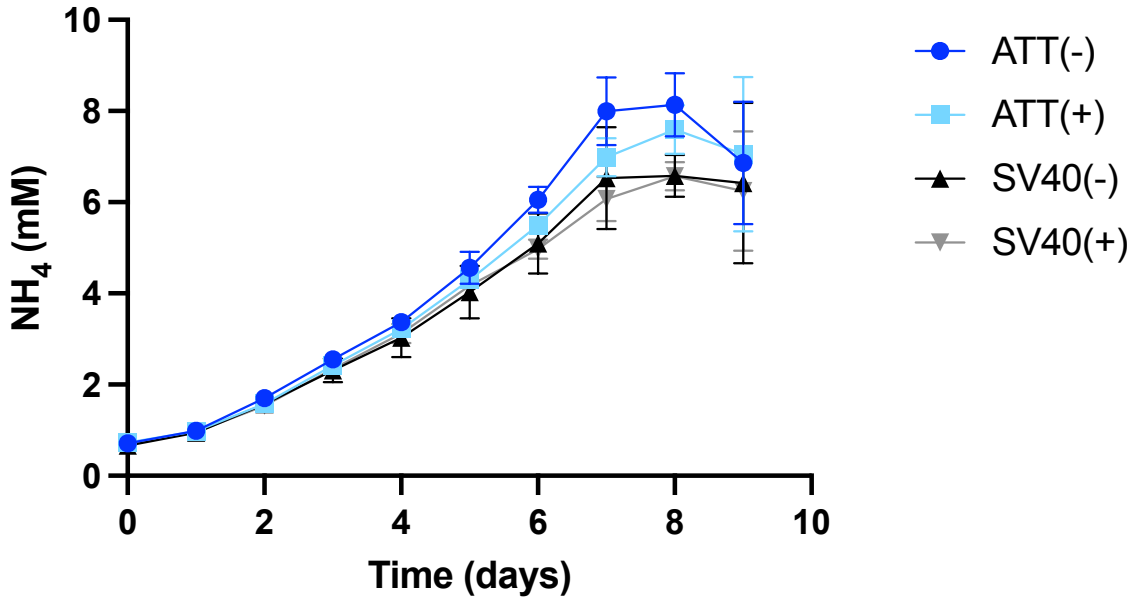

Figure 3.A1: **Concentration of ammonia over time.** Data indicate mean ± SEM.

Cell Line	Sum of Squared Residuals (SSR)	95% Confidence Interval LB (SSR)	95% Confidence Interval UB (SSR)	DOF
ATT(+)	167.1	133.1	204.7	167
ATT(-)	185.4	133.1	204.7	167
SV40(+)	126.8	133.1	204.7	167
SV40(-)	116.4	133.1	204.7	167

Table 3.A1: **Sum of squared residuals (SSR) for ^{13}C MFA best-fit solutions.** Confidence intervals are based on a chi-squared distribution with the indicated degrees of freedom (DOF). If SSR is below the UB threshold, the fit is acceptable. LB = lower bound, UB = upper bound

Pathway	Enzyme	Reaction	Net Flux	LB	UB
Glycolysis	HK	Glc ↔ G6P	1.630	1.585	1.673
	PGI	G6P ↔ F6P	0.983	0.882	1.270
	PFK	F6P → DHAP + GAP	1.393	1.348	1.503
	TPI	DHAP ↔ GAP	1.386	1.341	1.496
	GAPDH	GAP ↔ 3PG	2.985	2.902	3.112
	PGM	3PG ↔ PEP	3.011	2.928	3.139
	PK	PEP → PYR.C	3.406	3.276	3.544
	LDH	PYR.C ↔ LAC	0.141	0.156	0.126
PPP	G6PDH	G6P → Ru5P	0.629	0.348	0.733
	PPE	Ru5P ↔ X5P	0.410	0.199	0.480
	PPI	Ru5P ↔ R5P	0.219	0.088	0.245
	TKT1	X5P ↔ EC2 + GAP	0.410	0.199	0.480
	TKT2	F6P ↔ EC2 + E4P	-0.205	-0.240	-0.100
	TKT3	S7P ↔ EC2 + R5P	-0.205	-0.240	-0.100
	TAL1	F6P ↔ EC3 + GAP	-0.205	-0.240	-0.100
	TAL2	S7P ↔ EC3 + E4P	0.205	0.100	0.240
TCA Cycle	PDH	Pyr.m → AcCoA.m + CO2	2.876	2.774	3.063
	CS	OAA.m + AcCoA.m → Cit.m	3.092	2.971	3.260
	IDH.m	Cit.m ↔ aKG.m + CO2	2.821	2.631	3.069
	aKGDH	aKG.m → Suc.m + CO2	3.001	2.856	3.185
	SDH	Suc.m ↔ Fum.m	3.067	2.905	3.317
	FUS	Fum.m ↔ Mal.m	3.067	2.905	3.317
	MDH.m	Mal.m ↔ OAA.m	2.873	2.685	3.069
Anaplerosis	ME	Mal.m → Pyr.m + CO2	0.000	0.000	0.140
	PC	Pyr.m + CO2 → OAA.m	0.219	0.088	0.374
	ATP CS	Cit.c → AcCoa.c + OAA.c	0.151	0.129	0.173
	PEPCK	OAA.c → PEP + CO2	0.395	0.304	0.456
	IDH.c	Cit.c → aKG.c + CO2	0.120	0.000	0.282
	GOT1	OAA.c ↔ Asp.c	-0.050	-0.060	-0.039
	Carboxylase	ProCoA + CO2 → Suc.m	0.067	0.030	0.105
	MDH.c	OAA.c ↔ Mal.c	-0.194	-0.255	-0.100
Amino Acid Metabolism	GS	Gln ↔ Glu.m	-0.053	-0.056	-0.050
	GluDH	aKG.m ↔ Glu.m	-0.060	-0.081	-0.039
	AsnS	Asn → Asp.c	0.095	0.086	0.104
	SHMT	Ser ↔ Gly + C1	0.009	0.003	0.014
	PGHDH	3PG ↔ Ser	-0.026	-0.038	-0.011
	GlyS	CO2 + C1 ↔ Gly	0.015	0.013	0.018
	ALT	Pyr.c ↔ Ala.c	0.170	0.160	0.180
	Histidase	His → C1 + Glu.c	0.007	0.004	0.009
	PAH	Phe → Tyr	0.003	0.000	0.006
	TDO	Trp → CO2 + CO2 + Ala.c + aKetoadi	0.018	0.016	0.021
	AA Intermediates	aKetoadi → CO2 + CO2 + AcCoA.m + AcCoA.m	0.036	0.026	0.047
	SBCAD	Ile → AcCoA.m + CO2 + ProCoA	0.020	0.000	0.027
	IVD	Leu + CO2 → CO2 + AcCoA.m + AcCoA.m + AcCoA.m	0.041	0.029	0.052
	IBD	Val → CO2 + CO2 + ProCoA	0.032	0.000	0.069
	AASS	Lys → aKetoadi	0.018	0.008	0.028
	ARGS	Arg → Glu.c + Urea	0.019	0.013	0.024
	MAT	Met + Ser → C1 + Cys + ProCoA + Co2	0.014	0.011	0.018
Transport	Glucose	Glc.e → Glc	1.630	1.585	1.673
	Mal.m	Mal.c ↔ Mal.m	-0.194	-0.255	-0.100
	aKG.m	aKG.m ↔ aKG.c	-0.120	-0.282	0.000
	Glu.m	Glu.c ↔ Glu.m	0.113	0.093	0.132
	Asp.m	Asp.m ↔ Asp.c	0.000	0.000	0.000
	Cit.m	Cit.m → Cit.c	0.271	0.133	0.430
	Lys	Lys.e → Lys	0.062	0.053	0.070
	Thr	Thr.e → Thr	0.035	0.031	0.038
	Phe	Phe.e → Phe	0.021	0.019	0.023
	Tyr	Tyr.e → Tyr	0.013	0.009	0.017
	Val	Val.e → Val	0.068	0.034	0.106
	Leu	Leu.e → Leu	0.085	0.075	0.096
	Ile	Ile.e → Ile	0.043	0.037	0.049
	Trp	Trp.e → Trp	0.023	0.021	0.026
	His	His.e → His	0.018	0.016	0.020
	Met	Met.e → Met	0.024	0.021	0.027
	Ser	Ser.e ↔ Ser	0.090	0.082	0.098
	Ala	Ala.c ↔ Ala.e	0.146	0.138	0.154
	Arg	Arg.e ↔ Arg	0.045	0.040	0.050
	Asp	Asp.c ↔ Asp.e	0.018	0.014	0.021
	Cys	Cys.e ↔ Cys	-0.003	-0.006	0.001
	Glu	Glu.c ↔ Glu.e	-0.117	-0.135	-0.099
	Gln	Gln ↔ Gln.e	0.027	0.026	0.029
	Gly	Gly.e ↔ Gly	0.016	0.013	0.020
	Pro	Pro.e ↔ Pro	0.028	0.025	0.031
	Asn	Asn.e ↔ Asn	0.117	0.109	0.125
	Lac	Lac ↔ Lac.e	0.141	0.126	0.156
Antibody Production		0.033*Ala.c + 0.016*Cys + 0.031*Asp.c + 0.031*Glu.c + 0.021*Phe + 0.04*Gly + 0.013*His + 0.018*Ile + 0.047*Lys + 0.053*Leu + 0.007*Met + 0.026*Asn + 0.049*Pro + 0.031*Gln + 0.016*Arg + 0.078*Ser + 0.059*Thr + 0.058*Val + 0.012*Trp + 0.029*Tyr → Antibody	0.186	0.178	0.193
Biomass Production	Biomass (730 pg/cell)	0.438*Ala.c + 0.2752*Arg + 0.2621*Asp.c + 0.2102*Asn + 0.1058*Cys + 0.2351*Gln + 0.2818*Glu.c + 0.3927*Gly + 0.1044*His + 0.2365*Ile + 0.4117*Leu + 0.4161*Lys + 0.1007*Met + 0.1599*Phe + 0.2285*Pro + 0.3139*Ser + 0.2818*Thr + 0.03212*Trp + 0.1329*Tyr + 0.3037*Val + 0.2106*G6P + 0.17*R5P + 0.17*C1 + 0.0868*DHAP + 1.807*AcCoA.c → Biomass	0.085	0.073	0.098

Table 3.A2: **Net fluxes determined by ^{13}C MFA for the ATT(+) line**. The best-fit value and the 95% confidence interval upper bound (UB) and lower bound (LB) are indicated.

Pathway	Enzyme	Reaction	Net Flux	LB	UB
Glycolysis	HK	Glc ↔ G6P	1.588	1.492	1.689
	PGI	G6P ↔ F6P	1.155	0.703	1.367
	PFK	F6P → DHAP + GAP	1.419	1.129	1.521
	TPI	DHAP ↔ GAP	1.411	1.180	1.513
	GAPDH	GAP ↔ 3PG	2.962	2.777	3.149
	PGM	3PG ↔ PEP	2.979	2.790	3.162
	PK	PEP → PYR.C	3.374	3.184	3.561
	LDH	PYR.C ↔ LAC	0.148	0.231	0.066
PPP	G6PDH	G6P → Ru5P	0.412	0.209	0.726
	PPE	Ru5P ↔ X5P	0.264	0.130	0.472
	PPI	Ru5P ↔ R5P	0.149	0.081	0.253
	TKT1	X5P ↔ EC2 + GAP	0.264	0.130	0.472
	TKT2	F6P ↔ EC2 + E4P	-0.132	-0.236	-0.065
	TKT3	S7P ↔ EC2 + R5P	-0.132	-0.236	-0.065
	TAL1	F6P ↔ EC3 + GAP	-0.132	-0.236	-0.065
	TAL2	S7P ↔ EC3 + E4P	0.132	0.065	0.236
TCA Cycle	PDH	Pyr.m → AcCoA.m + CO2	2.868	2.650	3.074
	CS	OAA.m + AcCoA.m → Cit.m	3.117	2.872	3.344
	IDH.m	Cit.m ↔ aKG.m + CO2	2.940	2.691	3.180
	aKGDH	aKG.m → Suc.m + CO2	3.035	2.771	3.288
	SDH	Suc.m ↔ Fum.m	3.081	2.839	3.341
	FUS	Fum.m ↔ Mal.m	3.081	2.839	3.341
	MDH.m	Mal.m ↔ OAA.m	2.911	2.659	3.165
Anaplerosis	ME	Mal.m → Pyr.m + CO2	0.004	0.000	0.178
	PC	Pyr.m + CO2 → OAA.m	0.206	0.138	0.761
	ATP CS	Cit.c → AcCoa.c + OAA.c	0.177	0.143	0.203
	PEPCK	OAA.c → PEP + CO2	0.395	0.336	0.439
	IDH.c	Cit.c → aKG.c + CO2	0.000	0.000	0.077
	GOT1	OAA.c ↔ Asp.c	-0.052	-0.064	-0.041
	Carboxylase	ProCoA + CO2 → Suc.m	0.045	0.034	0.060
	MDH.c	OAA.c ↔ Mal.c	-0.166	-0.205	-0.097
Amino Acid Metabolism	GS	Gln ↔ Glu.m	-0.031	-0.035	-0.026
	GluDH	aKG.m ↔ Glu.m	-0.095	-0.120	-0.070
	AsnS	Asn → Asp.c	0.060	0.052	0.068
	SHMT	Ser ↔ Gly + C1	0.012	0.004	0.019
	PGHDH	3PG ↔ Ser	-0.017	-0.031	-0.004
	GlyS	CO2 + C1 ↔ Gly	0.013	0.010	0.017
	ALT	Pyr.c ↔ Ala.c	0.156	0.142	0.169
	Histidase	His → C1 + Glu.c	0.006	0.003	0.009
	PAH	Phe → Tyr	0.002	0.000	0.006
	TDO	Trp → CO2 + CO2 + Ala.c + aKetoadi	0.011	0.009	0.014
	AA Intermediates	aKetoadi → CO2 + CO2 + AcCoA.m + AcCoA.m	0.050	0.036	0.065
	SBCAD	Ile → AcCoA.m + CO2 + ProCoA	0.031	0.023	0.040
	IVD	Leu + CO2 → CO2 + AcCoA.m + AcCoA.m + AcCoA.m	0.039	0.025	0.052
	IBD	Val → CO2 + CO2 + ProCoA	0.002	0.000	0.008
	AASS	Lys → aKetoadi	0.039	0.025	0.053
	ARGS	Arg → Glu.c + Urea	0.015	0.008	0.022
	MAT	Met + Ser → C1 + Cys + ProCoA + Co2	0.012	0.009	0.016
Transport	Glucose	Glc.e → Glc	1.588	1.492	1.689
	Mal.m	Mal.c ↔ Mal.m	-0.166	-0.205	-0.097
	aKG.m	aKG.m ↔ aKG.c	0.000	-0.077	0.000
	Glu.m	Glu.c ↔ Glu.m	0.126	0.102	0.148
	Asp.m	Asp.m ↔ Asp.c	0.000	0.000	0.000
	Cit.m	Cit.m → Cit.c	0.177	0.143	0.260
	Lys	Lys.e → Lys	0.085	0.073	0.096
	Thr	Thr.e → Thr	0.034	0.028	0.038
	Phe	Phe.e → Phe	0.020	0.018	0.022
	Tyr	Tyr.e → Tyr	0.014	0.008	0.018
	Val	Val.e → Val	0.037	0.033	0.041
	Leu	Leu.e → Leu	0.085	0.073	0.096
	Ile	Ile.e → Ile	0.056	0.049	0.064
	Trp	Trp.e → Trp	0.016	0.013	0.018
	His	His.e → His	0.017	0.015	0.020
	Met	Met.e → Met	0.023	0.020	0.026
	Ser	Ser.e ↔ Ser	0.080	0.071	0.088
	Ala	Ala.c ↔ Ala.e	0.121	0.111	0.131
	Arg	Arg.e ↔ Arg	0.043	0.038	0.048
	Asp	Asp.c ↔ Asp.e	-0.021	-0.024	-0.018
	Cys	Cys.e ↔ Cys	0.000	-0.005	0.004
	Glu	Glu.c ↔ Glu.e	-0.136	-0.156	-0.115
	Gln	Gln ↔ Gln.e	0.005	0.002	0.008
	Gly	Gly.e ↔ Gly	0.018	0.012	0.024
	Pro	Pro.e ↔ Pro	0.027	0.023	0.031
	Asn	Asn.e ↔ Asn	0.083	0.076	0.090
	Lac	Lac ↔ Lac.e	0.148	0.066	0.231
Antibody Production		0.033*Ala.c + 0.016*Cys + 0.031*Asp.c + 0.031*Glu.c + 0.021*Phe + 0.04*Gly + 0.013*His + 0.018*Ile + 0.047*Lys + 0.053*Leu + 0.007*Met + 0.026*Asn + 0.049*Pro + 0.031*Gln + 0.016*Arg + 0.078*Ser + 0.059*Thr + 0.058*Val + 0.012*Trp + 0.029*Tyr → Antibody	0.101	0.092	0.109
Biomass Production	Biomass (730 pg/cell)	0.438*Ala.c + 0.2752*Arg + 0.2621*Asp.c + 0.2102*Asn + 0.1058*Cys + 0.2351*Gln + 0.2818*Glu.c + 0.3927*Gly + 0.1044*His + 0.2365*Ile + 0.4117*Leu + 0.4161*Lys + 0.1007*Met + 0.1599*Phe + 0.2285*Pro + 0.3139*Ser + 0.2818*Thr + 0.03212*Trp + 0.1329*Tyr + 0.3037*Val + 0.2106*G6P + 0.17*R5P + 0.17*C1 + 0.0868*DHAP + 1.807*AcCoA.c → Biomass	0.098	0.079	0.112

Table 3.A3: **Net fluxes determined by ^{13}C MFA for the ATT(-) line**. The best-fit value and the 95% confidence interval upper bound (UB) and lower bound (LB) are indicated.

Pathway	Enzyme	Reaction	Net Flux	LB	UB
Glycolysis	HK	Glc ↔ G6P	1.666	1.604	1.727
	PGI	G6P ↔ F6P	1.269	1.012	1.514
	PFK	F6P → DHAP + GAP	1.518	1.335	1.607
	TPI	DHAP ↔ GAP	1.512	1.453	1.602
	GAPDH	GAP ↔ 3PG	3.154	3.034	3.277
	PGM	3PG ↔ PEP	3.195	3.072	3.322
	PK	PEP → PYR.C	3.552	3.410	3.704
	LDH	PYR.C ↔ LAC	0.123	0.181	0.066
PPP	G6PDH	G6P → Ru5P	0.383	0.140	NaN
	PPE	Ru5P ↔ X5P	0.248	0.086	0.464
	PPI	Ru5P ↔ R5P	0.135	0.054	0.243
	TKT1	X5P ↔ EC2 + GAP	0.248	0.086	0.464
	TKT2	F6P ↔ EC2 + E4P	-0.124	-0.232	-0.043
	TKT3	S7P ↔ EC2 + R5P	-0.124	-0.232	-0.043
	TAL1	F6P ↔ EC3 + GAP	-0.124	-0.232	-0.043
	TAL2	S7P ↔ EC3 + E4P	0.124	0.043	0.232
TCA Cycle	PDH	Pyr.m → AcCoA.m + CO2	3.097	2.945	3.250
	CS	OAA.m + AcCoA.m → Cit.m	3.347	3.162	3.533
	IDH.m	Cit.m ↔ aKG.m + CO2	3.233	2.988	3.429
	aKGDH	aKG.m → Suc.m + CO2	3.307	3.106	3.512
	SDH	Suc.m ↔ Fum.m	3.360	3.153	3.573
	FUS	Fum.m ↔ Mal.m	3.360	3.153	3.573
	MDH.m	Mal.m ↔ OAA.m	3.169	2.936	3.374
Anaplerosis	ME	Mal.m → Pyr.m + CO2	0.000	0.000	0.171
	PC	Pyr.m + CO2 → OAA.m	0.177	0.101	0.371
	ATP CS	Cit.c → AcCoa.c + OAA.c	0.114	0.090	0.135
	PEPCK	OAA.c → PEP + CO2	0.357	0.284	0.444
	IDH.c	Cit.c → aKG.c + CO2	0.000	0.000	0.188
	GOT1	OAA.c ↔ Asp.c	-0.052	-0.075	-0.031
	Carboxylase	ProCoA + CO2 → Suc.m	0.053	0.032	0.076
	MDH.c	OAA.c ↔ Mal.c	-0.191	-0.268	-0.120
Amino Acid Metabolism	GS	Gln ↔ Glu.m	-0.065	-0.069	-0.061
	GluDH	aKG.m ↔ Glu.m	-0.074	-0.102	-0.047
	AsnS	Asn → Asp.c	0.090	0.069	0.111
	SHMT	Ser ↔ Gly + C1	-0.005	-0.013	0.003
	PGHDH	3PG ↔ Ser	-0.042	-0.072	-0.012
	GlyS	CO2 + C1 ↔ Gly	0.016	0.010	0.022
	ALT	Pyr.c ↔ Ala.c	0.155	0.117	0.193
	Histidase	His → C1 + Glu.c	0.012	0.007	0.017
	PAH	Phe → Tyr	0.007	0.000	0.012
	TDO	Trp → CO2 + CO2 + Ala.c + aKetoadi	0.012	0.005	0.019
	AA Intermediates	aKetoadi → CO2 + CO2 + AcCoA.m + AcCoA.m	0.037	0.015	0.060
	SBCAD	Ile → AcCoA.m + CO2 + ProCoA	0.023	0.009	0.037
	IVD	Leu + CO2 → CO2 + AcCoA.m + AcCoA.m + AcCoA.m	0.051	0.024	0.079
	IBD	Val → CO2 + CO2 + ProCoA	0.010	0.000	0.023
	AASS	Lys → aKetoadi	0.025	0.003	0.047
	ARGS	Arg → Glu.c + Urea	0.030	0.014	0.045
	MAT	Met + Ser → C1 + Cys + ProCoA + Co2	0.020	0.010	0.030
Transport	Glucose	Glc.e → Glc	1.666	1.604	1.727
	Mal.m	Mal.c ↔ Mal.m	-0.191	-0.268	-0.120
	aKG.m	aKG.m ↔ aKG.c	0.000	-0.188	0.000
	Glu.m	Glu.c ↔ Glu.m	0.139	0.112	0.166
	Asp.m	Asp.m ↔ Asp.c	0.000	0.000	0.000
	Cit.m	Cit.m → Cit.c	0.114	0.090	0.301
	Lys	Lys.e → Lys	0.055	0.034	0.076
	Thr	Thr.e → Thr	0.023	0.019	0.029
	Phe	Phe.e → Phe	0.018	0.012	0.024
	Tyr	Tyr.e → Tyr	0.004	0.000	0.011
	Val	Val.e → Val	0.034	0.023	0.047
	Leu	Leu.e → Leu	0.081	0.054	0.109
	Ile	Ile.e → Ile	0.039	0.025	0.053
	Trp	Trp.e → Trp	0.015	0.009	0.022
	His	His.e → His	0.019	0.014	0.024
	Met	Met.e → Met	0.027	0.017	0.037
	Ser	Ser.e ↔ Ser	0.083	0.055	0.112
	Ala	Ala.c ↔ Ala.e	0.137	0.100	0.174
	Arg	Arg.e ↔ Arg	0.048	0.033	0.064
	Asp	Asp.c ↔ Asp.e	0.018	0.014	0.023
	Cys	Cys.e ↔ Cys	-0.012	-0.023	-0.002
	Glu	Glu.c ↔ Glu.e	-0.118	-0.139	-0.097
	Gln	Gln ↔ Gln.e	0.047	0.045	0.050
	Gly	Gly.e ↔ Gly	0.017	0.012	0.022
	Pro	Pro.e ↔ Pro	0.019	0.016	0.021
	Asn	Asn.e ↔ Asn	0.105	0.085	0.126
	Lac	Lac ↔ Lac.e	0.123	0.066	0.181
Antibody Production		0.033*Ala.c + 0.016*Cys + 0.031*Asp.c + 0.031*Glu.c + 0.021*Phe + 0.04*Gly + 0.013*His + 0.018*Ile + 0.047*Lys + 0.053*Leu + 0.007*Met + 0.026*Asn + 0.049*Pro + 0.031*Gln + 0.016*Arg + 0.078*Ser + 0.059*Thr + 0.058*Val + 0.012*Trp + 0.029*Tyr → Antibody	0.085	0.077	0.094
Biomass Production	Biomass (730 pg/cell)	0.438*Ala.c + 0.2752*Arg + 0.2621*Asp.c + 0.2102*Asn + 0.1058*Cys + 0.2351*Gln + 0.2818*Glu.c + 0.3927*Gly + 0.1044*His + 0.2365*Ile + 0.4117*Leu + 0.4161*Lys + 0.1007*Met + 0.1599*Phe + 0.2285*Pro + 0.3139*Ser + 0.2818*Thr + 0.03212*Trp + 0.1329*Tyr + 0.3037*Val + 0.2106*G6P + 0.17*R5P + 0.17*C1 + 0.0868*DHAP + 1.807*AcCoA.c → Biomass	0.072	0.057	0.086

Table 3.A4: **Net fluxes determined by ^{13}C MFA for the SV40(+) line**. The best-fit value and the 95% confidence interval upper bound (UB) and lower bound (LB) are indicated.

Pathway	Enzyme	Reaction	Net Flux	LB	UB
Glycolysis	HK	Glc ↔ G6P	1.590	1.441	1.748
	PGI	G6P ↔ F6P	1.491	0.800	1.725
	PFK	F6P → DHAP + GAP	1.536	1.248	1.718
	TPI	DHAP ↔ GAP	1.529	1.241	1.711
	GAPDH	GAP ↔ 3PG	3.087	2.745	3.420
	PGM	3PG ↔ PEP	3.124	2.751	3.459
	PK	PEP → PYR.C	3.539	3.149	3.900
	LDH	PYR.C ↔ LAC	0.129	0.184	0.074
PPP	G6PDH	G6P → Ru5P	0.082	0.000	0.782
	PPE	Ru5P ↔ X5P	0.045	-0.011	0.513
	PPI	Ru5P ↔ R5P	0.037	0.007	0.269
	TKT1	X5P ↔ EC2 + GAP	0.045	-0.011	0.513
	TKT2	F6P ↔ EC2 + E4P	-0.023	-0.256	0.006
	TKT3	S7P ↔ EC2 + R5P	-0.023	-0.256	0.006
	TAL1	F6P ↔ EC3 + GAP	-0.023	-0.256	0.006
	TAL2	S7P ↔ EC3 + E4P	0.023	-0.006	0.256
TCA Cycle	PDH	Pyr.m → AcCoA.m + CO2	3.041	2.665	3.387
	CS	OAA.m + AcCoA.m → Cit.m	3.333	2.972	3.689
	IDH.m	Cit.m ↔ aKG.m + CO2	3.182	2.835	3.555
	aKGDH	aKG.m → Suc.m + CO2	3.287	2.897	3.668
	SDH	Suc.m ↔ Fum.m	3.327	2.922	3.716
	FUS	Fum.m ↔ Mal.m	3.327	2.922	3.716
	MDH.m	Mal.m ↔ OAA.m	3.102	2.755	3.445
Anaplerosis	ME	Mal.m → Pyr.m + CO2	0.000	0.000	0.195
	PC	Pyr.m + CO2 → OAA.m	0.231	0.157	0.388
	ATP CS	Cit.c → AcCoa.c + OAA.c	0.150	0.114	0.180
	PEPCK	OAA.c → PEP + CO2	0.415	0.335	0.497
	IDH.c	Cit.c → aKG.c + CO2	0.000	0.000	0.144
	GOT1	OAA.c ↔ Asp.c	-0.039	-0.057	-0.021
	Carboxylase	ProCoA + CO2 → Suc.m	0.040	0.026	0.057
	MDH.c	OAA.c ↔ Mal.c	-0.226	-0.310	-0.152
Amino Acid Metabolism	GS	Gln ↔ Glu.m	-0.033	-0.037	-0.028
	GluDH	aKG.m ↔ Glu.m	-0.105	-0.132	-0.078
	AsnS	Asn → Asp.c	0.079	0.064	0.094
	SHMT	Ser ↔ Gly + C1	0.003	-0.006	0.012
	PGHDH	3PG ↔ Ser	-0.037	-0.055	-0.019
	GlyS	CO2 + C1 ↔ Gly	0.016	0.011	0.021
	ALT	Pyr.c ↔ Ala.c	0.138	0.120	0.156
	Histidase	His → C1 + Glu.c	0.012	0.008	0.016
	PAH	Phe → Tyr	0.002	0.000	0.007
	TDO	Trp → CO2 + CO2 + Ala.c + aKetoadi	0.011	0.007	0.015
	AA Intermediates	aKetoadi → CO2 + CO2 + AcCoA.m + AcCoA.m	0.062	0.046	0.077
	SBCAD	Ile → AcCoA.m + CO2 + ProCoA	0.022	0.013	0.031
	IVD	Leu + CO2 → CO2 + AcCoA.m + AcCoA.m + AcCoA.m	0.049	0.033	0.065
	IBD	Val → CO2 + CO2 + ProCoA	0.003	0.000	0.011
	AASS	Lys → aKetoadi	0.051	0.036	0.065
	ARGS	Arg → Glu.c + Urea	0.015	0.007	0.023
	MAT	Met + Ser → C1 + Cys + ProCoA + Co2	0.015	0.010	0.020
Transport	Glucose	Glc.e → Glc	1.590	1.441	1.748
	Mal.m	Mal.c ↔ Mal.m	-0.226	-0.310	-0.152
	aKG.m	aKG.m ↔ aKG.c	0.000	-0.144	0.000
	Glu.m	Glu.c ↔ Glu.m	0.137	0.114	0.162
	Asp.m	Asp.m ↔ Asp.c	0.000	0.000	0.000
	Cit.m	Cit.m → Cit.c	0.150	0.114	0.280
	Lys	Lys.e → Lys	0.086	0.074	0.099
	Thr	Thr.e → Thr	0.025	0.019	0.030
	Phe	Phe.e → Phe	0.016	0.013	0.019
	Tyr	Tyr.e → Tyr	0.010	0.003	0.014
	Val	Val.e → Val	0.030	0.025	0.035
	Leu	Leu.e → Leu	0.085	0.070	0.098
	Ile	Ile.e → Ile	0.042	0.035	0.050
	Trp	Trp.e → Trp	0.014	0.010	0.018
	His	His.e → His	0.021	0.018	0.024
	Met	Met.e → Met	0.024	0.019	0.028
	Ser	Ser.e ↔ Ser	0.083	0.070	0.096
	Ala	Ala.c ↔ Ala.e	0.112	0.097	0.127
	Arg	Arg.e ↔ Arg	0.038	0.032	0.045
	Asp	Asp.c ↔ Asp.e	0.018	0.013	0.022
	Cys	Cys.e ↔ Cys	-0.006	-0.012	0.000
	Glu	Glu.c ↔ Glu.e	-0.135	-0.156	-0.114
	Gln	Gln ↔ Gln.e	0.012	0.011	0.013
	Gly	Gly.e ↔ Gly	0.014	0.007	0.022
	Pro	Pro.e ↔ Pro	0.020	0.016	0.024
	Asn	Asn.e ↔ Asn	0.097	0.083	0.112
	Lac	Lac ↔ Lac.e	0.129	0.074	0.184
Antibody Production		0.033*Ala.c + 0.016*Cys + 0.031*Asp.c + 0.031*Glu.c + 0.021*Phe + 0.04*Gly + 0.013*His + 0.018*Ile + 0.047*Lys + 0.053*Leu + 0.007*Met + 0.026*Asn + 0.049*Pro + 0.031*Gln + 0.016*Arg + 0.078*Ser + 0.059*Thr + 0.058*Val + 0.012*Trp + 0.029*Tyr → Antibody	0.027	0.024	0.030
Biomass Production	Biomass (730 pg/cell)	0.438*Ala.c + 0.2752*Arg + 0.2621*Asp.c + 0.2102*Asn + 0.1058*Cys + 0.2351*Gln + 0.2818*Glu.c + 0.3927*Gly + 0.1044*His + 0.2365*Ile + 0.4117*Leu + 0.4161*Lys + 0.1007*Met + 0.1599*Phe + 0.2285*Pro + 0.3139*Ser + 0.2818*Thr + 0.03212*Trp + 0.1329*Tyr + 0.3037*Val + 0.2106*G6P + 0.17*R5P + 0.17*C1 + 0.0868*DHAP + 1.807*AcCoA.c → Biomass	0.089	0.068	0.107

Table 3.A5: **Net fluxes determined by ^{13}C MFA for the SV40(-) line**. The best-fit value and the 95% confidence interval upper bound (UB) and lower bound (LB) are indicated.

References

[1] Sarah A Sacco, Angela M Tuckowski, Irina Trenary, Lauren Kraft, Michael J Betenbaugh, Jamey D Young, and Kevin D Smith. Attenuation of glutamine synthetase selection marker improves product titer and reduces glutamine overflow in Chinese hamster ovary cells. *Biotechnology and bioengineering*, mar 2022.

[2] F M Wurm. Production of recombinant protein therapeutics in cultivated mammalian cells. *Nat Biotechnol*, 22(11):1393–1398, 2004.

[3] Benjamin Leader, Quentin J. Baca, and David E. Golan. Protein therapeutics: A summary and pharmacological classification. *Nature Reviews Drug Discovery*, 7(1):21–39, 2008.

[4] Saurabh Rob Aggarwal. What's fueling the biotech engine-2012 to 2013. *Nature Biotechnology*, 32(1):32–39, 2014.

[5] M. De Jesus and F. M. Wurm. Manufacturing Recombinant Proteins in kg-ton Quantities Using Animal Cells in Bioreactors. *Comprehensive Biotechnology, Second Edition*, 3(2):357–362, 2011.

[6] Natalia I. Majewska, Max L. Tejada, Michael J. Betenbaugh, and Nitin Agarwal. N-Glycosylation of IgG and IgG-like recombinant proteins: Why is it important and how can we control it? *Annual Review of Chemical and Biomolecular Engineering*, 11(13):1–28, 2020.

[7] Allison G Mcatee, Neil Templeton, and Jamey D Young. Role of Chinese hamster ovary central carbon metabolism in controlling the quality of secreted biotherapeutic proteins. *Pharmaceutical Bioprocessing*, 2(1):63–74, 2014.

[8] Maria Elisa Rodrigues, Ana Rita Costa, Mariana Henriques, Philip Cunnah, David W. Melton, Joana Azeredo, and Rosário Oliveira. Advances and drawbacks of the adaptation to serum-free culture of CHO-K1 cells for monoclonal antibody production. *Applied Biochemistry and Biotechnology*, 169(4):1279–1291, 2013.

[9] Martin S Sinacore, Denis Drapeau, and S R Adamson. Adaptation of Mammalian Cells to Growth in Serum-Free Media. *Molecular Biotechnology*, 15, 2000.

[10] Martin Schröder, Kathrin Matischak, and Peter Friedl. Serum- and protein-free media formulations for the Chinese hamster ovary cell line DUKXB11. *Journal of Biotechnology*, 108(3):279–292, 2004.

[11] Simon Fischer, René Handrick, and Kerstin Otte. The art of CHO cell engineering : A comprehensive retrospect and future perspectives. *Biotechnology Advances*, 33(8):1878–1896, 2015.

[12] Jennifer Becker, Matthias Hackl, Oliver Rupp, Tobias Jakobi, Jessica Schneider, Rafael Szczepanowski, Thomas Bekel, Nicole Borth, Alexander Goesmann, Johannes Grillari, Christian Kaltschmidt, Thomas Noll, Alfred Pühler, Andreas Tauch, and Karina Brinkrolf. Unraveling the Chinese hamster ovary cell line transcriptome by next-generation sequencing. *Journal of Biotechnology*, 156(3):227–235, 2011.

[13] Neil Templeton, Kevin D Smith, Allison G Mcatee-pereira, Haimanti Dorai, J Betenbaugh, Steven E Lang, and Jamey D Young. Application of 13C flux analysis to identify high-productivity CHO metabolic phenotypes. *Metabolic Engineering*, 43(B):218–225, 2017.

[14] Karthik P. Jayapal, Katie F. Wlaschin, Wei Shou Hu, and Miranda G.S. Yap. Recombinant protein therapeutics from CHO Cells - 20 years and counting. *Chemical Engineering Progress*, 103(10):40–47, 2007.

[15] Chih Chung Kuo, Austin WT Chiang, Isaac Shamie, Mojtaba Samoudi, Jahir M. Gutierrez, and Nathan E. Lewis. The emerging role of systems biology for engineering protein production in CHO cells. *Current Opinion in Biotechnology*, 51:64–69, 2018.

[16] Huong Le, Santosh Kabbur, Luciano Pollastrini, Ziran Sun, Keri Mills, Kevin Johnson, George Karypis, and Wei Shou Hu. Multivariate analysis of cell culture bioprocess data—Lactate consumption as process indicator. *Journal of Biotechnology*, 162(2-3):210–223, 2012.

[17] Haimanti Dorai, Seung Kyung Yun, Dawn Ellis, Cheryl Ann Kinney, Chengbin Lin, David Jan, Gordon Moore, and Michael J. Betenbaugh. Expression of anti-apoptosis genes alters lactate metabolism of Chinese Hamster ovary cells in culture. *Biotechnology and Bioengineering*, 103(3):592–608, 2009.

[18] Mio Sam Lao and Derek Toth. Effects of ammonium and lactate on growth and metabolism of a recombinant Chinese hamster ovary cell culture. *Biotechnology Progress*, 13(5):688–691, 1997.

[19] Lianchun Fan, Christopher C Frye, and Andrew J Racher. The use of glutamine synthetase as a selection marker: recent advances in Chinese hamster ovary cell line generation processes. *Pharmaceutical Bioprocessing*, 1(5):487–502, 2013.

[20] Lianchun Fan, Ibrahim Kadura, Lara E. Krebs, Christopher C. Hatfield, Margaret M. Shaw, and Christopher C. Frye. Improving the efficiency of CHO cell line generation using glutamine synthetase gene knockout cells. *Biotechnology and Bioengineering*, 109(4):1007–1015, 2012.

[21] Soo Min Noh, Seunghyeon Shin, and Gyun Min Lee. Comprehensive characterization of glutamine synthetase-mediated selection for the establishment of recombinant CHO cells producing monoclonal antibodies. *Scientific Reports*, 8(1):1–11, 2018.

[22] Jun Tian, Qin He, Christopher Oliveira, Yueming Qian, Susan Egan, Jianlin Xu, Nan Xin Qian, Erik Langsdorf, Bethanne Warrack, Nelly Aranibar, Michael Reily, Michael Borys, and Zheng Jian Li. Increased MSX level improves biological productivity and production stability in multiple recombinant GS CHO cell lines. *Engineering in Life Sciences*, 20(3-4):112–125, 2020.

[23] Marc Feary, Andrew J. Racher, Robert J. Young, and C. Mark Smales. Methionine sulfoximine supplementation enhances productivity in GS–CHOK1SV cell lines through glutathione biosynthesis. *Biotechnology Progress*, 33(1):17–25, 2017.

[24] Lianchun Fan, Ibrahim Kadura, Lara E. Krebs, Jeffery L. Larson, Daniel M. Bowden, and Christopher C. Frye. Development of a highly-efficient CHO cell line generation system with engineered SV40E promoter. *Journal of Biotechnology*, 168(4):652–658, 2013.

[25] Pao Chun Lin, Kah Fai Chan, Irene A. Kiess, Joselyn Tan, Wahyu Shahreel, Sze Yue Wong, and Zhiwei Song. Attenuated glutamine synthetase as a selection marker in CHO cells to efficiently isolate highly productive stable cells for the production of antibodies and other biologics. *mAbs*, 11(5):965–976, 2019.

[26] Heena Dhiman, Marguerite Campbell, Michael Melcher, Kevin D. Smith, and Nicole Borth. Predicting favorable landing pads for targeted integrations in Chinese hamster ovary cell lines by learning stability characteristics from random transgene integrations. *Computational and Structural Biotechnology Journal*, 18:3632–3648, 2020.

[27] Neil Templeton, Jason Dean, Pranhitha Reddy, and Jamey D. Young. Peak antibody production is associated with increased oxidative metabolism in an industrially relevant fed-batch CHO cell culture. *Biotechnology and Bioengineering*, 110(7):2013–2024, 2013.

[28] Maciek R. Antoniewicz, Joanne K. Kelleher, and Gregory Stephanopoulos. Measuring deuterium enrichment of glucose hydrogen atoms by gas chromatography/mass spectrometry. *Analytical Chemistry*, 83(8):3211–3216, 2011.

[29] Neil Templeton, Abasha Lewis, Haimanti Dorai, Elaine A. Qian, Marguerite P. Campbell, Kevin D. Smith, Steven E. Lang, Michael J. Betenbaugh, and Jamey D. Young. The impact of anti-apoptotic gene Bcl-2 expression on CHO central metabolism. *Metabolic Engineering*, 25:92–102, 2014.

[30] Taylor A. Murphy and Jamey D. Young. ETA: Robust software for determination of cell specific rates from extracellular time courses. *Biotechnology and Bioengineering*, 110(6):1748–1758, 2013.

[31] Kashif Sheikh, Jochen Förster, and Lars K. Nielsen. Modeling hybridoma cell metabolism using a generic genome-scale metabolic model of Mus musculus. *Biotechnology Progress*, 21(1):112–121, 2005.

[32] Allison G. McAtee Pereira, Jason L. Walther, Myles Hollenbach, Jamey D. Young, Allison G. McAtee Pereira, Jason L. Walther, Myles Hollenbach, and Jamey D. Young. 13C Flux Analysis Reveals that Rebalancing Medium Amino Acid Composition can Reduce Ammonia Production while Preserving Central Carbon Metabolism of CHO Cell Cultures. *Biotechnology Journal*, 13(10):1–7, 2018.

[33] Averina Nicolae, Judith Wahrheit, Janina Bahnemann, An Ping Zeng, and Elmar Heinzle. Non-stationary 13C metabolic flux analysis of Chinese hamster ovary cells in batch culture using extracellular labeling highlights metabolic reversibility and compartmentation. *BMC Systems Biology*, 8(1):1–15, 2014.

[34] Jamey D. Young. INCA: A computational platform for isotopically non-stationary metabolic flux analysis. *Bioinformatics*, 30(9):1333–1335, 2014.

[35] Yi Ern Cheah and Jamey D. Young. Isotopically nonstationary metabolic flux analysis (INST-MFA): putting theory into practice. *Current Opinion in Biotechnology*, 54:80–87, 2018.

[36] Florian M. Wurm. CHO quasispecies-Implications for manufacturing processes. *Processes*, 1(3):296–311, 2013.

[37] Florian M. Wurm and Maria João Wurm. Cloning of CHO Cells, productivity and genetic stability-a discussion. *Processes*, 5(2), 2017.

[38] Cyrielle Calmels, Andréa McCann, Laetitia Malphettes, and Mikael Rørdam Andersen. Application of a curated genome-scale metabolic model of CHO DG44 to an industrial fed-batch process. *Metabolic Engineering*, 51(September 2018):9–19, 2019.

[39] Ahn Woo Suk and Maciek R. Antoniewicz. Parallel labeling experiments with [1,2-13C]glucose and [U-13C]glutamine provide new insights into CHO cell metabolism. *Metabolic Engineering*, 15(1):34–47, 2013.

[40] Lake Ee Quek, Stefanie Dietmair, Jens O. Krömer, and Lars K. Nielsen. Metabolic flux analysis in mammalian cell culture. *Metabolic Engineering*, 12(2):161–171, 2010.

[41] Jamey D. Young. 13C metabolic flux analysis of recombinant expression hosts. *Current Opinion in Biotechnology*, 30:238–245, 2014.

[42] Christopher P. Long and Maciek R. Antoniewicz. High-resolution 13C metabolic flux analysis. *Nature Protocols*, 14(10):2856–2877, 2019.

[43] Woo Suk Ahn and Maciek R. Antoniewicz. Metabolic flux analysis of CHO cells at growth and non-growth phases using isotopic tracers and mass spectrometry. *Metabolic Engineering*, 13(5):598–609, 2011.

[44] Peter G. Slade, R. Guy Caspary, Shilpa Nargund, and Chung Jr Huang. Mannose metabolism in recombinant CHO cells and its effect on IgG glycosylation. *Biotechnology and Bioengineering*, 113(7):1468–1480, 2016.

[45] Shilpa Nargund, Jinshu Qiu, and Chetan T. Goudar. Elucidating the role of copper in CHO cell energy metabolism using 13C metabolic flux analysis. *Biotechnology Progress*, 31(5):1179–1186, 2015.

[46] Neil Templeton, Sen Xu, David J. Roush, and Hao Chen. 13C metabolic flux analysis identifies limitations to increasing specific productivity in fed-batch and perfusion. *Metabolic Engineering*, 44(August):126–133, 2017.

[47] Neil Templeton and Jamey D. Young. Biochemical and metabolic engineering approaches to enhance production of therapeutic proteins in animal cell cultures. *Biochemical Engineering Journal*, 136:40–50, 2018.

[48] Fiona Hartley, Tracy Walker, Vicky Chung, and Karl Morten. Mechanisms driving the lactate switch in Chinese hamster ovary cells. *Biotechnology and Bioengineering*, 115(8):1890–1903, 2018.

[49] Bhanu Chandra Mulukutla, Andrew Yongky, Prodromos Daoutidis, and Wei Shou Hu. Bistability in glycolysis pathway as a physiological switch in energy metabolism. *PLoS ONE*, 9(6), 2014.

[50] Bhanu Chandra Mulukutla, Andrew Yongky, Simon Grimm, Prodromos Daoutidis, and Wei Shou Hu. Multiplicity of steady states in glycolysis and shift of metabolic state in cultured mammalian cells. *PLoS ONE*, 10(3):1–20, 2015.

[51] Andrew Yongky, Jongchan Lee, Tung Le, Bhanu Chandra Mulukutla, Prodromos Daoutidis, and Wei Shou Hu. Mechanism for multiplicity of steady states with distinct cell concentration in continuous culture of mammalian cells. *Biotechnology and Bioengineering*, 112(7):1437–1445, 2015.

[52] Judith Wahrheit, Jens Niklas, and Elmar Heinzle. Metabolic control at the cytosol-mitochondria interface in different growth phases of CHO cells. *Metabolic Engineering*, 23:9–21, 2014.

[53] Jamey D. Young. Metabolic flux rewiring in mammalian cell cultures. *Current Opinion in Biotechnology*, 24(6):1108–1115, 2013.

CHAPTER 4

Overexpression of peroxisome proliferator-activated receptor γ co-activator-1α (PGC-1α) in Chinese hamster ovary cells increases oxidative metabolism and IgG productivity

Abstract

Chinese hamster ovary (CHO) cells are used extensively to produce protein therapeutics, such as monoclonal antibodies (mAbs), in the biopharmaceutical industry. MAbs are large and energetically demanding to synthesize and secrete; therefore, high-producing CHO cell lines that are engineered for maximum metabolic efficiency are needed to meet increasing demands for mAb production. Previous studies have identified that high-producing cell lines possess a distinct metabolic phenotype when compared to low-producing cell lines. In particular, it was found that high mAb production is correlated to lactate consumption and elevated TCA cycle flux. We hypothesized that enhancing flux through the mitochondrial TCA cycle and oxidative phosphorylation would lead to increased mAb productivities and final titers. To test this hypothesis, we overexpressed peroxisome proliferator-activated receptor γ co-activator-1α (PGC-1α), a gene that promotes mitochondrial metabolism, in an IgG-producing parental CHO cell line. Stable cell pools overexpressing PGC-1α exhibited increased oxygen consumption, indicating increased mitochondrial metabolism, as well as increased mAb specific productivity compared to the parental line. We have also carried out ^{13}C metabolic flux analysis (MFA) to quantify how PGC-1α overexpression alters intracellular metabolic fluxes, revealing not only increased TCA cycle flux, but global upregulation of metabolic activity. In this chapter, we will also discuss a number of different techniques used to confirm the presence of active PGC-1α protein. This study highlights the possibility of rationally engineering the metabolism of industrial cell lines to improve overall mAb productivity and increase the abundance of high-producing clones in stable cell pools.

4.1 Introduction

Monoclonal antibodies (mAbs) represent the largest class of biopharmaceuticals, accounting for over 50% of new drug approvals and 65% of global biopharmaceutical sales [1]. MAbs are highly specific, allowing for less side effects during treatment, and are currently used to treat a wide range of diseases, such as autoimmune disorders, various cancers, and inflammatory diseases. Biopharmaceuticals are typically produced in mammalian cells due to their complexity. Chinese hamster ovary (CHO) cells are one of the most common mammalian host cell lines, used in the production of over 80% of recently approved mAbs [1]. CHO cells have the ability to perform human-like post-translational modifications that are necessary for efficacy of protein therapeutics [2, 3], can grow in serum-free media [4, 5, 6], and can be cultured in suspension [7, 8], all of which contribute to their preferred use in industry. While most of the optimization in the production of mAbs has occurred in media formulation and bioprocess parameters, little improvement has been made to the cell specific production rate (qP) by engineering metabolism of the host cell line [9, 10, 11]. With increasing demands for mAb treatments, there is an urgent need for maximal production; this can best be achieved by optimizing not only media and bioprocesses, but also the metabolic phenotypes of CHO host lines.

MAbs are energetically intensive for the cell to produce, requiring three ATP molecules per peptide bond [12]. During times of high production, mAbs can represent up to 20% of total cellular protein synthesis. Additional ATP is required to package and secrete mAbs into the extracellular medium [13]. It has been estimated that 2.3 pmol/cell/day of ATP are required for specific productivites in the range of 20-40 pg/cell/day [14]. Despite the demands for energy and biosynthetic precursors to produce mAbs at high yield, CHO cells often exhibit an inefficient central carbon metabolism. They typically consume excess nutrients (e.g., glucose and amino acids) and excrete waste products such as lactate, ammonia, and other byproducts that accumulate in the culture medium and inhibit cell growth and affect final product quality [15, 16, 17]. It has previously been observed that peak qP occurs

during the stationary growth phase, coinciding with a switch to lactate consumption that provides additional carbon and increased flux through oxidative metabolism, particularly the tricarboxylic acid (TCA) cycle [11, 18, 19]. Based on these observations, we hypothesized that increasing flux through the TCA cycle would lead to increased mAb productivity and final titers.

To promote higher TCA cycle flux, we engineered an industrial IgG-expressing CHO cell line to overexpress peroxisome proliferator-activated receptor γ co-activator-1α (PGC-1α), a transcriptional coactivator that has been shown to regulate oxidative metabolism in a variety of tissues (Fig. 4.1) [20, 21, 22, 23, 24]. PGC-1α has been implicated in controlling processes such as mitochondrial biogenesis and remodeling as well as cellular respiration via the expression of cytochrome C oxidases and electron transport chain components, in addition to other tissue-specific roles [20, 21, 22, 24]. In muscle, PGC-1α was shown to regulate oxidative phosphorylation and increase glucose uptake [21, 25]. In primary hepatocytes, PGC-1α was found to increase mitochondrial DNA content as well as the expression of citrate synthase and electron transport chain proteins [26]. Additionally, PGC-1α is an important regulator of gluconeogenesis in the liver [27, 28, 29]. Furthermore, in cardiac myocytes, PGC-1α overexpression increased the transcription of genes involved in energy-production pathways, cellular mitochondrial content, and oxygen consumption [30]. In PGC-1α knock-out cardiac tissue, lower levels of ATP were observed alongside lower ATP production per mole of oxygen consumed, indicating lower respiratory efficiency [31]. Overall, the role of PGC-1α in metabolism has been well characterized in a variety of different tissue and cell types. However, to the best of our knowledge, the overexpression of PGC-1α has not been studied in CHO cells. In other cell types, overexpression of PGC-1α has been shown to increase oxygen consumption, increase mitochondrial biogenesis, and increase mitochondrial metabolism. Overexpression of PGC-1α should lead to upregulation of genes involved in oxidative metabolism, leading to an overall upregulation of substrate oxidation and ATP production [21, 30, 26, 25].

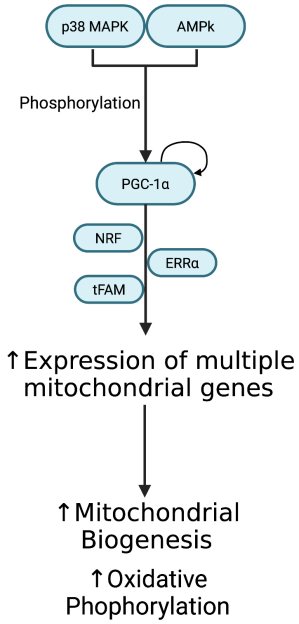

Figure 4.1: **Role of PGC-1α as a master regulator of mitochondrial biogenesis.** PGC-1α expression is thought to be partially controlled by an autoregulatory loop [32]. PGC-1α can be activated via phosphorylation by p38 MAPK and AMPK. Active PGC-1α co-activates, along with transcription factors such as NRF, tFAM, and ERRα, the expression of multiple mitochondrial genes. This leads to increased mitochondrial biogenesis and increased oxidative phosphorylation. Created with BioRender.com. MAPK, mitogen-activated protein kinase; AMPK, AMP kinase; NRF, nuclear respiratory factor; tFAM, mitochondrial transcription factor A; ERRα, estrogen related receptor alpha.

In this study, ^{13}C metabolic flux analysis (MFA) was applied to examine the parental CHO cell line and stable pools transfected with a PGC-1α expression vector to quantify the metabolic changes that occurred due to PGC-1α overexpression. By feeding ^{13}C-labeled glucose and analyzing the isotopic enrichment of intracellular metabolites, fluxes through central carbon metabolism were quantified using a mathematical model of CHO central carbon metabolism [33, 34]. Due to the short duration of stationary phase, isotopic steady state was not achieved before cell death rates began to affect cellular metabolism. Therefore, isotopically nonstationary metabolic flux analysis (INST-MFA) was used to assess metabolism during stationary growth phase. While INST-MFA is more computationally demanding than stationary MFA, it provides increased accuracy of flux estimation [35].

Due to the greater number of measurements used to regress fluxes in INST-MFA, net fluxes can be determined with greater precision. Additionally, reversible exchange fluxes, which are sometimes unobservable in steady state systems, can be accurately resolved with INST-MFA [35, 36].

In light of the extensive effects PGC-1α has on metabolism in other cell types, our study sought to assess the extent to which PGC-1α overexpression would enhance oxidative metabolism in an industrial CHO cell line and whether these metabolic alterations would correlate with increased qP. Previous studies have identified an association between high-producing CHO cell lines and elevated mitochondrial metabolism [37, 19]. Additionally, it has been shown that titers are increased by increasing pyruvate dehydrogenase (PDH) activity, which directs pyruvate into the TCA cycle [38, 39]. However, this is the first study, to our knowledge, that has attempted to evaluate the metabolic phenotypes of CHO cells engineered to increase oxidative metabolism on a global level. We have previously shown that in stable pools engineered to overexpress PGC-1α, oxygen uptake increased 2.4-fold, indicating increased oxidative metabolism. Additionally, qP increased up to 5.2-fold relative to the parental line. Herein, we will show that ^{13}C MFA corroborates these observations, revealing upregulated fluxes throughout metabolism.

The focus of this chapter will be to present the results from several different approaches used to determine the expression and activity of PGC-1α protein. While expression of PGC-1α protein was never confirmed, its activity was indirectly assessed by the measurement of endogenous PGC-1α expression. This chapter describes the use of western blotting and immunofluorescence to directly observe PGC-1α protein, luciferase assays and quantitative real-time polymerase chain reaction (qPCR) to quantify the expression of targets of PGC-1α protein, as well as the use of principal component analysis to identify significant differences between PGC-1α expressing and empty vector pools. Additionally, we report the observation of increased cell size in PGC-1α expressing pools.

4.2 Previously Reported Results

The results described in this section form the basis of the work described later in this chapter and are summarized from the dissertation of Allison G. McAtee Pereira [40].

4.2.1 Generation and selection of stable PGC-1α expressing pools

After transfection with the PGC-1α expression vector, a total of 20 PGC-1α stable cell lines were generated from the antibiotic-resistant mini-pools. Eight of the transfected lines exhibited disruption of mAb expression due to the selection process and were therefore not studied further. The remaining twelve cell lines were evaluated based on the measured qP compared to the parental line and the expression level of recombinant PGC-1α mRNA, as measured by RT-qPCR. (Fig. 4.2) Three pools exhibited significantly higher qP levels compared to the parental line and mid-range mRNA overexpression of recombinant PGC-1α. These three PGC-1α overexpressing lines were selected for further characterization and are referred to herein as pools 1, 2, and 3.

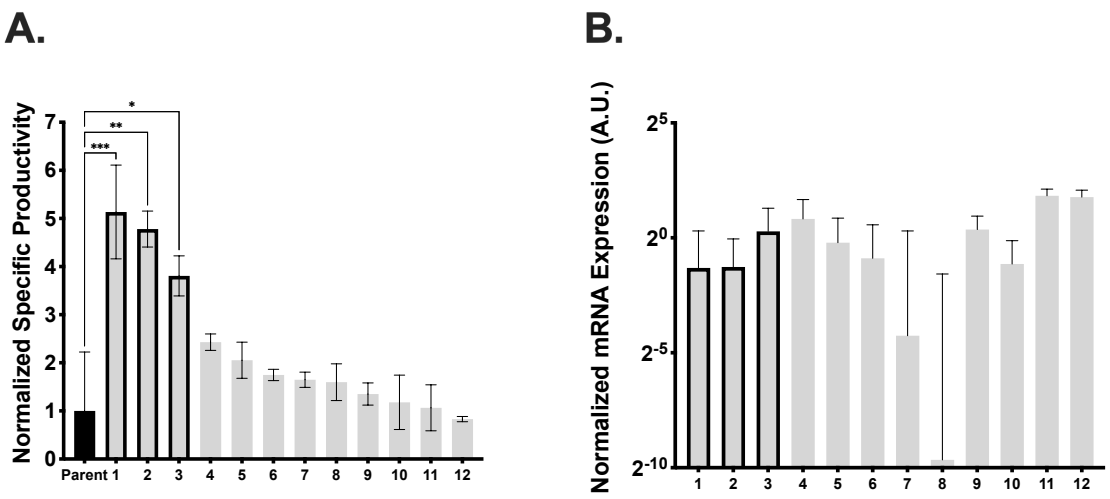

Figure 4.2: **Specific productivity and recombinant PGC-1α mRNA expression of selected pools.** (A) qP was measured for the parental line and 12 PGC-1α expressing pools. For each pool, qP was normalized to the parental qP; only three pools had significantly higher qP compared to the parental line. (B) mRNA expression of recombinant PGC-1α normalized to HPRT (housekeeping gene) expression as measured by qPCR. All 12 pools exhibited some level of recombinant PGC-1α mRNA expression; the three pools that were selected for further analysis (bars with black border) had mid-range levels of recombinant PGC-1α mRNA expression, but PGC-1α mRNA expression was not significantly different across all pools analyzed. Data represent mean $\pm$ SEM. * indicates statistical significance $p<0.05$, ** $p<0.01$, *** $p<0.01$, compared to parental line. (n=2)

4.2.2 PGC-1α expression attenuated growth but increased mAb specific productivity

VCD was measured daily over the course of the fed-batch experiment summarized in Table 1. Both the exponential growth rate and peak VCD were significantly lower in the PGC-1α expressing pools. (Fig. 4.3A, B) The lower growth of the PGC-1α pools is likely indicative of increased metabolic burden of producing recombinant PGC-1α in addition to the mAb product. Despite this reduction in growth, volumetric titers of the three PGC-1α pools were significantly higher compared to the parental line, final titers increasing by up to 1.5-fold. (Fig. 4.3C,D) The increased titers were due to significantly higher qP values that were nearly 4-fold greater than that of the parental line. (Fig. 4.3E)

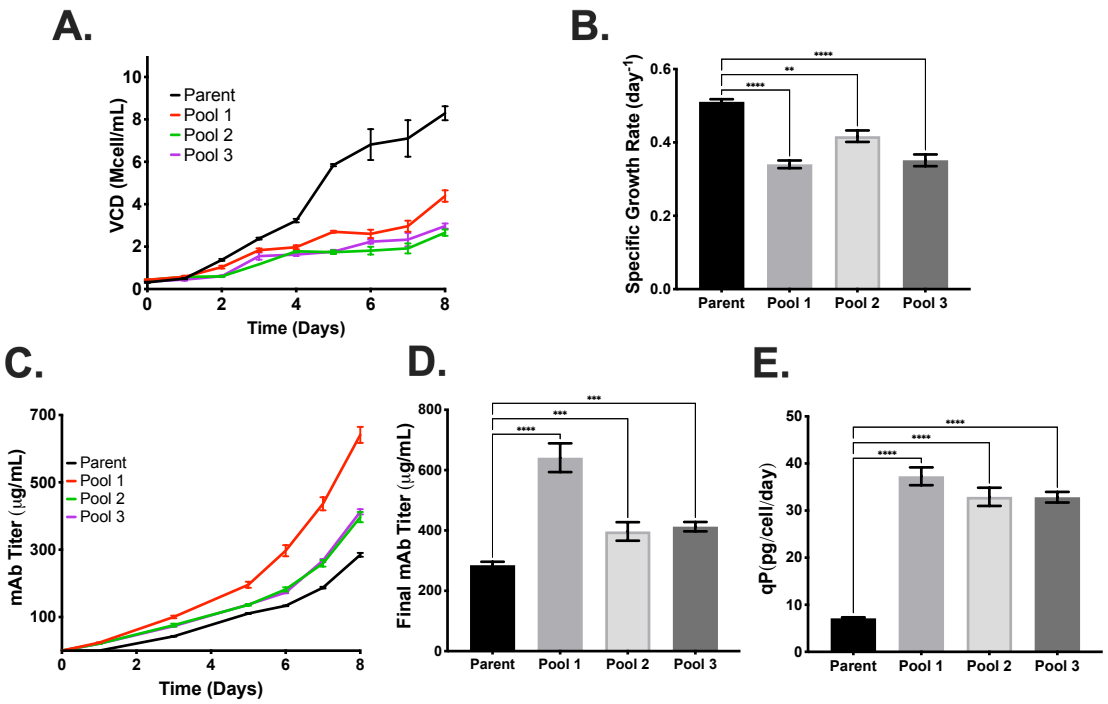

Figure 4.3: **Growth and productivity of the parental line and selected PGC-1α pools.** (A) Viable cell density during the fed-batch study. (B) Specific growth rates during exponential phase. (C) Volumetric titer over the course of the fed-batch study. (D) Final mAb titer measured on day 8 of culture. (E) Specific productivity during the ^{13}C labeling experiment. Data represent mean $\pm$ SEM. ** indicates statistical significance $p<0.01$, *** $p<0.001$, **** $p<0.0001$ compared to the parental line. (n=4)

4.2.3 PGC-1α expressing pools exhibit higher consumption of oxygen and carbon sources

Oxygen uptake rates (OURs) are typically elevated in cells and tissues that overexpress PGC-1α, which serves as an indicator of oxidative metabolism [30]. OURs were measured for each PGC-1α pool and compared to the parental line on the final day of the fed-batch experiment when the cultures were in the stationary growth phase (Table 4.1). All pools exhibited significantly higher OURs compared to the parental line (Fig. 4.4). These results indicate that the PGC-1α expressing pools exhibited substantial enhancements in oxidative metabolism during stationary phase. Supporting this observation, the consumption of several carbon sources from the media was significantly higher in the PGC-1α expressing pools. Glucose uptake rates during stationary phase were nearly doubled compared to the

parental line, while lactate uptake rates were at least 4-fold higher in the PGC-1α pools (Fig. 4.5). The increased consumption of these two major carbon sources likely fueled the increased metabolism observed in the PGC-1α expressing pools. Additionally, the consumption of nine out of fifteen measured amino acids was significantly higher, while the production of alanine, glutamine, and glycine were all significantly enhanced by expression of PGC-1α (Fig. 5.7).

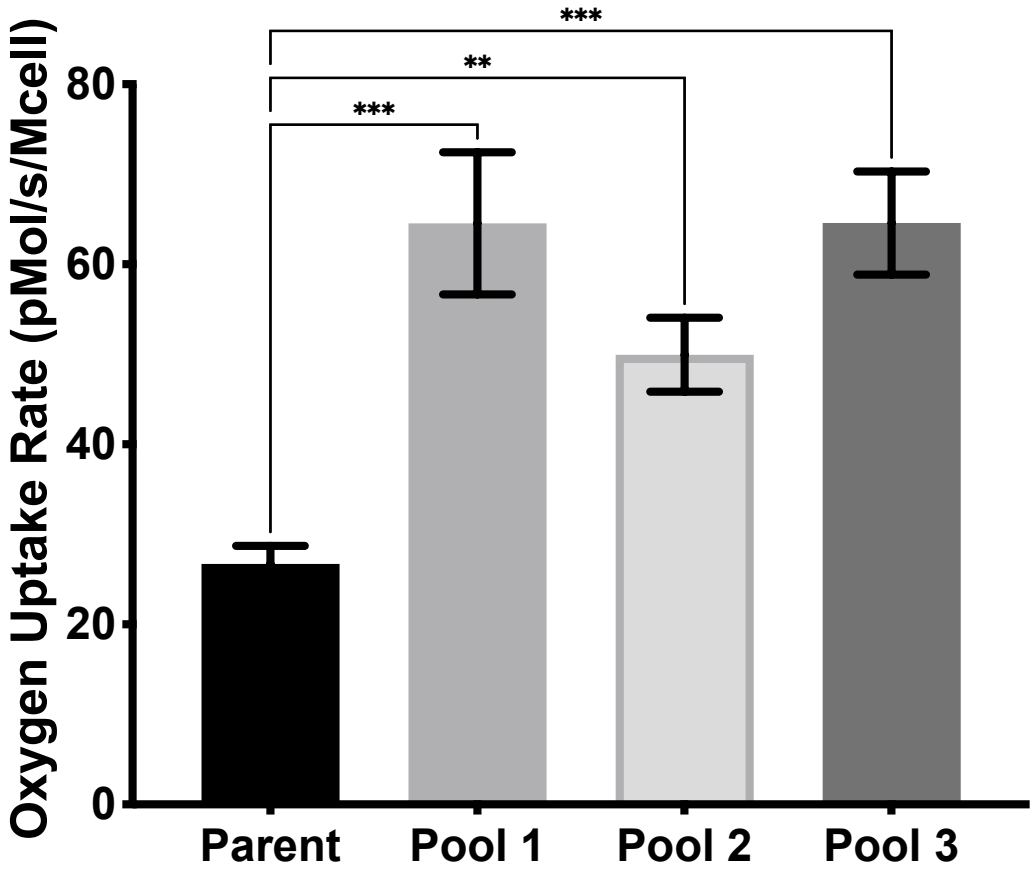

Figure 4.4: **Oxygen uptake rates of parental line and selected PGC-1α pools.** OUR was measured on the final day of culture. Data represent mean $\pm$ SEM. ** indicates statistical significance $p < 0.01$, *** $p < 0.001$, compared to parental line. (n=2)

High lactate consumption rates during stationary phase have been correlated to high productivities in CHO cell lines [37], a finding corroborated in this study. Higher LURs could prolong culture longevity by removing toxic lactate buildup from the media. Lactate can serve as an additional carbon source for the TCA upon its conversion to pyruvate.

The conversion of lactate to pyruvate by lactate dehydrogenase produces NADH, and it is widely thought that CHO cells switch from lactate production to lactate consumption to replenish the cytosolic pool of NADH when glycolytic rates are slowed [41]. The cytosolic NADH can indirectly enter the mitochondria through the malate-aspartate shuttle, further fueling oxidative phosphorylation. The observation of both increased lactate consumption as well as increased oxidative metabolism in the PGC-1α overexpressing lines supports the hypothesis that higher lactate uptake can fuel the increase in mitochondrial metabolism necessary to promote high productivities [41].

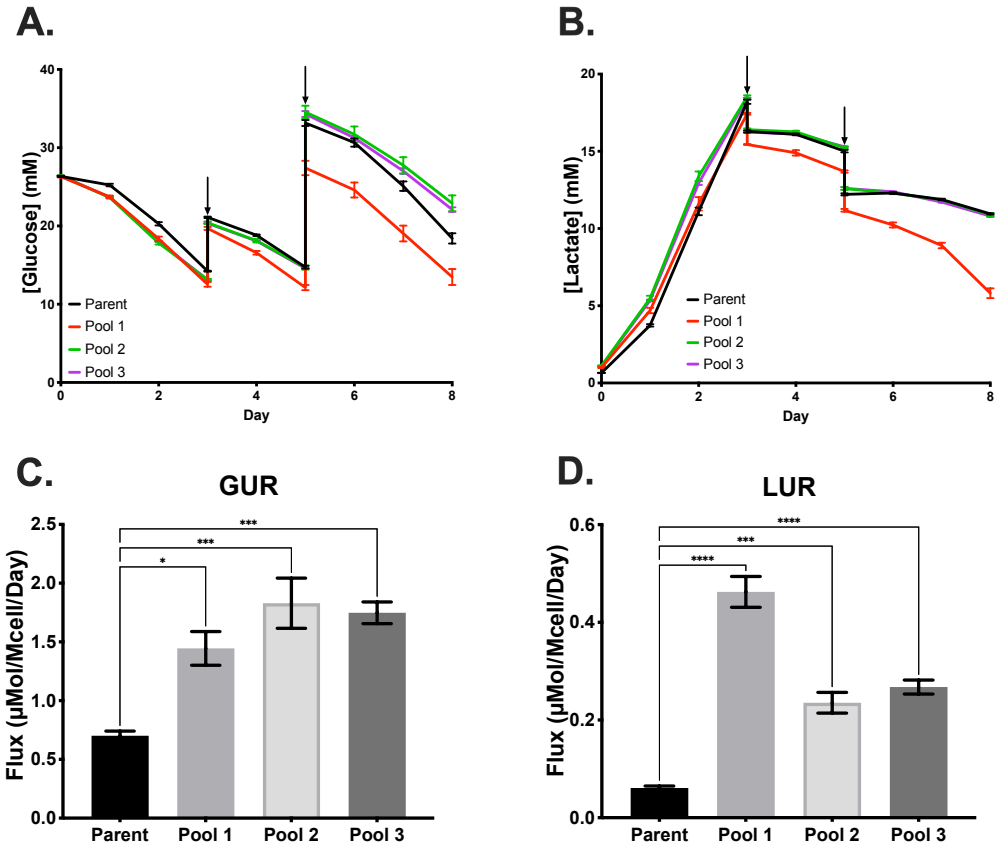

Figure 4.5: **Glucose and lactate consumption rates.** (A) Glucose profile over the course of the fed-batch study. (B) Lactate profile over the course of the fed-batch study. (C) Glucose uptake rate (GUR) measured during the ^{13}C labeling experiment. (D) Lactate uptake rate (LUR) measured during the ^{13}C labeling experiment. Arrows indicate addition of feed. Data represent mean $\pm$ SEM. ** indicates statistical significance $p<0.01$, *** $p<0.001$, **** $p<0.0001$ compared to parental line. (n=4)

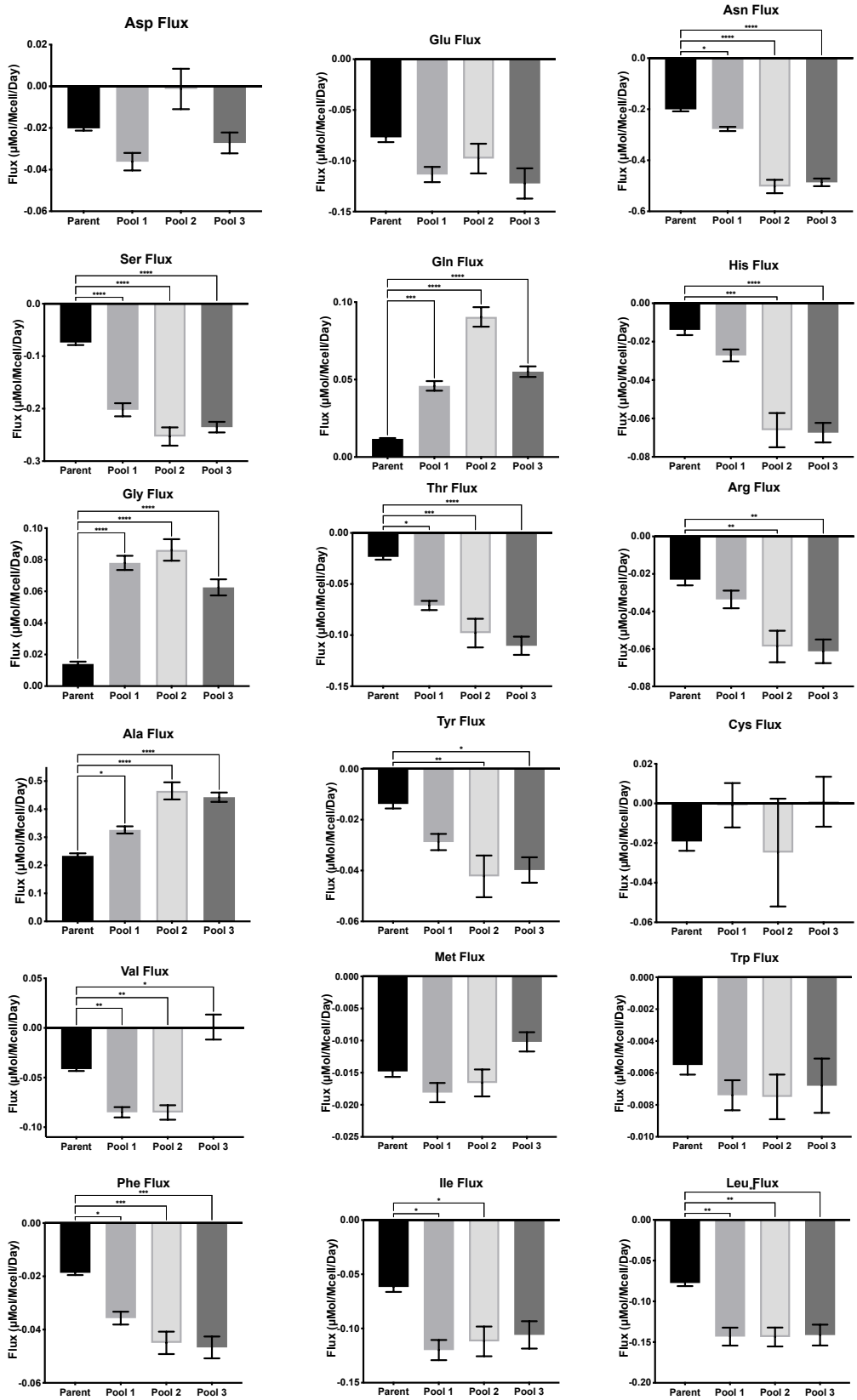

Figure 4.6: **Amino acid fluxes during the isotope labeling experiment.** Positive rates indicate production and negative rates indicate consumption. Data represent mean ± SEM. * indicates statistical significance $p < 0.05$, ** $p < 0.01$, *** $p < 0.001$, compared to parental line. (n=4)

4.3 Materials and Methods

4.3.1 Generation of cell lines

An industrial IgG-producing CHO cell line, provided by Janssen, was used for this study. The pcDNA4-c-Myc-PGC-1α plasmid was a gift from Toren Finkel (Addgene plasmid # 10974 ; http://n2t.net/addgene:10974 ; RRID:Addgene_10974) [42]. The plasmid featured the coding sequence for human PGC-1α under a CMV promoter with c-Myc and His tags on the C-terminus and zeocin resistance. An empty vector plasmid containing just a zeocin resistance marker was also used to generate empty vector control cell pools in the same manner described below. Two days preceding transfection with the vector, cells were seeded at 2x10^5 cells/mL in 50 mL fresh MACH-1 (SAFC; Burlington, MA) medium in 125 mL shake flasks at 37°C, 5% CO2, and shaking at 135 RPM. Since the mAb was expressed via the glutamine synthetase (GS) expression system, methionine sulfoximine (MSX) was added to the MACH-1 medium to inhibit endogenous GS activity. On the day of transfection, cells were seeded in T-25 flasks containing 1x10^7 live cells in 1 mL fresh medium + MSX. Then, 15 μg of purified expression vector was incubated in 1.8 mL MSX-containing MACH-1 medium. Meanwhile, 37.5 μL polyethyleneimine (PEI) was separately incubated in 1.8 mL MSX-containing MACH-1 medium. The PEI incubation was combined with the vector-containing aliquot and mixed thoroughly. The DNA/PEI mixture was incubated for 15 minutes at room temperature and then added to the T-25 flask containing the parental cells. The cultures were incubated for 48 hours, then harvested, centrifuged at 1000 RPM for five minutes, and the transfection medium was aspirated. The transfected cells were re-suspended in fresh MACH-1 containing MSX, phenol red, and 300 μg/mL zeocin (Invitrogen; Carlsbad, CA) at a density of 1.6x10^4 cells/200 μL. Phenol red (Sigma) was added for visual assessment of cell growth, while zeocin was added for antibiotic selection to kill any cells that did not integrate the DNA construct. The cell suspension was aliquoted into 96-well plates (200 μL/well) for mini-pool selection to obtain stable lines.

Roughly half of the medium in each well was removed via aspiration every three to four days and replaced with fresh growth medium. When the medium color change indicated rapid cell growth, the cells in those wells were expanded into 24-well plates, then to 12- and 6-well plates before being expanded to growth in T-25 and then T-75 flasks. Once the expanded mini-pools reached sufficiently high cell densities, they were seeded at $3x10^5$ cells/mL in 30 mL medium in 125 mL shake flasks as stable populations. Vials containing $15x10^6$ cells were frozen in culture media plus 10% dimethyl sulfoxide (DMSO) and stored in liquid nitrogen.

4.3.2 Total RNA isolation and reverse transcriptase quantitative real-time PCR (RT-qPCR)

Total RNA was isolated from cells using the RNeasy Mini Kit (Qiagen; Germantown, MD) according to the manufacturer's protocol. Isolated RNA was reverse transcribed to cDNA using an iScript Reverse Transcription kit, according to the manufacturer's protocol (BioRad, Hercules, CA). Reactions without reverse transcriptase were run in parallel to check for any DNA contamination. Quantitative real-time PCR (RT-qPCR) was performed on a BioRad CFX96 Cycler (BioRad, Hercules, CA) with 20 μL reactions containing 25 ng/well of cDNA, 250 nm forward and reverse primers (Table 4.A2), and 10 μL SYBR Green PCR Master Mix (BioRad, Hercules, CA). Reactions were run for 40 cycles, and the threshold cycle (Ct) was determined from amplification curves using the CFX Maestro software (BioRad, Hercules, CA). Target gene expression was normalized to the expression of hypoxanthine-guanine phosphoribosyltransferase (HPRT), a housekeeping gene. Data were analyzed using a modified $\Delta\Delta C_t$ method [43]; as no expression of PGC-1α, recombinant or endogenous, was observed in the parental control line, values are reported as $2^{-\Delta C_t}$, where ΔC_t represents the difference in C_t for the gene of interest relative to the HPRT housekeeping gene.

4.3.3 Cell culture

All suspension cultures were grown in 125 mL shake flasks at 37°C and 5% CO_2 while shaking at 135 RPM. For all experiments, a vial of banked cells was thawed in a 37°C water bath and immediately added to 9 mL of pre-warmed media. This mixture was spun down at 1000 RPM for 5 minutes, and the supernatant was aspirated. The cell pellet was resuspended in 10 mL of fresh, pre-warmed media, and a 40 mL working volume culture was seeded at $3x10^5$ cells/mL from the resuspension. This culture was grown for 4 days and then reseeded at $3x10^5$ cells/mL in a new 40 mL working volume culture for experimentation.

All adherent cultures were grown in T75 flasks at 37°C and 5% CO_2 in a working volume of 20 mL. A vial of banked cells was thawed in a 37°C water bath and immediately added to 19 mL of pre-warmed media. After cells were allowed to adhere overnight, media was replaced with fresh, pre-warmed media. Upon reaching $\sim 80-90\%$ confluency, cells were washed with pre-warmed PBS three times, trypsinized for three minutes at 37°C, and then resuspended in pre-warmed media. This cell suspension was then mixed with pre-warmed media in a new T75 flask to achieve the desired concentration.

4.3.4 Determination of growth and extracellular exchange rates

Culture viable cell densities (VCDs), percent viabilities, and average cell diameter were measured using a trypan blue exclusion method with a Cedex XS automated counter (Roche, Basel, Switzerland). Medium amino acid concentrations were analyzed using an Agilent 1200 series high performance liquid chromatograph (HPLC) as described previously [44]. Medium glucose and lactate concentrations were measured using a YSI 2300 biochemical analyzer (YSI, Yellow Springs, OH) and mAb titers were measured by a ForteBio Octet RED96 (Pall, Menlo Park, CA). Net growth rates, death rates, and extracellular fluxes were calculated by the ETA software package [45] as previously described [44].

4.3.5 ^{13}C isotopically non-stationary metabolic flux analysis (INST-MFA)

The timeline for the isotope labeling experiment is shown in Table 4.1. An isotopomer model was constructed based on a previously described CHO cell metabolic network to simulate the mass isotopomer distributions (MIDs) of intracellular metabolites [44]. The model comprised 80 metabolic reactions, 22 extracellular metabolite exchange rates, and two macromolecular products (mAb and biomass) as detailed in Tables 4.A3 - 4.A6. Isotopomer models were regressed by the INCA software package [46] to fit the experimental data sets for each cell line as previously described [44]. All model fits were overdetermined and calculated from a random starting point with a minimum of 50 random restarts to ensure the identification of a global minimum. Due to the absence of isotopic steady state, isotopically non-stationary metabolic flux analysis (INST- MFA) was used to regress flux maps of the studied lines based on measurements collected between days six through eight of culture. Goodness-of-fit metrics for the models are given in Table 4.A1. The Cytoscape software package was utilized to visualize the resulting flux maps [47].

Day	0	1	2	3	4	5	6	7	8
Event	Inoculate			Feed		Feed ^{13}C		RT-qPCR	OUR
								Sample Harvests	
						RT-qPCR		t=40 hrs. t=48 hrs.	t=60 hrs. t=72 hrs.

Table 4.1: **Experimental timeline of ^{13}C labeling experiment.** Cultures were fed ^{13}C labeled glucose on day 5 such that ^{13}C labeled glucose accounted for approximately 50% of the total glucose in the culture. Days 5-8 are shaded to indicate the presence of ^{13}C-glucose in the cell culture media. Cell pellet and media samples were collected for metabolite analysis on days 7 and 8 at the times indicated (t=40, 48, 60, 72 hrs) following the introduction of ^{13}C-glucose on day 5 (t=0). Samples for RT-qPCR analysis to measure gene expression levels were collected on days 5 and 7. Live cells were harvested on day 8 to measure the oxygen uptake rate (OUR).

4.3.6 Transfection

All plasmid DNA was purified using a QIAgen maxi-prep kit (QIAgen; Germantown, MD), according to manufacturer's protocol.

4.3.6.1 Adherent cells

After trypsinization, cells were resuspended in fresh, pre-warmed media and counted using a hemacytometer. Based on the viable cell density, the cell suspension was diluted to achieve a cell density of 75,000 cells/mL. Two mL of the diluted suspension was added to each well of a 6-well plate, resulting in a final concentration of 150,000 cells/well. Cells were grown in a 37°C and 5% CO_2 incubator for $\sim$ 36 hours, or to approximately 60% confluency.

To perform transfections, purified plasmid DNA was diluted to the desired concentration using Opti-MEM (ThermoFisher Scientific; Waltham, MA.) In a separate dilution, Lipofectamine 2000 (ThermoFisher Scientific; Waltham, MA) was diluted to the desired concentration using Opti-MEM. DNA and Lipofectamine dilutions were mixed at a 1:1 ratio and allowed to incubate for 30 minutes at room temperature. Ten minutes before adding the DNA:Lipofectamine complex, media was aspirated from the wells and 2 mL of pre-warmed OptiMEM was added to each well. After the 30-minute incubation, the DNA:Lipofectamine complex was diluted 5-fold using pre-warmed Opti-MEM. Media was again removed from the wells and replaced with 1 mL of the diluted DNA:Lipofectamine complex. Plates were incubated at 37°C for 5 hours. At the end of this incubation, the transfection mixture was aspirated, and 2 mL of pre-warmed culture media was added to each well. Cells were allowed to incubate for 18-20 hours before harvest.

To harvest cells, each well was washed once with pre-warmed PBS and then trypsinized with 200 μL of Trypsin/EDTA for 3 minutes at 37°C. Cells were rinsed from each well using 800 μL of pre-warmed culture media, and this suspension was transferred to a microcentrifuge tube. The cell suspension was centrifuged at 6000 RPM for 1 minute at

room temperature. The supernatant was removed, cells were resuspended in PBS, and centrifuged again at 6000 RPM for 1 minute at room temperature. PBS was removed and then each cell pellet was resuspended in 1X Passive Lysis Buffer (PLB) and frozen at -80°C.

4.3.6.2 Suspension Cells

DNA:Lipofectamine complexes were created in the same manner described as for the adherent cells. After the dilution of the DNA:Lipofectamine complex, suspension cells were harvested from culture such that $1x10^6$ cells were available for each well. The suspension cell culture was centrifuged at 1000 RPM for 5 minutes at room temperature, and the supernatant was removed. The cell pellet was resuspended in the DNA:Lipofectamine complex to a cell density of $1x10^6$ cells/mL, and 1 mL of the cell suspension was added to each well. Plates were allowed to incubate for 24 hours. After this incubation, cells were harvested in the same manner as described for the adherent cells.

4.3.7 Dual luciferase assay

The dual luciferase assay was performed using a Dual-Luciferase Reporter Assay kit (Promega; Madison, WI) according to the manufacturer's protocol. In brief, cells frozen in PLB were thawed in a 37°C water bath for 2 minutes and then refrozen at -80°C for 30 minutes. Plastic luminometer tubes were prepped by adding 100 μL of LAR II reagent to each tube. Samples were thawed again in a 37°C water bath for 2 minutes and kept on ice throughout the assay. The sample was vortexed, the desired volume was added to the LAR II reagent, and the tube was quickly vortexed before taking the first luminescence reading (for the luciferase reporter plasmid). Then, 100 μL of the Stop-n-Glo reagent was added to the tube, the sample was vortexed again, and the second luminescence reading was taken (for the luciferase control plasmid).

4.3.8 Western blot

For western blots, $10x10^6$ cells were harvested per sample, centrifuged at 1000 RPM for 5 minutes, and the supernatant was removed. These cell pellets were further processed dependent on the fraction of protein desired: whole cell protein, nuclear protein, His-tagged protein, or c-Myc-tagged protein.

For analysis of the whole cell lysate, the resulting cell pellet was resuspended in 100 μL Lysis buffer, which consisted of RIPA buffer with 1% phenylmethylsulfonyl fluoride (PMSF), 1% sodium orthovanadate (NaOV), and 1% Halt protease/phosphatase inhibitor (ThermoFisher Scientific; Waltham, MA). This suspension was incubated on ice for 30 minutes, vortexing every 5 minutes during the incubation. The suspension was centrifuged at 13,000 RPM for 30 minutes at 4°C. The protein-containing lysate was collected, and the concentration of protein was measured using a BCA kit (ThermoFisher; Waltham, MA) according to the manufacturer's protocol prepared for electrophoresis as described below.

For analysis of the nuclear fraction, nuclear proteins were extracted using a Nuclear Extraction Kit (Abcam; Cambridge, UK) according to the manufacturer's protocol. The concentration of protein in the resulting protein containing lysate was determined using a BCA kit (ThermoFisher; Waltham, MA) according to the manufacturer's protocol and prepared for electrophoresis as described below.

To isolate proteins with a His tag, the MagneHis Protein Purification System (Promega; Madison, WI) was used according to the manufacturer's protocol. This system utilizes magnetic nickel-based beads which bind to the His tag, allowing for the isolation of His-tagged proteins. To purify proteins with a c-Myc tag, the Pierce c-Myc-Tag Magnetic IP/Co-IP Kit (ThermoFisher; Waltham, MA) was used according to the manufacturer's protocol. This system utilizes a concept similar to that of the MagneHis system, where magnetic beads which feature an anti-c-Myc antibody are used to isolate c-Myc tagged proteins. For samples that were purified based on the protein tag, the concentration was not measured; however, a set volume was added to each well of the gel, as the resulting protein

isolate was already prepared for electrophoresis.

Protein lysates were diluted with deionized water to the desired concentration in a final volume of 30 μL. The diluted lysates were mixed with 10 μL of NuPAGE Buffer (ThermoFisher; Waltham, MA) plus 2.5% β-mercaptoethanol. The sample was boiled on a dry heating block at 95°C for 2 minutes and then allowed to cool to room temperature.

Mini-PROTEAN 4-20% tris-glycine precast gels (Bio-Rad; Hercules, CA) were placed inside the electrophoresis chamber, which was then filled with tris-glycine SDS running buffer. Ten μL of sample or PagePlus Protein Ruler (ThermoFisher; Waltham, MA) ladder was loaded into each lane. The electrophoresis was run at 100 volts for 90 minutes. The gel was transferred to a membrane using an iBlot 2 transfer stack (Nitrocellulose or PVDF) (ThermoFisher; Waltham, MA) according to the manufacturer's protocol. The resulting membrane was blocked with 5% bovine serum albumin (BSA) in tris-buffered saline (TBS) overnight at 4°C with constant rocking. The primary antibody was diluted to the desired concentration in 5% BSA in TBS plus 1% Tween-20 (TBS-T), and the blocked membrane was incubated with the primary antibody solution at 4°C overnight with constant rocking. After the primary antibody incubation, the membrane was washed three times at room temperature for 10 minutes each in TBS-T with constant rocking. The secondary antibody was diluted to the desired concentration in 2.5% BSA in TBS-T; for PVDF membranes, an additional 0.01% SDS was added to this solution. The membrane was incubated with the secondary antibody dilution for 1 hour at room temperature with constant rocking and then was washed three times for ten minutes each with TBS-T with constant rocking. The final membrane was imaged using a Li-Cor IR imager (Li-Cor Biosciences; Lincoln, NE) according to the manufacturer's protocol.

4.3.9 Immunofluorescence

4.3.9.1 Adherent Method

For the adherent method of immunofluorescence, sterilized glass microscope slides were treated with poly-L-lysine or fibronectin to allow cells to attach. The treated slide was placed in a 6 cm petri dish, and a suspension of cells containing $1x10^6$ cells/mL was added on top of the treated slide. The cells were allowed to attach overnight, after which time the slide was washed with pre-warmed PBS. All further incubations occurred with constant rocking. Next, the cells were fixed with -20°C 80% acetone for 15 minutes at room temperature. The slide was then washed with PBS three times for five minutes each at room temperature. The cells were then blocked with 5% normal goat serum (NGS) in PBS for 1 hour at room temperature. Without washing, the cells were then incubated in a solution containing the primary antibody diluted to the desired concentration in 1% BSA in PBS overnight at 4°C. The slide was then washed with PBS three times for ten minutes each at room temperature. Then, the cells were incubated in the dark for one hour at room temperature in a solution containing the secondary antibody diluted to the desired concentration in 1% BSA in PBS. The slide was then washed with PBS three times for 15 minutes each at room temperature, in the dark. Finally, a glass slide cover was mounted on top of the cells using VectaShield PLUS Antifade Mounting Media with DAPI (Vector; Burlingame, CA) and allowed to dry for at least 30 minutes before imaging.

4.3.9.2 Suspension Method

For the suspension method of immunofluorescence, the protocol described by Wang et al. [48] was adapted. Five million cells were harvested per sample. The harvested cells were centrifuged at 1000xG for 3 minutes at room temperature. The supernatant was removed, leaving just a cell pellet. This cell pellet was washed in 1 mL PBS once, centrifuged at 1000xG for 3 minutes at room temperature, and the supernatant was removed. The remaining cell pellet was then fixed and permeabilized using one of the fixation methods

described below.

For fixation and permeabilization with acetone, the cell pellet was resuspended in 800 μL of -20°C 80% acetone. This suspension was vortexed for 15 minutes at room temperature before being centrifuged at 1000xG for 3 minutes at room temperature. The acetone was removed and cells were washed once with PBS.

For fixation and permeabilization with methanol, the cell pellet was resuspended in 800 μL of -20°C methanol. This suspension was vortexed for 15 minutes at room temperatures, centrifuged at 1000xG for 3 minutes at room temperature, and the methanol was removed. The resulting cell pellet was washed once with PBS.

For all immunofluorescence experiments that included phalloidin staining, cells were fixed with 10% formalin. The cell pellet was resuspended in 10% formalin and incubated at room temperature on a Rotoshaker for ten minutes. The cells were washed twice with PBS and then resuspended in a 0.25% Triton-X 100 in PBS solution for permeabilization. The suspension was incubated for 15 minutes at room temperature on a Rotoshaker and then washed twice with PBS.

After fixation and permeabilization, cells were resuspended in a blocking solution consisting of 5% normal goat serume (NGS) in PBS and incubated at room temperature for one hour on a Rotoshaker. Cells were centrifuged at 1000xG for 3 minutes at room temperature and then resuspended in a primary antibody solution consisting of the primary antibody diluted to the desired concentration in 1% bovine serum albumin (BSA) in PBS. This suspension was incubated overnight at 4°C in a Rotoshaker. After incubation, cells were washed twice with PBS and then resuspended in a solution containing the secondary antibody at the desired dilution as well as the phalloidin stain, diluted 1000x, in 1% BSA in PBS. This suspension was incubated for 1 hour at room temperature on a Rotoshaker in the dark. Cells were washed twice with PBS, resuspended in VectaShield PLUS Antifade Mounting Media with DAPI (Vector; Burlingame, CA) and then carefully transferred to a microscope slide and covered with a coverslip. Slides were allowed to dry for at least 30

minutes before imaging to ensure media had set.

4.3.9.3 Quantification via ImageJ

In order to allow for the quantification of images from IF, all images were captured using identical settings for intensity, exposure, and gain. Images were quantified using ImageJ, using an adaptation of the method described by Handala et al. [49], as shown in Figure 4.A1. In brief, based on the image for the channel of the phalloidin membrane stain, the cell boundaries were defined using the Threshold Tool. These cell boundaries were then applied to each other channel (DAPI and the secondary antibody) so that only fluorescence measured within those boundaries was included. The Average Gray Value (AGV), which represents the sum of all gray values in the defined area divided by the number of pixels in that area, was provided for each channel. The AGV effectively quantifies the intensity of the fluorescence in that channel normalized to the total area of cells. The AGV for the secondary antibody channel could then be normalized to both the AGV of the phalloidin channel or the DAPI channel to normalize for any differences in dye uptake.

4.3.10 Statistical Analysis

One-way ANOVA was used to determine statistically significant differences between cell lines (α = 0.05). A Tukey multiple comparison test was applied if significant differences were detected. The standard error of the mean (SEM) was estimated for intracellular fluxes using the formula SEM = (UB-LB)/3.92, where UB and LB represent the upper and lower bounds of the 95% confidence intervals, respectively, and 3.92 is the number of standard errors that span the 95% confidence interval of a normally distributed random variable. The principal component analysis (PCA) was carried out using the `prcomp` function in R. All variables were shifted to be centered around 0, and all values were scaled to unit variance (divided by the standard deviation of the variable).

4.4 Results and Discussion

4.4.1 PGC-1α expressing pools exhibited increased average cell size

While the growth rates and peak VCDs of the PGC-1α expressing pools were significantly lower than the parental line, we observed a substantial increase in average cell size of PGC-1α expressing pools. Average cell diameters increased by approximately 1.5 μm, which corresponded to a 50% increase in cell volume, assuming a spherical cell shape (Fig. 4.7). A previous study of PGC-1α disruption via short-hairpin RNA (shRNA) in glioma cells found that PGC-1α knockdown significantly decreased cell size [50]. Therefore, the observation that overexpression of PGC-1α increased cell size is not particuarly surprising. The correlation of increased cell size with increased antibody productivity has been reported [51, 52]. It has been previously shown that treatment with 5'-deoxy-5'-(methylthio)adenosine (MTA), an additive that arrests cell cycle progression, leads to increased cell size and productivity in CHO cells [53]. The observed increase in both cell size and qP in PGC-1α expressing pools agrees with these previous studies.

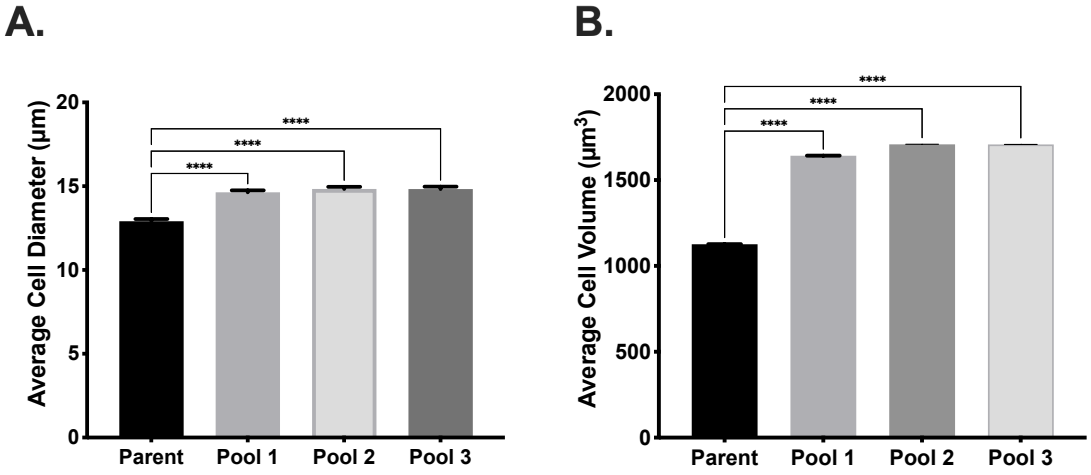

Figure 4.7: **Cell Size Comparison.** (A) average cell diameter was measured using a Cedex XS automated cell counter. (B) Cell volume was calculated using the measured cell diameter, assuming cells were spherical. Data represent mean $\pm$ SEM. **** indicates statistical significance $p < 0.0001$, compared to parental line. ($n \geq 7$)

4.4.2 ^{13}C MFA reveals increased flux through the TCA cycle in PGC-1α expressing pools

To quantify the intracellular metabolic alterations indicated by the increased OUR and substrate consumption rates, a ^{13}C MFA study was performed. Nearly all fluxes in glycolysis and the TCA cycle were elevated in the three PGC-1α expressing pools compared to the parental line (Fig. 4.8). The model-determined increases in glycolytic fluxes were consistent with the directly measured increases in GUR (Fig. 4.5C). Although the direct OUR measurements were not used to constrain the flux solution, the increases in TCA fluxes determined by MFA also agreed with the observed increases in OUR (Fig. 4.4). Therefore, the MFA results provide further evidence for global upregulation of oxidative metabolism in the PGC-1α expressing pools.

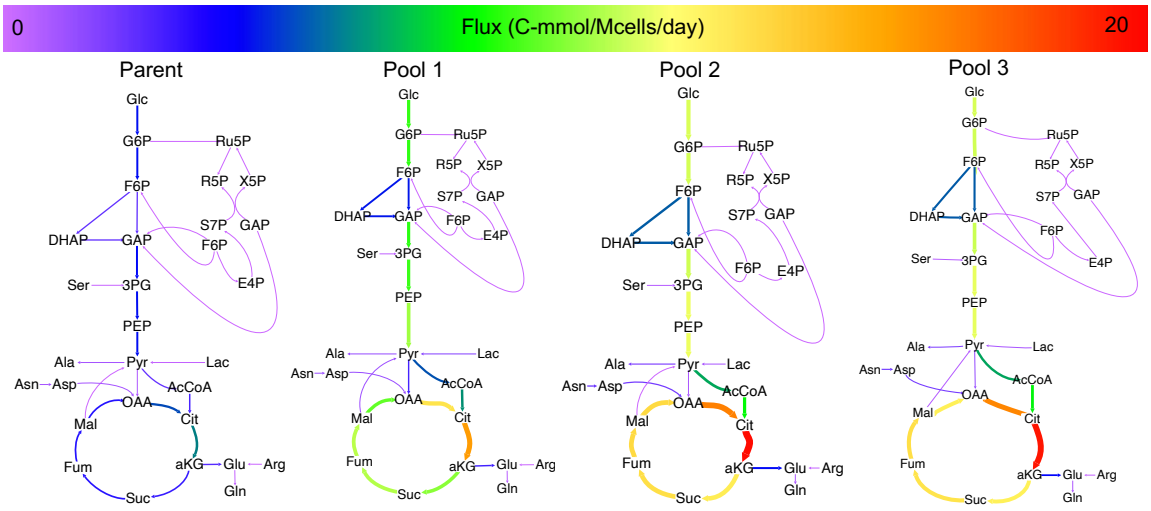

Figure 4.8: **Comparison of metabolic flux maps for the parental line and PGC-1α expressing pools.** Fluxes are shown in units of C-mmol/Mcell/day. The width and color of arrows are scaled to the magnitude of carbon flux.

Pyruvate fluxes have been previously found to vary strongly in response to shifts in oxidative metabolic capacity [44]. Although total pyruvate flux increased in the PGC-1α pools, the percentage of carbon entering the pyruvate node via pyruvate kinase (PK) was consistent across all cell lines, regardless of PGC-1α overexpression (Fig. 6.13A). The percentage of pyruvate consumed by pyruvate dehydrogenase (PDH), the major pyruvate

sink and carbon source for the TCA cycle, was also not significantly different between the parental line and the PGC-1α expressing pools (Fig. 6.13B). This observation suggests that metabolism of PGC-1α expressing pools was elevated at a global level, as opposed to a local redistribution of fluxes surrounding the pyruvate branch point.

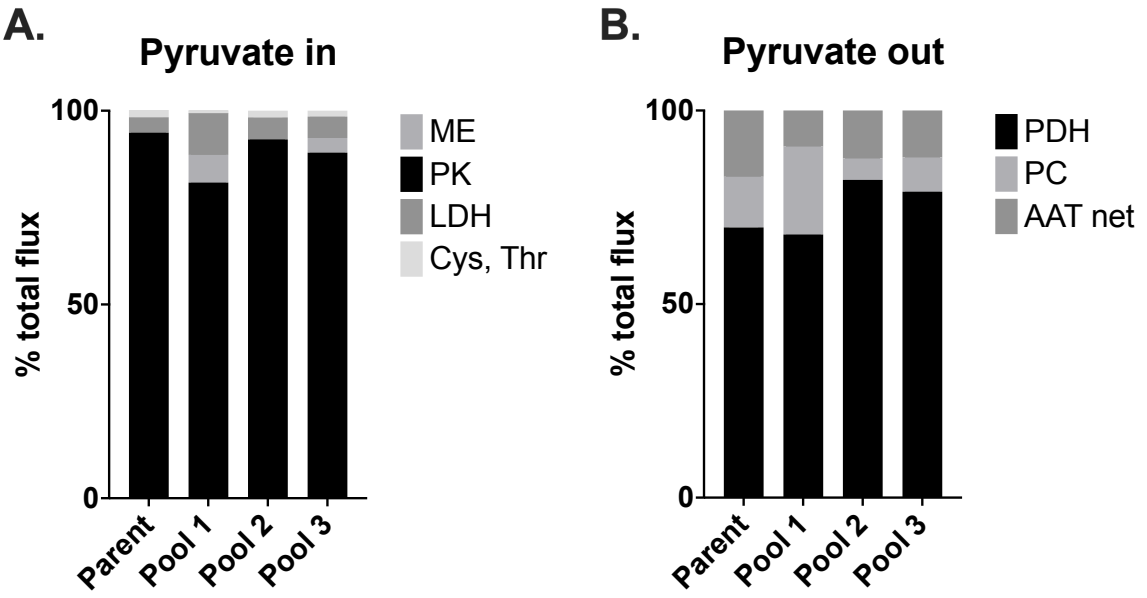

Figure 4.9: **Flux distribution at the pyruvate node.** The percent contributions of (A) pyruvate-forming or (B) pyruvate-consuming reactions were calculated based on best-fit fluxes determined by ^{13}C MFA. ME, malic enzyme; PK, pyruvate kinase; LDH, lactate dehydrogenase; Cys, cysteine; Thr, threonine; PDH, pyruvate dehydrogenase; PC, pyruvate carboxylase; AAT, alanine aminotransferase.

While increased oxidative metabolism was previously found to correlate with increased qP in CHO cells, it has remained an open question whether the increase in qP was a *cause* or an *effect* of the increase in oxidative metabolism. Here, we show that CHO cells specifically engineered to upregulate oxidative metabolism exhibit enhanced qP, supporting the hypothesis that increased oxidative capacity may promote mAb production. These findings also further establish that high-producing CHO cell lines require a highly active TCA cycle to support the energetic demands of product biosynthesis and secretion. The results also indicate an inherent trade-off between mAb production and growth, as evidenced by the significantly decreased growth rates and peak VCDs observed in the PGC-1α overexpress-

ing pools. This trade-off has been previously reported for other production CHO cell lines, and highlights that total protein production (biomass and mAb) needs to be considered [54]. In order to achieve maximum titers of the desired product, biomass production needs to be reduced to a minimal amount during the production phase.

4.4.3 Recombinant and endogenous PGC-1α mRNA observed in engineered pools, but without upregulation of other gene targets

To confirm successful integration and expression of PGC-1α in the three selected pools, mRNA levels of both recombinant (human) and endogenous (CHO) PGC-1α were evaluated using RT-qPCR. Isoform-specific primers were designed to independently quantify mRNA expression of each PGC-1α gene. To confirm specificity, endpoint-PCR cDNA products were run on an agarose gel; a single band at the expected size would indicate specific amplification of the desired product. For the recombinant human PGC-1α primers, a single band was observed at the expected size only in the PGC-1α expressing pools. While no bands were observed for the endogenous CHO PGC-1α primers, RT-qPCR later showed that expression was quite low on day 5 of culture, so it is possible that this method was not sensitive enough to detect such low levels of RNA

On both days 5 and 7 of culture, high levels of recombinant PGC-1α mRNA were detected in all three pools (Fig. 4.10). No recombinant PGC-1α expression was detected in the parental line, implying there was no endogenous interference or non-specific binding of primers. Endogenous PGC-1α mRNA levels were also evaluated as a proxy for recombinant PGC-1α activity, as PGC-1α expression is known to be autoregulatory [55, 32]. Relatively low endogenous levels of PGC-1α were detected on day 5 of culture in the three engineered pools, but expression increased over 100-fold by day 7 (Fig. 4.10). No endogenous expression of PGC-1α was detected in the parental line, suggesting that recombinant expression of human PGC-1α upregulated the expression of endogenous CHO PGC-1α to detectable levels in the stable pools.

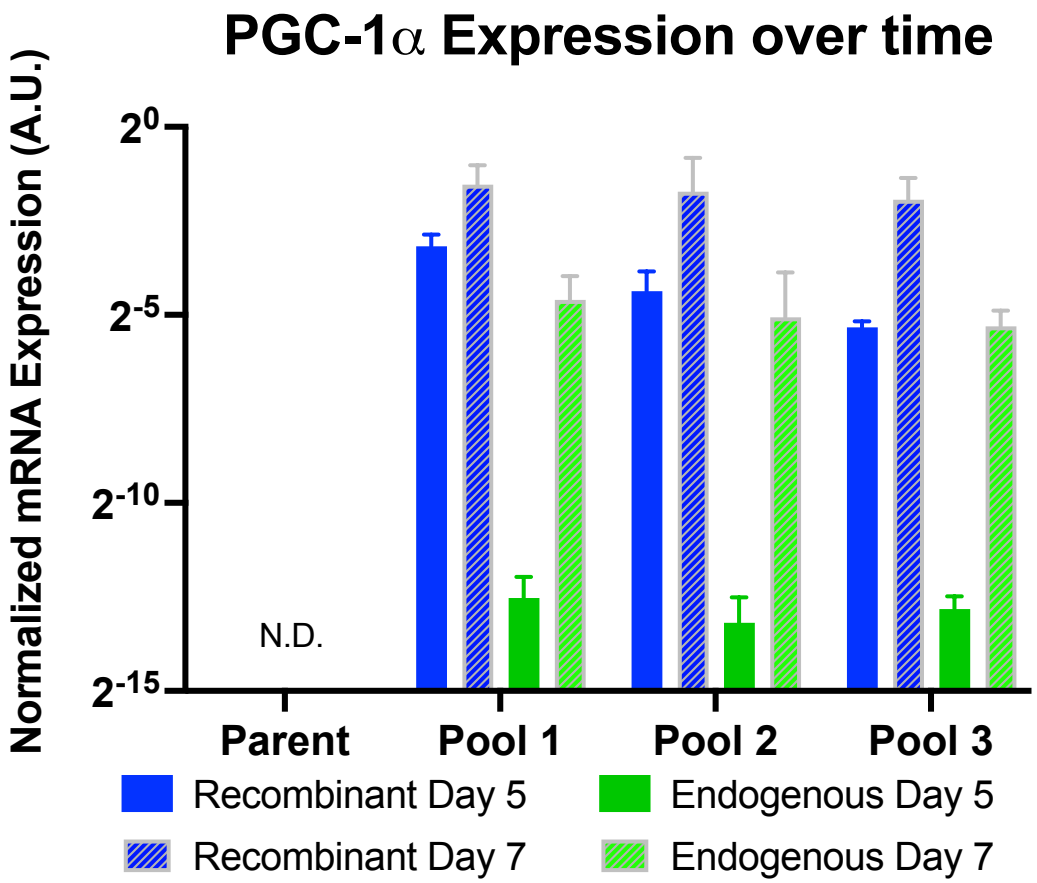

Figure 4.10: **PGC-1α mRNA expression of selected pools normalized to HRPT expression.** The expression levels of both recombinant (human) and endogenous (CHO) PGC-1α were evaluated on days 5 and 7 of culture for the parental line and three selected pools. No expression of either recombinant or endogenous PGC-1α was detected in the parental line at either time point. Recombinant PGC-1α mRNA levels were maintained at relatively high levels for both day 5 and 7 time points. Endogenous PGC-1α expression increased by nearly 100-fold from day 5 to day 7. Data represent mean $\pm$ SEM. (n=4)

In addition to endogenous PGC-1α, the expression of other downstream targets of PGC-1α were quantified using RT-qPCR. The six downstream targets and their roles are summarized in Table 4.2. Samples were taken on days 3, 5, and 7 of culture in order to determine the dynamic relationship between PGC-1α and the various downstream targets. The timepoints above represent different phases of culture growth; mid-exponential (day 3), the switch from exponential to stationary (day 5), and stationary phase (day 7). Overall, no obvious or consistent trends were observed. Pool 3 appears to peak in expression of all

genes on day 5, while pool 1 peaks on day 7. Pool 2 exhibited similar expression levels to the parental line on days 3 and 6, but had lower expression of all genes on day 5 (Figure 4.11).

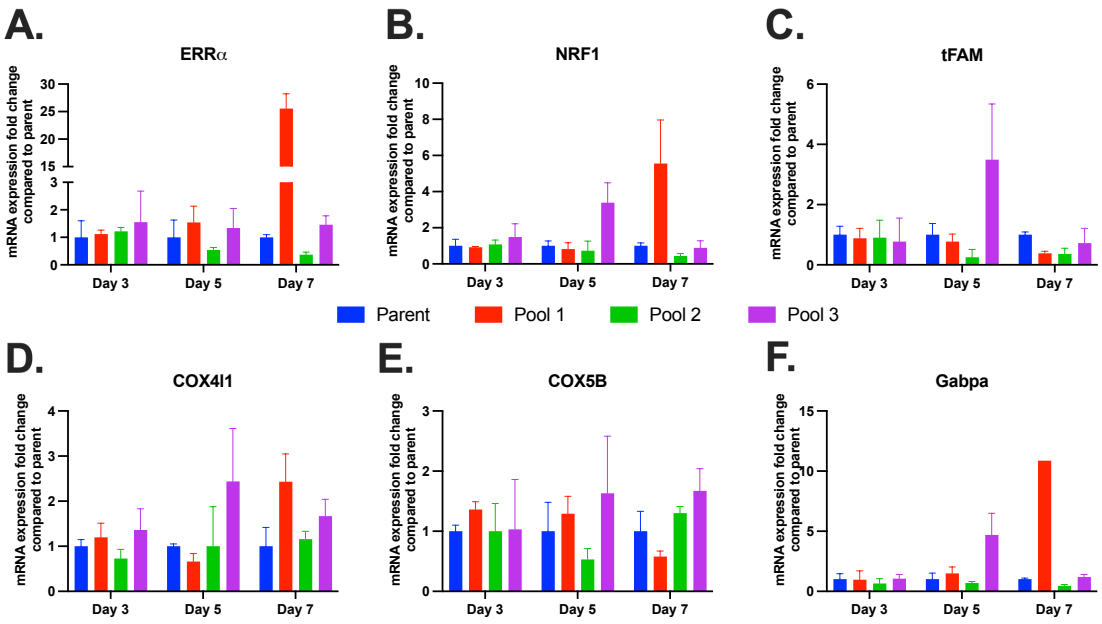

Figure 4.11: **mRNA expression fold-change of PGC-1α target genes in PGC-1α overexpression pools.** RT-qPCR was used to quantify expression of the six target genes; target gene expression was normalized to housekeeping gene HPRT expression and analyzed using the $\Delta\Delta C_t$ method. Overall, no trends in PGC-1α target gene expression were observed. N = 4 biological replicates, 4 technical replicates. Data represents mean $\pm$ SEM. ERRα, estrogen related receptor α; NRF1, nuclear respiratory factor 1; tFAM, transcription factor A, mitochondrial; COX4I1, cytochrome C oxidase subunit 4I1; COX5B, cytochrome C oxidase subunit 5B; Gabpa, GA-binding protein alpha chain;

Gene Name	Role	Reference(s)
ERRα	Nuclear receptor that acts as a transcription factor for genes involved in energy production and mitochondrial biogenesis	[56, 25]
NRF1	Nuclear receptor which regulates the expression of genes related to respiration and mitochondrial DNA transcription	[57]
tFAM	Mitochondrial transcription factor	[57]
Gabpa	Transcription factor which regulates oxidative phosphorylation	[25]
COX4l1	Cytochrome C oxidase subunit	[57]
COX5b	Cytochrome C oxidase subunit	[57]

Table 4.2: **Downstream PGC-1α targets and their roles** ERRα, estrogen related receptor α; NRF1, nuclear respiratory factor 1; tFAM, transcription factor A, mitochondrial; COX4l1, cytochrome C oxidase subunit 4l1; COX5B, cytochrome C oxidase subunit 5B; Gabpa, GA-binding protein alpha chain.

One issue with studying CHO cell biology is the extreme genetic diversity across cell lines; this diversity could help to explain the lack of consistent trends in downstream target mRNA expression. This diversity is due to the development of "quasi-species" caused by high mutation rates inherent to CHO cells [58]. Even within a single clonal CHO cell line, chromosome numbers in the range of 10-30 have been observed [59]. Therefore, because PGC-1α expression, recombinant or otherwise, has not been well-characterized in CHO cells, the mechanisms of action at a genetic level may be different in CHO cells compared to other model systems. It is possible that the PGC-1α target genes that have been identified for other cell types are not PGC-1α targets in CHO cells, leading to the seemingly confounding target gene expression data.

4.4.4 Western blot analysis

Western blotting is a technique which allows for a semi-quantitative analysis of protein expression [60]. The protein fraction of the cell is isolated and then separated by size using

electrophoresis. The separated protein is then transferred to a membrane and probed for using an antibody (the primary antibody) that is specific to the protein of interest. Then, a secondary antibody featuring an enzyme allowing for visualization of the primary antibody is applied. The membrane is then imaged to identify protein bands where the secondary antibody has bound.

The PGC-1α plasmid used to generate the stable PGC-1α expressing pools featured both a His and a c-Myc tag. Initially, we were interested in validating both an anti-PGC-1α antibody (4C1.3) from CalBioChem and an anti-His tag antibody from the Vanderbilt Antibody Protein Resource core. PGC-1α was expressed in H4IIEC3 cells, an adherent rat hepatoma cell line, via transient transfection with a plasmid featuring the human PGC-1α coding sequence under a CMV promoter. PGC-1α is a nuclear protein, so both whole cell protein extracts (PE) and nuclear protein extracts (NE) were harvested from the transfected cells. These extracts were probed with either the anti-PGC-1α antibody or the anti-His tag antibody and an anti-β-actin antibody as a loading control (Fig. 4.12). PGC-1α has an expected molecular weight of $\sim$ 100 kDa; a band at the expected molecular weight (MW) was not observed in either of the blots. A band at $\sim$70 kDa appears to be darker in the positive control lanes (Figure 4.12B), but the MW is lower than expected. Additionally, no additional or increased bands were observed in the PGC-1α positive control compared to the empty vector negative control.

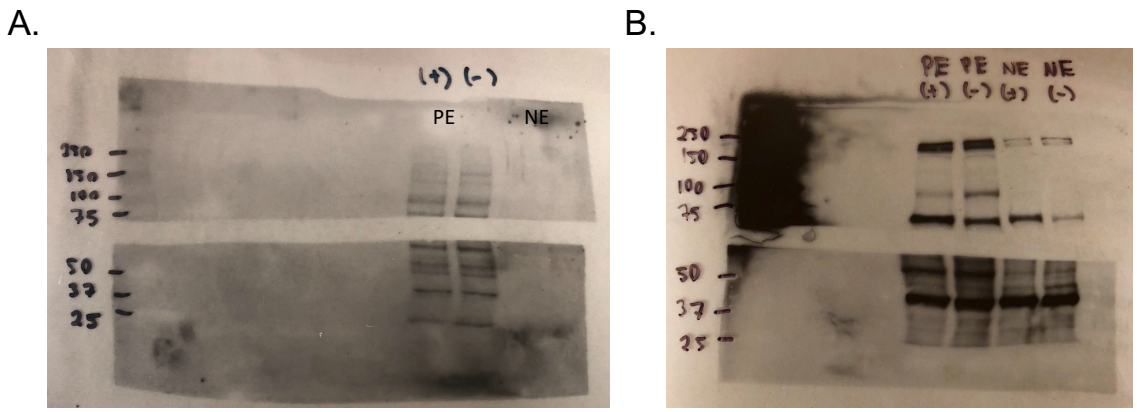

Figure 4.12: **Western blot for PGC-1α in H4IIEC3 cells.** A PGC-1α expression plasmid was transiently transfected into H4IIEC3 cells. PE and NE from both H4IIEC3 cells transfected with the expression plasmid and a negative control transfected with an empty vector were used. (A.) 10 μg of PE and NE from the H4IIEC3 cells were probed with both an anti-PGC-1α antibody (top) and an anti-β-actin antibody (bottom). (B.) 100 μg of PE and NE from the H4IIEC3 cells were probed with both an anti-His tag antibody (top) and an anti-β-actin antibody (bottom). The anti-His antibody appears to interact strongly with the ladder, leading to the large black smudge in the anti-His membrane. Anti-PGC-1α - 1:1,000 1°, 1:1,000 2°. Anti-His - 1:1,000 1°, 1:1,000 2°; Anti-β-actin - 1:5,000 1°, 1:20,000 2°.

The same antibodies were also used with PE from four of the stable PGC-1α expressing pools and the parental CHO cell line (Fig. 4.13). Again, no obvious differences were noted between the PGC-1α expressing pools and the parental line. The only notable band occurred in the C1 pool at approximately 37 kDa; the C1 pool was phenotypically similar to the parental line. While there is a PGC-1α isoform that is only 37 kDa (NT-PGC-1α [27, 61, 62], since the recombinant PGC-1α was expressed from a plasmid that did not contain any introns. Unless an internal stop codon was present or a proteolytic product was formed, the expression of such an isoform from the plasmid is unlikely.

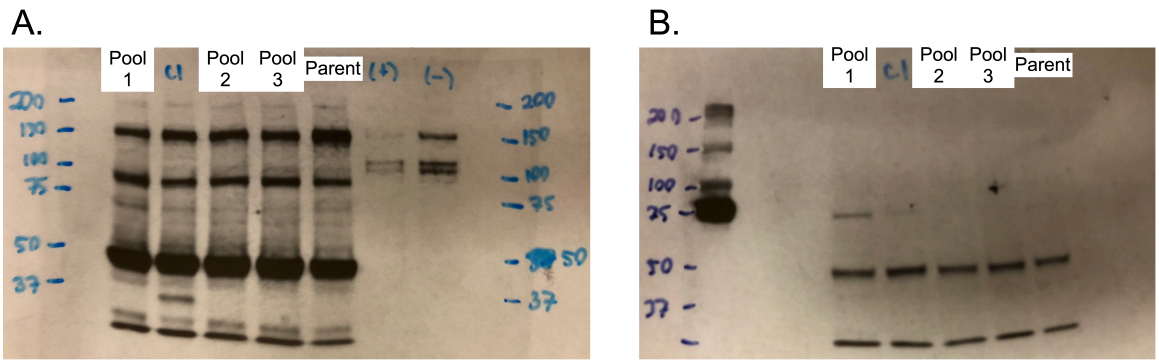

Figure 4.13: **Western blot for PGC-1α in CHO cells.** PE from four stable PGC-1α expressing pools, the parental line, and H4IIEC3 cells transfected with either a PGC-1α expressing plasmid (+) or empty vector (-) were probed with either an (A.) anti-PGC-1α or (B.) anti-His tag antibody. Anti-PGC-1α - 1:1,000 1°, 1:1,000 2°. Anti-His - 1:1,000 1°, 1:1,000 2°.

Due to the large amounts of non-specific binding in previous Western blots (Figs. 4.12 and 4.13), the His tag on the recombinant PGC-1α was used to isolate the protein in hopes of reducing background in the blots. In two biological replicates of the blot, bands did appear to have greater intensity in the three stable PGC-1α pools that were characterized in the ^{13}C MFA study, while bands were less intense in the parental and C1 pools (Fig. 4.14). However, because the samples were prepared using a His-tag pulldown method, no bands were expected to be seen in the parental line. Additionally, the molecular weight ($\sim$ 130 kDa) was much higher than expected. This antibody provided similarly inconclusive results when used for immunofluorescence, as described in Section 4.4.5. Two other anti-PGC-1α antibodies (Santa Cruz Biotechnology, D-5 and C-4) were also tested in a similar manner, but no bands were apparent despite optimization efforts.

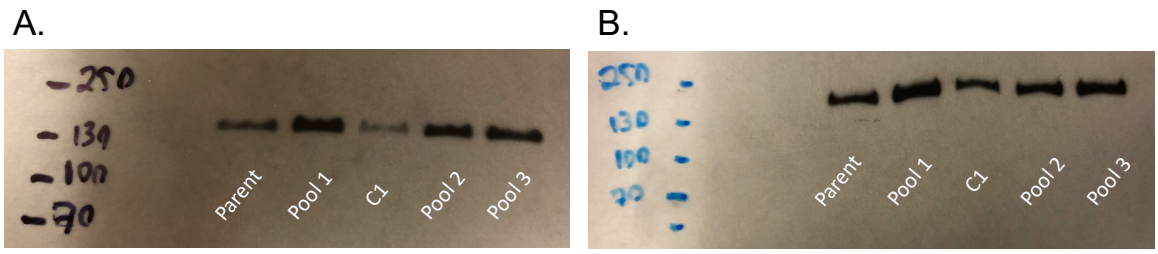

Figure 4.14: **Western blot for PGC-1α in CHO cells protein extracts after His-tag pull-down.** Two biological replicates of CHO cell protein extracts subjected to pulldown of His-tagged proteins were probed with an anti-PGC-1α antibody from CalBioChem (4C1.3). Anti-PGC-1α - 1:1,1000 1°, 1:1,000 2°.

Due to the inconclusive results from the anti-PGC-1α and anti-His tag antibodies described above, anti-c-Myc antibodies were tested. The recombinant PGC-1α used to generate the stable PGC-1α expressing pools featured both a His and a c-Myc tag. As a positive control for the anti-c-Myc antibody (Cell Signaling Technologies, 2276S), P493-6 B-cells were used, which have been engineered to express c-Myc at high levels under normal conditions [63]. Samples were harvested from cultures of the parental line and PGC-1α expressing pool 1 on days 3, 5, and 8 of culture to determine if culture length had any effect on PGC-1α expression. As shown in Figure 4.15, the P493 cell positive control has a strong band below 70 kDa, which is near the expected molecular weight for c-Myc ($\sim$ 60 kDa). However, no bands were apparent in the parental or pool 1 extracts. One other anti-c-Myc antibody (Santa Cruz Biotechnology, 9E10) was tested in the same manner, but did not result in any visible bands despite optimization efforts.

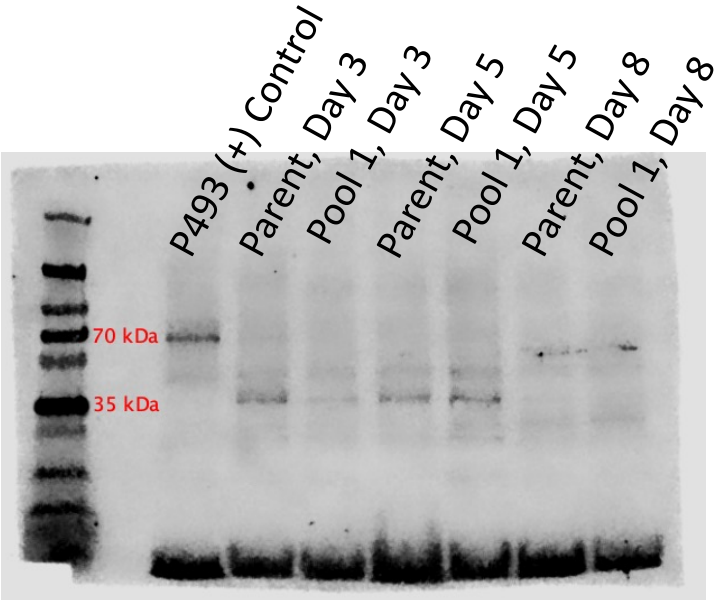

Figure 4.15: **Western blot for PGC-1α using anti-c-Myc antibody.** PE samples from the parental line and PGC-1α expressing pool 1 were harvested on days 3, 5, and 8. Anti-c-Myc - 1:1,000 1°, 1:15,000 2°.

PGC-1α protein has been reported to have a half life of approximately 20 minutes due to degradation by proteasomes [64]. It is possible that the lack of observation of PGC-1α in any western blots is due to inherently low concentrations. In order to limit the degradation of PGC-1α, cells were treated with MG132, a selective inhibitor of the proteasome, and samples were harvested both before and after 2 hrs. of MG132 treatment. The protein fraction from these samples was then isolated via PE, NE, His-tag pulldown, or c-Myc-tag immunoprecipitation and then probed with an anti-c-Myc antibody (Cell Signaling Technologies, 2276S). Bands were only observed in whole cell lysates harvested by PE, and no bands at the expected molecular weight ($\sim$ 100 kDa) were observed. Overall, despite the use of a variety of different antibodies and extensive optimization efforts, Western blot analysis was inconclusive.

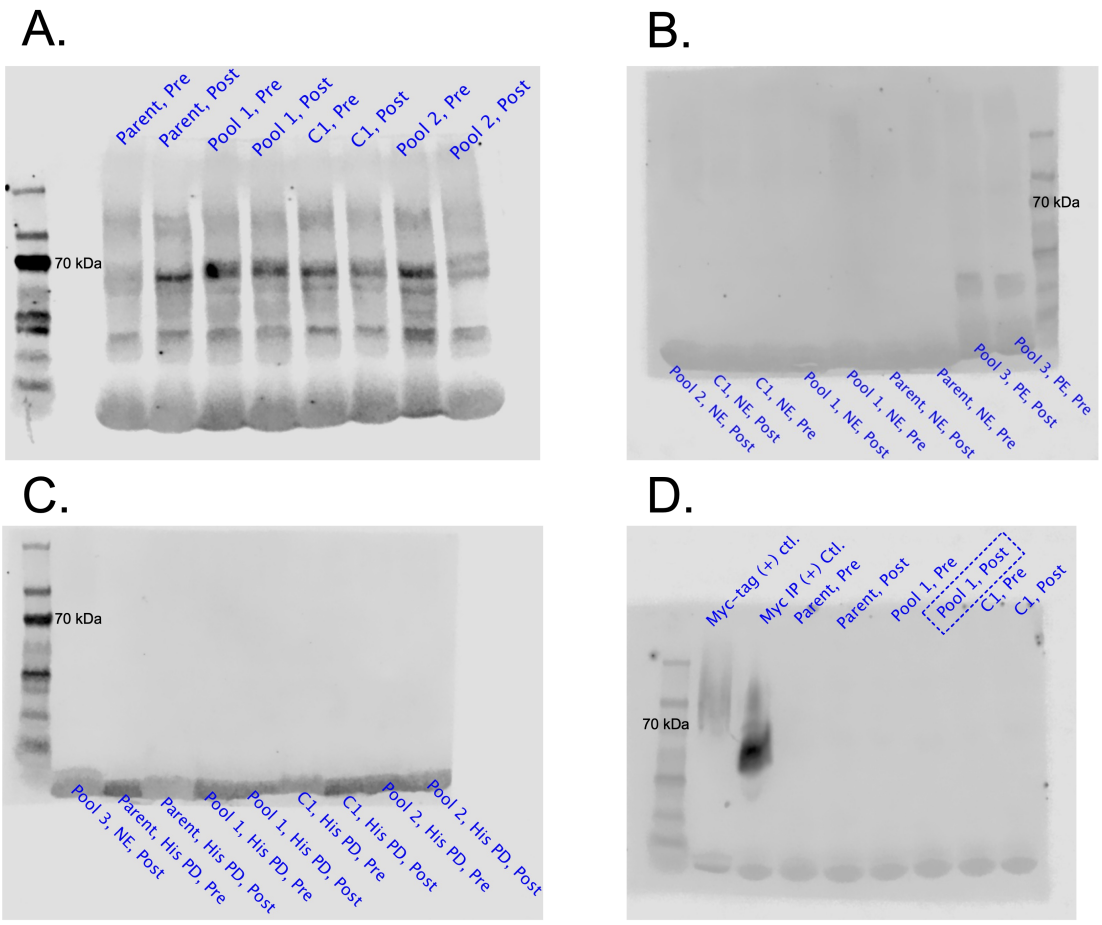

Figure 4.16: **Western blots for PGC-1α protein after MG132 treatment.** CHO cells were treated with the proteasome inhibitor, MG132, and samples were harvested before (Pre) or after a 2 hour incubation in the presence of MG132 (Post). Protein fractions were isolated either from (A.) whole cell extracts (PE), (B.) nuclear extracts (NE), (C.) by pull-down with nickel beads for His-tagged proteins (His PD), or (D.) by immunoprecipitation with an anti-c-Myc antibody (Myc IP). Anti-c-Myc - 1:1,000 1°, 1:15,000 2°.

4.4.5 Immunofluorescence

Immunofluorescence (IF) is a technique that allows for the visualization of protein localization within the cell [65, 66]. Indirect IF, the technique used in this section, utilizes a primary antibody to identify the epitope of interest and a secondary antibody, featuring a fluorophore, to bind to the primary antibody. The fluorophore on the secondary antibody allows for easy visualization of where the antibodies bind. There are two methods to perform IF on suspension cells: (1) by forcing the cells to adhere to a microscope slide and

proceeding as if the cells were adherent ("adherent method" herein) or (2) by keeping the cells in suspension throughout the entire IF protocol ("suspension method" herein). Both of these methods were tested, as described below

At first, since we were interested in determining the presence of PGC-1α protein, we used an anti-PGC-1α primary antibody (CalBioChem, 4C1.3). A HepG2 cell line, an immortalized adherent human hepatocellular carcinoma line that is known to express PGC-1α at high levels, was used as a positive control for this experiment. This antibody was initially tested using the adherent method, described in section 4.3.9.1, with a DAPI stain to identify the presence of a nucleus. As shown in Figure 4.17, the antibody appears to successfully bind to the HepG2 cells, Pool 1, and Pool 2 quite well, with little binding in the parental line. Pool 3 shows some binding, but not to the same extent as pools 1 and 2; there also appear to be fewer cells in Pool 3, likely due to experimental error.

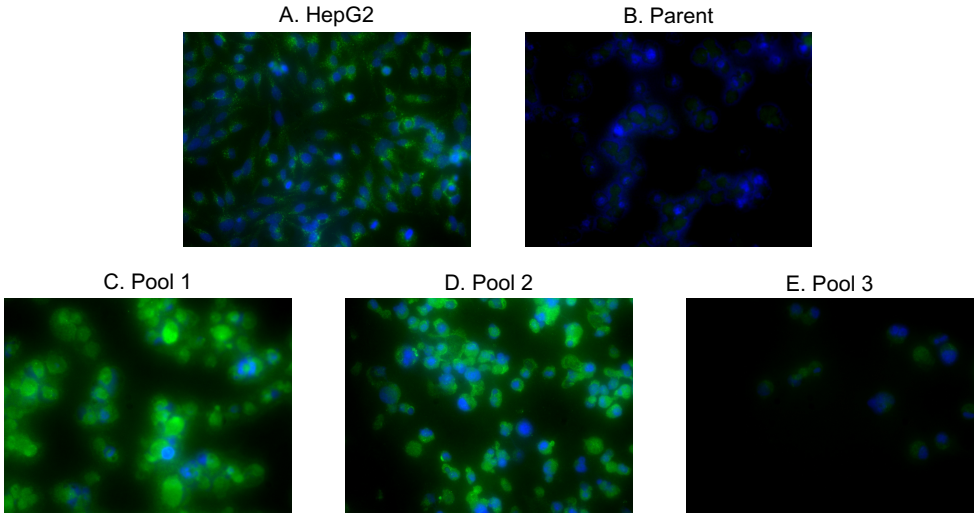

Figure 4.17: **Immunofluorescence for PGC-1α using the adherent protocol.** Cells were stained with an anti-PGC-1α primary antibody, a fluorophore containing secondary antibody, and DAPI. HepG2 cells acted as a positive control. Green = PGC-1α, Blue = DAPI.

When the anti-PGC-1α antibody was used with the suspension protocol, results were less clear. While there was very strong fluorescence in the three stable pools, there was

still a fairly high level of fluorescence in the parental line, which would be expected to have none (Figure 4.18). Also, the no-primary antibody control for pool 3 had fairly high background, which is indicative of possible non-specific binding of the secondary antibody (Figure 4.19)[67]. For the anti-PGC-1α antibody, no positive control cells that could be grown in suspension were identified; additionally, the anti-PGC-1α antibody was unable to discriminate between endogenous and recombinant PGC-1α protein. Therefore, we decided to test antibodies which would recognize the c-Myc epitope tag that was present on the recombinant PGC-1α protein.

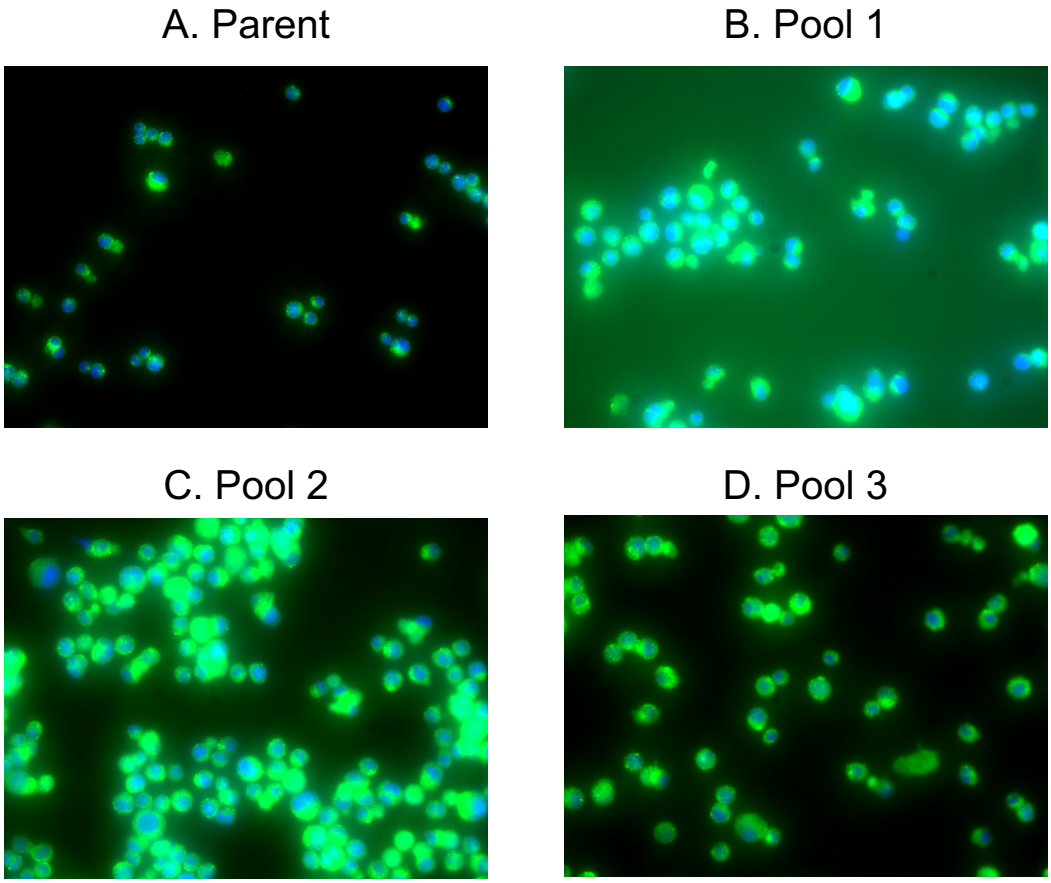

Figure 4.18: **Immunofluorescence for PGC-1α using the suspension protocol.** Cells were stained with an anti-PGC-1α primary antibody, a fluorophore containing secondary antibody, and DAPI. Green = PGC-1α, Blue = DAPI.

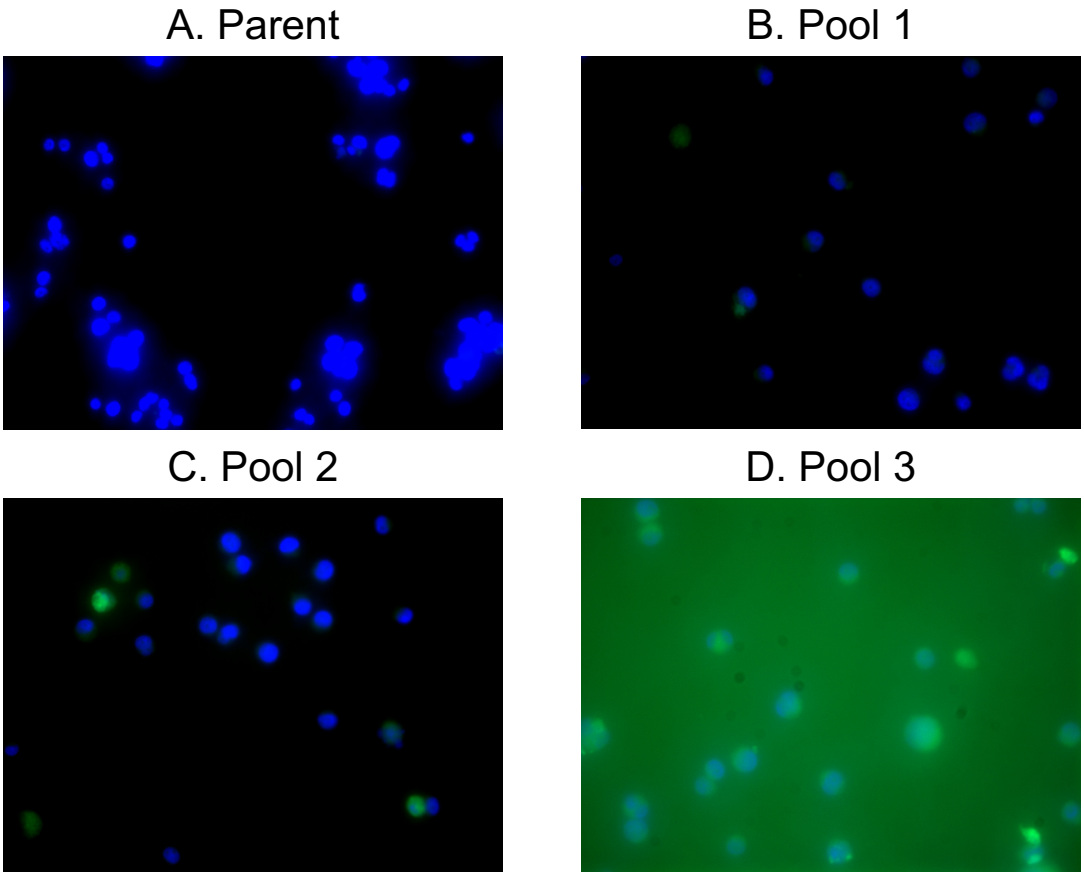

Figure 4.19: **Negative controls for immunofluorescence for PGC-1α using the suspension protocol.** Cells were stained with only a fluorophore containing secondary antibody (no primary antibody) and DAPI. Green = PGC-1α, Blue = DAPI.

As a positive control for the anti-c-Myc antibodies, P493-6 B-cells were used, which have been engineered to express c-Myc at high levels under normal growth conditions [63]. High fluorescence in the c-Myc channel was observed in the P493-6 cells and all three pools, while some background fluorescence was observed in the parental line (Figure 4.20). However, in no-primary antibody controls, there was still high fluorescence in all three engineered pools (Figure 4.21), which was indicative of non-specific binding of the secondary antibody. Therefore, a new primary anti-c-Myc antibody and a new secondary antibody were purchased from Cell Signaling Technologies (CST). Additionally, a phalloidin stain was used in combination with a DAPI stain in order to identify both the cell

membrane and the nucleus in future imaging.

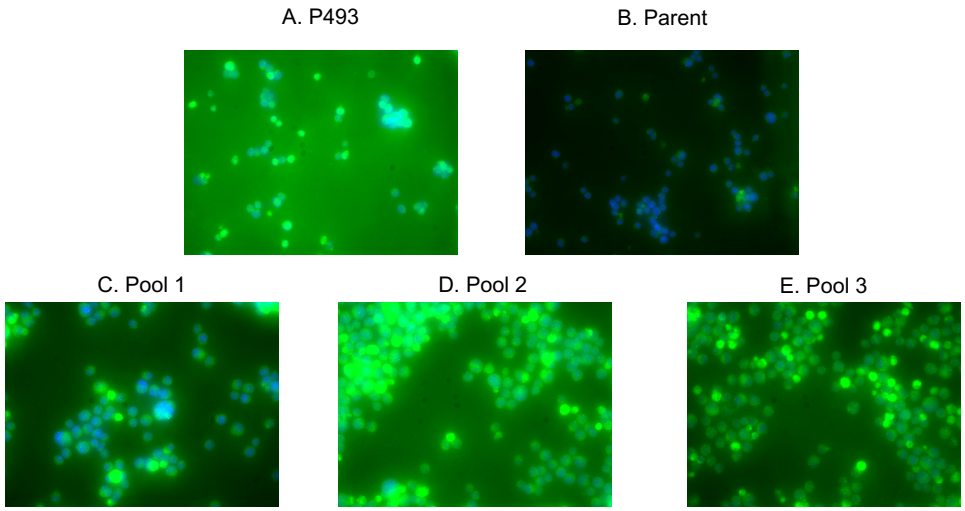

Figure 4.20: **Immunofluorescence for c-Myc tag using the suspension protocol.** Cells were stained with an anti-c-Myc primary antibody, a fluorophore containing secondary antibody, and DAPI. Green = c-Myc, Blue = DAPI.

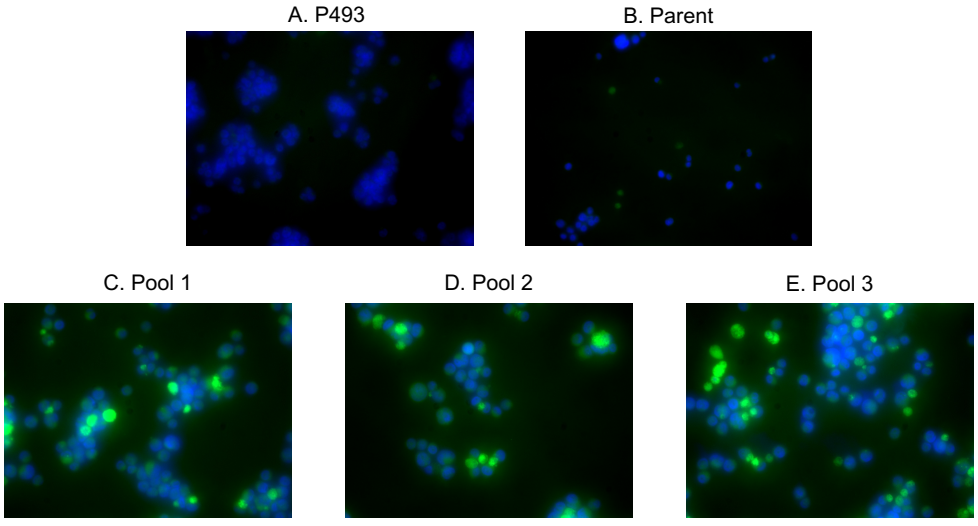

Figure 4.21: **Negative controls for immunofluorescence for c-Myc tag using the suspension protocol.** Cells were stained with only a fluorophore containing secondary antibody (no primary antibody) and DAPI. Green = c-Myc, Blue = DAPI.

With the CST primary and secondary antibodies, the presence of c-Myc was identified in the positive control P493-6 cells (Figure 4.22A). There was also no non-specific binding of the secondary antibody observed in no-primary antibody controls (Figure 4.23). While fluorescence in the c-Myc channel was identified in the pool 1 cells, results in the parental line were inconsistent; while sometimes no fluorescence in the c-Myc channel was observed, sometimes there was strong fluorescence (Figure 4.22B,C).

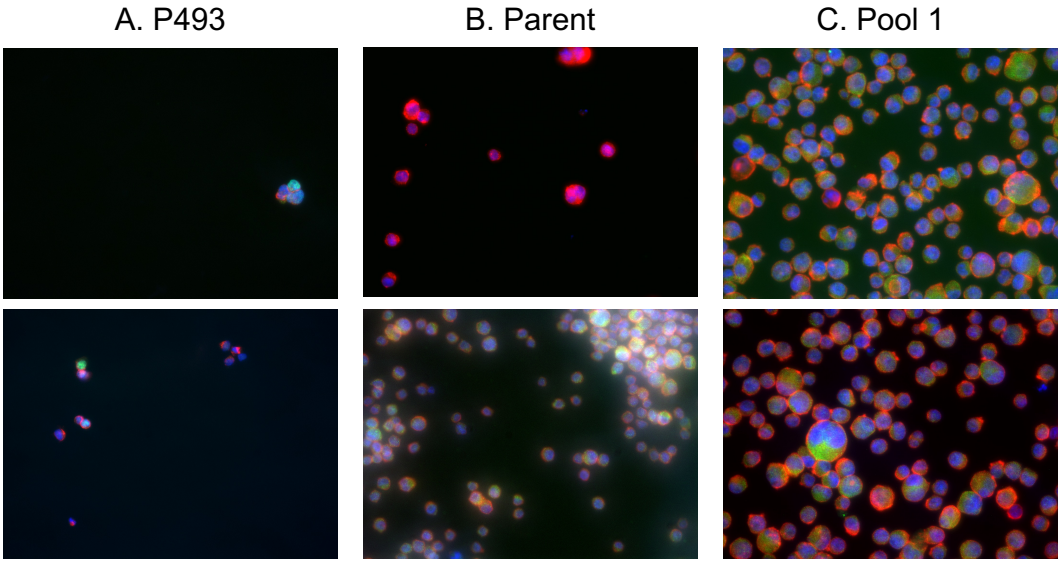

Figure 4.22: **Immunofluorescence for c-Myc tag using CST antibody.** P493 acted as a positive control. Only Pool 1 was sampled to allow for higher throughput during optimization. Cells were stained with an anti-c-Myc primary antibody, a fluorophore containing secondary antibody, DAPI, and phalloidin. Green = c-Myc, Blue = DAPI, Red = phalloidin.

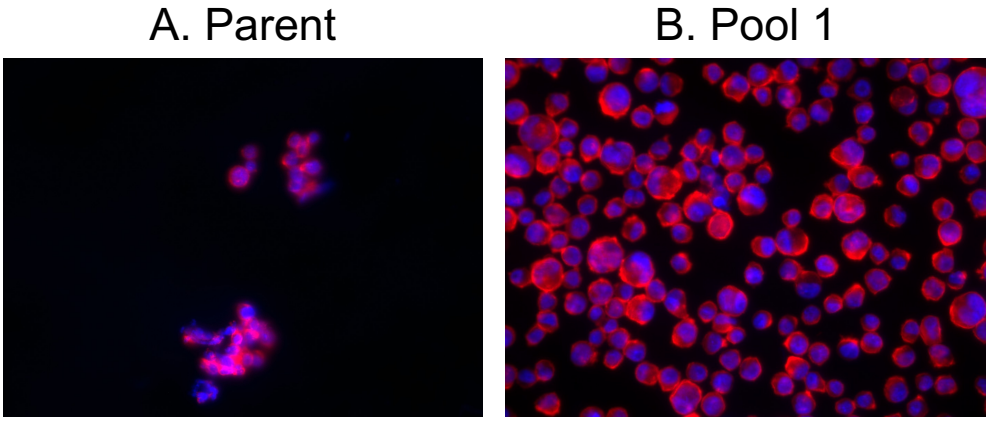

Figure 4.23: **Negative controls for immunofluorescence for c-Myc tag using CST antibody.** P493 acted as a positive control. Only Pool 1 was sampled to allow for higher throughput during optimization. Cells were stained with only a fluorophore containing secondary antibody, DAPI, and phalloidin. Blue = DAPI, Red = phalloidin.

Because CHO cells have cancer-like characteristics [68], endogenous expression of c-Myc is present [69]; this could be confounding the assay by leading to high background levels of fluorescence. c-Myc is typically more highly expressed during periods of cell growth, so a time-course experiment was devised to see whether background levels of c-Myc fluorescence varied over the course of the culture. Samples were harvested on day 3 (mid-exponential phase), day 5 (late exponential/early stationary phase), and day 8 (late stationary phase). It was expected that background c-Myc expression would decrease over time, as cell proliferation slowed upon entering stationary phase. As shown in Figure 4.24A and B, fluorescence in the c-Myc channel does appear to decrease over time in the parental line while fluorescence remained in pool 1. These visual observations are corroborated by the quantification of signal in the c-Myc channel normalized to both phalloidin signal and DAPI signal (Figure 4.25); the normalized signal in pool 1 remained constant over time, while it trended down in the parental line. When samples were collected on Day 7, all three PGC-1α expressing pools showed increased fluorescence in the c-Myc channel.

Upon normalization to phalloidin signal, pools 1 and 2 exhibited a significant increase in c-Myc signal; upon normalization to DAPI, only pool 2 had significantly higher c-Myc signal (Figure 4.26).

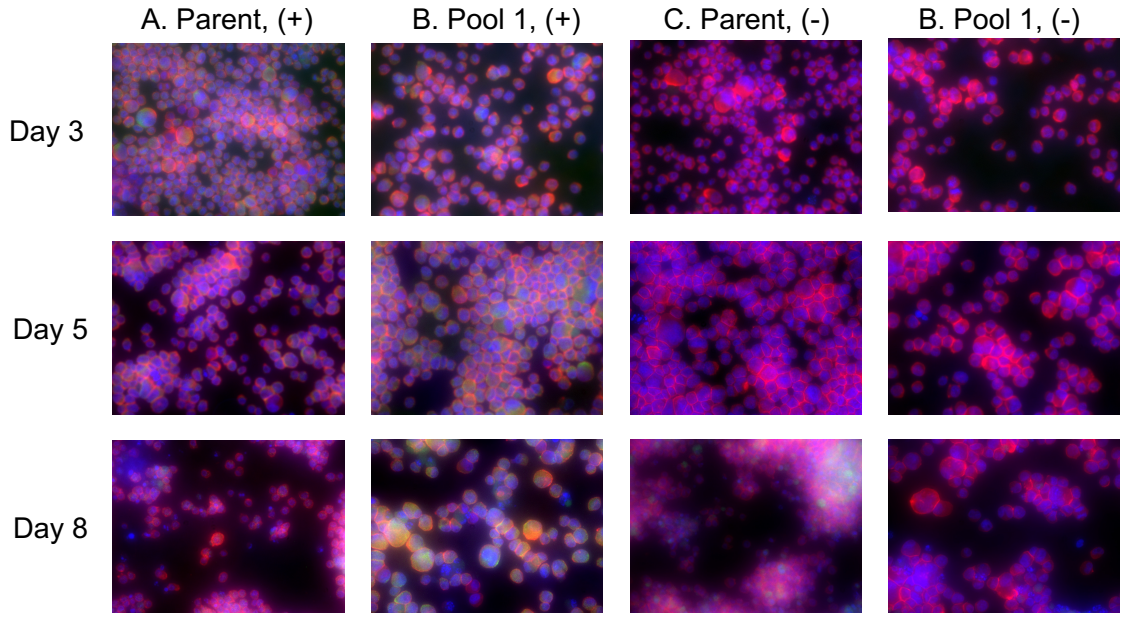

Figure 4.24: **Immunofluorescence for c-Myc tag over time.** Samples were harvested on days 3, 5, and 8 of culture. Cells were stained with an anti-c-Myc primary antibody, a fluorophore containing secondary antibody, DAPI, and phalloidin. Green = c-Myc, Blue = DAPI, Red = phalloidin. (+) = with primary antibody, (-) = no primary antibody control.

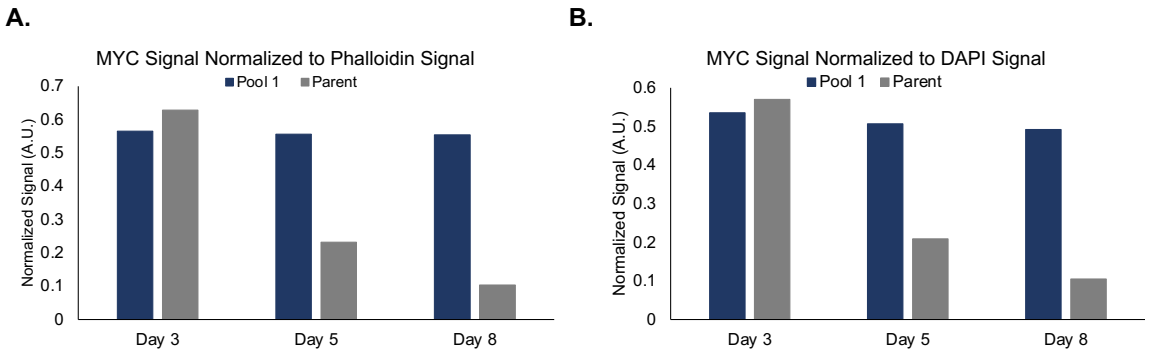

Figure 4.25: **Quantification of immunofluorescence for c-Myc over time.** Signal intensity was quantified suing ImageJ as described in section 4.3.9.3. c-Myc signal intensity was normalized to both DAPI and phalloidin signal intensities.

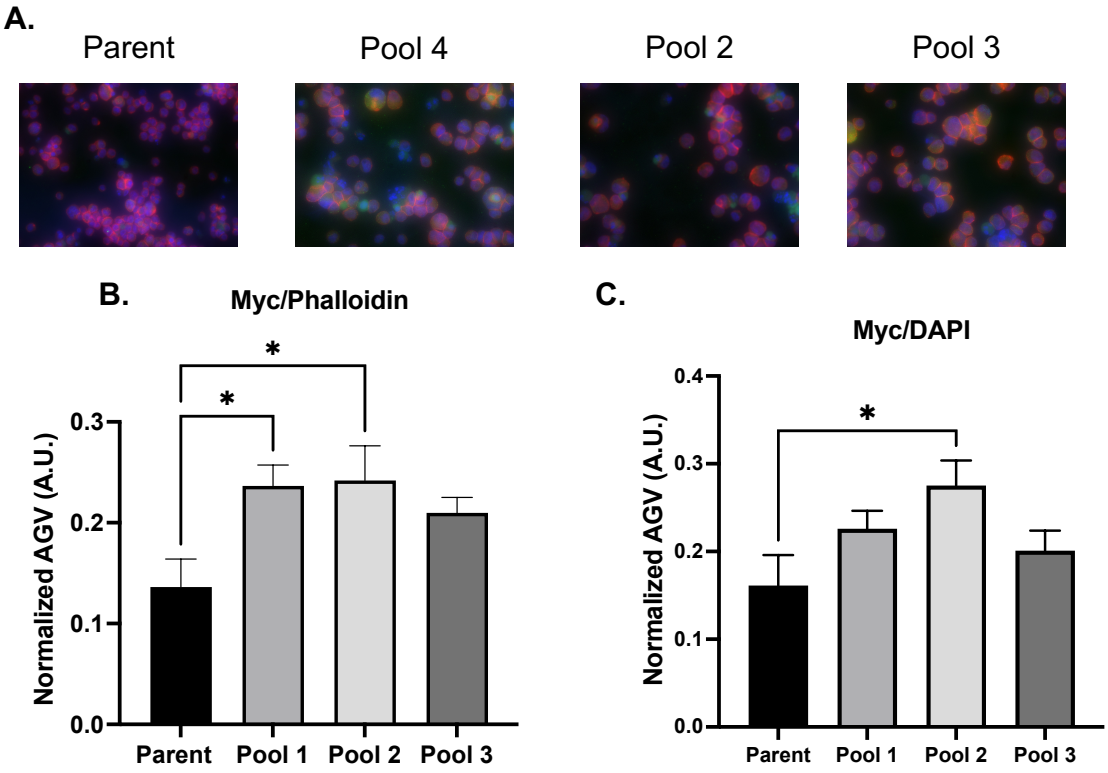

Figure 4.26: **Immunofluorescence for c-Myc tag on Day 7 of culture.**(A.) Representative composite images of immunofluorescence for stable poolss. [Red = phalloidin, Blue = DAPI, Green = c-Myc] Note that the 3 cell lines are derived from a mixed population, so variation of phenotype at the cellular level is expected. (B. and C.) c-Myc signal normalized to phalloidin trends higher in poolss 1, 2, and 3. c-Myc signal normalized to DAPI signal trends higher in all poolss. Quantification of c-Myc, phalloidin, and DAPI intensity was performed using ImageJ. c-Myc signal was normalized to either phalloidin (B.) or DAPI (C.) (n=5)

While it does appear that IF using the anti-c-Myc antibody showed higher c-Myc signal in all three engineered pools, we were unable to confirm these results using western blot. Immunofluorescence is highly dependent upon the antibodies that are used [65]. Increased fluorescence from the antibodies can be indicative of increased presence of the protein of interest. However, the correct identification of the protein needs to be confirmed with a technique such as western blot, where the expected molecular weight can be confirmed. Therefore, without confirmation that the anti-c-Myc antibody used is able to specifically bind to our protein of interest, the IF results remain inconclusive.

4.4.6 Luciferase assay

A luciferase assay was used to measure PGC-1α expression and activity. A schematic of the assay is shown in Figure 4.27. In brief, a promoter region that is activated by PGC-1α protein is followed by the coding sequence for recombinant Firefly luciferase. Cells are transiently transfected with this reporter plasmid and another plasmid, which constitutively expresses a different luciferase (*Renilla*) and acts as a transfection control. PGC-1α protein binds to the promoter region of the reporter plasmid, activating the transcription of Firefly luciferase. The level of Firefly luminescence serves as an indicator of the amount of active PGC-1α protein and is normalized to the *Renilla* luminescence to account for any differences in transfection efficiency.

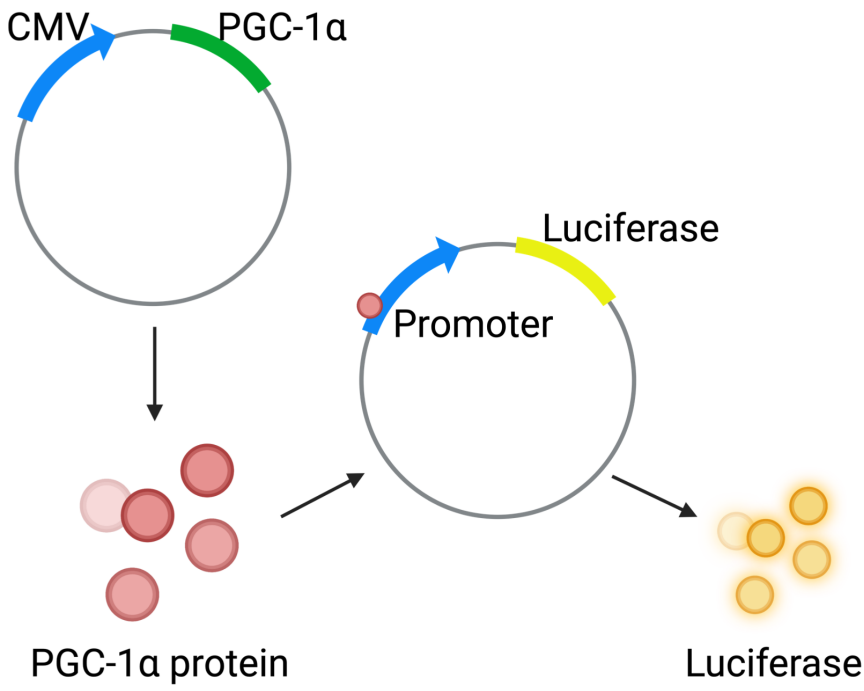

Figure 4.27: **Schematic of the luciferase assay.** PGC-1α protein is produced either from a recombinant plasmid, as shown, endogenously, or from a stably integrated transgene. The PGC-1α protein will co-activate the promoter on the luciferase reporter plasmid, leading to the transcription of the luciferase gene. The expression of luciferase can be easily measured through the use of a kit and a luminometer, and serves as a proxy of PGC-1α expression and activity.

In the development of this assay, two different reporter plasmids expressing Firefly lu-

ciferase were tested. One featured the promoter region from the glucose-6-phosphatase catalytic subunit 1 (*G6pc1*) gene, which can be co-activated by PGC-1α and hepatocyte nuclear factor-4α (HNF-4α) and has previously been used to measure PGC-1α expression in hepatocytes (G6Pc1-Luc) [70, 71]. A second reporter plasmid featured the promoter region from estrogen related receptor α (ERRα), which can be co-activated by PGC-1α and ERRα and has previously been used in human embryonic kidney (HEK) 293 cells (AAB-Luc) [73, 74]. Additionally, a transfection control plasmid which constitutively expressed a *Renilla* luciferase was co-transfected alongside the reporter plasmid, and all luminescence was normalized to the luminescence from the *Renilla* luciferase to account for any differences in transfection efficiency.

To serve as positive controls for future assays, two different plasmids which express PGC-1α were tested in H4IIEC3 cells. One plasmid featured the simian virus 40 (SV40) promoter while the other featured the cytomegalovirus (CMV) promoter; both are constitutive promoters. We sought to determine which plasmid allowed for stronger expression of PGC-1α. As shown in Figure 4.28, the CMV promoter plasmid exhibited 4-fold higher expression of PGC-1α compared to the SV40 promoter plasmid when measured with the G6pc1-Luc reporter plasmid. For all subsequent studies, the CMV promoter plasmid was used as a positive control.

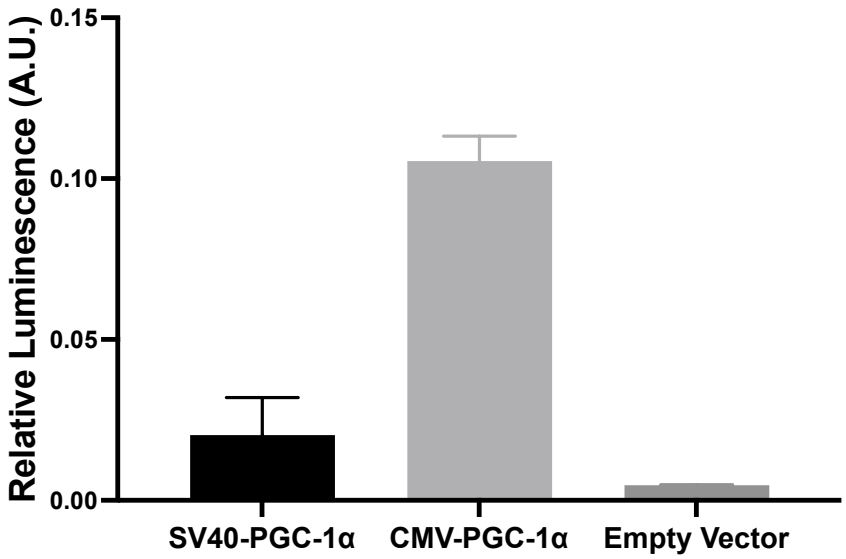

Figure 4.28: **Comparison of SV40 and CMV driven PGC-1α expression in H4IIEC3 cells for Luciferase quantification.** In order to determine an adequate positive control for future luciferase assays, two different plasmids containing different constitutive promoters for PGC-1α were transfected into H4IIEC3 cells. The SV40 promoter exhibited only slightly higher expression of PGC-1α when compared to an empty vector control to account for endogenous PGC-1α expression. Meanwhile, the CMV promoter had a 4-fold increase in signal. For future assays, the CMV promoter plasmid was used.

First, the reporter plasmid which featured the promoter region from *G6pc1* was tested in an adherent CHOK1 line and a suspension CHO line (Figure 4.29.) In the CHOK1 line, luminescence was detected at levels substantially higher than empty reporter vector controls. Three different concentrations of PGC-1α expression plasmid were used as well as three different concentrations of the transfection agent, Lipofectamine 2000. There did not appear to be a dose-dependent response to changing concentrations of either. However, there appeared to be little difference between endogenous PGC-1α expression levels (shown by wells transfected with an eGFP expression plasmid and a reporter vector) and wells which were transfected with a recombinant PGC-1α expression plasmid. In the suspension CHO cell lines, there were no significant differences observed between the reporter plasmid wells and empty vector wells. This indicates that the reporter plasmid used in these assays was not properly activated. In order for the G6pc1-Luc reporter plasmid to function correctly, it must be co-activated by both PGC-1α and HNF4α. It is likely that HNF4α was not

expressed in high enough levels in suspension CHO cells to successfully co-activate the reporter plasmid. While HNF4α expression has been reported in two out of seven CHOK1 lines analyzed by RNA-seq, only one of twelve suspension CHO cells analyzed had HNF-4α expression.

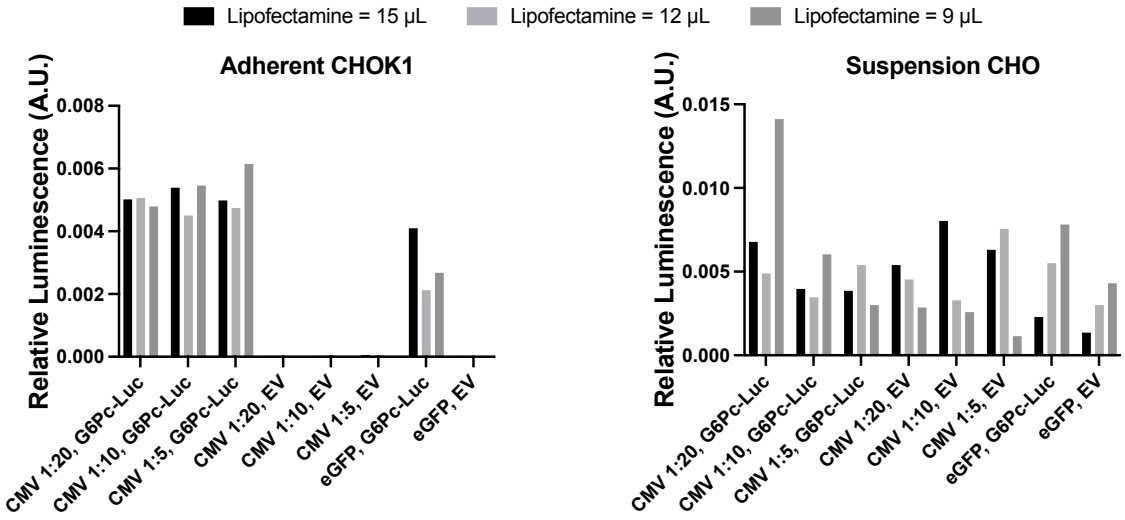

Figure 4.29: **The use of a G6Pc-Luciferase reporter in adherent CHOK1 and suspension CHO cells.** Three different concentrations of the transfection reagent, Lipofectamine, as well as three different ratios of CMV-PGC-1α expression plasmid to G6Pc-luciferase reporter plasmid were tested. In the adherent CHOK1 line, luciferase reporter samples were expressing at much higher levels than empty vector controls. However, in the suspension CHO cell line, there was no discernible difference between luciferase reporter samples and empty vector control samples. CMV, cytomegalovirus promoter; G6Pc-Luc, G6Pc-luciferase reporter plasmid; EV, empty vector; eGFP, enhanced green fluorescent protein.

Due to the apparent lack of expression of HNF4α in suspension CHO cells, a new reporter plasmid which features the ERRα promoter region and is coactivated by ERRα was tested in a variety of cell lines. HEK293 cells — which the AAB-Luc plasmid had already been verified in — H4IIEC3 cells, CHOK1 cells, and suspension CHO cells all exhibited dose-dependent behavior (Figure 4.30). For increasing amounts of PGC-1α expression plasmid, higher levels of luminescence were observed in all cell types. Based on these data, it appeared that the AAB-Luc plasmid could effectively measure PGC-1α expression in suspension CHO cells. However, it should be noted that these initial studies were per-

formed during transient expression of PGC-1α; expression levels in transient transfections are typically higher than in stable pools due to the abundance of gene copies present.

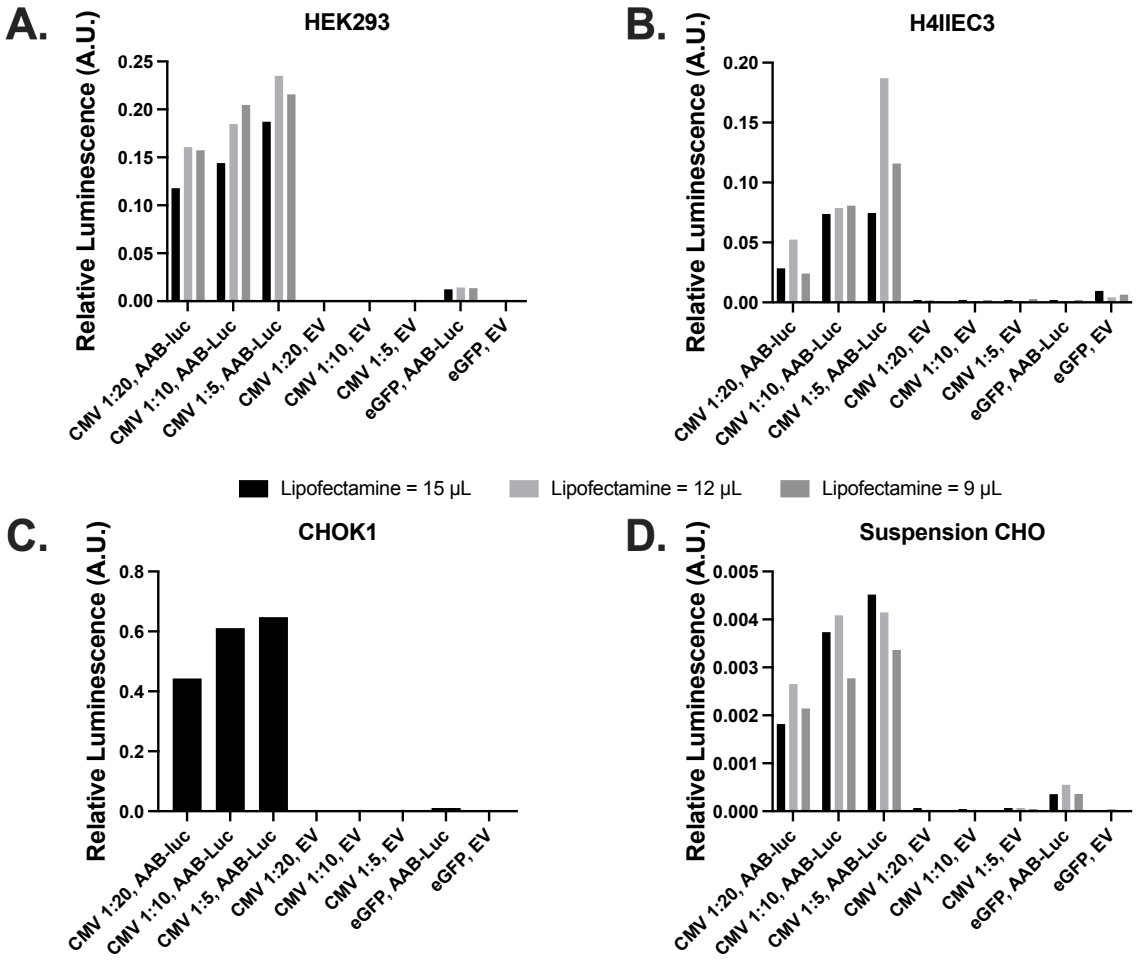

Figure 4.30: **The use of the AAB-Luciferase reporter plasmid in a variety of cell lines.** The AAB-Luciferase reporter plasmid features the ERRα promoter region. The reporter plasmid was tested in (A) HEK293, (B) H4IIEC3, (C) CHOK1, and (D) suspension CHO cells. In all four cell lines, the reporter behaved in a dose dependent manner with increasing concentrations of CMV-PGC-1α expression plasmid. CMV, cytomegalovirus; AAB-Luc, AAB-Luciferease reporter plasmid; EV, empty vector; eGFP, enhanced GFP.

Based on the transient transfections, the AAB-Luc plasmid appeared to function in suspension CHO cells. Therefore, to measure PGC-1α expression and activity in the previously generated stable pools, a time-course experiment was devised. Samples were taken on days 1, 3, and 5 and cells were transiently transfected with just the reporter plasmid and control plasmid. Only pool 1 showed increased luminescence compared to the parental line

(Fig. 4.31). For the transfection of the reporter and control plasmids, cells were kept in well plates for 24 hours. The suspension lines require constant agitation to maintain viability; it is possible that during these 24 hours of stationary culture, the cellular phenotype was altered.

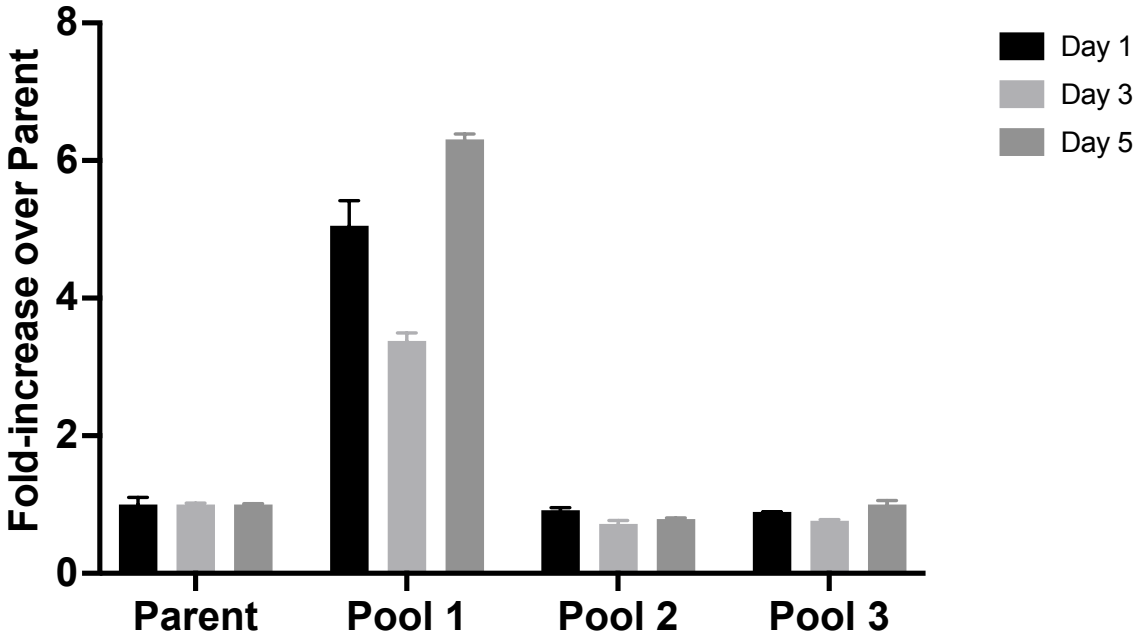

Figure 4.31: **Luciferase expression in stable PGC-1α expressing pools over time.** The parental line was grown alongside the three PGC-1α expressing pools and samples were harvested on days 1, 3, and 5 of culture. These samples were transiently transfected with the AAB-Luc reporter plasmid and the *Renilla* control plasmid. AAB-Luc luminescence was normalized to *Renilla* luminescence and all data are reported as a fold-increase over normalized luminescence in the parental line. Only pool 1 showed increased luminescence compared to the parental line.

4.4.7 Principal component analysis identified different groups within PGC-1α and empty vector pools

In order to determine whether the selection process that was used to generate the PGC-1α expressing pools had brought about the phenotypic changes observed, stable pools were transfected with an empty vector in an identical manner. Metabolic parameters such as qP, glucose uptake rates, and lactate production and uptake rates were measured for 12 PGC-1α expressing pools and 14 empty vector pools. The resulting dataset was then analyzed

using principal component analysis, which is a mathematical transformation that enables a multi-dimensional dataset to be visualized in two dimensions. The reduction in dimensionality makes the interpretation of a large dataset simpler, without substantially reducing the amount of information included [75].

The PGC-1α expressing pools and empty vector pools were grouped into two categories, "high-producing" and "low-producing". High-producers were defined as pools that exhibited qPs at least 1 standard deviation higher than the average qP of like pools; low-producers were all other pools. As shown in Figure 4.32, the pools in the same group clustered near each other, indicating similar phenotypes. High-producing EV pools were differentiated from the low-producing EV pools, indicating a level of clonal variation leading to increased qP in these EV pools. Of note, the three highest producing PGC-1α pools clustered together and separated from all other pools. This indicates that the three pools studied in-depth via ^{13}C MFA were metabolically distinct from the low-producing PGC-1α expressing pools and all empty vector pools.

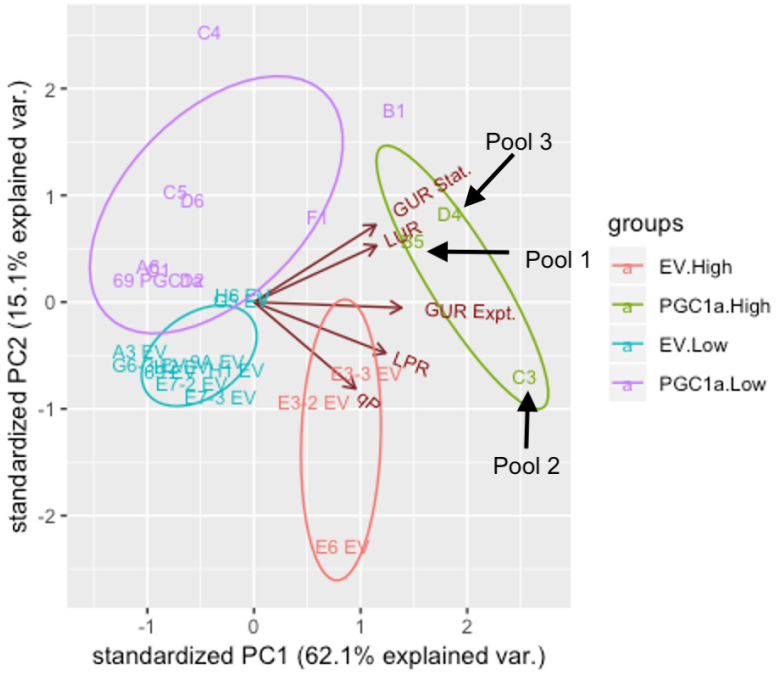

Figure 4.32: **Principal component analysis of PGC-1α expressing and empty vector pools.** Metabolic characteristics were measured for PGC-1α expressing and empty vector pools, and principal component analysis was performed to allow for easier interpretation of the multi-dimensional dataset. Pools that were grouped together based on qP also clustered together, indicating they exhibited similar metabolic phenotypes. GUR Stat. = Glucose uptake rate during stationary phase; GUR Expt. = Glucose uptake rate during exponential phase; LUP = lactate uptake rate; LPR = lactate production rate; qP = specific productivity; PGC1a = PGC-1α; EV = empty vector.

4.5 Conclusions, Caveats, and Future Works

In previous work, we generated stable PGC-1α expressing pools. These pools were found to have attenuated growth, increased specific productivity, and increased consumption of oxygen and carbon sources. Here, we show that PGC-1α expression leads to increased average cell diameter and cell volume. Additionally, ^{13}C MFA revealed major metabolic flux alterations throughout central carbon metabolism in PGC-1α expressing pools. While fluxes were significantly increased, the overall distribution of fluxes was not significantly altered by PGC-1α expression, indicating a global upregulation of flux. When principal component analysis was applied to both PGC-1α expressing and empty vector pools, high-producing PGC-1α pools were separated from all other pools, indicating an altered

metabolic phenotype.

A main focus of this chapter was to confirm the expression and activity of PGC-1α expressing pools. At the mRNA level, both recombinant and endogenous PGC-1α were upregulated in pools engineered to overexpress PGC-1α. Since PGC-1α is reported to be autoregulatory [32], the increase in endogenous PGC-1α could indicate the presence of active PGC-1α. However, at the protein level, various assays proved inconclusive in identifying PGC-1α protein expression. Western blotting for either PGC-1α or the c-Myc-tag present on the recombinant PGC-1α protein did not appear to show any bands at the expected locations. Immunofluorescence for the c-Myc tag appeared promising, but without a western blot to confirm that the antibodies used specifically bind to the protein of interest, these results are inconclusive. The luciferase assay which used the ERRα promoter reporter plasmid showed increased PGC-1α activity in pool 1, but pool 2 and pool 3 had activity levels similar to the parental line (Figure 4.31).

There are some important caveats to the above findings related to PGC-1α that should be addressed. First, high levels of expression of PGC-1α mRNA does not directly correlate with high levels of PGC-1α protein. Morris et al. found a nearly 2000-fold increase in PGC-1α mRNA in hepatocytes transduced with a PGC-1α expressing adeno-associated viral (AAV) vector; in those same cells, a less than two-fold increase in protein was found [26]. Benton et al. utilized an adenoviral (AV) vector to overepxress PGC-1α in rat myoctyes, leading to a 20-fold increase in PGC-1α mRNA which corresponded to a five-fold increase in PGC-1α protein [76]. Additionally, slight increases in PGC-1α protein expression have been found to have profound metabolic effects in muscle tissues [77]. PGC-1α protein is also intrinsically disordered, resulting in a half-life of less than 20 minutes [64]. Such a short half-life can make direct observation of PGC-1α protein difficult, due to generally low concentrations. While the presence of PGC-1α protein was not conclusively confirmed, significant metabolic alterations were observed in pools engineered to overexpress PGC-1α, and increases in PGC-1α at the mRNA level were shown.

The data presented herein supports the hypothesis that increased oxidative metabolism is required for maximal qP in CHO cells. However, some caveats in the cell line generation process need to be addressed. First, the selection process used to obtain stable pools for this study was inherently biased. Initial pools were selected based on growth and VCD. Given the observed decrease in growth rate of the PGC-1α pools relative to the parental line, the initial selection could have discarded pools that exhibited even higher qP levels but grew slowly. Pools selected for in-depth characterization were chosen based on increased qP, another source of potential bias. However, the selection process used is not altogether different from the process used in industry to identify lead production cell lines, where large numbers of clones are generated and screened based on their relative production levels. In fact, given that we only examined 12 stable pools, it is somewhat remarkable that we identified three with substantially elevated qP compared to the parental line (Fig. 4.2).

In addition to the bias inherent in the selection process, clonal variation is a widely reported observation in CHO cells [78, 79, 80]. In this study, random chromosomal integration was used to generate the PGC-1α expressing mini-pools. Due to the inherent genomic variation of CHO cells, the integration site has a strong effect on the expression of the transgene and possibly other endogenous genes nearby [81, 68]. Even in daughter clones generated from a single stable clone, a variety of different phenotypes have been observed, due to the plasticity of the CHO genome [82]. In light of the poorly understood effects of clonal variation, the emergence of metabolic phenotypes that are not directly due to PGC-1α expression remains a possibility. However, the use of stable pools rather than single-cell clones tends to average these random effects over a larger population of cells and thereby minimizes the chances that clonal variation would mask the impact of PGC-1α in our study.

For future work related to this study, we have designed a gene expression plasmid which features the PGC-1α gene under a cumate inducible promoter [83]. By utilizing an inducible system instead of a constitutive promoter, the observed attenuation in growth

can theoretically be avoided. If the attenuation in growth is in fact due to the increased metabolic burden of constitutively producing PGC-1α, then by "turning on" PGC-1α production via the addition of cumate once cells have reached peak VCD, any growth attenuation should be avoided. This new expression system features a FLAG tag instead of a c-Myc tag, which will help to avoid any interference from endogenous expression of c-Myc in future protein assays. Finally, instead of relying upon random integration for the generation of stable cell lines, the new expression system utilizes a PiggyBac transposon system. This should allow for not only higher efficiency in integration of the PGC-1α gene, but also shorter clonal pool selection times, reducing any residual effects of the selection process.

4.6 Appendix

	SSR Best Fit	SSR Expected Range	DOF
Parent	142.2	104.7-169.1	135
Pool 1	127.7	85.5-144.3	113
Pool 2	88.7	103.8-167.9	134
Pool 3	79.1	89.8-150.0	118

Table 4.A1: Model goodness-of-fit metrics as determined by the INCA software

Gene	Primer Pair
Recombinant (human) PGC-1α	5'-GTCACCACCCAAATCCTTAT-3' (forward) 5'-ATCTACTGCCTGGAGACCTT-3' (reverse)
Endogenous (CHO) PGC-1α	5'- ACACACCGCAATTCTCCCTT-3' (forward) 5'- ACGGCGTTCTTCAATTGCTT-3' (reverse)
ERRα	5'-GGT GGG CGA CAG AAG TAC AA-3' (forward) 5'-CAG CTT CTC AGG CTC AAC CA-3' (reverse)
NRF1	5'-GGC TGA TGG AGA GGT GGA AC-3' (forward) 5'-GAG TGG CCT CTG ATG CTT GT-3' (reverse)
tFAM	5'-GAC CAG CTA ACT CCA GCT CA-3' (forward) 5'-GTC TTC AGT CTT CCC GGA G-3' (reverse)
COX4l1	5'-GCC AAG TGG GAC TAC GAC AA-3' (forward) 5'-TTG GAC ACA GCA GCT TCC TT -3' (reverse)
COX5B	5'-AAT AGT GGG CTG CAT CTG TGA-3' (forward) 5'-TTG GTG GGG CAC CAG CTT AT-3' (reverse)
Gabpa	5'-TGC ATC CCC GTT TCA AGA TG-3' (forward) 5'-GTC TGT TCC ACG ATG CTC TCT-3' (reverse)
HPRT	5'- GGA CCT CTC GAA GTG TTG GA-3' (forward) 5'- ATG GGA CTC CTC GTG TTT GC-3' (reverse)

Table 4.A2: **qPCR Primers.** PGC-1α, peroxisome proliferator-activated receptor γ co-activator-1α; CHO, chinese hamster ovary; ERRα, estrogen related receptor α; NRF1, nuclear respiratory factor 1; tFAM, transcription factor A, mitochondrial; COX4l1, cytochrome C oxidase subunit 4l1; COX5B, cytochrome C oxidase subunit 5B; Gabpa, GA-binding protein alpha chain; HPRT, hypoxanthine-guanine phosphoribosyltransferase

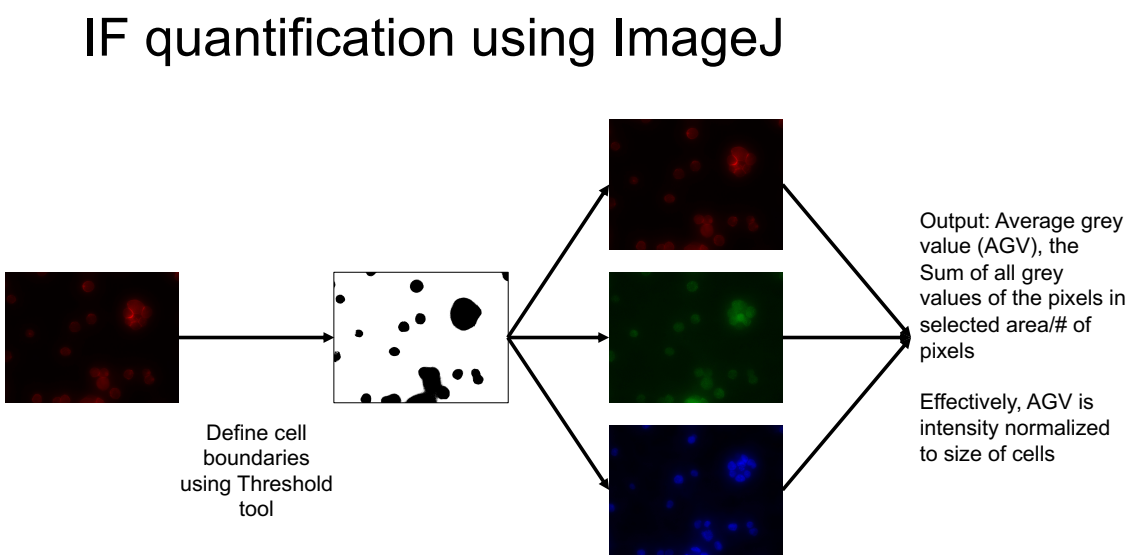

Figure 4.A1: **Quantification of immunofluorescence images using ImageJ.** Using the phalloidin (membrane stain) image, the Threshold tool can be used to define cell boundaries. These boundaries can then be applied to all channels (c-Myc, DAPI, and phalloidin); only signal within these boundaries will be quantified. The signal is measured as the average gray value within the defined cell boundaries, which is effectively the intensity normalized to the area of the imaged cells.

Pathway	Enzyme	Reaction	Net Flux	LB	UB
Glycolysis	HK	Glc ↔ G6P	0.7197	0.6446	0.7965
	PGI	G6P ↔ F6P	0.7094	0.4692	0.7865
	PFK	F6P → DHAP + GAP	0.7038	0.6117	0.7808
	TPI	DHAP ↔ GAP	0.6995	0.6049	0.7761
	GAPDH	GAP ↔ 3PG	1.4005	1.2474	1.5546
	PGM	3PG ↔ PEP	1.4247	1.269	1.5801
	PK	PEP → PYR.C	1.427	1.2718	1.6777
	LDH	LAC ↔ PYR.C	0.0601	0.0519	0.0681
PPP	G6PDH	G6P → Ru5P	1E-07	0	0.2434
	PPE	Ru5P ↔ X5P	-0.0056	-0.0069	0.1522
	PPI	Ru5P ↔ R5P	0.0056	0.0042	0.0866
	TKT1	X5P ↔ EC2 + GAP	-0.0056	-0.0069	0.1522
	TKT2	F6P ↔ EC2 + E4P	0.0028	-0.0761	0.0034
	TKT3	S7P ↔ EC2 + R5P	0.0028	-0.0761	0.0034
	TAL1	F6P ↔ EC3 + GAP	0.0028	-0.0761	0.0034
	TAL2	S7P ↔ EC3 + E4P	-0.0028	-0.0034	0.0761
TCA Cycle	PDH	Pyr.m → AcCoA.m + CO2	1.0409	0.8311	1.2541
	CS	OAA + AcCoA.m → Cit	1.3065	1.087	1.5264
	IDH.m	Cit ↔ aKG + CO2	1.2179	0.9924	1.4437
	aKGDH	aKG → Suc + CO2	0.7462	0.5508	1.6589
	SDH	Suc ↔ Fum	0.8245	0.6256	1.7373
	FUS	Fum ↔ Mal	0.8377	0.639	1.7516
	MDH.m	Mal ↔ OAA	0.8377	0.4856	1.1635
Anaplerosis	ME	Mal → Pyr.m + CO2	1E-07	0	1.0217
	PC	Pyr.m + CO2 → OAA	0.195	0.0786	0.3803
	ATP CS	Cit.c → AcCoa.c + OAA	0.0886	0.0674	0.1098
	PEPCK	OAA → PEP + CO2	0.0023	-0.0804	0.1609
	GOT1	OAA ↔ Asp	-0.1875	-0.2045	-0.1705
	Carboxylase	ProCoA + CO2 → Suc	0.0783	0.0657	0.0908
Amino Acid Metabolism	GS	Gln ↔ Glu	-0.0262	-0.0292	-0.0233
	GluDH	aKG ↔ Glu	0.4717	-0.4619	0.5682
	AsnS	Asn → Asp	-0.1874	-0.2031	-0.1717
	SHMT	Ser ↔ Gly + C1	0.017	0.011	0.0231
	PGHDH	3PG ↔ Ser	0.0242	0.0114	0.0369
	GlyS	CO2 + C1 ↔ Gly	0.0243	0.0211	0.0275
	ALT	Ala ↔ PYR.c	-0.2552	-0.274	-0.2365
	Histidase	His → C1 + Glu.c	0.0073	0.0018	0.0127
	PAH	Phe → Tyr	0.0088	0.0063	0.0113
	TDO	Trp → CO2 + CO2 + Ala + aKetoadi	0.0028	0.0015	0.004
	AA Intermediates	aKetoadi → CO2 + CO2 + AcCoA.m + AcCoA.m	0.0179	0.0051	0.0307
	SBCAD	Ile → AcCoA.m + CO2 + ProCoA	0.0481	0.0387	0.0576
	IVD	Leu + CO2 → CO2 + AcCoA.m + AcCoA.m + AcCoA.m	0.0518	0.0428	0.0607
	IBD	Val → CO2 + CO2 + ProCoA	0.021	0.0158	0.0262
	AASS	Lys → aKetoadi	0.0151	0.0026	0.0277
	ARGS	Arg → Glu + Urea	0.0081	0.0013	0.0148
	PO	Glu ↔ Pro	0.5209	-0.4081	0.6239
	CTH	Cys → Pyr	0.0216	0.0186	0.0246
	MAOX	Thr → Pyr.m + CO2	0.004	0	0.0102
	TH	Tyr → CO2 + Fum + AcCoA.m + AcCoA.m	0.0132	0.008	0.0184
	MAT	Met + Ser → C1 + Cys + ProCoA + Co2	0.0092	0.0071	0.0112
Transport	Glucose	Glc.e → Glc	0.7197	0.6446	0.7965
	Pyr.m	Pyr.c ↔ Pyr.m	1.2319	1.073	1.4833
	Lys	Lys.e → Lys	0.0401	0.0289	0.0518
	Thr	Thr.e → Thr	0.0235	0.0185	0.0288
	Phe	Phe.e → Phe	0.0187	0.017	0.0204
	Tyr	Tyr.e → Tyr	0.0137	0.0102	0.0173
	Val	Val.e → Val	0.0415	0.0378	0.0452
	Leu	Leu.e → Leu	0.0771	0.0696	0.0846
	Ile	Ile.e → Ile	0.0615	0.0525	0.0706
	Trp	Trp.e → Trp	0.0055	0.0043	0.0067
	His	His.e → His	0.0137	0.0083	0.019
	Met	Met.e → Met	0.0148	0.0131	0.0165
	Ser	Ser.e ↔ Ser	0.0737	0.064	0.0834
	Ala	Ala ↔ Ala.e	0.2333	0.2155	0.2512
	Arg	Arg.e ↔ Arg	0.0231	0.0172	0.029
	Asp	Asp ↔ Asp.e	-0.02	-0.0222	-0.0178
	Cys	Cys.e ↔ Cys	0.0192	0.0188	0.0196
	Glu	Glu ↔ Glu.e	-0.0769	-0.0862	-0.0677
	Gln	Gln ↔ Gln.e	-0.0117	-0.0127	-0.0107
	Gly	Gly.e ↔ Gly	-0.0139	-0.0169	-0.011
	Pro	Pro.e ↔ Pro	-0.5049	-0.6097	0.4238
	Asn	Asn.e ↔ Asn	0.2003	0.1849	0.2156
	Lac	Lac ↔ Lac.e	-0.0601	-0.0681	-0.0519
Antibody Production		0.033*Ala + 0.016*Cys + 0.031*Asp + 0.031*Glu + 0.021*Phe + 0.04*Gly + 0.013*His + 0.018*Ile + 0.047*Lys + 0.053*Leu + 0.007*Met + 0.026*Asn + 0.049*Pro + 0.031*Gln + 0.016*Arg + 0.078*Ser + 0.059*Thr + 0.058*Val + 0.012*Trp + 0.029*Tyr → Antibody	0.0969	0.0911	0.1027
Biomass Production		0.1776*Ala + 0.1116*Arg + 0.1396*Asp + 0.08529*Asn + 0.04292*Cys + 0.09528*Gln + 0.1143*Glu + 0.1948*Gly + 0.04229*His + 0.09591*Ile + 0.167*Leu + 0.1687*Lys + 0.04085*Met + 0.06487*Phe + 0.09267*Pro + 0.1305*Ser + 0.1143*Thr + 0.01305*Trp + 0.05389*Tyr + 0.1232*Val + 0.08538*G6P + 0.06892*R5P + 0.07548*C1 + 0.03599*DHAP + 0.7326*AcCoA.c -> Biomass	0.1209	0.0921	0.1499

Table 4.A3: **Net fluxes determined by ^{13}C MFA for the parental line**. The best-fit value and the 95% confidence interval upper bound (UB) and lower bound (LB) are indicated.

Pathway	Enzyme	Reaction	Net Flux	LB	UB
Glycolysis	HK	Glc ↔ G6P	1.4859	1.2317	1.7547
	PGI	G6P ↔ F6P	1.4738	1.1654	1.7418
	PFK	F6P → DHAP + GAP	1.4672	1.2108	1.7366
	TPI	DHAP ↔ GAP	1.4621	1.2059	1.7313
	GAPDH	GAP ↔ 3PG	2.9261	2.4169	3.4628
	PGM	3PG ↔ PEP	3.0051	2.4944	3.5426
	PK	PEP → PYR.C	3.4641	2.4666	4.208
	LDH	LAC ↔ PYR.C	0.4583	0.3967	0.5201
PPP	G6PDH	G6P → Ru5P	3.96E-06	0	0.2949
	PPE	Ru5P ↔ X5P	-0.0065	-0.0085	0.1578
	PPI	Ru5P ↔ R5P	0.0065	0.0045	0.1046
	TKT1	X5P ↔ EC2 + GAP	-0.0065	-0.0085	0.1578
	TKT2	F6P ↔ EC2 + E4P	0.0033	-0.0789	0.0043
	TKT3	S7P ↔ EC2 + R5P	0.0033	-0.0789	0.0043
	TAL1	F6P ↔ EC3 + GAP	0.0033	-0.0789	0.0043
	TAL2	S7P ↔ EC3 + E4P	-0.0033	-0.0043	0.0789
TCA Cycle	PDH	Pyr.m → AcCoA.m + CO2	2.6836	2.1434	3.3595
	CS	OAA + AcCoA.m → Cit	3.1804	2.6262	3.8659
	IDH.m	Cit ↔ aKG + CO2	3.0765	2.5147	3.7667
	aKGDH	aKG → Suc + CO2	2.5229	1.815	4.1005
	SDH	Suc ↔ Fum	2.6673	1.9419	4.2471
	FUS	Fum ↔ Mal	2.6898	1.9871	4.266
	MDH.m	Mal ↔ OAA	2.3854	1.5513	3.4272
Anaplerosis	ME	Mal → Pyr.m + CO2	0.3043	0	1.8372
	PC	Pyr.m + CO2 → OAA	0.8972	0	1.2358
	ATP CS	Cit.c → AcCoa.c + OAA	0.1039	0.0715	0.1362
	PEPCK	OAA → PEP + CO2	0.459	-0.5451	0.9399
	GOT1	OAA ↔ Asp	-0.2529	-0.2735	-0.2321
	Carboxylase	ProCoA + CO2 → Suc	0.1444	0.1202	0.1686
Amino Acid Metabolism	GS	Gln ↔ Glu	-0.075	-0.0824	-0.0675
	GluDH	aKG ↔ Glu	0.5536	-0.8559	1.0805
	AsnS	Asn → Asp	-0.2521	-0.2686	-0.2354
	SHMT	Ser ↔ Gly + C1	0.0564	0.0468	0.0659
	PGHDH	3PG ↔ Ser	0.079	0.0509	0.1071
	GlyS	CO2 + C1 ↔ Gly	0.0692	0.0636	0.0749
	ALT	Ala ↔ PYR.c	-0.3677	-0.3941	-0.3414
	Histidase	His → C1 + Glu.c	0.0146	0.0083	0.021
	PAH	Phe → Tyr	0.0159	0.0104	0.0215
	TDO	Trp → CO2 + CO2 + Ala + aKetoadi	1E-07	0	0.0014
	AA Intermediates	aKetoadi → CO2 + CO2 + AcCoA.m + AcCoA.m	0.039	0.0179	0.0603
	SBCAD	Ile → AcCoA.m + CO2 + ProCoA	0.0971	0.0783	0.1159
	IVD	Leu + CO2 → CO2 + AcCoA.m + AcCoA.m + AcCoA.m	0.0922	0.0694	0.1152
	IBD	Val → CO2 + CO2 + ProCoA	0.0384	0.0266	0.0502
	AASS	Lys → aKetoadi	0.039	0.0178	0.0603
	ARGS	Arg → Glu + Urea	0.0097	0	0.0202
	PO	Glu ↔ Pro	0.5847	-0.8259	1.1218
	CTH	Cys → Pyr	1E-07	0	0.0189
	MAOX	Thr → Pyr.m + CO2	0.0261	0.0157	0.0365
	TH	Tyr → CO2 + Fum + AcCoA.m + AcCoA.m	0.0225	0.0128	0.0321
	MAT	Met + Ser → C1 + Cys + ProCoA + Co2	0.0089	0.0055	0.0123
Transport	Glucose	Glc.e → Glc	1.4859	1.2317	1.7547
	Pyr.m	Pyr.c ↔ Pyr.m	3.5547	2.5385	4.3111
	Lys	Lys.e → Lys	0.0866	0.0667	0.1065
	Thr	Thr.e → Thr	0.0719	0.0631	0.0808
	Phe	Phe.e → Phe	0.0357	0.0309	0.0404
	Tyr	Tyr.e → Tyr	0.0288	0.0224	0.0351
	Val	Val.e → Val	0.085	0.0748	0.0952
	Leu	Leu.e → Leu	0.1425	0.1208	0.1642
	Ile	Ile.e → Ile	0.1197	0.1014	0.1381
	Trp	Trp.e → Trp	0.0079	0.0071	0.0092
	His	His.e → His	0.0272	0.0211	0.0333
	Met	Met.e → Met	0.0182	0.0152	0.0211
	Ser	Ser.e ↔ Ser	0.2019	0.1774	0.2265
	Ala	Ala ↔ Ala.e	0.326	0.3007	0.3515
	Arg	Arg.e ↔ Arg	0.0336	0.0244	0.0428
	Asp	Asp ↔ Asp.e	-0.0362	-0.0444	-0.0279
	Cys	Cys.e ↔ Cys	0.0049	0.000259	0.0235
	Glu	Glu ↔ Glu.e	-0.1135	-0.1282	-0.0988
	Gln	Gln ↔ Gln.e	-0.0459	-0.052	-0.0398
	Gly	Gly.e ↔ Gly	-0.0779	-0.0867	-0.069
	Pro	Pro.e ↔ Pro	-0.547	-1.08	0.8671
	Asn	Asn.e ↔ Asn	0.2772	0.261	0.2933
	Lac	Lac ↔ Lac.e	-0.4583	-0.5201	-0.3967
Antibody Production		0.033*Ala + 0.016*Cys + 0.031*Asp + 0.031*Glu + 0.021*Phe + 0.04*Gly + 0.013*His + 0.018*Ile + 0.047*Lys + 0.053*Leu + 0.007*Met + 0.026*Asn + 0.049*Pro + 0.031*Gln + 0.016*Arg + 0.078*Ser + 0.059*Thr + 0.058*Val + 0.012*Trp + 0.029*Tyr → Antibody	0.5019	0.4537	0.5502
Biomass Production		0.1776*Ala + 0.1116*Arg + 0.1396*Asp + 0.08529*Asn + 0.04292*Cys + 0.09528*Gln + 0.1143*Glu + 0.1948*Gly + 0.04229*His + 0.09591*Ile + 0.167*Leu + 0.1687*Lys + 0.04085*Met + 0.06487*Phe + 0.09267*Pro + 0.1305*Ser + 0.1143*Thr + 0.01305*Trp + 0.05389*Tyr + 0.1232*Val + 0.08538*G6P + 0.06892*R5P + 0.07548*C1 + 0.03599*DHAP + 0.7326*AcCoA.c -> Biomass	0.1418	0.0976	0.1859

Table 4.A4: **Net fluxes determined by ^{13}C MFA for the PGC-1α expressing Pool 1.**. The best-fit value and the 95% confidence interval upper bound (UB) and lower bound (LB) are indicated.

Pathway	Enzyme	Reaction	Net Flux	LB	UB
Glycolysis	HK	Glc ↔ G6P	1.8678	1.4806	2.2778
	PGI	G6P ↔ F6P	1.8533	1.4426	2.2632
	PFK	F6P → DHAP + GAP	1.8455	1.4563	2.2557
	TPI	DHAP ↔ GAP	1.8394	1.4499	2.2496
	GAPDH	GAP ↔ 3PG	3.681	2.9045	4.5016
	PGM	3PG ↔ PEP	3.8255	3.0147	4.647
	PK	PEP → PYR.C	3.8255	2.9082	4.9468
	LDH	LAC ↔ PYR.C	0.235	0.1933	0.2766
PPP	G6PDH	G6P → Ru5P	1E-07	0	0.3436
	PPE	Ru5P ↔ X5P	-0.0078	-0.0107	0.1756
	PPI	Ru5P ↔ R5P	0.0078	0.0048	0.0997
	TKT1	X5P ↔ EC2 + GAP	-0.0078	-0.0107	0.1756
	TKT2	F6P ↔ EC2 + E4P	0.0039	-0.0878	0.0053
	TKT3	S7P ↔ EC2 + R5P	0.0039	-0.0878	0.0053
	TAL1	F6P ↔ EC3 + GAP	0.0039	-0.0878	0.0053
	TAL2	S7P ↔ EC3 + E4P	-0.0039	-0.0053	0.0878
TCA Cycle	PDH	Pyr.m → AcCoA.m + CO2	3.3766	2.5751	4.3977
	CS	OAA + AcCoA.m → Cit	4.0608	3.2389	5.0949
	IDH.m	Cit ↔ aKG + CO2	3.9367	3.1047	4.9331
	aKGDH	aKG → Suc + CO2	3.0928	2.2498	4.6725
	SDH	Suc ↔ Fum	3.2248	2.3789	4.8058
	FUS	Fum ↔ Mal	3.2692	2.4205	4.8503
	MDH.m	Mal ↔ OAA	3.2692	2.4206	4.851
Anaplerosis	ME	Mal → Pyr.m + CO2	1E-07	0	0.679
	PC	Pyr.m + CO2 → OAA	0.2272	0	0.4786
	ATP CS	Cit.c → AcCoa.c + OAA	0.1241	0.0766	0.17
	PEPCK	OAA → PEP + CO2	0	-0.3858	0.7174
	GOT1	OAA ↔ Asp	-0.4403	-0.497	-0.3837
	Carboxylase	ProCoA + CO2 → Suc	0.132	0.0972	0.1672
Amino Acid Metabolism	GS	Gln ↔ Glu	-0.1204	-0.1342	-0.1066
	GluDH	aKG ↔ Glu	0.8439	NaN	1.0594
	AsnS	Asn → Asp	-0.4765	-0.5282	-0.4248
	SHMT	Ser ↔ Gly + C1	0.0451	0.0291	0.0609
	PGHDH	3PG ↔ Ser	0.1445	0.1045	0.1845
	GlyS	CO2 + C1 ↔ Gly	0.092	0.0808	0.1032
	ALT	Ala ↔ PYR.c	-0.5097	-0.5705	-0.4487
	Histidase	His → C1 + Glu.c	0.0531	0.0355	0.0708
	PAH	Phe → Tyr	0.0245	0.0153	0.0338
	TDO	Trp → CO2 + CO2 + Ala + aKetoadi	1E-07	0	0.0028
	AA Intermediates	aKetoadi → CO2 + CO2 + AcCoA.m + AcCoA.m	0.1178	0.0725	0.1634
	SBCAD	Ile → AcCoA.m + CO2 + ProCoA	0.0872	0.0597	0.1147
	IVD	Leu + CO2 → CO2 + AcCoA.m + AcCoA.m + AcCoA.m	0.0909	0.0658	0.1162
	IBD	Val → CO2 + CO2 + ProCoA	0.0383	0.0219	0.0549
	AASS	Lys → aKetoadi	0.1178	0.0724	0.1632
	ARGS	Arg → Glu + Urea	0.0326	0.0147	0.0506
	PO	Glu ↔ Pro	0.8737	0.2133	1.104
	CTH	Cys → Pyr	0.0171	0	0.0708
	MAOX	Thr → Pyr.m + CO2	0.053	0.0245	0.0815
	TH	Tyr → CO2 + Fum + AcCoA.m + AcCoA.m	0.0444	0.0248	0.0642
	MAT	Met + Ser → C1 + Cys + ProCoA + Co2	0.0065	0.0017	0.0114
Transport	Glucose	Glc.e → Glc	1.8678	1.4806	2.2778
	Pyr.m	Pyr.c ↔ Pyr.m	3.5508	2.6298	4.6739
	Lys	Lys.e → Lys	0.1674	0.1234	0.2115
	Thr	Thr.e → Thr	0.0988	0.0714	0.1262
	Phe	Phe.e → Phe	0.0449	0.0367	0.0532
	Tyr	Tyr.e → Tyr	0.042	0.026	0.0581
	Val	Val.e → Val	0.0852	0.0709	0.0995
	Leu	Leu.e → Leu	0.143	0.1203	0.1657
	Ile	Ile.e → Ile	0.1115	0.0846	0.1384
	Trp	Trp.e → Trp	0.0076	0.0066	0.0102
	His	His.e → His	0.0661	0.0487	0.0836
	Met	Met.e → Met	0.0166	0.0125	0.0207
	Ser	Ser.e ↔ Ser	0.2532	0.2191	0.2874
	Ala	Ala ↔ Ala.e	0.4648	0.405	0.5246
	Arg	Arg.e ↔ Arg	0.0587	0.0422	0.0752
	Asp	Asp ↔ Asp.e	-0.0013	-0.0203	0.0177
	Cys	Cys.e ↔ Cys	0.025	0.0017	0.0783
	Glu	Glu ↔ Glu.e	-0.0978	-0.1264	-0.0692
	Gln	Gln ↔ Gln.e	-0.0904	-0.1027	-0.0781
	Gly	Gly.e ↔ Gly	-0.0862	-0.0995	-0.0729
	Pro	Pro.e ↔ Pro	-0.836	-1.0694	NaN
	Asn	Asn.e ↔ Asn	0.5026	0.4513	0.554
	Lac	Lac ↔ Lac.e	-0.235	-0.2766	-0.1933
Antibody Production		0.033*Ala + 0.016*Cys + 0.031*Asp + 0.031*Glu + 0.021*Phe + 0.04*Gly + 0.013*His + 0.018*Ile + 0.047*Lys + 0.053*Leu + 0.007*Met + 0.026*Asn + 0.049*Pro + 0.031*Gln + 0.016*Arg + 0.078*Ser + 0.059*Thr + 0.058*Val + 0.012*Trp + 0.029*Tyr → Antibody	0.4483	0.397	0.4989
Biomass Production		0.1776*Ala + 0.1116*Arg + 0.1396*Asp + 0.08529*Asn + 0.04292*Cys + 0.09528*Gln + 0.1143*Glu + 0.1948*Gly + 0.04229*His + 0.09591*Ile + 0.167*Leu + 0.1687*Lys + 0.04085*Met + 0.06487*Phe + 0.09267*Pro + 0.1305*Ser + 0.1143*Thr + 0.01305*Trp + 0.05389*Tyr + 0.1232*Val + 0.08538*G6P + 0.06892*R5P + 0.07548*C1 + 0.03599*DHAP + 0.7326*AcCoA.c -> Biomass	0.1695	0.1046	0.2321

Table 4.A5: **Net fluxes determined by ^{13}C MFA for the PGC-1α expressing Pool 2.**. The best-fit value and the 95% confidence interval upper bound (UB) and lower bound (LB) are indicated.

Pathway	Enzyme	Reaction	Net Flux	LB	UB
Glycolysis	HK	Glc ↔ G6P	1.8604	1.4598	2.2787
	PGI	G6P ↔ F6P	1.8441	0.4448	2.2581
	PFK	F6P → DHAP + GAP	1.8353	0.6966	2.2499
	TPI	DHAP ↔ GAP	1.8284	0.6879	2.243
	GAPDH	GAP ↔ 3PG	3.6594	2.8578	4.4887
	PGM	3PG ↔ PEP	3.7975	2.9699	4.6567
	PK	PEP → PYR.C	3.7954	2.8317	4.6549
	LDH	LAC ↔ PYR.C	0.235	0.1935	0.2768
PPP	G6PDH	G6P → Ru5P	1.71E-06	0	3.8244
	PPE	Ru5P ↔ X5P	-0.0088	-0.0172	-0.0088
	PPI	Ru5P ↔ R5P	0.0088	0	1.2854
	TKT1	X5P ↔ EC2 + GAP	-0.0088	-0.0172	-0.0088
	TKT2	F6P ↔ EC2 + E4P	0.0044	0.0044	0.0086
	TKT3	S7P ↔ EC2 + R5P	0.0044	0.0044	0.0086
	TAL1	F6P ↔ EC3 + GAP	0.0044	0.0044	0.0086
	TAL2	S7P ↔ EC3 + E4P	-0.0044	-0.0086	-0.0044
TCA Cycle	PDH	Pyr.m → AcCoA.m + CO2	3.3515	2.4661	4.4856
	CS	OAA + AcCoA.m → Cit	4.0168	3.0332	5.2946
	IDH.m	Cit ↔ aKG + CO2	3.8768	2.8142	5.2951
	aKGDH	aKG → Suc + CO2	3.055	2.0218	4.6609
	SDH	Suc ↔ Fum	3.1819	2.1233	4.8093
	FUS	Fum ↔ Mal	3.2241	2.1459	4.8728
	MDH.m	Mal ↔ OAA	3.0639	2.1528	4.3362
Anaplerosis	ME	Mal → Pyr.m + CO2	0.1601	0	0.8722
	PC	Pyr.m + CO2 → OAA	0.3751	0	0.6576
	ATP CS	Cit.c → AcCoa.c + OAA	0.1399	-4.44E-16	0.2744
	PEPCK	OAA → PEP + CO2	-0.0021	-0.4832	0.1864
	GOT1	OAA ↔ Asp	-0.4356	-0.5259	-0.3642
	Carboxylase	ProCoA + CO2 → Suc	0.1269	0.0681	0.2031
Amino Acid Metabolism	GS	Gln ↔ Glu	-0.1224	-0.1451	-0.0935
	GluDH	aKG ↔ Glu	0.8218	0.2183	1.209
	AsnS	Asn → Asp	-0.4748	-0.5356	-0.4203
	SHMT	Ser ↔ Gly + C1	0.049	0.0056	0.0834
	PGHDH	3PG ↔ Ser	0.1382	0.0742	0.2203
	GlyS	CO2 + C1 ↔ Gly	0.0922	0.079	0.104
	ALT	Ala ↔ PYR.c	-0.5137	-0.5841	-0.4255
	Histidase	His → C1 + Glu.c	0.0519	0.0324	0.0751
	PAH	Phe → Tyr	0.0232	0.008	0.0428
	TDO	Trp → CO2 + CO2 + Ala + aKetoadi	1E-07	0	0.0045
	AA Intermediates	aKetoadi → CO2 + CO2 + AcCoA.m + AcCoA.m	0.1157	0.0599	0.188
	SBCAD	Ile → AcCoA.m + CO2 + ProCoA	0.0855	0.0523	0.127
	IVD	Leu + CO2 → CO2 + AcCoA.m + AcCoA.m + AcCoA.m	0.088	0.0478	0.1395
	IBD	Val → CO2 + CO2 + ProCoA	0.0358	0.0076	0.0716
	AASS	Lys → aKetoadi	0.1157	0.0599	0.1857
	ARGS	Arg → Glu + Urea	0.0302	0.0024	0.0658
	PO	Glu ↔ Pro	0.8435	0.2072	1.3037
	CTH	Cys → Pyr	0.0151	0	0.0776
	MAOX	Thr → Pyr.m + CO2	0.0497	0.0138	0.0953
	TH	Tyr → CO2 + Fum + AcCoA.m + AcCoA.m	0.0422	0.0124	0.0805
	MAT	Met + Ser → C1 + Cys + ProCoA + Co2	0.0057	0	0.017
Transport	Glucose	Glc.e → Glc	1.8604	1.4598	2.2787
	Pyr.m	Pyr.c ↔ Pyr.m	3.5167	2.5176	4.4152
	Lys	Lys.e → Lys	0.1689	0.1244	0.2129
	Thr	Thr.e → Thr	0.0979	0.0702	0.1253
	Phe	Phe.e → Phe	0.045	0.0367	0.0532
	Tyr	Tyr.e → Tyr	0.0422	0.0261	0.0583
	Val	Val.e → Val	0.0852	0.0709	0.0995
	Leu	Leu.e → Leu	0.1436	0.1207	0.1664
	Ile	Ile.e → Ile	0.1118	0.0849	0.1388
	Trp	Trp.e → Trp	0.0079	0.0053	0.0105
	His	His.e → His	0.0658	0.0483	0.0834
	Met	Met.e → Met	0.0166	0.0125	0.0207
	Ser	Ser.e ↔ Ser	0.2526	0.2184	0.2868
	Ala	Ala ↔ Ala.e	0.465	0.4051	0.5248
	Arg	Arg.e ↔ Arg	0.0587	0.0422	0.0752
	Asp	Asp ↔ Asp.e	-0.0013	-0.0203	0.0177
	Cys	Cys.e ↔ Cys	0.0248	-0.0088	0.0781
	Glu	Glu ↔ Glu.e	-0.0977	-0.1264	-0.069
	Gln	Gln ↔ Gln.e	-0.0904	-0.1027	-0.078
	Gly	Gly.e ↔ Gly	-0.0861	-0.0995	-0.0727
	Pro	Pro.e ↔ Pro	-0.8039	-1.2829	-0.1582
	Asn	Asn.e ↔ Asn	0.5027	0.4512	0.5541
	Lac	Lac ↔ Lac.e	-0.235	-0.2768	-0.1935
Antibody Production		0.033*Ala + 0.016*Cys + 0.031*Asp + 0.031*Glu + 0.021*Phe + 0.04*Gly + 0.013*His + 0.018*Ile + 0.047*Lys + 0.053*Leu + 0.007*Met + 0.026*Asn + 0.049*Pro + 0.031*Gln + 0.016*Arg + 0.078*Ser + 0.059*Thr + 0.058*Val + 0.012*Trp + 0.029*Tyr → Antibody	0.4466	0.4165	0.4769
Biomass Production		0.1776*Ala + 0.1116*Arg + 0.1396*Asp + 0.08529*Asn + 0.04292*Cys + 0.09528*Gln + 0.1143*Glu + 0.1948*Gly + 0.04229*His + 0.09591*Ile + 0.167*Leu + 0.1687*Lys + 0.04085*Met + 0.06487*Phe + 0.09267*Pro + 0.1305*Ser + 0.1143*Thr + 0.01305*Trp + 0.05389*Tyr + 0.1232*Val + 0.08538*G6P + 0.06892*R5P + 0.07548*C1 + 0.03599*DHAP + 0.7326*AcCoA.c -> Biomass	0.191	0	0.3746

Table 4.A6: **Net fluxes determined by ^{13}C MFA for the pPGC-1α expressing Pool 3.**. The best-fit value and the 95% confidence interval upper bound (UB) and lower bound (LB) are indicated.

References

[1] Gary Walsh. Biopharmaceutical benchmarks 2018. *Nature Biotechnology*, 36(12):1136–1145, 2018.

[2] Natalia I. Majewska, Max L. Tejada, Michael J. Betenbaugh, and Nitin Agarwal. N-Glycosylation of IgG and IgG-like recombinant proteins: Why is it important and how can we control it? *Annual Review of Chemical and Biomolecular Engineering*, 11(13):1–28, 2020.

[3] Allison G Mcatee, Neil Templeton, and Jamey D Young. Role of Chinese hamster ovary central carbon metabolism in controlling the quality of secreted biotherapeutic proteins. *Pharmaceutical Bioprocessing*, 2(1):63–74, 2014.

[4] Maria Elisa Rodrigues, Ana Rita Costa, Mariana Henriques, Philip Cunnah, David W. Melton, Joana Azeredo, and Rosário Oliveira. Advances and drawbacks of the adaptation to serum-free culture of CHO-K1 cells for monoclonal antibody production. *Applied Biochemistry and Biotechnology*, 169(4):1279–1291, 2013.

[5] Martin Schröder, Kathrin Matischak, and Peter Friedl. Serum- and protein-free media formulations for the Chinese hamster ovary cell line DUKXB11. *Journal of Biotechnology*, 108(3):279–292, 2004.

[6] Martin S Sinacore, Denis Drapeau, and S R Adamson. Adaptation of Mammalian Cells to Growth in Serum-Free Media. *Molecular Biotechnology*, 15, 2000.

[7] Jennifer Becker, Matthias Hackl, Oliver Rupp, Tobias Jakobi, Jessica Schneider, Rafael Szczepanowski, Thomas Bekel, Nicole Borth, Alexander Goesmann, Johannes Grillari, Christian Kaltschmidt, Thomas Noll, Alfred Pühler, Andreas Tauch, and Karina Brinkrolf. Unraveling the Chinese hamster ovary cell line transcriptome by next-generation sequencing. *Journal of Biotechnology*, 156(3):227–235, 2011.

[8] Simon Fischer, René Handrick, and Kerstin Otte. The art of CHO cell engineering : A comprehensive retrospect and future perspectives. *Biotechnology Advances*, 33(8):1878–1896, 2015.

[9] Karthik P. Jayapal, Katie F. Wlaschin, Wei Shou Hu, and Miranda G.S. Yap. Recombinant protein therapeutics from CHO Cells - 20 years and counting. *Chemical Engineering Progress*, 103(10):40–47, 2007.

[10] Chih Chung Kuo, Austin WT Chiang, Isaac Shamie, Mojtaba Samoudi, Jahir M. Gutierrez, and Nathan E. Lewis. The emerging role of systems biology for engineering protein production in CHO cells. *Current Opinion in Biotechnology*, 51:64–69, 2018.

[11] Neil Templeton, Kevin D Smith, Allison G Mcatee-pereira, Haimanti Dorai, J Betenbaugh, Steven E Lang, and Jamey D Young. Application of 13C flux analysis

to identify high-productivity CHO metabolic phenotypes. *Metabolic Engineering*, 43(B):218–225, 2017.

[12] Gargi Seth, Patrick Hossler, Joon Chong Yee, and Wei-Shou Hu. Engineering Cells for Cell Culture Bioprocessing- Physiological Fundamentals. *Adv Biochem Eng Biotechnol*, 101:119–164, 2006.

[13] Jahir M. Gutierrez, Amir Feizi, Shangzhong Li, Thomas B. Kallehauge, Hooman Hefzi, Lise M. Grav, Daniel Ley, Deniz Baycin Hizal, Michael J. Betenbaugh, Bjorn Voldborg, Helene Faustrup Kildegaard, Gyun Min Lee, Bernhard O. Palsson, Jens Nielsen, and Nathan E. Lewis. Genome-scale reconstructions of the mammalian secretory pathway predict metabolic costs and limitations of protein secretion. *Nature Communications*, 11(1):1–10, 2020.

[14] Neha Dhami, Drupad K. Trivedi, Royston Goodacre, David Mainwaring, and David P. Humphreys. Mitochondrial aconitase is a key regulator of energy production for growth and protein expression in Chinese hamster ovary cells. *Metabolomics*, 14(10):1–16, 2018.

[15] Haimanti Dorai, Seung Kyung Yun, Dawn Ellis, Cheryl Ann Kinney, Chengbin Lin, David Jan, Gordon Moore, and Michael J. Betenbaugh. Expression of anti-apoptosis genes alters lactate metabolism of Chinese Hamster ovary cells in culture. *Biotechnology and Bioengineering*, 103(3):592–608, 2009.

[16] Mio Sam Lao and Derek Toth. Effects of ammonium and lactate on growth and metabolism of a recombinant Chinese hamster ovary cell culture. *Biotechnology Progress*, 13(5):688–691, 1997.

[17] Anne Le, Andrew N. Lane, Max Hamaker, Sminu Bose, Arvin Gouw, Joseph Barbi, Takashi Tsukamoto, Camilio J. Rojas, Barbara S. Slusher, Haixia Zhang, Lisa J. Zimmerman, Daniel C. Liebler, Robbert J.C. Slebos, Pawel K. Lorkiewicz, Richard M. Higashi, Teresa W.M. Fan, and Chi V. Dang. Glucose-independent glutamine metabolism via TCA cycling for proliferation and survival in b cells. *Cell Metabolism*, 15(1):110–121, 2012.

[18] Neil Templeton, Jason Dean, Pranhitha Reddy, and Jamey D. Young. Peak antibody production is associated with increased oxidative metabolism in an industrially relevant fed-batch CHO cell culture. *Biotechnology and Bioengineering*, 110(7):2013–2024, 2013.

[19] Neil Templeton and Jamey D. Young. Biochemical and metabolic engineering approaches to enhance production of therapeutic proteins in animal cell cultures. *Biochemical Engineering Journal*, 136:40–50, 2018.

[20] Shane Austin and Julie St-Pierre. PGC1α and mitochondrial metabolism–emerging concepts and relevance in ageing and neurodegenerative disorders. *Journal of cell science*, 125(Pt 21):4963–4971, 2012.

[21] Mun Chun Chan and Zolt Arany. The many roles of PGC-1α in muscle - Recent developments. *Metabolism: Clinical and Experimental*, 63(4):441–451, 2014.

[22] Pere Puigserver and Bruce M. Spiegelman. Peroxisome proliferator-activated receptor-γ coactivator 1α (PGC-1α): Transcriptional coactivator and metabolic regulator. *Endocrine Reviews*, 24(1):78–90, 2003.

[23] Joseph T Rodgers, Carles Lerin, Zachary Gerhart-hines, and Pere Puigserver. Metabolic adaptations through the PGC-1 a and SIRT1 pathways. *FEBS letters*, 582:46–53, 2008.

[24] Richard C Scarpulla. Metabolic control of mitochondrial biogenesis through the PGC-1 family regulatory network. *Biochimica et Biophysica Acta*, 1813(7):1269–1278, 2011.

[25] Vamsi K Mootha, Christoph Handschin, Dan Arlow, Xiaohui Xie, Julie St Pierre, Smita Sihag, Wenli Yang, David Altshuler, Pere Puigserver, Nick Patterson, Patricia J Willy, Ira G Schulman, Richard a Heyman, Eric S Lander, and Bruce M Spiegelman. Erralpha and Gabpa/b specify PGC-1alpha-dependent oxidative phosphorylation gene expression that is altered in diabetic muscle. *Proceedings of the National Academy of Sciences of the United States of America*, 101(17):6570–6575, 2004.

[26] E. Matthew Morris, Grace M.E. Meers, Frank W. Booth, Kevin L. Fritsche, Christopher D. Hardin, John P. Thyfault, and Jamal A. Ibdah. Pgc-1α overexpression results in increased hepatic fatty acid oxidation with reduced triacylglycerol accumulation and secretion. *American Journal of Physiology - Gastrointestinal and Liver Physiology*, 303(8):979–992, 2012.

[27] Ji Suk Chang, Hee-Jin Jun, and Minsung Park. Transcriptional coactivator NT-PGC-1α promotes gluconeogenic gene expression and enhances hepatic gluconeogenesis. *Physiological reports*, 4(20):1–14, 2016.

[28] Thomas K. Felder, Selma M. Soyal, Hannes Oberkofler, Penelope Hahne, Simon Auer, Richard Weiss, Gabriele Gadermaier, Karl Miller, Franz Krempler, Harald Esterbauer, and Wolfgang Patsch. Characterization of novel peroxisome proliferator-activated receptor γ coactivator-1α (PGC-1α) isoform in human liver. *Journal of Biological Chemistry*, 286(50):42923–42936, 2011.

[29] J C Yoon, P Puigserver, G Chen, J Donovan, Z Wu, J Rhee, G Adelmant, J Stafford, C R Kahn, D K Granner, C B Newgard, and B M Spiegelman. Control of hepatic gluconeogenesis through the transcriptional coactivator PGC-1. *Nature*, 413(6852):131–138, 2001.

[30] John J Lehman, Philip M Barger, Attila Kovacs, Jeffrey E Saffitz, Denis M Medeiros, and Daniel P Kelly. Peroxisome proliferator – activated receptor γ coactivator-1 promotes cardiac mitochondrial biogenesis. *The Journal of Clinical Investigation*, 106(7):847–856, 2000.

[31] J. J. Lehman, S. Boudina, N. H. Banke, N. Sambandam, X. Han, D. M. Young, T. C. Leone, R. W. Gross, E. D. Lewandowski, E. D. Abel, and D. P. Kelly. The transcriptional coactivator PGC-1 is essential for maximal and efficient cardiac mitochondrial fatty acid oxidation and lipid homeostasis. *AJP: Heart and Circulatory Physiology*, 295(1):H185–H196, 2008.

[32] Christoph Handschin, James Rhee, Jiandie Lin, Paul T. Tarr, and Bruce M. Spiegelman. An autoregulatory loop controls peroxisome proliferator-activated receptor γ coactivator 1α expression in muscle. *Proceedings of the National Academy of Sciences of the United States of America*, 100(12):7111–7116, 2003.

[33] Maciek R. Antoniewicz. A guide to metabolic flux analysis in metabolic engineering: Methods, tools and applications. *Metabolic Engineering*, 63:2–12, 2020.

[34] Sarah A Sacco and Jamey D Young. 13C metabolic flux analysis in cell line and bioprocess development. *Current Opinion in Chemical Engineering*, 34, 2021.

[35] Yi Ern Cheah and Jamey D. Young. Isotopically nonstationary metabolic flux analysis (INST-MFA): putting theory into practice. *Current Opinion in Biotechnology*, 54:80–87, 2018.

[36] Wolfgang Wiechert and Katharina Nöh. Isotopically non-stationary metabolic flux analysis: Complex yet highly informative. *Current Opinion in Biotechnology*, 24(6):979–986, 2013.

[37] Neil Templeton, Sen Xu, David J Roush, and Hao Chen. 13C metabolic flux analysis identifies limitations to increasing specific productivity in fed-batch and perfusion. *Metabolic Engineering*, 44(September):126–133, 2017.

[38] Maria Buchsteiner, Lake Ee Quek, Peter Gray, and Lars K. Nielsen. Improving culture performance and antibody production in CHO cell culture processes by reducing the Warburg effect. *Biotechnology and Bioengineering*, 115(9):2315–2327, 2018.

[39] Meixia Zhou, Yongping Crawford, Domingos Ng, Jack Tung, Abigail F.J. Pynn, Angela Meier, Inn H. Yuk, Natarajan Vijayasankaran, Kimberly Leach, John Joly, Bradley Snedecor, and Amy Shen. Decreasing lactate level and increasing antibody production in Chinese Hamster Ovary cells (CHO) by reducing the expression of lactate dehydrogenase and pyruvate dehydrogenase kinases. *Journal of Biotechnology*, 153(1-2):27–34, 2011.

[40] Allison G. McAtee Pereira. *13C metabolic flux analysis of industrial Chinese hamster ovary (CHO) cell cultures*. Ph.d. thesis, Vanderbilt University, 2018.

[41] Fiona Hartley, Tracy Walker, Vicky Chung, and Karl Morten. Mechanisms driving the lactate switch in Chinese hamster ovary cells. *Biotechnology and Bioengineering*, 115(8):1890–1903, 2018.

[42] Masaru Ichida, Shino Nemoto, and Toren Finkel. Identification of a specific molecular repressor of the peroxisome proliferator-activated receptor γ coactivator-1 α (PGC-1α). *Journal of Biological Chemistry*, 277(52):50991–50995, 2002.

[43] Kenneth J. Livak and Thomas D. Schmittgen. Analysis of relative gene expression data using real-time quantitative PCR and the 2-$\Delta\Delta$CT method. *Methods*, 25(4):402–408, 2001.

[44] Neil Templeton, Abasha Lewis, Haimanti Dorai, Elaine A. Qian, Marguerite P. Campbell, Kevin D. Smith, Steven E. Lang, Michael J. Betenbaugh, and Jamey D. Young. The impact of anti-apoptotic gene Bcl-2 expression on CHO central metabolism. *Metabolic Engineering*, 25:92–102, 2014.

[45] Taylor A. Murphy and Jamey D. Young. ETA: Robust software for determination of cell specific rates from extracellular time courses. *Biotechnology and Bioengineering*, 110(6):1748–1758, 2013.

[46] Jamey D Young, Douglas K Allen, and John A Morgan. Chapter 7 Isotopomer Measurement Techniques in Metabolic Flux Analysis II : Mass Spectrometry. *Plant Metabolism: Methods and Protocols*, 1083:85–108, 2014.

[47] Paul Shannon, Andrew Markiel, Owen Ozier, Nitin S. Baliga, Jonathan T. Wang, Daniel Ramage, Nada Amin, Benno Schwikowski, and Trey Ideker. Cytoscape: A Software Environment for Integrated Models of Biomolecular Interaction Networks. *Genome Research*, 13:2498–2504, 2003.

[48] Chun Chao Wang, Sameer S. Bajikar, Leen Jamal, Kristen A. Atkins, and Kevin A. Janes. A time- and matrix-dependent TGFBR3-JUND-KRT5 regulatory circuit in single breast epithelial cells and basal-like premalignancies. *Nature Cell Biology*, 16(4):345–356, 2014.

[49] Lynda Handala, Tony Fiore, Yves Rouillé, and Francois Helle. QuantIF: An ImageJ Macro to automatically determine the percentage of infected cells after immunofluorescence. *Viruses*, 11(2), 2019.

[50] Ines Bruns, Benedikt Sauer, Michael C. Burger, Jule Eriksson, Ute Hofmann, Yannick Braun, Patrick N. Harter, Anna Luisa Luger, Michael W. Ronellenfitsch, Joachim P. Steinbach, and Johannes Rieger. Disruption of peroxisome proliferator–activated receptor coactivator (PGC)-1 reverts key features of the neoplastic phenotype of glioma cells. *Journal of Biological Chemistry*, 294(9):3037–3050, 2019.

[51] David R. Lloyd, Paul Holmes, Lee P. Jackson, A. Nicholas Emery, and Mohamed Al-Rubeai. Relationship between cell size, cell cycle and specific recombinant protein productivity. *Cytotechnology*, 34(1-2):59–70, 2000.

[52] Marc Feary, Andrew J. Racher, Robert J. Young, and C. Mark Smales. Methionine sulfoximine supplementation enhances productivity in GS–CHOK1SV cell lines through glutathione biosynthesis. *Biotechnology Progress*, 33(1):17–25, 2017.

[53] Andy Wiranata Wijaya, Natascha Verhagen, Attila Teleki, and Ralf Takors. Compartment-specific 13C metabolic flux analysis reveals boosted NADPH availability coinciding with increased cell-specific productivity for IgG1 producing CHO cells after MTA treatment. *Engineering in Life Sciences*, 21(12):832–847, 2021.

[54] Neil Templeton, Sen Xu, David J. Roush, and Hao Chen. 13C metabolic flux analysis identifies limitations to increasing specific productivity in fed-batch and perfusion. *Metabolic Engineering*, 44(August):126–133, 2017.

[55] Ramon Amat, Anna Planavila, Shen Liang Chen, Roser Iglesias, Marta Giralt, and Francesc Villarroya. SIRT1 controls the transcription of the peroxisome proliferator-activated receptor-γ co-activator-1α(PGC-1α) gene in skeletal muscle through the PGC-1α autoregulatory loop and interaction with MyoD. *Journal of Biological Chemistry*, 284(33):21872–21880, 2009.

[56] Josep A Villena and Anastasia Kralli. ERR a : a metabolic function for the oldest orphan. *Trends in Endocrinology and Metabolism*, 19(8):269–276, 2008.

[57] Alexandra E. Charos, Brian D. Reed, Debasish Raha, Anna M. Szekely, Sherman M. Weissman, and Michael Snyder. A highly integrated and complex PPARGC1A transcription factor binding network in HepG2 cells. *Genome Research*, 22(9):1668–1679, 2012.

[58] Florian M. Wurm. CHO quasispecies-Implications for manufacturing processes. *Processes*, 1(3):296–311, 2013.

[59] E. Hazelwood. *Molecular analysis of clonal variation in GS-CHO cell lines*. Ph.d. thesis, University of Manchester, 2006.

[60] Biji T. Kurien and R. Hal Scofield. Western blotting: Methods and protocols. *Western Blotting: Methods and Protocols*, 1312:1–509, 2015.

[61] Ji Suk Chang, Sujoy Ghosh, Susan Newman, and J. Michael Salbaum. A map of the PGC-1α-and NT-PGC-1α-regulated transcriptional network in brown adipose tissue. *Scientific Reports*, 8(1):1–10, 2018.

[62] Ji Suk Chang and Kyoungsoo Ha. An unexpected role for the transcriptional coactivator isoform NT-PGC-1α in the regulation of mitochondrial respiration in brown adipocytes. *Journal of Biological Chemistry*, 292(24):9958–9966, 2017.

[63] Taylor A. Murphy, Chi V. Dang, and Jamey D. Young. Isotopically nonstationary 13C flux analysis of Myc-induced metabolic reprogramming in B-cells. *Metabolic Engineering*, 15(1):206–217, 2013.

[64] Julie Trausch-azar, Teresa C Leone, Daniel P Kelly, and Alan L Schwartz. Ubiquitin proteasome dependent degradation of the transcriptional coactivator PGC-1alpha via the N-terminal pathway. *Journal of Biological Chemistry*, (8), 2010.

[65] Ian D. Odell and Deborah Cook. Immunofluorescence techniques. *Journal of Investigative Dermatology*, 133(1):1–4, 2013.

[66] Jonathan Bergeman and Marc Étienne Huot. Quantitative immunofluorescence to measure global localized translation. *Journal of Visualized Experiments*, 2017(126):1–11, 2017.

[67] Igor Buchwalow, Vera Samoilova, Werner Boecker, and Markus Tiemann. Non-specific binding of antibodies in immunohistochemistry: Fallacies and facts. *Scientific Reports*, 1:1–6, 2011.

[68] Florian M. Wurm and Maria João Wurm. Cloning of CHO Cells, productivity and genetic stability-a discussion. *Processes*, 5(2), 2017.

[69] Ankita Singh, Helene F. Kildegaard, and Mikael R. Andersen. An Online Compendium of CHO RNA-Seq Data Allows Identification of CHO Cell Line-Specific Transcriptomic Signatures. *Biotechnology Journal*, 1800070:1–11, 2018.

[70] Jared N Boustead, Beth T Stadelmaier, Angela M Eeds, Peter O Wiebe, Christina A Svitek, James K Oeser, and Richard M O Brien. Hepatocyte nuclear factor-4a mediates the stimulatory effect of peroxisome proliferator-activated receptor g coactivator-1a (PGC-1a) on glucose-6-phosphatase catalytic subunit gene transcription in H4IIE cells. *Biochem. J.*, 369:17–22, 2003.

[71] M M Schilling, J K Oeser, J K Chandy, B P Flemming, S R Allen, and R M O'Brien. Sequence variation between the mouse and human glucose-6-phosphatase catalytic subunit gene promoters results in differential activation by peroxisome proliferator activated receptor gamma coactivator-1alpha. *Diabetologia*, 51(8):1505–14, 2008.

[72] Kayla A. Boortz, Kristen E. Syring, Lynley D. Pound, Yingda Wang, James K. Oeser, and Richard M. O'Brien. Functional analysis of mouse G6pc1 mutations using a novel in situ assay for glucose-6-phosphatase activity and the effect of mutations in conserved human G6PC1/G6PC2 amino acids on G6PC2 protein expression. *PLoS ONE*, 11(9), 2016.

[73] D. Liu, Z Zhang, and C T Teng. Estrogen-related receptor-gamma and peroxisome proliferator-activated receptor-gamma coactivator-1alpha regulate estrogen-related receptor-alpha gene expression via a conserved multi-hormone response element. *Journal of molecular endocrinology*, 34(2):473–87, 2005.

[74] Christina T. Teng, Burton Beames, B. Alex Merrick, Negin Martin, Charles Romeo, and Anton M. Jetten. Development of a stable cell line with an intact PGC-1α/ERRα axis for screening environmental chemicals. *Biochemical and Biophysical Research Communications*, 444(2):177–181, 2014.

[75] Ian T. Jollife and Jorge Cadima. Principal component analysis: A review and recent developments. *Philosophical Transactions of the Royal Society A: Mathematical, Physical and Engineering Sciences*, 374(2065), 2016.

[76] Carley R. Benton, James G. Nickerson, James Lally, Xiao Xia Han, Graham P. Holloway, Jan F.C. Glatz, Joost J.F.P. Luiken, Terry E. Graham, John J. Heikkila, and Arend Bonen. Modest PGC-1α overexpression in muscle in vivo is sufficient to increase insulin sensitivity and palmitate oxidation in subsarcolemmal, not intermyofibrillar, mitochondria. *Journal of Biological Chemistry*, 283(7):4228–4240, 2008.

[77] Timothy R. Koves, Ping Li, Jie An, Takayuki Akimoto, Dorothy Slentz, Olga Ilkayeva, G. Lynis Dohm, Zhen Yan, Christopher B. Newgard, and Deborah M. Muoio. Peroxisome proliferator-activated receptor-?? co-activator 1??-mediated metabolic remodeling of skeletal myocytes mimics exercise training and reverses lipid-induced mitochondrial inefficiency. *Journal of Biological Chemistry*, 280(39):33588–33598, 2005.

[78] Arpan A. Bandyopadhyay, Sofie A. O'Brien, Liang Zhao, Hsu Yuan Fu, Nandita Vishwanathan, and Wei Shou Hu. Recurring genomic structural variation leads to clonal instability and loss of productivity. *Biotechnology and Bioengineering*, 116(1):41–53, 2019.

[79] Atefeh Ghorbaniaghdam, Jingkui Chen, Olivier Henry, and Mario Jolicoeur. Analyzing clonal variation of monoclonal antibody-producing CHO cell lines using an in silico metabolomic platform. *PLoS ONE*, 9(3), 2014.

[80] Jae Seong Lee, Jin Hyoung Park, Tae Kwang Ha, Mojtaba Samoudi, Nathan E. Lewis, Bernhard O. Palsson, Helene Faustrup Kildegaard, and Gyun Min Lee. Revealing Key Determinants of Clonal Variation in Transgene Expression in Recombinant CHO Cells Using Targeted Genome Editing. *ACS Synthetic Biology*, 7:2867–2878, 2018.

[81] Won Dong Lee, Dzmitry Mukha, Elina Aizenshtein, and Tomer Shlomi. Spatial-fluxomics provides a subcellular-compartmentalized view of reductive glutamine metabolism in cancer cells. *Nature Communications*, 10(1):1–14, 2019.

[82] Peggy Ko, Shahram Misaghi, Zhilan Hu, Dejin Zhan, Joni Tsukuda, Mandy Yim, Mark Sanford, David Shaw, Masaru Shiratori, Brad Snedecor, Michael Laird, and Amy Shen. Probing the importance of clonality: Single cell subcloning of clonally derived CHO cell lines yields widely diverse clones differing in growth, productivity, and product quality. *Biotechnology Progress*, 34(3):624–634, 2018.

[83] Bruno Gaillet, Rénald Gilbert, Sophie Broussau, Amélie Pilotte, Félix Malenfant, Alaka Mullick, Alain Garnier, and Bernard Massie. High-level recombinant protein production in CHO cells using lentiviral vectors and the cumate gene-switch. *Biotechnology and Bioengineering*, 106(2):203–215, 2010.

CHAPTER 5

Development and validation of a metabolic model of glycosylation precursor production

5.1 Introduction

Monoclonal antibodies are large proteins ($\sim$150 kDa) that consist of two heavy chains and two light chains [1]. These chains are connected by disulfide bonds, which provide stability [2]. Both the heavy and light chains feature conserved regions and highly variable regions, the latter of which are responsible for antigen binding [2]. All mAbs have one glycosylation site in the Fc region of the heavy chain, while about 20% have a second site in the variable region [2]. Glycosylation occurs in the endoplasmic reticulum and Golgi apparatus, and involves the attachment of oligosaccharides to various amino acids in a protein [3].

Glycosylation is important for structure, with different glycans altering the conformation of the mAbs; glycans stabilize the mAbs, preventing unfolding of the protein [4]. Upon antigen binding, mAbs bind effector proteins, and this binding is dependent on proper glycosylation [2]. mAbs typically have a half-life of 10-25 days in the body, but this timeframe is also dependent on glycosylation [2]. A consistent half-life is necessary to determine dosage timing and quantity. Overall, the structure, stability, function, and pharmacokinetics of mAbs are highly dependent on glycosylation. Therefore, a thorough understanding of how glycosylation is affected by metabolic alterations is necessary, particularly with the current growth of the biosimilars market [5].

Most previous modeling work in CHO cells has focused on two main areas: studying how the host metabolism affects growth and yield and understanding the glycosylation process [6]. Metabolic modeling has focused on identifying ways to limit byproducts and optimize media compositions [7]. Meanwhile glycosylation modeling has focused on how enzyme expression or media composition affect final product glycosylation [8, 9, 10, 11]. Thus far, there have been very few models that have attempted to combine metabolism

and glycosylation. Flux balance analysis (FBA) attempts to optimize a parameter, such as cell growth, based on a set of defined constraints and has been used to assess the effects of low temperature on the availability of nucleotide (NT) sugars, which are precursors to glycosylation [12]. A similar model was also used to assess the effects of glutamine concentration in the media on intracellular NT sugar concentrations [13]. In addition, a stoichiometric model has been used to estimate the demand of NT sugars for both host cell proteins and recombinant proteins [14].

Enzymes are regulated by allosteric feedback and substrate availability, which cannot be discerned from mRNA or protein expression data, and intracellular metabolic flux cannot be determined solely by measuring intracellular and extracellular concentrations of metabolites [15]. Through the application of carbon-13 metabolic flux analysis (^{13}C MFA), intracellular metabolism can be quantified and characterized. On the experimental side of ^{13}C MFA, cultures are fed stable isotope labeled substrates. Samples are analyzed using nuclear magnetic resonance (NMR) or mass spectrometry (MS) to determine the distribution of these isotopes in downstream metabolites. At its computational core, ^{13}C MFA involves solving an optimization problem; the parameters (metabolic fluxes) are adjusted until an objective function (the sum of squared residuals between the experimentally measured labeling data and simulated labeling data) is minimized [16]. This optimization is subject to constraints from stoichiometric mass balances and isotopomer balances on the metabolite in the biochemical network [16]. Overall, the final result of ^{13}C MFA is to provide a quantitative map of metabolism, by providing flux values and confidence intervals for each metabolic reaction in the model [17].

The feeding of alternate carbon sources to manipulate CHO cell metabolism has been well studied [18, 19]. Galactose, an isomer of glucose, has been shown to reduce lactate production and alter mAb glycosylation. It is hypothesized that galactose feeding reduces lactate production by limiting flux through glycolysis, due to the extra steps needed for galactose to enter glycolysis (Figure 5.1) [20]. Galactose feeding has also been shown to

increase intracellular concentrations of UDP-hexose (defined herein as the sum of UDP-glucose and UDP-galactose) as well as alter the glycosylation of mAbs by increasing sialylation and increase the presence as well as abundance of terminal galactose residues and galactosylated glycans [19, 21].

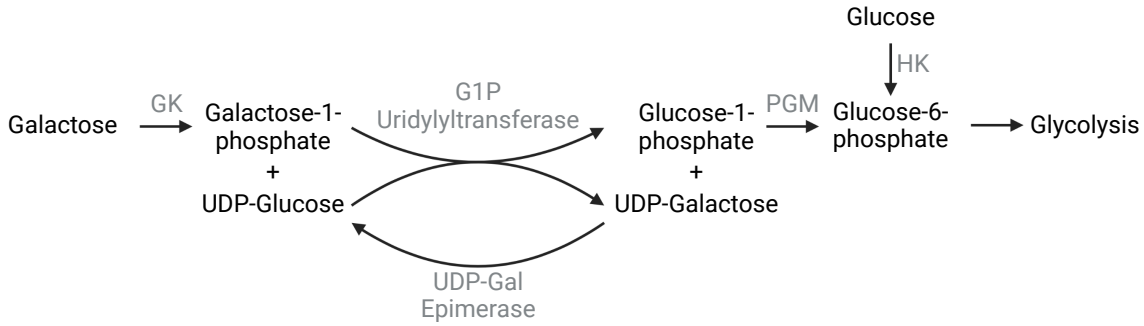

Figure 5.1: **Galactose metabolism.** Glucose-1-phosphate is converted to glucose-6-phosphate and enters glycolysis after the hexokinase reaction. GK, galactokinase; G1P, Galactose-1 phosphate; PGM, phosphoglucomerase; HK, hexokinase.

To the best of our knowledge, ^{13}C MFA has not been used to quantify the metabolic reactions that lead to the biosynthesis of glycosylation precursors, such as nucleotides (NTs) and NT-sugars. Herein, we describe the development of a metabolic model which incorporates the biosynthesis reactions for NTs and NT sugars in addition to central carbon metabolism. In addition to developing this metabolic model, an LC-MS/MS method to determine the labeling profiles of various NTs and NT sugars was also developed. Finally, both the metabolic model and LC-MS/MS method were applied to a ^{13}C MFA labeling study of CHO cell cultures fed either glucose or galactose. The MFA study found that growth and mAb production were not altered by galactose feeding during stationary phase. Extracellular fluxes of glucose, lactate, galactose, and various amino acids were significantly different in the galactose fed cultures. Finally, ^{13}C MFA revealed altered central carbon metabolism in galactose fed cultures compared to glucose fed cultures. While labeling patterns of NT sugars were altered by galactose feeding, fluxes throughout NT sugar biosynthesis were not well-resolved.

5.2 Materials and Methods

5.2.1 Cell Culture

An industrial IgG-producing CHO cell lines (5466A) was provided by Janssen Pharmaceuticals for use in this study. All cultures were grown in 40 mL working volume cultures in 125 mL shake flasks in 37°C, 5% CO_2, humidified incubators while shaking at 135 RPM. To seed an initial culture, a vial of banked cells was thawed in a 37°C water bath and resuspended in 9 mL of pre-warmed Forti-CHO media (ThermoFisher; Waltham, MA). This resuspension was centrifuged at 1000 RPM for 5 minutes, and the supernatant was aspirated to remove any residual dimethylsulfoximine (DMSO) from freezing. The cell pellet was resuspended in pre-warmed media and then used to seed a 40 mL working volume culture at $3x10^5$ cells/mL. This culture was allowed to grow for 3 days before being reseeded into a fresh 40 mL working volume culture for experimentation.

5.2.2 Isotope Labeling Experiment (ILE)

Eight flasks were seeded for the ILE, two per feeding condition (labeled glucose, unlabeled glucose, labeled galactose, unlabeled galactose). Viable cell density (VCD), viability, glucose, lactate, amino acid, and titer measurements were taken daily from all flasks. If feeding occurred, metabolite samples were taken both before and after the feed. All eight flasks received a bolus of glucose such that the glucose concentration increased by 10 mM and a bolus of BRX, a proprietary glucose-free amino acid feed from Janssen, on day 3. When the residual glucose reached 10 mM after the day 3 feed, each flask received a bolus of feed such that the glucose or galactose concentration increased by 20 mM. This bolus contained either [1,2-$^{13}C_2$]glucose, unlabeled glucose, [1,2-$^{13}C_2$]galactose, or unlabeled galactose, and marked the beginning of the ILE. After this tracer feed, samples were taken every 12 hours until viability dropped below 90%, which occurred after 60 hours. Sampling consisted of both spent media and quenched cell pellets. For media samples, 1 mL of culture was removed and centrifuged to remove cells. The supernatant was transferred

to a new microcentrifuge tube and stored at -80°C util further analysis. Cold-quenching of cell pellets was performed as previously described [22]. A quenching solution of 60% methanol and 40% ammonium bicarbonate (0.85% w/v solution in water) was pre-chilled to at least -40°C in a 4.5 M $CaCl_2$ bath. Sampling volume was calculated such that $5x10^6$ cells were harvested per sample; this volume was added to a volume of quenching solution equal to 5 times the sample volume. Samples were then centrifuged at 0°C at 1000 RCF for 1 minutes. One mL of supernatant was retained for metabolite leakage analysis, while the rest was removed and cell pellets were stored at -80°C until further analysis.

5.2.3 Extraction and derivatization of intracellular metabolites

Extraction and derivatization of metabolites were performed as previously described [22]. In brief, 6 mL of a 2:1 mixture of chloroform and methanol at -20°C was added to each quenched cell pellet. This solution was vortexed for 30 min at 4°C. Next, 1.5 mL of 4°C water and 6 μL of a 10 mM norvaline internal standard solution were added. Samples were again vortexed for 5 min at 4°C. The resulting suspension was centrifuged at 4000 RCF for 20 minute at 4°C. The upper aqueous phase was transferred to a microcentrifuge tube and allowed to dry under air flow overnight.

For LC-MS/MS analysis, the dried sample was resuspended in the mobile phase (described below), centrifuged at 14,000 RPM for 10 min to remove any solid debris, and transferred to a vial For GC-MS analysis, The dried sample was dissolved in 50 μL of methoxyamine reagent (Pierce; Rockford, IL) and sonicated for 30 min at room temperature. The dissolved sample was incubated at 40°C for 90 minutes before adding 70 μL of MTBSTFA + 1% TBDMCS in pyridine (Pierce; Rockford, IL). The sample was then incubated for 30 min at 70°C, centrifuged at 14,000 RPM for 10 min to remove any solid debris, and then transferred to a vial.

5.2.4 Extraction and derivatization of extracellular metabolites

Since glucose and galactose are isomers, they cannot be differentiated based on molecular weight and therefore must be fully resolved chromatographically for GC-MS analysis. Three different glucose derivatization methods—aldonitrile pentapropionate (Aldo), di-*O*-isopropylidene propionate (DIO) and methyloxime pentapropionate (MOX)—were tested on standards containing either glucose or galactose. The samples were run using the same GC parameters to evaluate differences in retention time (RT) [23]. As shown in Figure 5.2, DIO derivatization resulted in the greatest difference in RT. Media samples containing [1,2-$^{13}C_2$]glucose and [1,2-$^{13}C_2$]galactose were derivatized using the DIO method, as described previously [24].

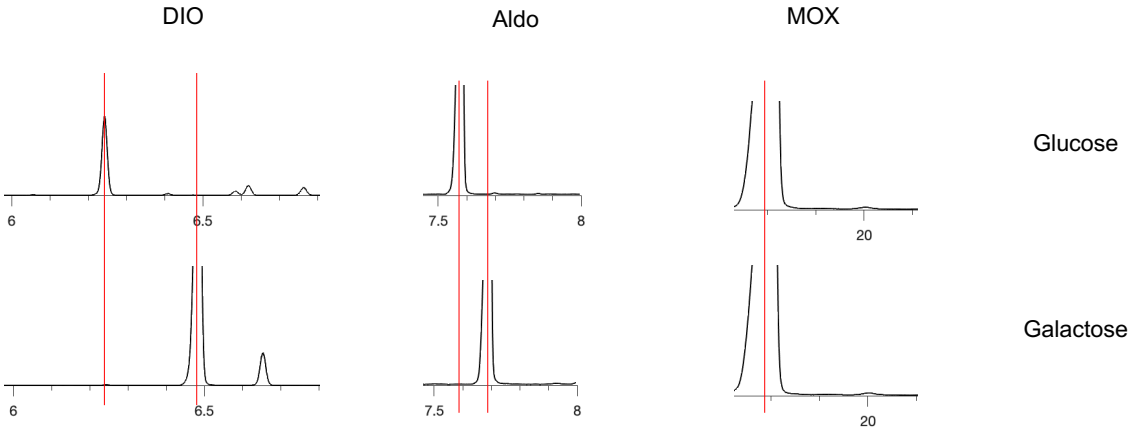

Figure 5.2: **Comparison of three different derivatization methods for glucose and galactose.** The DIO, Aldo, and MOX derivatization methods were tested.

5.2.5 Gas chromatography-mass spectrometry (GC-MS)

As described previously [24], derivatized extracts were injected into an Agilent 7890A gas chromatograph with an Agilent HP-5ms column (30m x 0.25 mm i.d. x 0.25μm) connected to an Agilent 5977B MSD. TBDMS-derivatized cell pellet samples were injected at a sample volume of 1 μL using a split ratio of 5:1 and a column flow rate of 1 mL/min. The oven program was as follows: held at 80°C for 1 min, increased at a rate of 20°C/min to 140°C, increased at a rate of 4°C/min from 140°C to 234°C, held at 234°C for 5 min,

then increased to 285°C at a rate of 20°C/min. The gain factor was dynamically adjusted using the timed event mode to account for a wide range of metabolite concentrations in the cell pellets. DIO-derivatized media samples were analyzed using the same injection volume and column flow rate, but with a 30:1 split ratio. The oven program was as follows: held at 80°C for 1 min, increased from 80°C to 220°C at a rate of 40°C/min, then increased from 220°C to 240°C at a rate of 10°C/min.

5.2.6 Liquid chromatrography-mass spectrometry (LC-MS/MS)

An LC-MS/MS based method was developed to quantify labeling patterns in nucleotide sugars (NT-sugars); the development process is described in more detail in Section 5.3.1. For the LC, a Shimadzu LC-30AD with SIL-30AC autosampler was used with a Waters XSelect HSS T3 XP column (100 Å, 2.5 μm, 2.1 mm X 150 mm) connected to an AB Sciex QTrap 6500 mass spectrometer. The mobile phase (solvent A) consisted of 10 mM tributylamine (Sigma Aldrich; St. Louis, MO) and 10 mM glacial acetic acid in a solution of 97:3 v/v H_2O/methanol. The stationary phase (solvent B) consisted of 100% isopropanol. Extracted samples resuspended in 100 μL of solvent A were injected at a sample volume of 10 μL onto a column equilibrated with solvent A at 50°C and a total flow of 0.3 mL/min The elution gradient was based on the those reported by Nakajima et al. [25] and McCloskey et al. [26] and is shown in Table 5.1. Eluate from the LC was ionized in negative mode by passing through an electrospray ionization (ESI) source and then introduced into the MS. MS parameters were as follows: scan range of 50-900 Da, negative polarity, temperature of 500°C, scan rate of 1000 Da/sec, and a detection window of 240 seconds.

Time (min)	Solvent B concentration (%)
0	0
15	0
35	20
36	100
50	100

Table 5.1: **Elution gradient for LC-MS/MS Method.**

5.2.7 Determination of growth and extracellular uptake rates

A Cedex XS automated counter (Roche; Basel Switzerland) was used to measure viable cell densities (VCDs) and percent viabilities. Amino acid concentrations in the media were measured using an Agilent 1200 series high performance liquid chromatograph (HPLC) as described previously [22]. Medium glucose, lactate, glutamate, and glutamine concentrations were measured using a YSI 2950 biochemical analyzer (YSI; Yellow Springs, OH). Galactose concentrations were measured using an enzyme based galactose assay, according to the manufacturer's protocols (Abcam; Cambridge, UK). MAb titers were measured using an OCTET RED96 (Sartorius; Aubagne, France) with Protein A Dip and Read sensors (Sartorius; Aubagne, France). Samples were run against a protein-specific standard curve to measure titer. All dilutions were made in phosphate-buffered saline (PBS, Gibco; Waltham, MA). Net growth rates, death rates, and extracellular fluxes were calcualted using the ETA software package [27] as previously described [22].

5.2.8 Metabolic network model

A previously published metabolic network model [24] was adapted to include biosynthesis reactions for nucleotides and nucleotide sugars. The model contained 108 reactions representing glycolysis, the pentose phosphate pathway (PPP), the tricarboxylic acid (TCA) cycle, amino acid catabolism, cell growth, IgG biosynthesis, and nucleotide and nucleotide

sugar biosynthesis. A full list of reactions is provided in Tables 5.A1 and 5.A2.

5.2.9 Carbon-13 metabolic flux analysis (^{13}C MFA)

The INCA software package [28] (publically available at http://mfa.vueinnovations.com) was used to fit the experimental data to the metabolic model, as previously described [22]. Fluxes were regressed using the Levenberg-Marquardt optimization algorithm. A minimum of 50 restarts from random initial guesses were used for each flux estimation to ensure a global minimum was found. Flux results were subjected to a chi-squared statistical test to assess goodness of fit, and 95% confidence intervals were calculated for each flux value using the parameter continuation function in INCA.

5.2.10 Statistical analysis

One-way ANOVA was used to determine statistical significance between feeding conditions (α = 0.05). A Tukey multiple comparison test was applied if significant differences were detected. The standard error of the mean (SEM) was estimated for intracellular fluxes using the formula SEM = (UB-LB)/3.92, where UB and LB represent the upper and lower bounds of the 95% confidence intervals, respectively, and 3.92 is the number of standard deviations that span the 95% confidence interval of a normally distributed random variable.

5.3 Results and Discussion

5.3.1 Development of LC-MS/MS method to measure nucleotide sugar (NT-sugar) labeling

In order to measure the labeling patterns of NT-sugars, a mass spectrometry (MS) method had to be developed. Liquid-chromatography (LC) is a popular method for the separation of samples and can be advantageous over gas-chromatography (GC) based methods. Molecules do not need to be volatile in order to be analyzed, removing the derivatization step necessary for GC analysis. Also, the solutions used in LC separation can be easily changed and optimized for different types of metabolites. Upon eluting from the LC col-

umn, the sample then flows into an MS where the metabolites in the sample are ionized and detected. Different metabolites are distinguished by the mass-to-charge (m/z) ratio of the ions produced. For our method development, we used an AB Sciex Qtrap 6500 MS, which is a triple quadrupole instrument. This means there are three chambers the ions must pass through before being detected, two of which are mass selective filters, resulting in this technique being called LC-MS/MS. The first quadrupole is a mass filter where a desired "parent ion" m/z can be selected. The parent ion is then passed to the second quadrupole where it is subjected to large amounts of energy via the introduction of a collision gas, which fragments the parent ion into daughter ions. Finally, the third quadrupole selects daughter ions based on their m/z before passing them to the detector. The third quadrupole in this case is an ion trap, which allows for the detection of multiple daughter ions concurrently. Due to our interest in labeling which results in multiple mass isotopmers, this capability is a necessary component to achieve high-quality data from our experiments, but this can be achieved with a standard triple-quad instrument as well.

First, standards containing the metabolites of interest were directly injected into the MS in order to optimize the acquisition parameters. Through direct injection, the declustering potential (DP), entrance potential (EP), and collision energy (CE) were tuned to ensure that the parent ion was fragmented and daughter ions were identifiable. If these values are too high, the parent ion and daughter ions will be fragmented to the point that they are unidentifiable; if they are too low, little fragmentation of the parent ion will occur. Based on the daughter ion masses and the known structure of the parent ion, the structures of the daughter ions were determined. Metabolites of interest were selected based on previous reports of NTs and NT-sugars detected in CHO cells [29]. For the 11 NTs and NT-sugars initially characterized, the mass spectra and unique daughter ions for each metabolite are shown in Appendix Figures 5.A1 through 5.A11. Unique daughter ions were identified as fragments that result from only one possible fragmentation of the parent ion. Additionally, the optimized parameters for the 8 NT-sugars determined from direct injection of standards

are summarized in Table 5.2.

Metabolite	Fragment	Mass	RT	Carbons	DP	EP	CE
UDP-GlcA	Parent	579	19.97	1-15	-60	-5	-45
	Daughter 1	403		1-9			
	Daughter 2	255		10-15			
GDP-Glc	Parent	604	15.76	1-16	-60	-5	-45
	Daughter 1	362		1-10			
	Daughter 2	241		11-16			
GDP-Fuc	Parent	588	16.1	1-16	-60	-5	-45
	Daughter 1	424		1-10			
	Daughter 2	305		11-16			
UDP-Glc/UDP-Gal	Parent	565	15.75	1-15	-60	-5	-45
	Daughter 1	385		1-9			
	Daughter 2	241		10-15			
UDP-GlcNAc/UDP-GalNAc	Parent	606	15.76	1-17	-60	-5	-50
	Daughter 1	385		1-9			
	Daughter 2	362		10-17			
CMP-NeuAc	Parent	617	5.91	1-20	-60	-5	-20
	Daughter 1	322		12-20			
	Daughter 2	290		1-11			

Table 5.2: **Optimal LC-MS/MS parameters determined for the 8 NT-sugars.** Daughter ions were identified from fragmentation mass spectra from direct injection of standards into the MS. The structures and carbons present in the daughter ions were determined using the Fragmentation Tool in ChemDraw. Optimal MS parameters for each metabolite were also determined from direct injection. Retention times (RT) were determined from running individual standards on the LC-MS/MS. RT, retention time; DP, declustering potential; EP, entrance potential; CE, collision energy.

After MS parameters were optimized by direct injection into the MS, standards contain-

ing each individual metabolite of interest were injected into the LC system to determine retention times. Our initial goal was to resolve the different isomers of NT-sugars (e.g., UDP-glucose and UDP-galactose or UDP-GlcNAc and UDP-GalNAc). This has been previously reported in studies where only the concentration of the NT-sugar was desired [30]. For example, Nakajima et al. were able to successfully resolve UDP-Gal and UDP-Glc with an RT difference of 0.8 minutes and UDP-GlcNAc and UDP-GalNAc with an RT difference of 0.6 minutes [31]. This separation was achieved using HPLC connected to an absorbance detector, which allowed for concentrations to be determined based on a standard curve. Del Val et al. reported separations of 0.4 minutes for UDP-Glc and UDP-Gal and 0.2 minutes for UDP-GlcNAc and UDP-GalNAc [29]. Again, this separation was achieved using HPLC and an absorbance detector for the purpose of determining concentrations. One study has shown successful separation of NT-sugar isomers with UHPLC connected to a linear ion trap-orbitrap MS, but they found that RT differences were highly dependent on extensive column rinsing (3 hrs. between sample injections), and RTs were not stable during long runs [32]. The use of MS based methods to measure labeling in NT-sugars has been reported [25], where different hexose isomers were measured together (e.g., UDP-Gal and UDP-Glc as UDP-Hex). Ultimately, we were unable to resolve the NT-sugar isomers sufficiently by RT and instead used the combined MIDs for subsequent analysis.

5.3.2 Development of feeding strategy for 5466A suspension CHO cells

For this study, a new glutamine synthetase knockout (GS-KO) IgG producing CHO cell line was used. Therefore, a feeding strategy that allowed for cell growth without the depletion of key nutrients needed to be developed. An experiment was devised to compare eight different feeding schemes to an unfed control, as summarized in Table 5.3. As shown in Figure 5.3, the viability in the unfed flask dropped dramatically after day 5. Meanwhile, flasks that were fed a bolus to increase the glucose concentration by 10 mM on day 5 had a drop in viability after day 7. Flasks that were fed a bolus to increase the glucose

concentration by 20 mM on day 5 maintained high viabilities to day 8 of culture.

Flask	Day 3: +10 mM glucose	Day 3: +BRX	Day 5: +10 mM glucose	Day 5: +20 mM glucose	Day 5: +BRX
1					
2	X		X		
3	X	X	X		
4	X		X		X
5	X	X	X		X
6	X			X	
7	X	X		X	
8	X			X	X
9	X	X		X	X

Table 5.3: **Summary of the different feeding schemes tested.** An unfed control flask was compared to eight different feeding schemes. All flasks received a bolus of glucose that increased the glucose concentration by 10 mM on day 3. On day 5, half the flasks received a bolus of glucose that increased the glucose concentration by 10 mM, while the other half received a bolus that increased the glucose concentration by 20 mM. Additionally, half the flasks received a bolus of BRX, a proprietary glucose-free amino acid feed provided by Janssen, on either day 3 or day 5.

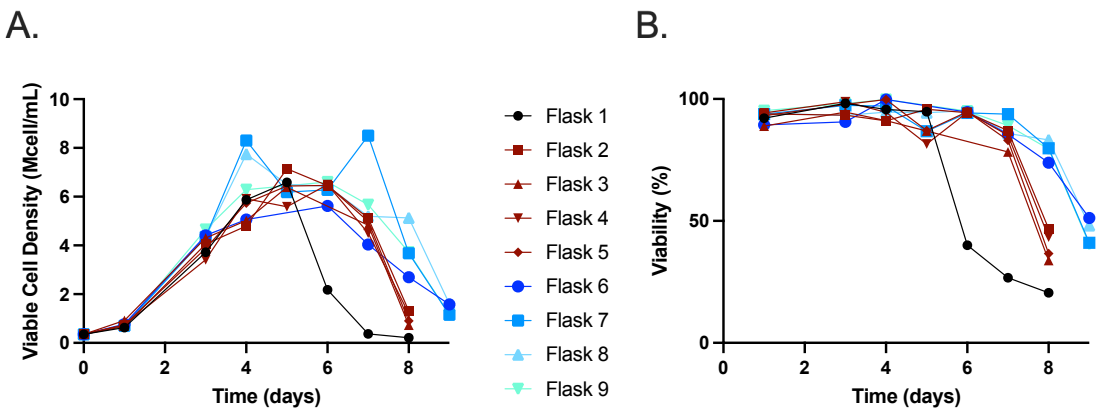

Figure 5.3: **VCD and viability of the different feeding schemes.** The VCD and viability for each of the different feeding schemes over the course of the experiment are shown. Flask 1 contained the unfed control culture, flasks 2-5 were fed a bolus of +10 mM glucose on day 5, and flasks 6-9 were fed a bolus of +20 mM glucose on day 5.

As shown in Figure 5.4A, glucose was completely depleted in the unfed reactor by day 5; this likely caused the observed drop in viability. Similarly, the flasks fed a bolus to increase glucose by 10 mM on day 5 also depleted glucose by day 7, coinciding with a drop in viability. By day 8 of culture, residual glucose levels were still around 8 mM in the flasks fed a bolus to increase glucose by 20 mM on day 5. Based on these results, it was decided that a bolus feed to increase glucose by 20 mM on day 5 would allow cultures to maintain viability throughout a proposed 2-3 day labeling study. Other figures only present the data for the +20 mM flasks, for clarity.

Figure 5.4B shows lactate concentrations over the course of the culture. Interestingly, flasks 8 and 9, which received the BRX feed on day 5, exhibit a switch back to lactate production after the day 5 feed. This appears to indicate a shift in metabolism as a result of the BRX feed on day 5. This is further corroborated by an increase in glutamine production after the BRX feed (Figure 5.4D). Due to the apparent shift in metabolism after the day 5 BRX feed, it was decided that BRX should not be fed on this day for any future labeling studies. For flasks 6 and 7, which did receive not BRX on day 5, lactate and glutamine profiles were fairly similar. The main difference between these flasks appears in the glutamate profile, where flask 6 (which did not receive BRX at all) switches to glutamate production

after day 5, while flask 7 (which only received BRX on day 3) maintains a low but fairly constant consumption of glutamate throughout the culture (Figure 5.4C). Based on these results, the feeding scheme used for flask 7 (Table 5.3) was determined to be optimal for the labeling study described below.

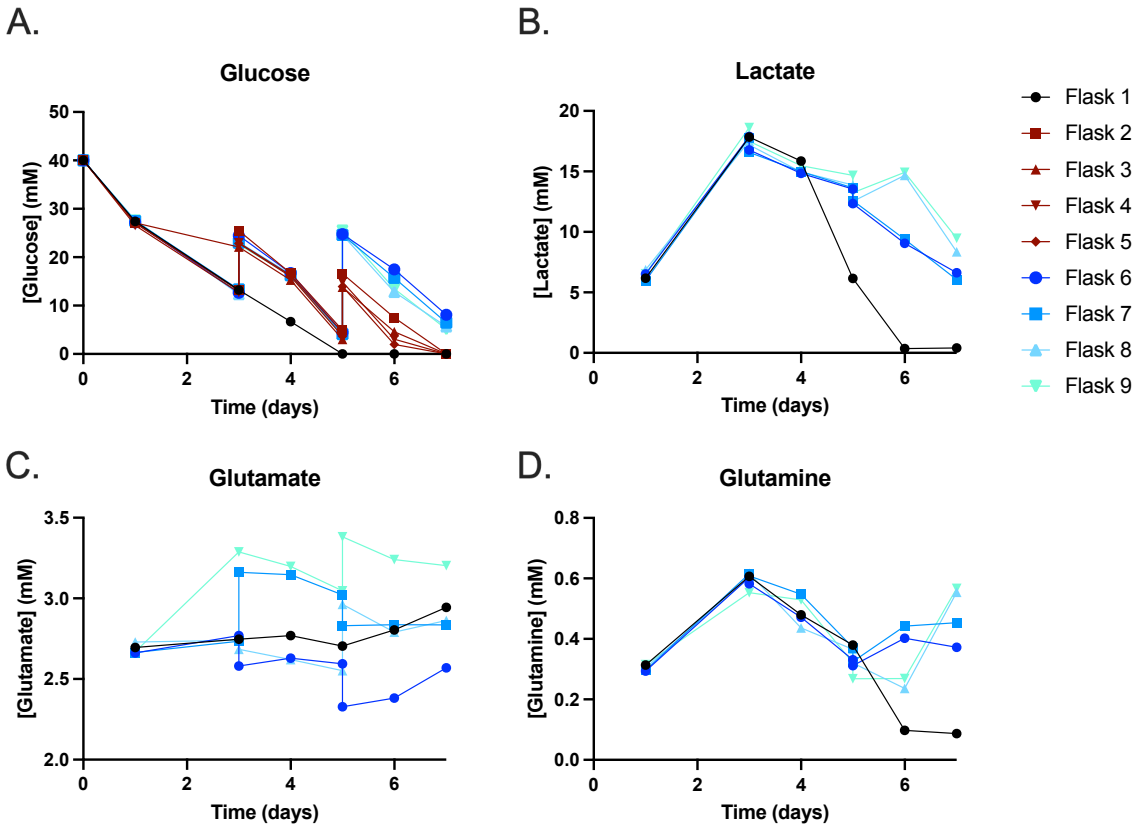

Figure 5.4: **Metabolite profiles for the different feeding schemes.** The concentration profiles for (A) glucose, (B) lactate, (C) glutamate, and (D) glutamine over time are shown for each feeding scheme. Feeding occurred on days 3 and 5 and consisted of a bolus of glucose and/or a glucose-free amino acid feed, as outlined in Table 5.3. For clarity, only flasks 1 and 6-9 are shown in panels (B), (C), and (D).

5.3.3 Growth is not altered by galactose feeding during early stationary phase

Galactose feeding has been implemented as a way to reduce lactate production, since galactose feeding reduces glycolytic fluxes and thereby reduces the need to divert excess flux towards lactate production. This is hypothesized to be due to the extra steps required for galactose to enter glycolysis. While reduced lactate production is a desirable characteris-

tic, it has also been reported that galactose supplementation can lead to reduced cell growth [20]. Therefore, it was decided that galactose would not be fed until stationary phase had been reached, to ensure that peak VCDs would be achieved before galactose was introduced. As shown in Figure 5.5A, there was little difference in VCD between glucose and galactose fed cultures until the final time point. Viability was also very similar in both cultures until the final time point (Figure. 5.5B). Growth rates during exponential phase, before galactose addition, were unchanged (Figure 5.5C). Overall, by allowing cells to grow exclusively on glucose before galactose addition, peak VCDs were not dependent on feeding condition; also, VCDs and viabilities were not affected by galactose feeding until the final time point of culture.

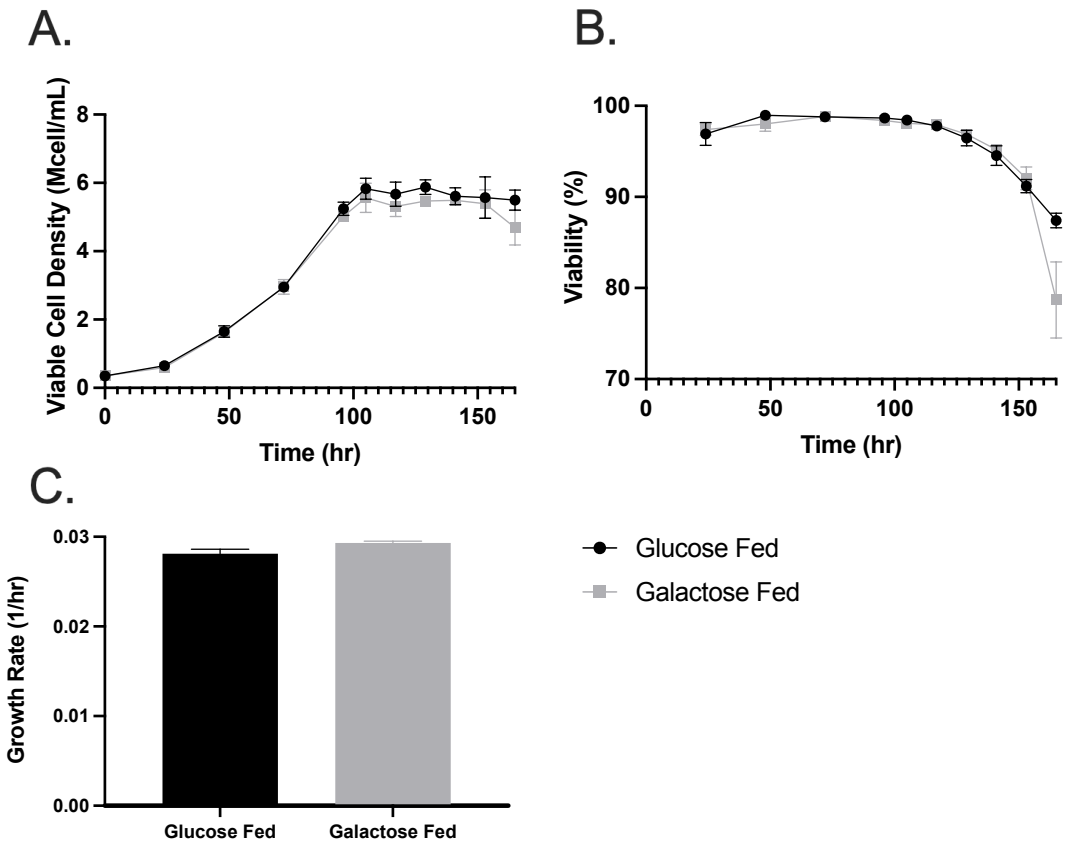

Figure 5.5: **Growth characteristics of glucose and galactose fed cultures.** The (A) VCDs and (B) viabilities were measured every day until day 4, after which they were measured every 12 hours. (C) Exponential growth rates were calculated based on the data from 24 to 96 hrs. Data represent means ± SEM. n=4.

5.3.4 Carbon source consumption is altered in galactose fed cultures

The concentration profiles for glucose, galactose, and lactate are shown in Figures 5.6A-C, respectively. Glucose profiles were identical across all cultures until the feed addition at 105 hr., after which time the galactose fed cultures consumed glucose until its depletion at 141 hr., while the glucose fed cultures maintained a consistent glucose consumption rate after feeding. Galactose was not present in the cultures before the feed additions at 105 hr. The consumption of galactose did not begin until 12 hours after the feed addition, but a consistent galactose consumption rate was maintained after that point. The lactate profiles exhibited the classic "lactate switch", where production of lactate occurred mostly during exponential phase, after which it plateaued before a switch to lactate consumption during stationary phase. While both the glucose and galactose fed cultures consumed lactate, the galactose fed cultures consumed lactate at a higher rate.

Specific carbon-mole consumption rates for glucose, lactate, and galactose are shown in Figure 5.6D. For the galactose fed cultures, these rates are broken down into two phases: the first phase before glucose was depleted (with glucose, from 105 hr. to 141 hr.) and then the second phase after glucose was depleted (no glucose, from 141 hr. to 165 hr.) Before glucose was depleted, the glucose and lactate consumption rates were effectively the same in the glucose and galactose fed cultures. Galactose consumption in the presence of glucose increased the total uptake in the galactose fed cultures. After glucose depletion, both the lactate and galactose consumption rates increased, and the total consumption rate was similar to the total consumption rate of the glucose fed culture. While it appears that galactose is a supplementary carbon source in the presence of glucose, the consumption rates of galactose and lactate increase after glucose depletion to compensate for the loss of glucose.

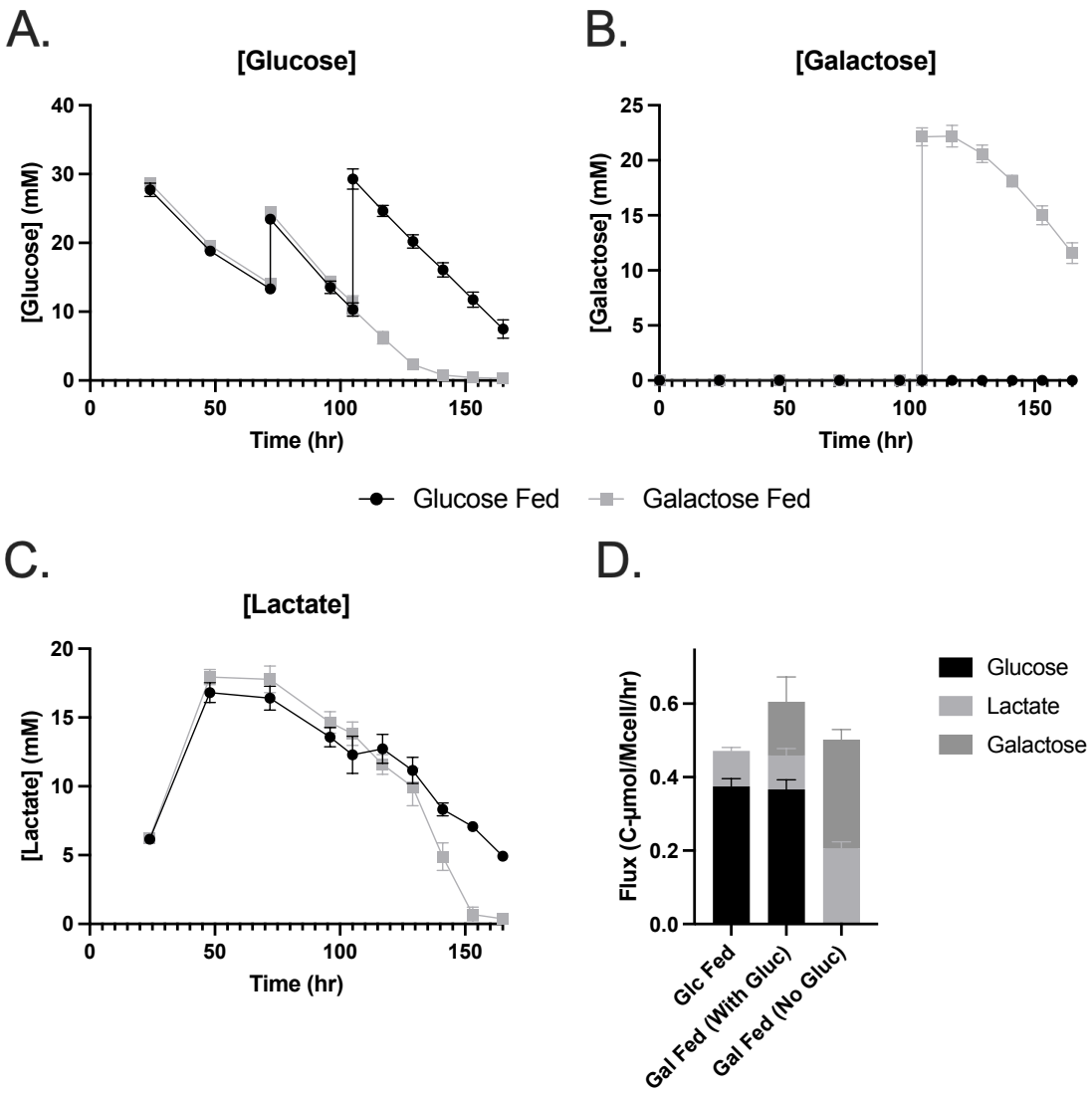

Figure 5.6: **Concentration profiles and consumption rates of glucose, galactose, and lactate.** The concentrations of (A) glucose, (B) galactose, and (C) lactate were measured throughout the culture duration. The (D) consumption rates were calculated after feed addition on day 5. For the galactose fed cultures, consumption rates were calculated for the time periods before (with gluc) and after (no gluc) glucose depletion. Data represent the means ± SEM. n=4.

The consumption and production rates of amino acids after the day 5 feed were also calculated (Figure 5.7). Overall, the amino acid fluxes were similar in the two different feeding conditions. The significant differences occurred in alanine production and phenylalanine and threonine consumption. Alanine production was significantly higher in the

glucose fed cultures; alanine has a role similar to lactate, in that it is a byproduct produced directly from pyruvate. Since galactose feeding has been shown to reduce lactate production, by extension, reduced alanine production is not surprising. Phenylalanine was consumed more rapidly in the glucose fed cultures, while threonine was consumed at a higher rate in the galactose fed cultures. Phenylalanine is a precursor to the TCA intermediate fumarate, so lower consumption of phenylalanine could indicate reduced TCA cycle flux in the galactose fed cultures. Threonine is eventually converted to pyruvate, so the higher consumption in the galactose fed cultures could indicate the use of threonine as a secondary carbon source to fuel central carbon metabolism.

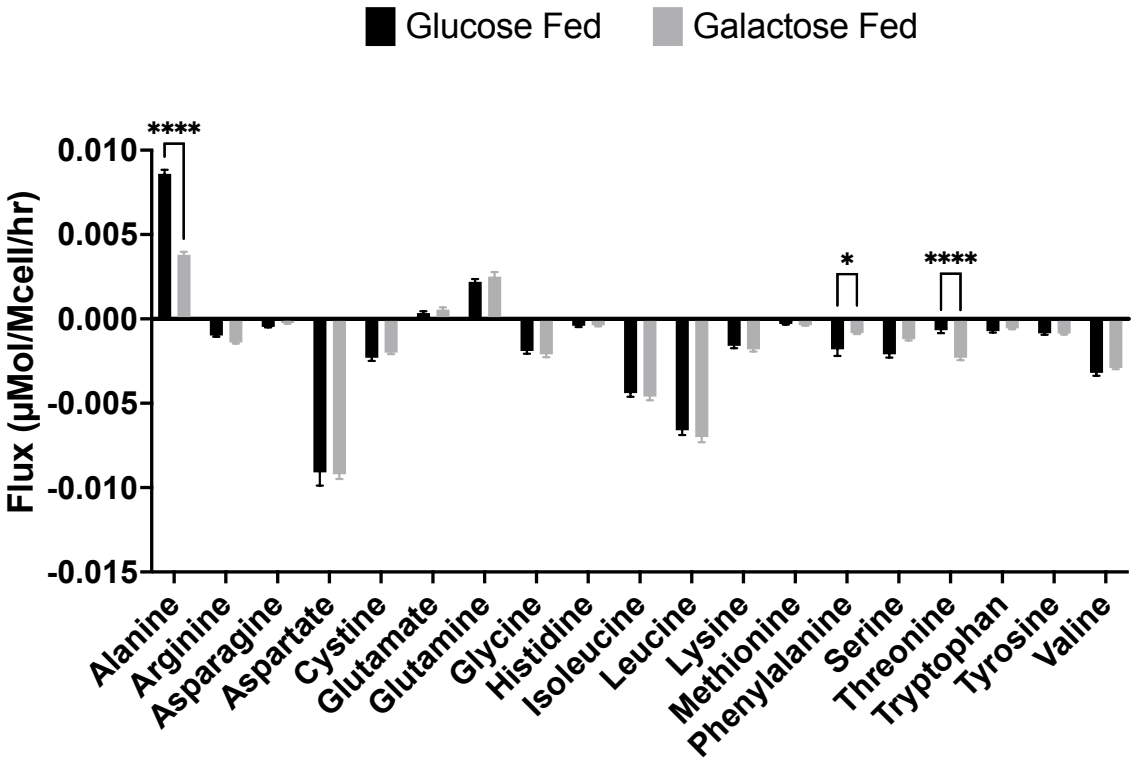

Figure 5.7: **Consumption and production rates of amino acids in glucose and galactose fed cultures.** The specific flux rates of the 19 measured amino acids were calculated using the ETA software package. Positive flux values indicate production while negative flux values indicate consumption. Data represent the means ± SEM. n = 4. Significance was determined by a two-way ANOVA with a Tukey post-hoc test. $^{*} = p < 0.05, ^{****} = p < 0.001$.

5.3.5 Galactose feeding did not alter IgG production

While galactose feeding has been shown to alter glycosylation in product mAbs, it is not reported to have significant effects on IgG production [10]. This observation was further corroborated in this study. As shown in Figure 5.8A, the volumetric titer was effectively the same throughout the culture duration, both before and after feed addition. Specific productivity was also unchanged by galactose feeding (Figure 5.8B).

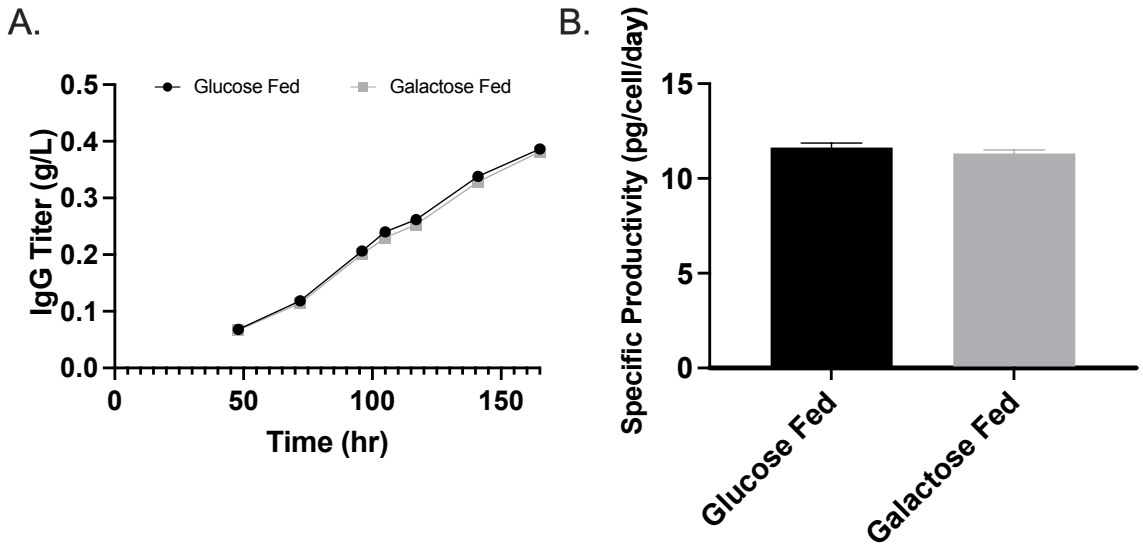

Figure 5.8: **Titer and specific productivity in glucose and galactose fed cultures.** (A) IgG titer was measured starting at 48 hrs. until the end of culture. (B) Specific productivity was calculated based on the IgG production rates after the day 5 feed addition. Data represent the means ± SEM. n=4.

5.3.6 ^{13}C MFA reveals metabolic differences between glucose fed and galactose fed cultures

^{13}C MFA was performed on galactose fed and glucose fed cultures during stationary phase. Galactose feeding led to alterations throughout central carbon metabolism. As shown in Figure 5.9A, glycolytic fluxes were lower in galactose fed cultures compared to glucose fed cultures, despite slightly increased galactose consumption (Figure 5.6D). However, fluxes throughout the TCA cycle were unaltered (Figure 5.9C). This is likely due to the increased lactate uptake in the galactose fed cultures compensating for the reduced carbon influx

from glycolysis. Fluxes through the PPP were small in magnitude (about three orders of magnitude lower than fluxes through glycolysis), but they did trend slightly higher in the galactose fed cultures (Figure 5.9B). The trend was not significant, however, due to the larger relative uncertainties in these small flux values. Other selected fluxes (Figure 5.9D) were similar, except for alanine aminotransferase (AAT) and lactate dehydrogenase (LDH). AAT flux, which catalyzes the formation of alanine from pyruvate, was higher in glucose fed cultures, and correlates with their increased alanine excretion (Figure 5.7). Meanwhile, LDH flux, which catalyzes the formation of pyruvate from lactate, was higher in the galactose fed cultures, and aligns well with their increased lactate consumption (Figure 5.6D).

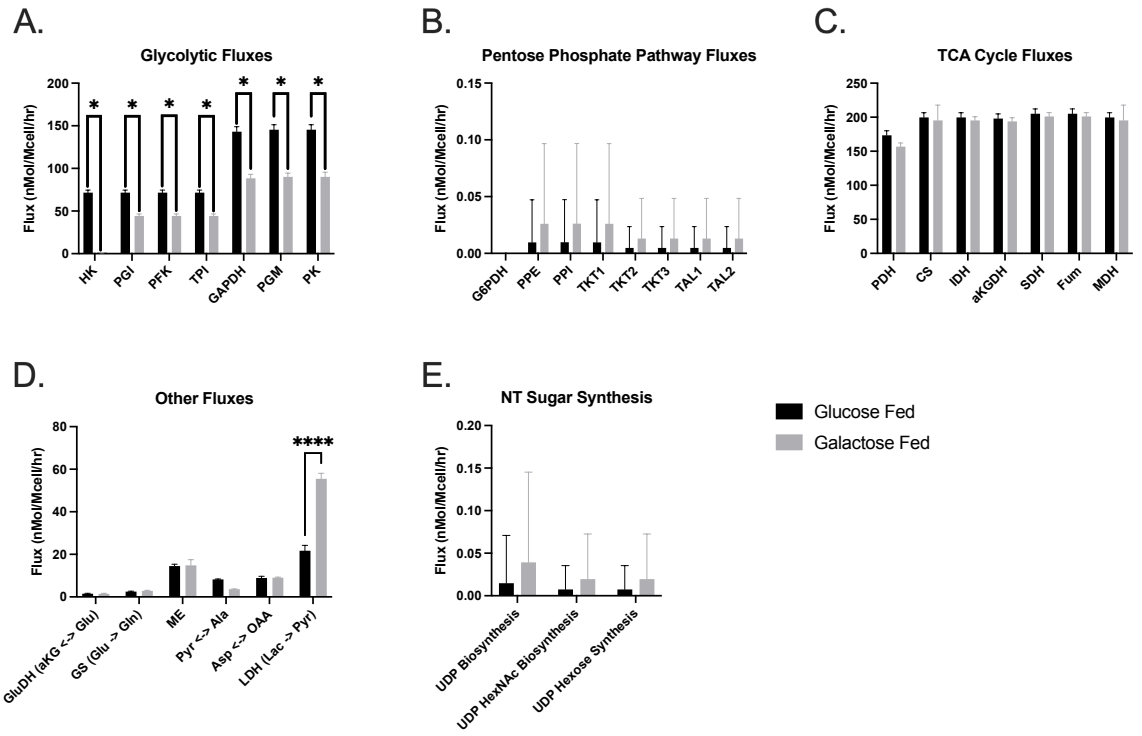

Figure 5.9: **Metabolic fluxes in glucose and galactose fed cultures.** The fluxes through (A) glycolysis, (B) the pentose phosphate pathway (PPP), (C) the TCA cycle, (D) cataplerosis and anaplerosis, and (E) nucleotide sugar synthesis are shown. Data represent the means $\pm$ SEM.

5.3.7 NT-sugar labeling is altered by galactose feeding, but fluxes through NT-sugar biosynthesis are not well-resolved

While 6 different NT-sugar standards were included in the LC-MS/MS method, as described in section 5.3.1, only two were present in high enough concentrations in the biological samples to be detected (UDP-Hexose and UDP-HexNAc). Therefore, only the measurements for these are reported.

Fluxes through NT-sugar synthesis pathways were about three orders of magnitude smaller than fluxes through glycolysis. Therefore, similar to the PPP fluxes, relative uncertainties were quite high. However, fluxes through UDP, UDP-HexNAc, and UDP-Hexose biosynthesis reactions all trended higher in the galactose fed cultures. Since galactose is metabolized by way of UDP-glucose (Figure 5.1), the increased flux through UDP and UDP-hexose biosynthesis aligns with the increased demand for UDP-glucose to metabolize galactose. These increased fluxes also correspond with the higher M2 labeling that was observed in UDP-hexose (Figure 5.10A); since a [1,2-$^{13}C_2$]galactose tracer was used, we would expect to see high levels of M2 labeling in UDP-galactose as well as its isomer, UDP-glucose.

The increased flux through UDP-HexNAc synthesis was unexpected, as labeling in UDP-HexNAc was actually lower in the galactose fed cultures, as shown by the higher fraction of M0 in Figure 5.10B. UDP-HexNAc incorporates carbon from several precursors; UDP contains carbons from aspartate and the PPP intermediate ribose-5-phosphate, the hexose portion comes from glucose or galactose, and the acetyl group originates from acetyl-CoA. It is possible that the higher glycolytic flux in the glucose fed cultures contributed to more labeling in the acetyl group despite a lower UDP-HexNAc biosynthetic flux.

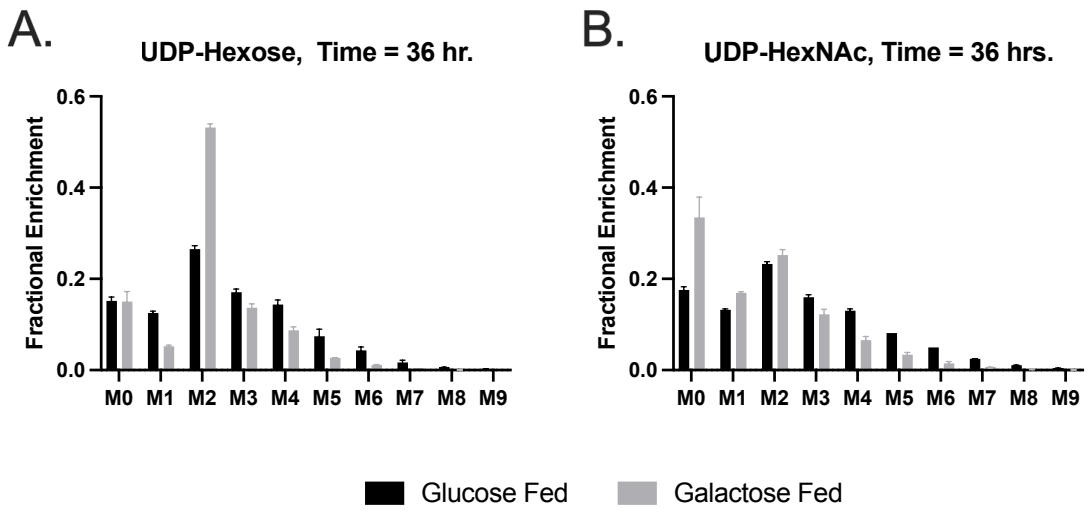

Figure 5.10: **Mass isotopomer distributions (MIDs) for UDP-Hexose and UDP-HexNAc.** The MIDs are shown for the time point 36 hours after labeling, as this was approximately halfway through the ILE. Data represent the means $\pm$ SEM. n=2.

A possible explanation for the differences in labeling lies in the pool sizes of the UDP-Hexose and UDP-HexNAc NT-sugars. The total ion count (TIC) for each daughter ion was normalized to the TIC for the internal standard, norvaline. The normalized TICs serve as a measure of the relative concentration of a metabolite in the sample. Because the daughter ions have different masses and are monitored separately, the values of the normalized TICs are different, but the trends remain the same. As shown in Figure 5.11, UDP-Hexose fragment pool sizes were significantly higher in the galactose fed reactors; this agrees well with previous studies [19, 33]. Conversely, UDP-HexNAc fragment pool sizes trend higher in the glucose fed cultures, with a significantly higher peak occurring at 48 hours after the feed. The differences in UDP-Hexose and UDP-HexNAc production, particularly the higher production of UDP-Hexose in galactose fed cultures and UDP-HexNAc in glucose fed cultures, can explain why the MIDs are so different but flux values are not.

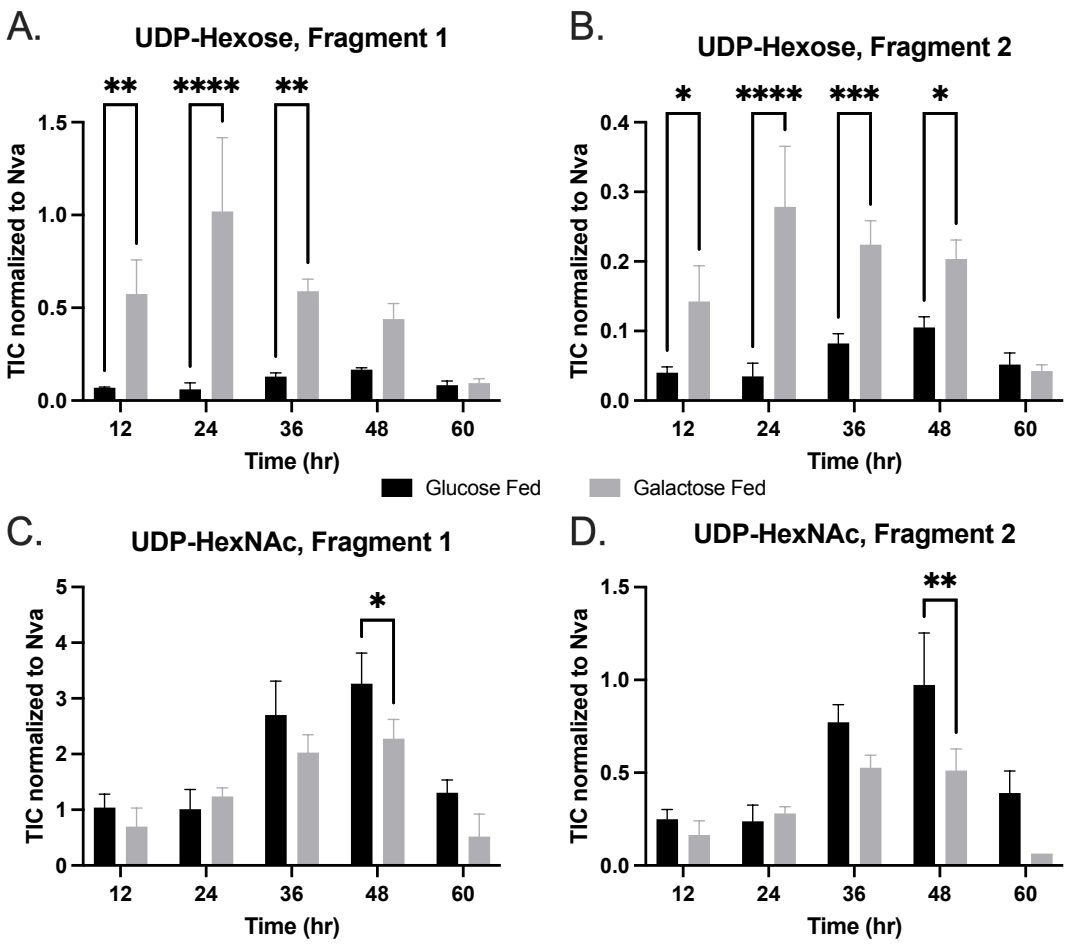

Figure 5.11: **Total ion counts (TIC) for each fragment normalized to Norvaline.** The TIC for each daughter ion fragment for UDP-Hexose and UDP-HexNAc was nromalized to the TIC for the internal standard, norvaline. Data represent the means ± SEM. n=3. TIC, total ion count; Nva, norvaline. $^{*}p < 0.05, ^{**}p < 0.01, ^{***}p < 0.001, ^{****}p < 0.0001$.

5.4 Conclusions

A metabolic model which incorporated NT and NT-sugar biosynthesis reactions was developed along with an LC-MS/MS method to measure labeling in NT and NT-sugars. This model was applied to a ^{13}C MFA study that characterized glucose and galactose fed cultures. Growth and titer were unaffected by galactose feeding, while consumption rates of glucose, lactate, and some amino acids were altered. Galactose feeding also led to reduced glycolytic fluxes, despite higher glucose and galactose consumption, but TCA cycle fluxes were unaltered. Fluxes through the PPP and NT sugar synthesis also trended higher in the

galactose fed cultures, but the magnitudes of flux through these pathways was about 1000x lower than flux through glycolysis. Differences in MIDs in the measured NT sugars were apparent, and the flux trends agreed with the observed MIDs. Overall, the model developed in this chapter provides insight into the complex relationship between central carbon metabolism and the biosynthesis of glycosylation precursors.

However, a number of improvements could be made to the workflow described herein to increase the resolution of fluxes through the NT-sugar biosynthesis pathways. First, the assessment of more metabolites that are intermediates in the NT-sugar biosynthesis pathways could help to improve the flux estimates for these pathways. Particularly, the assessment of the labeling of AcCoA, which contributes the NAc group in the UDP-HexNAc NT-sugars [25].

Additionally, further constraints on the final sink for the NT-sugars could help to increase the resolution of the fluxes through NT-sugar biosynthesis. By knowing the glycan distribution on the IgGs produced by the cells, additional terms to the antibody equation can be included that define stoichiometric coefficients for each NT-sugar based on the glycan distributions. Also, because the demand for NT-sugars on both IgGs and host cell proteins has been estimated, additional terms in the biomass equation can also be included [34]. By providing demands for how much of the NT-sugars are actually being consumed, this can help to constrain the biosynthesis reactions, increasing the resolution.

Perhaps the most interesting result of this study was the observation that, while glycolytic fluxes were reduced in the galactose fed cultures, TCA cycle fluxes were similar to those in the glucose fed cultures. While galactose feeding to reduce lactate production and alter glycan profiles has been fairly well studied in CHO cells [18, 19, 33, 20, 21], a thorough understanding of the metabolic alterations that occur during galactose-only feeding has not yet been reported. A study by Torres et al. performed metabolic flux analysis on CHO cell cultures that were co-fed galactose and lactate [35]. In this study, they also found reduced glycolytic rates in galactose fed cultures while TCA cycle fluxes were de-

pendent on both the galactose and lactate uptake, similar to what is reported here. Since glycolysis and lactate are two major sources of pyruvate, which then enters the TCA cycle, it does make sense that TCA cycle fluxes would be similar in magnitude to the summation of glycolytic fluxes and lactate uptake.

Overall, this study provides a novel metabolic model for CHO which incorporates NT and NT-sugar biosynthesis reactions alongside central carbon metabolism. Additionally, a novel LC-MS/MS method to measure MIDs in NT-sugars was also developed. While further improvements to the model and data collection workflow can be made, the data presented herein provide insights into the metabolic alterations that occur during galactose feeding and can be used to guide further experimentation to improve the resolution of flux estimations in NT-sugar biosynthesis pathways.

5.5 Appendix

Pathway	Enzyme	Reaction
Glycolysis	HK	Glc ↔ G6P
	PGI	G6P ↔ F6P
	PFK	F6P → DHAP + GAP
	TPI	DHAP ↔ GAP
	GAPDH	GAP ↔ 3PG
	PGM	3PG ↔ PEP
	PK	PEP → PYR.C
	LDH	PYR.C ↔ LAC
PPP	G6PDH	G6P → Ru5P
	PPE	Ru5P ↔ X5P
	PPI	Ru5P ↔ R5P
	TKT1	X5P ↔ EC2 + GAP
	TKT2	F6P ↔ EC2 + E4P
	TKT3	S7P ↔ EC2 + R5P
	TAL1	F6P ↔ EC3 + GAP
	TAL2	S7P ↔ EC3 + E4P
TCA Cycle	PDH	Pyr.m → AcCoA.m + CO2
	CS	OAA.m + AcCoA.m → Cit.m
	IDH.m	Cit.m ↔ aKG.m + CO2
	aKGDH	aKG.m → Suc.m + CO2
	SDH	Suc.m ↔ Fum.m
	FUS	Fum.m ↔ Mal.m
	MDH.m	Mal.m ↔ OAA.m
Anaplerosis	ME	Mal.m → Pyr.m + CO2
	PC	Pyr.m + CO2 → OAA.m
	ATP CS	Cit.c → AcCoa.c + OAA.c
	PEPCK	OAA.c → PEP + CO2
	IDH.c	Cit.c → aKG.c + CO2
	GOT1	OAA.c ↔ Asp.c
	Carboxylase	ProCoA + CO2 → Suc.m
	MDH.c	OAA.c ↔ Mal.c
Amino Acid Metabolism	GS	Gln ↔ Glu.m
	GluDH	aKG.m ↔ Glu.m
	AsnS	Asn → Asp.c
	SHMT	Ser ↔ Gly + C1
	PGHDH	3PG ↔ Ser
	GlyS	CO2 + C1 ↔ Gly
	ALT	Pyr.c ↔ Ala.c
	Histidase	His → C1 + Glu.c
	PAH	Phe → Tyr
	TDO	Trp → CO2 + CO2 + Ala.c + aKetoadi
	AA Intermediates	aKetoadi → CO2 + CO2 + AcCoA.m + AcCoA.m
	SBCAD	Ile → AcCoA.m + CO2 + ProCoA
	IVD	Leu + CO2 → CO2 + AcCoA.m + AcCoA.m + AcCoA.m
	IBD	Val → CO2 + CO2 + ProCoA
	AASS	Lys → aKetoadi
	ARGS	Arg → Glu.c + Urea
	MAT	Met + Ser → C1 + Cys + ProCoA + Co2

Table 5.A1: **List of reactions included in metabolic model, Part 1.**

Pathway	Enzyme	Reaction
NT and NT-sugar biosynthesis	Carbamoyl Phosphate Synthase	Gln + HCO3 -> Glu.c + CarbomylPhos
	Asp Carbamoyltransferase	CarbomylPhos + Asp.c -> NCarbLAsp
	Dihydroorotase	NCarbLAsp <-> Orotate
	Orotate PRT	Orotate + PRPP -> Orit5Phos
	O5P Decarboxylase	Orit5Phos -> UMP + CO2
	UMP Kinase	UMP -> UDP
	UDP Kinase	UDP <-> UTP
	Gln-F6P Transaminase	F6P + Gln -> Glc6P + Glu.c
	Glc6P Acetyltransferase	Glc6P + AcCoA.c -> GlcNAc6P
	NAcP Mutase	GlcNAc6P <-> GlcNAc1P
	NAcP Uridylytransferase	GlcNAc1P + UTP -> UDPGlcNAc
	UDPGlcNAc Epimerase	UDPGlcNAc <-> UDPGalNAc
	Glycan sink	UDPGlcNAc + UDPGalNAc + UDPGal + UDPGlc -> glycans
	Labeled Gal	Gal.l -> Gal.e
	Unlabeled Gal	Gal.u -> Gal.e
	Gal uptake	Gal.e -> Gal
	Galactosekinase	Gal -> Gal1P
	UDPgal uridylytransferase	UDPGlc + Gal1P -> UDPGal + G1P
	UDPGlc Epimerase	UDPGal <-> UDPGlc
	Phosphoglucosemutase	G1P <-> G6P
	UDPGlc pyrophosphorylase	G1P + UTP -> UDPGlc
	Ribose-phosphate pyrophosphokinase	R5P -> PRPP
Transport	Glucose	Glc.e → Glc
	Mal.m	Mal.c ↔ Mal.m
	aKG.m	aKG.m ↔ aKG.c
	Glu.m	Glu.c ↔ Glu.m
	Asp.m	Asp.m ↔ Asp.c
	Cit.m	Cit.m → Cit.c
	Lys	Lys.e → Lys
	Thr	Thr.e → Thr
	Phe	Phe.e → Phe
	Tyr	Tyr.e → Tyr
	Val	Val.e → Val
	Leu	Leu.e → Leu
	Ile	Ile.e → Ile
	Trp	Trp.e → Trp
	His	His.e → His
	Met	Met.e → Met
	Ser	Ser.e ↔ Ser
	Ala	Ala.c ↔ Ala.e
	Arg	Arg.e ↔ Arg
	Asp	Asp.c ↔ Asp.e
	Cys	Cys.e ↔ Cys
	Glu	Glu.c ↔ Glu.e
	Gln	Gln ↔ Gln.e
	Gly	Gly.e ↔ Gly
	Pro	Pro.e ↔ Pro
	Asn	Asn.e ↔ Asn
	Lac	Lac ↔ Lac.e
Antibody Production		0.033*Ala.c + 0.016*Cys + 0.031*Asp.c + 0.031*Glu.c + 0.021*Phe + 0.04*Gly + 0.013*His + 0.018*Ile + 0.047*Lys + 0.053*Leu + 0.007*Met + 0.026*Asn + 0.049*Pro + 0.031*Gln + 0.016*Arg + 0.078*Ser + 0.059*Thr + 0.058*Val + 0.012*Trp + 0.029*Tyr → Antibody
Biomass Production		0.438*Ala.c + 0.2752*Arg + 0.2621*Asp.c + 0.2102*Asn + 0.1058*Cys + 0.2351*Gln + 0.2818*Glu.c + 0.3927*Gly + 0.1044*His + 0.2365*Ile + 0.4117*Leu + 0.4161*Lys + 0.1007*Met + 0.1599*Phe + 0.2285*Pro + 0.3139*Ser + 0.2818*Thr + 0.03212*Trp + 0.1329*Tyr + 0.3037*Val + 0.2106*G6P + 0.17*R5P + 0.17*C1 + 0.0868*DHAP + 1.807*AcCoA.c → Biomass

Table 5.A2: **List of reactions included in metabolic model, Part 2.**

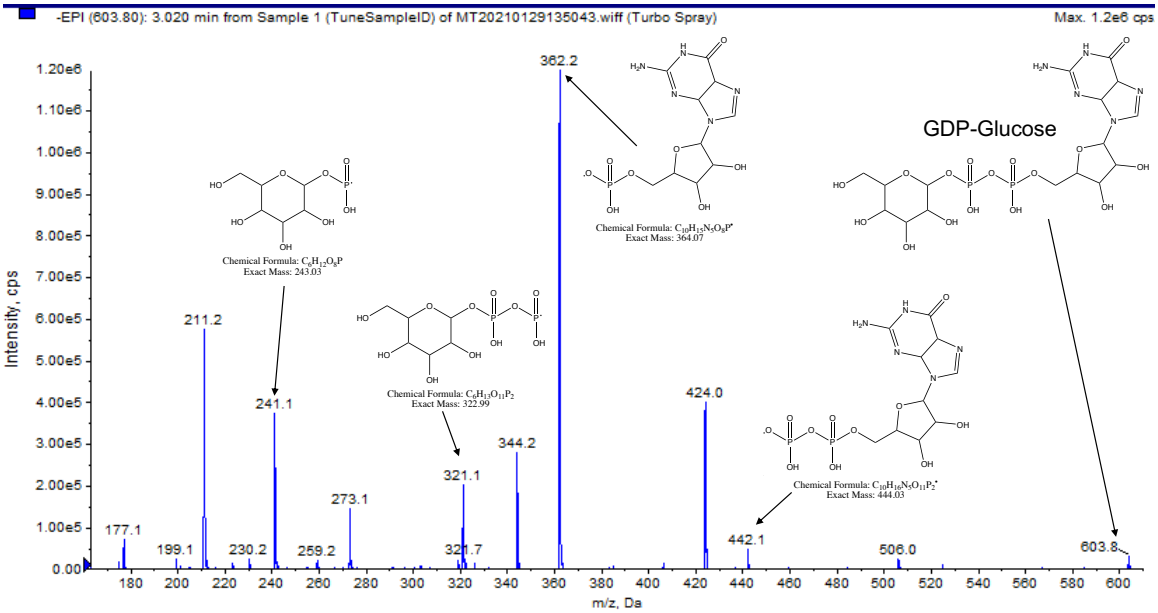

Figure 5.A1: **Mass spectrum and unique fragments for GDP-Glucose.**

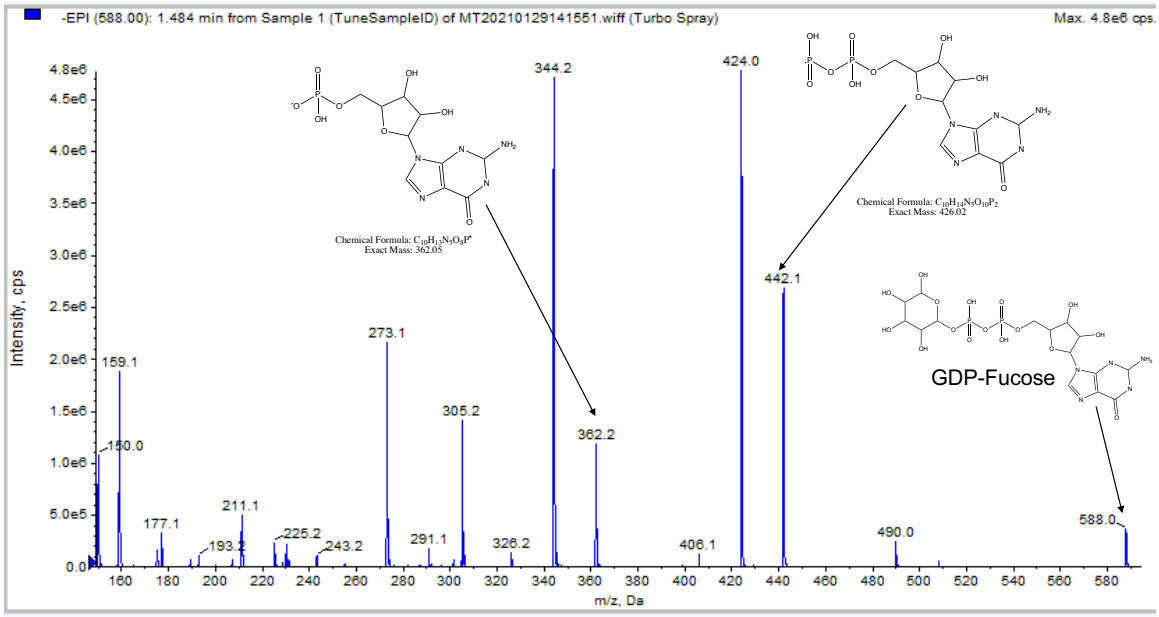

Figure 5.A2: **Mass spectrum and unique fragments for GDP-Fucose.**

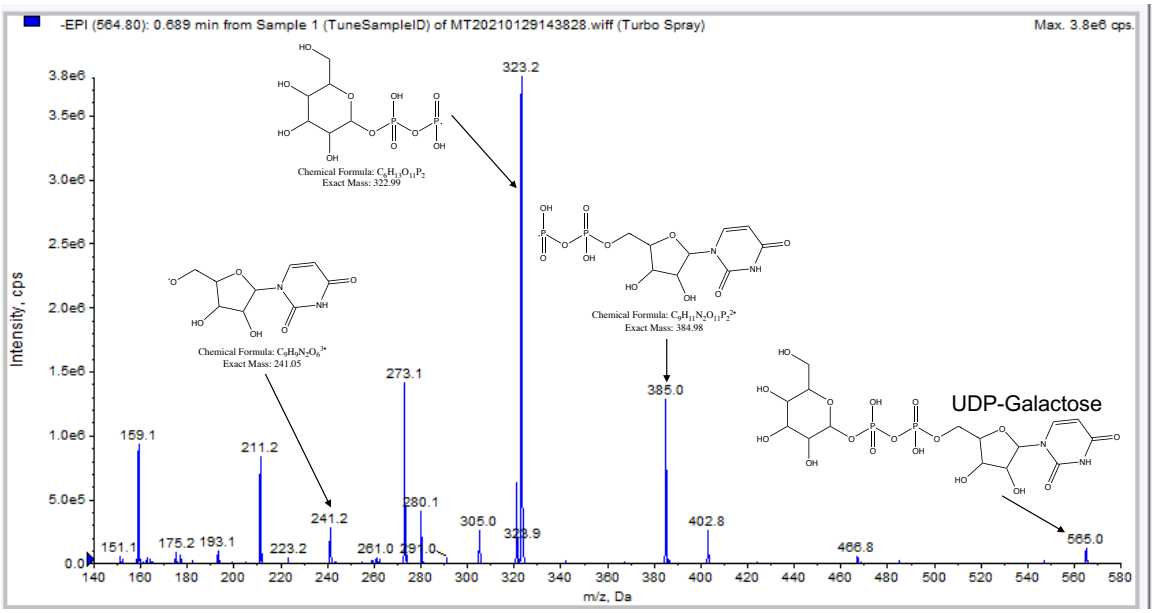

Figure 5.A3: **Mass spectrum and unique fragments for UDP-Galactose.**

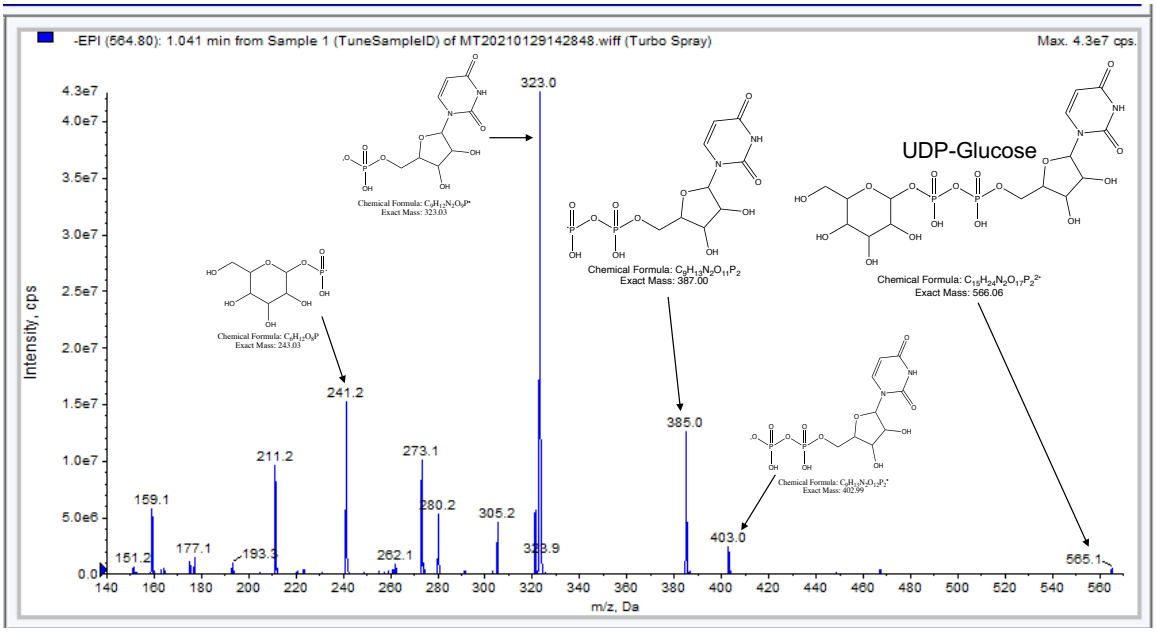

Figure 5.A4: **Mass spectrum and unique fragments for UDP-Glucose.**

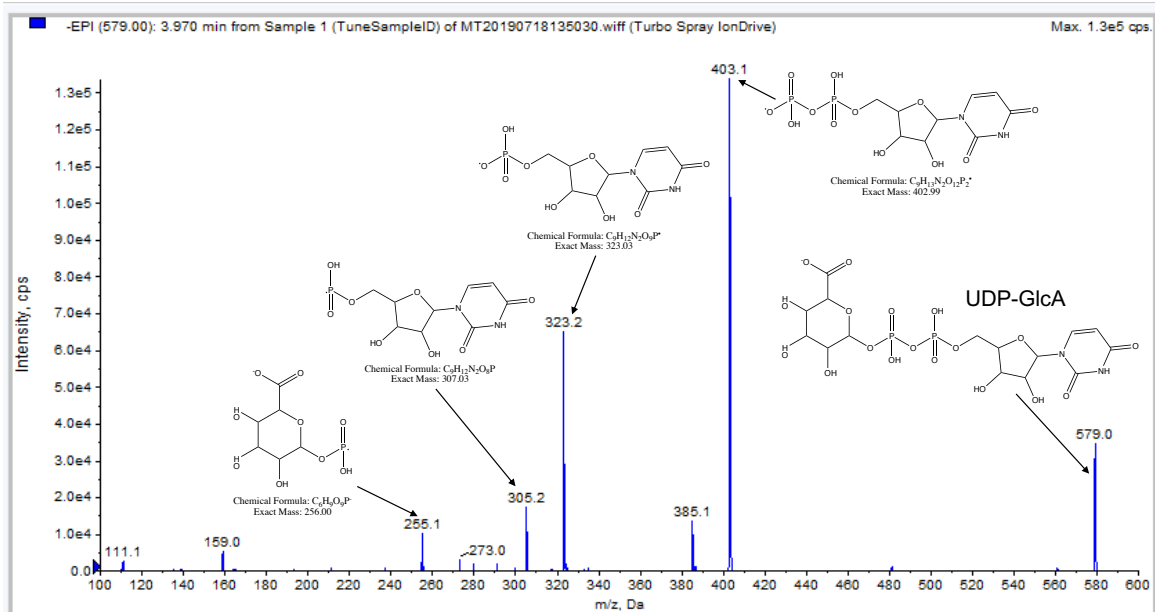

Figure 5.A5: **Mass spectrum and unique fragments for UDP-Glucaronate.**

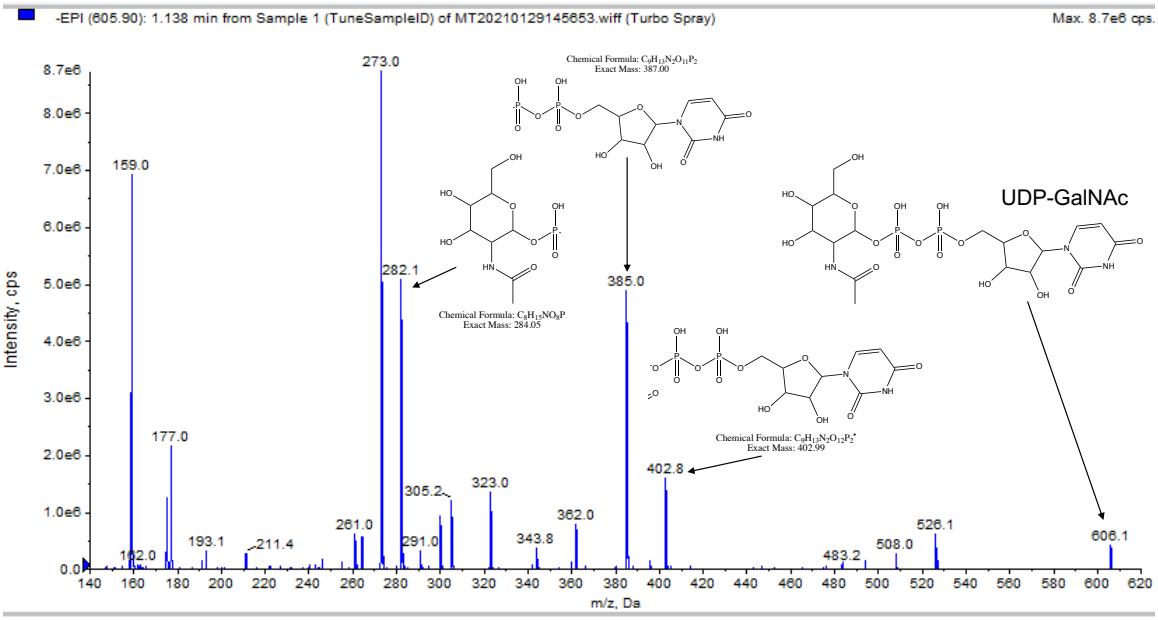

Figure 5.A6: **Mass spectrum and unique fragments for UDP-N-acetyl-galactosamine.**

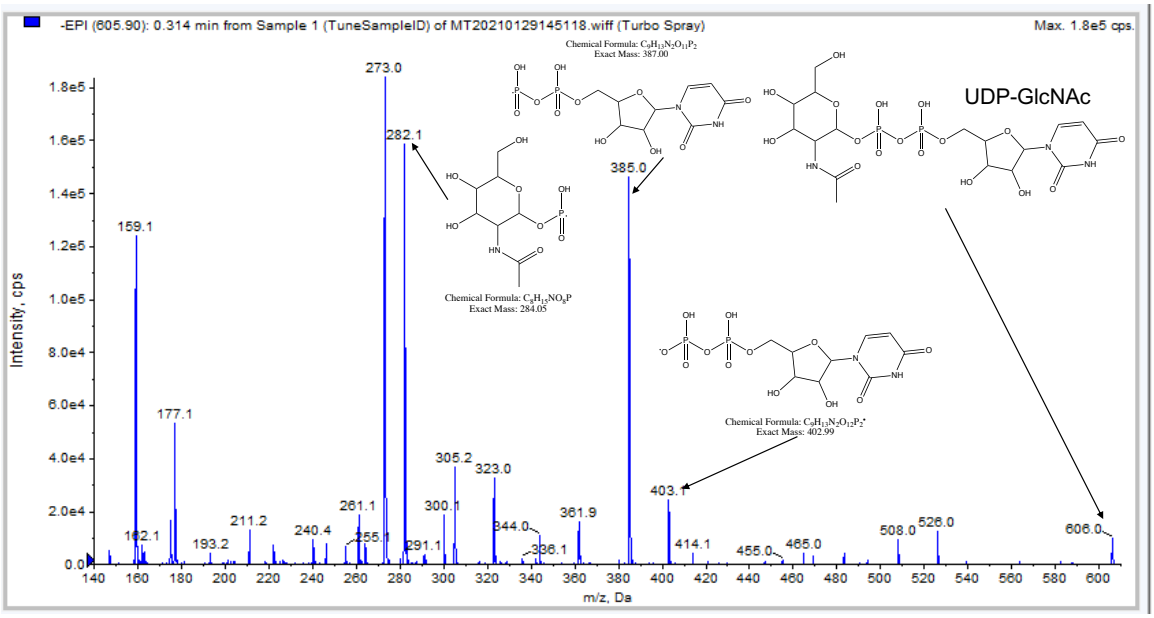

Figure 5.A7: **Mass spectrum and unique fragments for UDP-N-acetyl-glucosamine.**

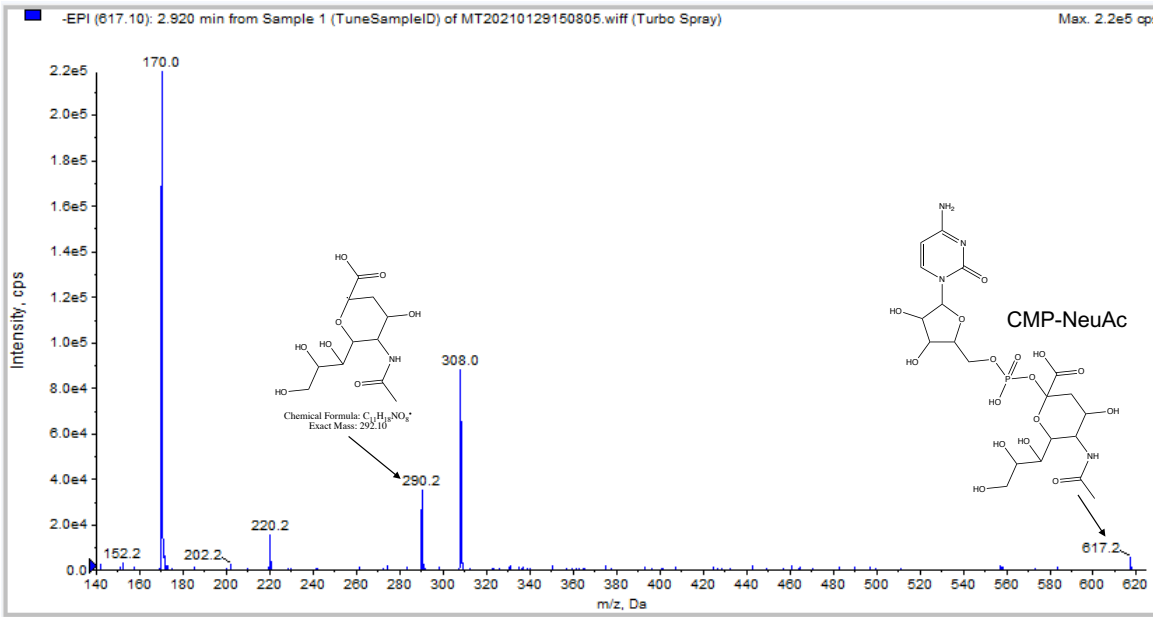

Figure 5.A8: **Mass spectrum and unique fragments for CMP-N-acetylneuraminic acid.**

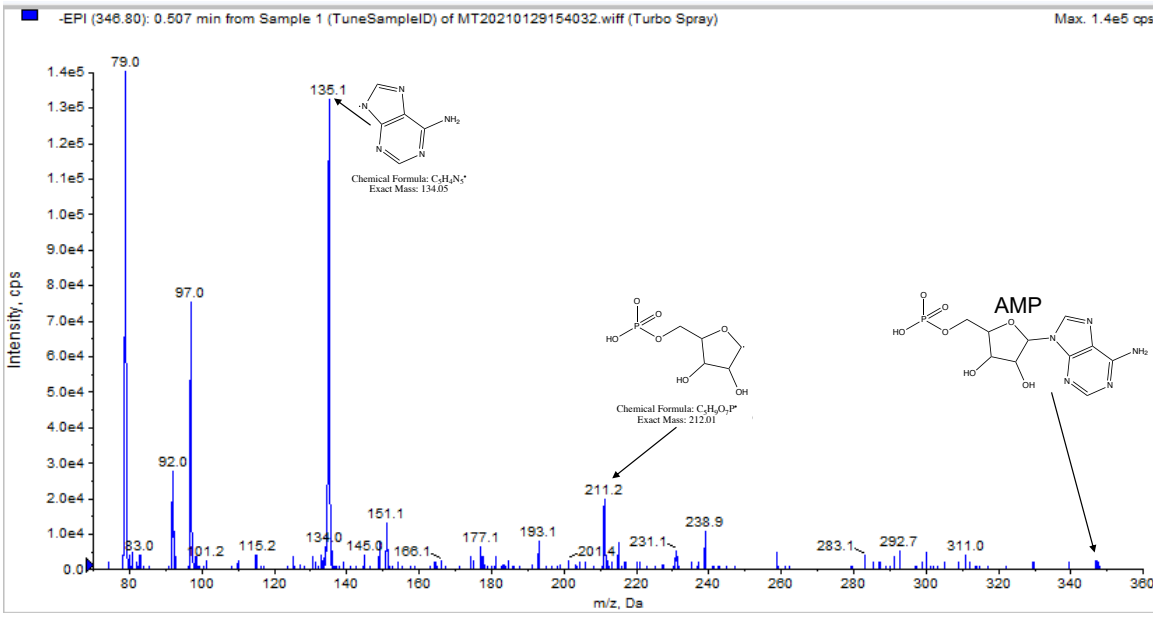

Figure 5.A9: **Mass spectrum and unique fragments for AMP.**

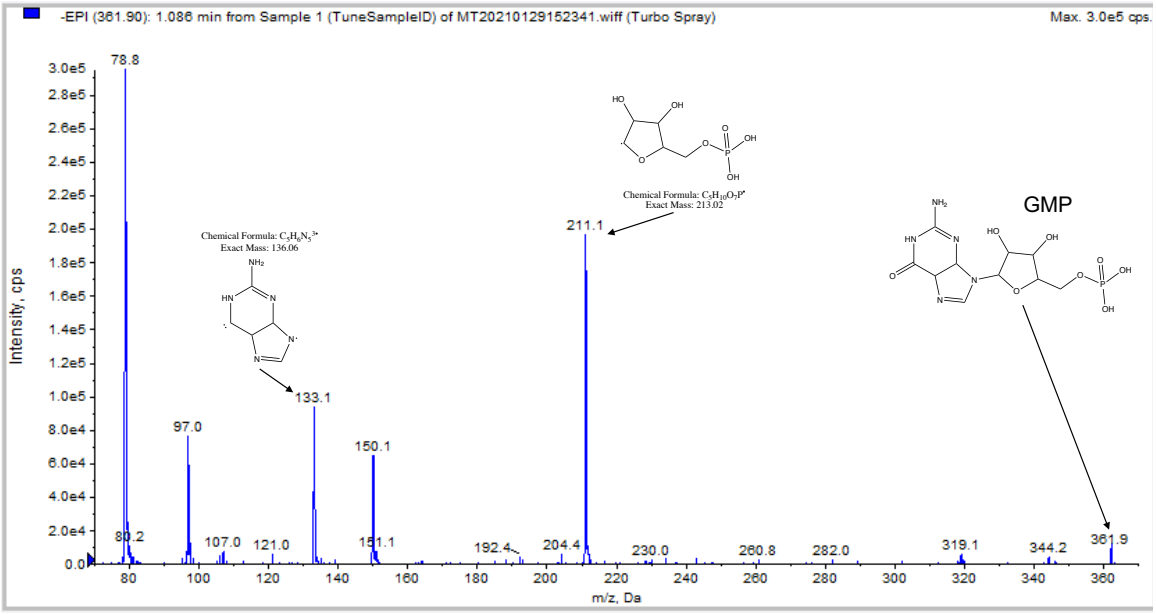

Figure 5.A10: **Mass spectrum and unique fragments for GMP**

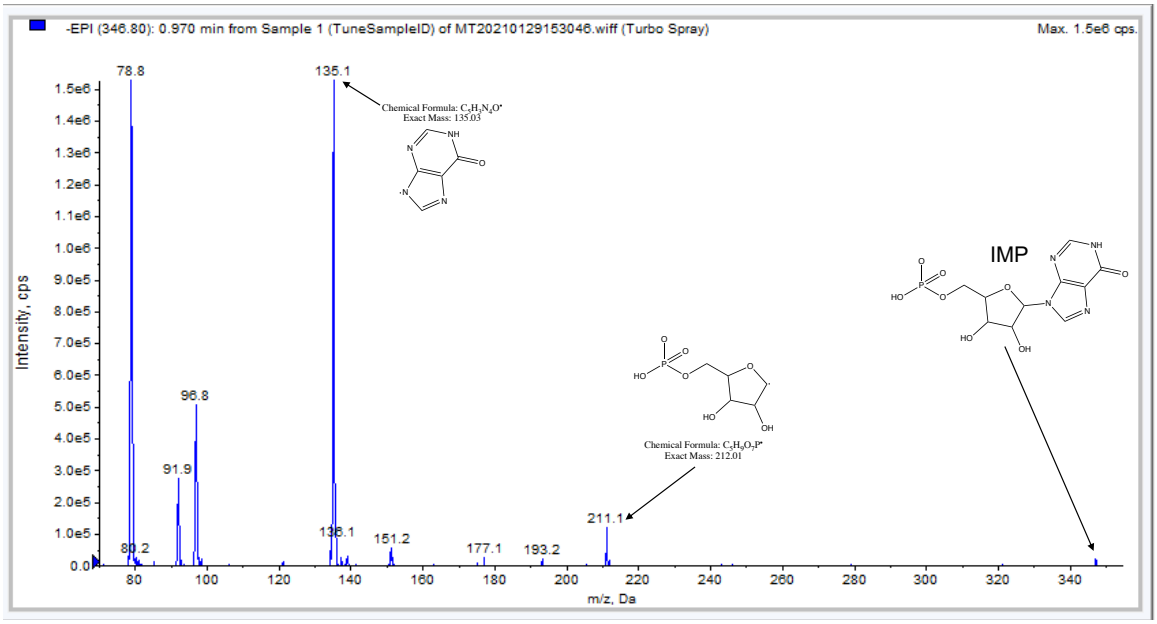

Figure 5.A11: **Mass spectrum and unique fragments for IMP.**

References

[1] Christopher L. Gaughan. The present state of the art in expression, production and characterization of monoclonal antibodies. *Molecular Diversity*, 20(1):255–270, 2016.

[2] Fabian Higel, Andreas Seidl, Fritz Sörgel, and Wolfgang Friess. N-glycosylation heterogeneity and the influence on structure, function and pharmacokinetics of monoclonal antibodies and Fc fusion proteins. *European Journal of Pharmaceutics and Biopharmaceutics*, 100:94–100, 2016.

[3] Thomas K. Villiger, Ernesto Scibona, Matthieu Stettler, Hervé Broly, Massimo Morbidelli, and Miroslav Soos. Controlling the time evolution of mAb N-linked glycosylation - Part II: Model-based predictions. *Biotechnology Progress*, 32(5):1135–1148, 2016.

[4] Kai Zheng, Mark Yarmarkovich, Christopher Bantog, Robert Bayer, Kai Zheng, Mark Yarmarkovich, Christopher Bantog, Robert Bayer, and Thomas W Patapoff. Influence of glycosylation pattern on the molecular properties of monoclonal antibodies Influence of glycosylation pattern on the molecular properties of monoclonal antibodies. 0862(February):649–658, 2016.

[5] Malgorzata Kesik-Brodacka. Progress in biopharmaceutical development. *Biotechnology and Applied Biochemistry*, 65(3):306–322, 2018.

[6] Sarah N Galleguillos, David Ruckerbauer, Matthias P Gerstl, Nicole Borth, Michael Hanscho, and Jürgen Zanghellini. What can mathematical modelling say about CHO metabolism and protein glycosylation ? *Computational and Structural Biotechnology Journal*, 15:212–221, 2017.

[7] Sarah A Sacco and Jamey D Young. 13C metabolic flux analysis in cell line and bioprocess development. *Current Opinion in Chemical Engineering*, 34, 2021.

[8] Andrew G. McDonald, Jerrard M. Hayes, and Gavin P. Davey. Metabolic flux control in glycosylation. *Current Opinion in Structural Biology*, 40:97–103, 2016.

[9] Pavlos Kotidis, Philip Jedrzejewski, Si Nga Sou, Christopher Sellick, Karen Polizzi, Ioscani Jimenez del Val, and Cleo Kontoravdi. Model-based optimization of antibody galactosylation in CHO cell culture. *Biotechnology and Bioengineering*, 116(7):1612–1626, 2019.

[10] Liang Zhang, Ming Liang Wang, Andreas Castan, Joanne Stevenson, Nathalie Chatzissavidou, Håkan Hjalmarsson, Francisco Vilaplana, and Veronique Chotteau. Glycan Residues Balance Analysis - GReBA: A novel model for the N-linked glycosylation of IgG produced by CHO cells. *Metabolic Engineering*, 57(August 2019):118–128, 2020.

[11] Yuzhou Fan, Ioscani Jimenez Del Val, Christian Müller, Jette Wagtberg Sen, Søren Kofoed Rasmussen, Cleo Kontoravdi, Dietmar Weilguny, and Mikael Rørdam Andersen. Amino acid and glucose metabolism in fed-batch CHO cell culture affects antibody production and glycosylation. *Biotechnology and Bioengineering*, 112(3):521–535, 2015.

[12] Si Nga Sou, Christopher Sellick, Ken Lee, Alison Mason, Sarantos Kyriakopoulos, Karen M Polizzi, and Cleo Kontoravdi. How does mild hypothermia affect monoclonal antibody glycosylation? *Biotechnology and Bioengineering*, 112(6):1165–1176, 2015.

[13] Ohadi Kaveh, Aghamohseni Hengameh, Gädke Johannes, Moo Young Murray, Raymond L. Legge, Scharer Jeno, and Hector M. Budman. *Novel dynamic model to predict the glycosylation pattern of monoclonal antibodies from extracellular cell culture conditions*, volume 12. IFAC, 2013.

[14] Ioscani Jimenez Del Val, Karen M. Polizzi, and Cleo Kontoravdi. A theoretical estimate for nucleotide sugar demand towards Chinese Hamster Ovary cellular glycosylation. *Scientific Reports*, 6(June):1–15, 2016.

[15] Neil Templeton, Kevin D Smith, Allison G Mcatee-pereira, Haimanti Dorai, J Betenbaugh, Steven E Lang, and Jamey D Young. Application of 13C flux analysis to identify high-productivity CHO metabolic phenotypes. *Metabolic Engineering*, 43(B):218–225, 2017.

[16] Maciek R. Antoniewicz. A guide to 13C metabolic flux analysis for the cancer biologist. *Experimental Molecular Medicine*, 50(4):19, 2018.

[17] Maciek R. Antoniewicz. A guide to metabolic flux analysis in metabolic engineering: Methods, tools and applications. *Metabolic Engineering*, 63:2–12, 2020.

[18] Peter G. Slade, R. Guy Caspary, Shilpa Nargund, and Chung Jr Huang. Mannose metabolism in recombinant CHO cells and its effect on IgG glycosylation. *Biotechnology and Bioengineering*, 113(7):1468–1480, 2016.

[19] Harnish Mukesh Naik, Natalia I. Majewska, and Michael J. Betenbaugh. Impact of nucleotide sugar metabolism on protein N-glycosylation in Chinese Hamster Ovary (CHO) cell culture. *Current Opinion in Chemical Engineering*, 22:167–176, 2018.

[20] Frank V. Ritacco, Yongqi Wu, and Anurag Khetan. Cell culture media for recombinant protein expression in Chinese hamster ovary (CHO) cells: History, key components, and optimization strategies. *Biotechnology Progress*, 34(6):1407–1426, 2018.

[21] Bo Liu, Maureen Spearman, John Doering, Erica Lattová, Hélène Perreault, and Michael Butler. The availability of glucose to CHO cells affects the intracellular lipid-linked oligosaccharide distribution, site occupancy and the N-glycosylation profile of a monoclonal antibody. *Journal of Biotechnology*, 170(1):17–27, 2014.

[22] Neil Templeton, Jason Dean, Pranhitha Reddy, and Jamey D. Young. Peak antibody production is associated with increased oxidative metabolism in an industrially relevant fed-batch CHO cell culture. *Biotechnology and Bioengineering*, 110(7):2013–2024, 2013.

[23] Maciek R. Antoniewicz, Joanne K. Kelleher, and Gregory Stephanopoulos. Measuring deuterium enrichment of glucose hydrogen atoms by gas chromatography/mass spectrometry. *Analytical Chemistry*, 83(8):3211–3216, 2011.

[24] Sarah A Sacco, Angela M Tuckowski, Irina Trenary, Lauren Kraft, Michael J Betenbaugh, Jamey D Young, and Kevin D Smith. Attenuation of glutamine synthetase selection marker improves product titer and reduces glutamine overflow in Chinese hamster ovary cells. *Biotechnology and bioengineering*, mar 2022.

[25] Kazuki Nakajima, Emi Ito, Kazuaki Ohtsubo, Ken Shirato, Rina Takamiya, Shinobu Kitazume, Takashi Angata, and Naoyuki Taniguchi. Mass Isotopomer Analysis of Metabolically Labeled Nucleotide Sugars and N- and O-Glycans for Tracing Nucleotide Sugar Metabolisms. *Molecular Cellular Proteomics*, 12(9):2468–2480, 2013.

[26] Douglas McCloskey, Jamey D. Young, Sibei Xu, Bernhard O. Palsson, and Adam M. Feist. MID Max: LC-MS/MS Method for Measuring the Precursor and Product Mass Isotopomer Distributions of Metabolic Intermediates and Cofactors for Metabolic Flux Analysis Applications. *Analytical Chemistry*, 88(2):1362–1370, 2016.

[27] Taylor A. Murphy and Jamey D. Young. ETA: Robust software for determination of cell specific rates from extracellular time courses. *Biotechnology and Bioengineering*, 110(6):1748–1758, 2013.

[28] Jamey D. Young. INCA: A computational platform for isotopically non-stationary metabolic flux analysis. *Bioinformatics*, 30(9):1333–1335, 2014.

[29] Ioscani Jimenez Del Val, Sarantos Kyriakopoulos, Karen M. Polizzi, and Cleo Kontoravdi. An optimized method for extraction and quantification of nucleotides and nucleotide sugars from mammalian cells. *Analytical Biochemistry*, 443(2):172–180, 2013.

[30] Xuan Qin and Xin Wang. Quantification of nucleotides and their sugar conjugates in biological samples: Purposes, instruments and applications. *Journal of Pharmaceutical and Biomedical Analysis*, 158:280–287, 2018.

[31] Kazuki Nakajima, Shinobu Kitazume, Takashi Angata, Reiko Fujinawa, Kazuaki Ohtsubo, Eiji Miyoshi, and Naoyuki Taniguchi. Simultaneous determination of nucleotide sugars with ion-pair reversed-phase HPLC. *Glycobiology*, 20(7):865–871, 2010.

[32] Robert Behmüller, Ines C. Forstenlehner, Raimund Tenhaken, and Christian G. Huber. Quantitative HPLC-MS analysis of nucleotide sugars in plant cells following offline SPE sample preparation. *Analytical and Bioanalytical Chemistry*, 406(13):3229–3237, 2014.

[33] Natalia I. Majewska, Max L. Tejada, Michael J. Betenbaugh, and Nitin Agarwal. N-Glycosylation of IgG and IgG-like recombinant proteins: Why is it important and how can we control it? *Annual Review of Chemical and Biomolecular Engineering*, 11(13):1–28, 2020.

[34] Ioscani Jimenez Del Val, Karen M. Polizzi, and Cleo Kontoravdi. A theoretical estimate for nucleotide sugar demand towards Chinese Hamster Ovary cellular glycosylation. *Scientific Reports*, 6(June):1–15, 2016.

[35] Mauro Torres, Julio Berrios, Yandi Rigual, Yesenia Latorre, Mauricio Vergara, Alan J. Dickson, and Claudia Altamirano. Metabolic flux analysis during galactose and lactate co-consumption reveals enhanced energy metabolism in continuous CHO cell cultures. *Chemical Engineering Science*, 205:201–211, 2019.

CHAPTER 6

^{13}C metabolic flux analysis of TCA cycle intermediate feeding strategies in CHO cell cultures

6.1 Introduction

Chinese hamster ovary (CHO) cells are the "workhorse" of the biopharmaceutical industry, where they are used in nearly 70% of all protein therapeutic production processes [1, 2]. The popularity of CHO cells is due to their ability to perform post-translational modifications, grow in suspension, and survive without serum supplementation [3, 4, 5]. Major improvements in viable cell density (VCD) and volumetric titer have occurred due to media and bioprocess optimization, with final yields routinely reaching 10 g/L [6]. Such high levels of productivity are energetically demanding – a single peptide bond requires three ATP molecules and a typical monoclonal antibody (mAb) can contain over 600 individual amino acids[7]. Previous studies have found that high-producing CHO cell lines typically exhibit upregulated tricarboxylic acid (TCA) cycle flux, likely to meet the high energy demands of these high-producers. The main carbon source for CHO cells is extracellular glucose, which is metabolized via glycolysis and the TCA cycle to provide energy and biosynthetic precursors for cell growth and mAb production.

Another important carbon source for CHO cells is lactate, which is typically produced during periods of high glycolytic flux (such as the exponential phase of growth), resembling the Warburg effect, and consumed during periods of high TCA cycle flux (such as the stationary phase). It has been hypothesized that this so-called "lactate switch" occurs in order to maintain redox balance and is typically a hallmark of high-producing lines. Excess lactate production can reduce the pH of non-pH controlled reactors or increase the osmolality to unsustainable levels in the case of base addition to control pH. High lactate concentrations can also indicate low oxidative metabolism, inhibit cell growth, and limit product formation [8, 9]. While lactate can serve as a secondary carbon source to feed the

TCA cycle during stationary phase, there are inherent drawbacks of high lactate concentrations [10].

Other carbon sources can be utilized to provide the necessary fuel for high TCA cycle fluxes, such as TCA cycle intermediates. A previous study by Zhang et al. [8] characterized the effects of adding TCA cycle intermediates in the basal media as well as in the feed solution. The addition of TCA cycle intermediates in the basal media was found to have no effect on the growth of the culture or detrimental effects when supplied at higher concentrations, while supplementation of TCA cycle intermediates during stationary phase increased lactate consumption, reduced ammonia accumulation, and increased specific productivity (qP).

It was previously identified that TCA cycle intermediate feeding during stationary phase improved culture characteristics [8]; however, it was not obvious why this occurred metabolically. A carbon-13 metabolic flux analysis (^{13}C MFA) study was carried out on bioreactors that utilized TCA intermediates for pH control. The ^{13}C MFA labeling study was run using the same parameter settings and performance indicators, such as lactate and ammonia concentrations and mAb production, aligned well with previously published data [8]. Additionally, we provide an in-depth analysis of the metabolic alterations caused by the feeding of TCA intermediates. TCA cycle fluxes were higher in the malic acid, succinic acid, and α-ketoglutaric (α-KG) acid fed reactors, while lactate and ammonia concentrations were lower. The final volumetric titer was also higher in the TCA intermediate fed reactors, as was qP. Overall, the cultures that used TCA intermediates for pH control in place of CO_2 had more desirable characteristics for biotherapeutic production.

6.2 Materials and Methods

6.2.1 Cell culture

An in-house IgG1 expressing CHO cell line developed by Merck & Co., Inc. was used for all of the experiments in this study, and culture conditions were as previously reported

[8]. In brief, cell bank vials were thawed and expanded in shake flasks maintained at 5% CO_2 and 36.5°C in humidified bioreactors. Twenty-four independently controlled ambr®250 bioreactors were inoculated to a target cell density of $2.0x10^6$ cells/mL in a glucose-containing proprietary basal media. A glucose-containing feed media was fed once daily at amounts determined based on the residual glucose concentration to achieve a final concentration of 6 g/L. Glutamic acid was fed as needed, once daily, to maintain a target concentration of 5 mM. Dissolved oxygen (DO) was maintained above 30% air saturation by sparging O_2. The pitched blade impellers in each reactor were set to an initial rate of 400 RPM; once the O_2 sparge rate reached 5 mL/min, the agitation speed was increased as a secondary control element for DO. Temperature was maintained at 36.5°C. For foam control, EX-CELL antifoam (Sigma-Aldrich, St. Louis, MO) was added as needed. For pH control, CO_2 was sparged as needed for the first six days of culture for all reactors to maintain a pH of 6.90 with a deadband of 0.05. On day six, control reactors continued to receive CO_2 as pH control while the TCA intermediate fed reactors began to receive either malic acid, succinic acid, or α-KG as needed to control pH.

6.2.2 Isotope labeling experiment (ILE)

The isotope labeling experiment was carried out on-site at Merck & Co., Inc. in Kenilworth, NJ after consultation with the Young lab. Three time periods of interest were studied: days 6-8 (early stationary phase), days 10-12 (late stationary phase), and days 14-16 (decline phase). For each time period of interest, eight reactors (two control and two for each TCA cycle intermediate) were used. At the beginning of the time period of interest (day 6, 10, or 14) a 6 g/L bolus of [U-$^{13}C_6$]-glucose was added to each reactor, resulting in glucose concentrations of 8-9 g/L. This final concentration was calculated to ensure glucose would not become fully depleted by the end of the labeling study. The feeding (Tables 6.1 and 4.1) and sampling (Table 6.3) schemes are shown below.

MFA Time Period	Days 1-5	Days 6-8	Day 9	Days 10-12	Day 13	Days 14-16
Days 6-8	PFS Glc GA	**ILE**				
Days 10-12	PFS Glc GA	PFS Glc GA	PFS Glc GA	**ILE**		
Days 14-16	PFS Glc GA	PFS Glc GA	PFS Glc GA	PFS Glc GA	PFS Glc GA	**ILE**

Table 6.1: **Feeding plan for cell culture duration.** Each day, reactors were fed a proprietary feeding solution (PFS), glucose (Glc) to a final concentration of 6 g/L, and glutamic acid (GA) to a final concentration of 5 mM. Addition of TCA intermediates for pH control began on day 6 on culture. During the isotope labeling experiment (ILE), the feeding plan and sampling plan were altered, as described in Tables 6.2 and 6.3.

T = 0 hr.	T = 24 hr.	T = 48 hr.
Proprietary feed solution Glutamic acid 6 g/L [U-$^{13}C_6$]-glucose	Proprietary feed solution Glutamic acid	Harvest remaining culture

Table 6.2: **Example feeding plan for a reactor during the labeling study.** The tracer ([U-^{13}C]-glucose) was added at T=0 hr. along with a proprietary amino acid containing feed solution and glutamic acid, as needed. Twenty-four hours after the tracer was added, the proprietary feed solution and glutamic acid were added as needed. Forty-eight hours after adding the tracer, the remaining culture was quenched.

Before adding tracer (t=0 hr.)	Quenched cell pellet, spent media
After adding tracer (t=24 hr.)	Quenched cell pellet, spent media
t=36 hr.	Quenched cell pellet, spent media
t=48 hr.	Quenched cell pellet, spent media

Table 6.3: **Sampling plan for ILE.** Samples were taken just before adding tracer and at 24, 36, and 48 hours after tracer addition.

Samples were collected just before the tracer was added and again at 24, 36, and 48 hours after tracer addition. For spent media samples, 1 mL of culture was taken from each reactor, centrifuged to remove cells, and the supernatant was stored at -80°C. Cell pellets were cold-quenched as previously described [11]. In brief, a quenching solution consisting of 60% methanol and 40% ammonium bicarbonate (AMBIC; 0.85% w/v solution in water) was pre-chilled to at least -40°C in a 4.5 M $CaCl_2$ bath. Based on VCD, the volume of cell culture containing $5x10^6$ cells was calculated; an amount of quenching solution equal to five-times the volume of cell culture was aliquoted for each sample. The required volume of cell culture was removed and immediately mixed with the aliquoted quenching solution. Samples were then centrifuged at 1000 RCF at 0°C for 1 minute. One mL of supernatant was retained for metabolite leakage analysis, while the remainder was removed and cell pellets were stored at -80°C. Quenched cell pellets and media samples were shipped to the Young lab on dry ice for all further analyses.

6.2.3 Extraction and derivatization of intracellular metabolites

Metabolites were extracted from the quenched cell pellets and derivatized as previously described [11]. In brief, each cell pellet was resuspended in a mixture of 4 mL of -20°C chloroform and 2 mL of -20°C methanol. The resuspension was then vortexed at 4°C for 30 min. Next, 1.5 mL of ice-cold water and 6 μL of a 10 mM norvaline internal standard were added, and samples were vortexed for another 5 min at 4°C. Samples were then centrifuged at 4000 RCF for 20 minutes at 4°C. After centrifugation, the top, aqueous

phase was collected and allowed to dry under air flow overnight. The dried sample was then resuspended in 50 μL of methoxyamine (MOX) reagent (Pierce; Rockford, IL). The resuspension was sonicated for 30 min at room temperature and then incubated at 40°C for 90 minutes. Next, 70 μL of MTBSTFA + 1% TBDMCS in pyridine (Pierce; Rockford, IL) was added and the sample was incubated at 70°C for 30 min. Finally, the sample was centrifuged at 14,000 RPM for 10 minutes and transferred to a vial before analysis using GC-MS.

6.2.4 Extraction and derivatization of metabolites from spent media

For analysis of the glucose tracer enrichment in the media, glucose was converted to its di-*O*-isopropylidene propionate (DIO) derivative as described previously [12]. In brief, 20 μL of media was mixed with 300 μL of ice-cold acetone. After centrifugation, the supernatant was transferred to a glass test tube and dried under air flow at 60°C. The dried sample was resuspended in 500 μL of a 1:46 v/v mixture of 96% sulfuric acid and acetone, then incubated at room temperature for 60 minutes. The reaction was neutralized with 400 μL of 0.44 mM sodium carbonate then mixed with 1.5 mL of saturated sodium chloride solution and 1 mL of ethyl acetate. Tubes were vortexed and allowed to incubate at room temperature until phases were completely separated. The upper organic layer was transferred to a microcentrifuge tube and evaporated to dryness under air flow at room temperature. The dried sample was resuspended in 150 μL of a 2:1 propionic anhydride and pyridine mixture and incubated for 30 minutes at 60°C. Samples were evaporated to dryness under air flow at 60°C. The dried sample was redissolved in 100 μL ethyl acetate, transferred to a glass GC-MS vial insert, and analyzed using GC-MS.

To measure the residual concentrations of the TCA intermediates, spent media samples were extracted and derivatized alongside standard curves containing the metabolites at known concentrations of 0.15625 mM, 0.3125 mM, 0.625 mM, 1.25 mM, 2.5 mM, and 5 mM. For the extraction, 30 μL of either sample or standard was mixed with 360 μL of

a 2:1 mixture of ice-cold methanol and chloroform. This mixture was vortexed at 4°C for 10 minutes. Next, 120 μL of ice-cold chloroform, 210 μL of ice-cold water, and 6 μL of a 10 mM norvaline internal standard were added to each sample. Samples were vortexed to ensure they were well-mixed, then centrifuged at 14,000 RPM at 0°C for 10 minutes. The aqueous phase was transferred to a new microcentrifuge tube and the sample was dried under air flow overnight at room temperature. The dried sample was then derivatized as described in Section 6.2.3.

6.2.5 Gas chromatography-mass spectrometry (GC-MS)

Derivatized extracts were injected into an Agilent 7890A gas chromatograph with an Agilent HP-5ms column (30m x 0.25mm i.d. x 0.25μm) connected to an Agilent 5977B GC/MSD. As described previously [13], TBDMS-derivatized cell pellet samples were analyzed using an oven program as follows: held at 80°C for 1 min, increased to 140°C at a rate of 20°C/min, then increased from 140°C to 234°C at 4°C/min, held at 234°C for 5 min, and finally increased from 234°C to 285°C at a rate of 20°C/min. A sample volume of 1 μL was injected at a 5:1 split ratio and a column flow rate of 1 mL/min. The gain factor was dynamically adjusted using the timed event mode to account for a wide range of metabolite concentrations; this allowed for lower sensitivity for more concentrated metabolites alongside higher sensitivity for more dilute metabolites. The same parameters were used to analyze TBDMS-derivatized media samples, but with a 15:1 split ratio. DIO-derivatized media samples were analyzed using the following oven program: held at 80°C for 1 min, increased to 220°C at a rate of 40°C/min, then increased to 240°C at a rate of 10°C/min. A sample volume of 1μL was injected at a 30:1 split ratio and a column flow rate of 1 mL/min.

6.2.6 Determination of growth and extracellular flux rates

VCD and viability were measured on a Cedex Hi-Res cell counter (Roche; Mannheim, Germany) using the trypan blue exclusion method to determine viability. Culture pH, pO_2,

and pCO_2 were measured offline using an ABL80 blood gas analyzer (Radiometer; Copenhagen, Denmark). Glucose, lactate, glutamate, glutamine, and ammonia were measured daily before any feeding using a BioProfile® FLEX2 (Nova Biomedical; Waltham, MA). Antibody titer was measured using an Agilent 1100 high-performance liquid chromatography (HPLC) with a Protein A column (Agilent Technologies; Santa Clara, CA). All titer results were normalized to the peak titer in the control reactor.

Specific growth rate and cell-specific consumption and production rates for unfed metabolites were determined using the ETA software package [14], as previously described [11]. For metabolites that were fed during the ILE, cell specific rates were calculated using the equation:

$$q_i = \frac{(c_i \cdot V_i) - (c_{i-1} \cdot V_{i-1}) - \sum_j c_f \cdot V_{f,j}}{X_i - X_{i-1}} \tag{6.1}$$

where q_i is the cell-specific production rate, c_i is the component's concentration in the bioreactor at time t_i, V_i is the working volume of the reactor at time t_i, c_f is the component's concentration in the feed, $V_{f,j}$ is the volume fed between times t_{i-1} and t_i, and X_i is the integrated viable cell density at time t_i.

6.2.7 Determination of extracellular and intracellular metabolite pool sizes and redox markers

Total ion counts (TIC) for all metabolites measured in the TBDMS-derivatized samples and standards were normalized to the TIC for norvaline 288, a fragment ion of the internal standard added during extraction. Using external calibration curves, the absolute abundances of all target metabolites in the media and in the cell pellets were determined. For extracellular metabolites, this amount was normalized to the volume of media extracted to provide absolute concentrations. For intracellular metabolites, this amount was normalized to total cellular volume, which was estimated based on cell counts for each sample and the assumption of an average cellular volume of 1714 μm^3, based on average cell diameter

of 14.85 μm and a spherical cell shape. As described previously [15, 16], the cytosolic NADH/NAD^+ ratio was estimated based on the equilibrium of lactate dehydrogenase:

$$\frac{NADH}{NAD^+} = \frac{[Lactate]}{[Pyruvate] \cdot \frac{1}{K_{LDH}}} \tag{6.2}$$

where the concentrations of lactate and pyruvate were determined as described above and $K_{LDH} = 1.11x10^{-4}$. The cytosolic NADPH/$NADP^+$ ratio was estimated based on the equilibrium of malate dehydrogenase:

$$\frac{NADPH}{NADP^+} = \frac{[Malate]}{[Pyruvate][CO_2] \cdot K_{MDH}} \tag{6.3}$$

where the concentrations of malate and pyruvate were determined as described above, the concentration of CO_2 was estimated to be 1.5 mM based on Henry's law and a 5% CO_2 atmosphere, and $K_{MDH} = 34.4$ mM.

6.2.8 ^{13}C metabolic flux analysis (^{13}C MFA)

A previously published model of CHO cell metabolism was used for the MFA performed in this study [13]. This model is a compartmentalized representation of the cell and contains equations for reactions in glycolysis, the pentose phosphate pathway (PPP), the TCA cycle, amino acid catabolism, cell growth, and IgG biosynthesis (84 reactions). Exchange reactions between the media and the cytosol for the three fed TCA cycle intermediates were added. Coefficients for the cell growth equation were based on a previously published study using the same cell line [17].

The INCA software package [18] (publicly available at http://mfa.vueinnovations.com) was used to fit experimental data to the metabolic model, as previously described [19]. Isotopic steady state was not achieved; therefore, isotopically nonstationary MFA (INST-MFA) was utilized to regress fluxes [20]. Fluxes were regressed using the Levenberg-Marquardt optimization algorithm. A minimum of 50 restarts from random initial guesses

were used for each flux estimation to ensure a global minimum was found. To assess goodness-of-fit, flux results were subjected to a chi-square statistical test; results are reported in Table 6.A1. 95% confidence intervals were calculated for each flux using INCA's parameter continuation function.

6.2.9 Statistical analysis

One-way and two-way ANOVA were used to determine statistical significance between different feeding conditions, with $\alpha = 0.05$. A Tukey multiple comparison test was applied if differences were detected. The standard error of the mean (SEM) was estimated for intracellular fluxes using the formula SEM = (UB-LB)/3.92, where UB and LB represent the upper and lower bounds of the calculated 95% confidence intervals and 3.92 is the number of standard errors that span the 95% confidence interval of a normally distributed random variable.

6.3 Results and Discussion

6.3.1 Late culture stage cell density and viability trend higher in fed reactors

Viable cell densities (VCDs), growth rates and viability did not vary with feeding condition exponential phase (Fig. 6.1). Peak VCDs of approximately 20x10^6 cell/mL were achieved in all conditions on day 7 of culture, followed by a steady decline in VCD until the end of the experiment. After day 13 of culture, the control reactors had slightly reduced VCDs compared to reactors fed TCA cycle intermediates. After day 9 of culture, viabilities began to stratify, with succinic acid and malic acid fed reactors maintaining higher viabilities until the end of culture while α-KG fed reactors had similar viabilities when compared to the control reactors. Overall, by the late culture phase (Days 14-16), the TCA intermediate fed reactors had slightly higher VCDs and viabilities despite similar growth profiles in earlier culture phases.

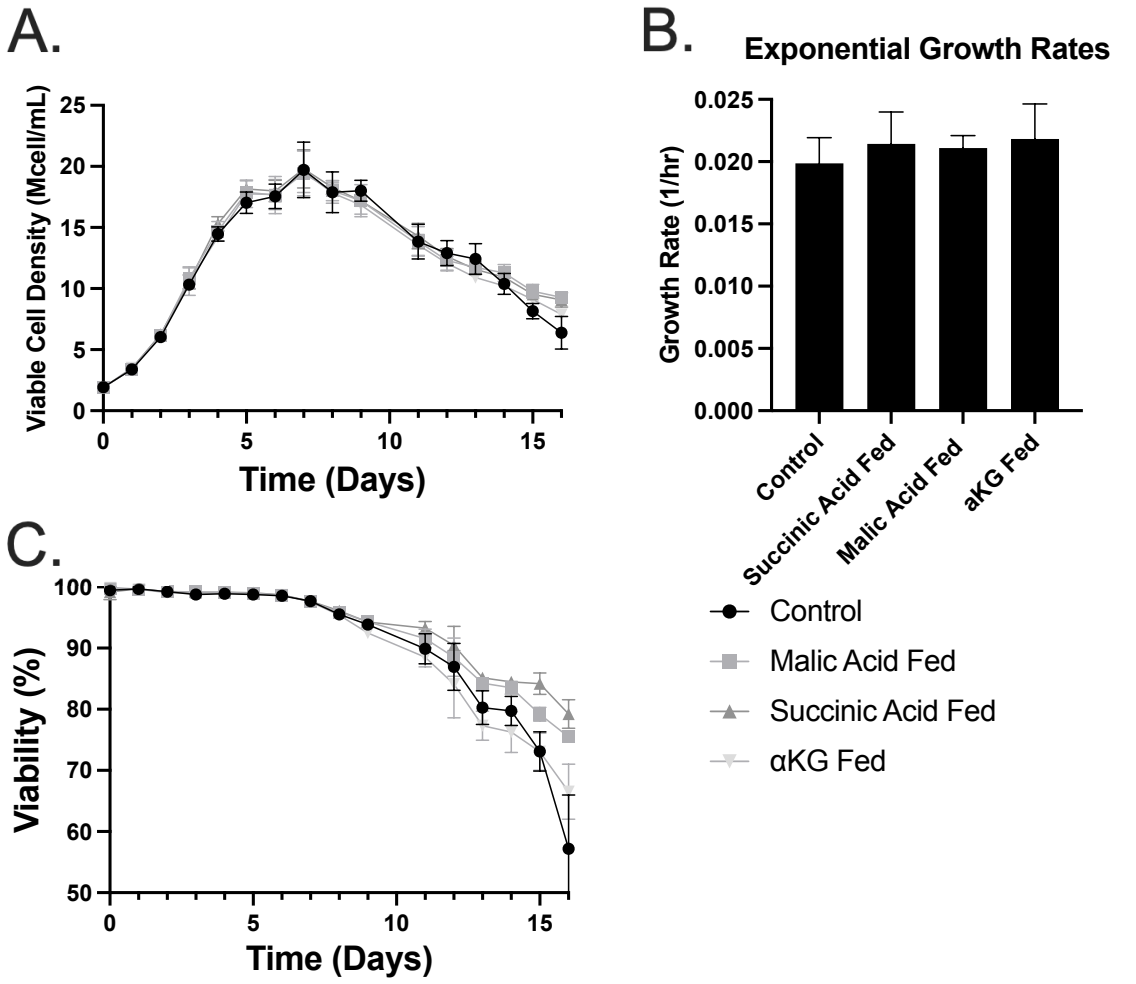

Figure 6.1: **Growth characteristics for the cultures under different feeding conditions.** (A) Viable cell density, (B) growth rates during exponential phase, and (C) viability for each of the four feeding conditions. Data represent means $\pm$ SEM. $n \geq 2$.

6.3.2 TCA intermediate feeding reduce lactate accumulation and ammonia production

Lactate and ammonia are two major byproducts of CHO cell growth; however, they can inhibit cultures from reaching their maximum peak VCD and also affect product quality [8, 9]. Therefore, reduced lactate and ammonia production are desirable metabolic characteristics. All reactors underwent the "lactate switch" from production to consumption at approximately day 7 of culture. All TCA intermediate fed reactors exhibited reduced lactate concentrations compared to the control reactors after day 10 of culture (Fig. 6.2A),

which agrees with previously reported results [8]. Additionally, lactate consumption during days 6-8 was higher in the TCA intermediate fed reactors compared to the controls, while during days 14-16 lactate production was lower and during days 10-12 the net lactate flux was nearly zero (Fig. 6.3A).

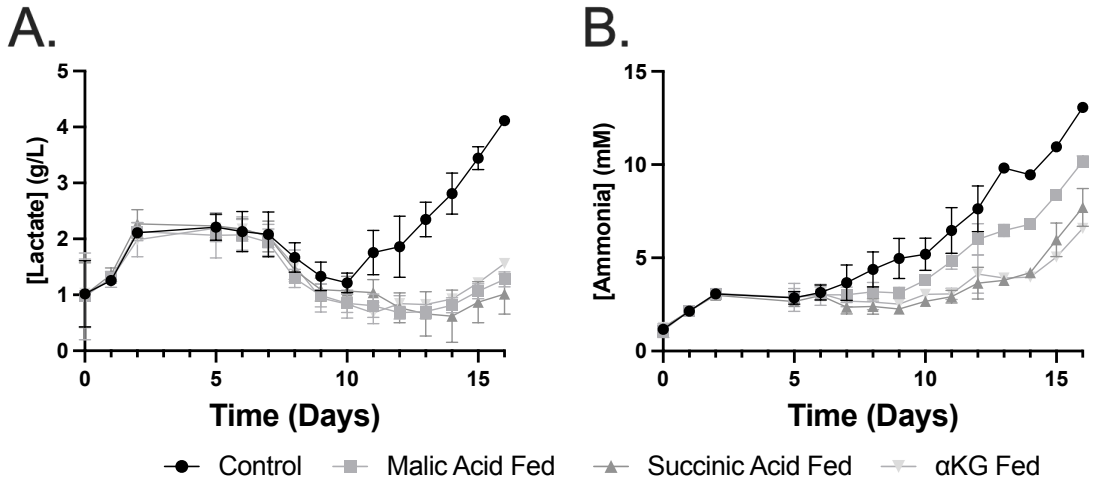

Figure 6.2: **Lactate and ammonia profiles.** The concentrations of (A) lactate and (B) ammonia in the reactors over the length of the culture for each feeding condition. Data represent the means $\pm$ SEM. $n \geq 2$.

The switch back to lactate production in the control reactor was previously postulated to occur due to elevated partial pressure of CO_2 (pCO_2) [8]. While it is not well understood why this occurs, it has been reported that the shift to lactate consumption does not occur at elevated pCO_2 [21] and cultures will even resume lactate production if pCO_2 becomes elevated after lactate consumption [22]. High pCO_2 levels could be inhibiting the TCA cycle, reducing the demand for lactate consumption. Since the control reactors were the only ones where pH was controlled with CO_2, as in the previous study, increased pCO_2 in the control reactor was still the likely cause of the increased lactate production in the control lines. Additionally, increased TCA cycle flux in the TCA intermediate fed reactors likely lead to an increased demand for pyruvate, limiting the need for a pyruvate sink such as lactate production.

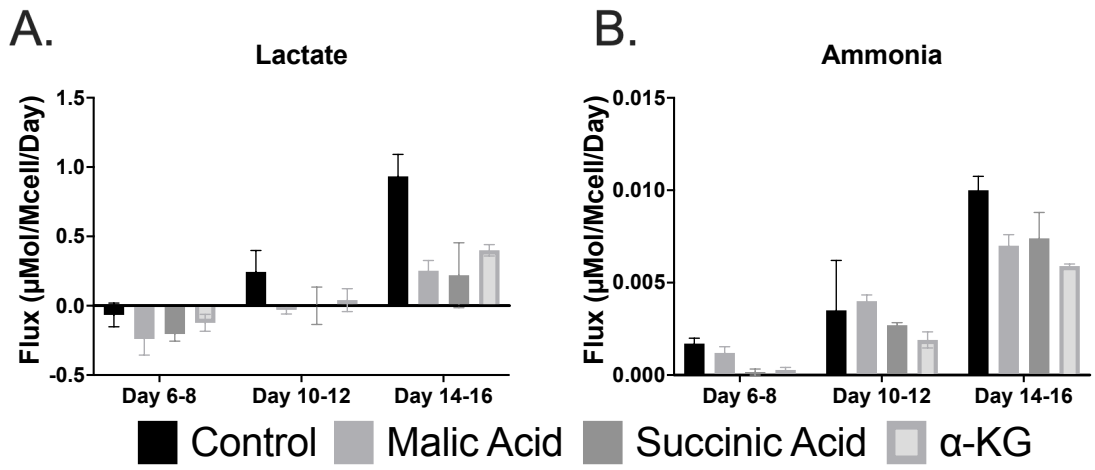

Figure 6.3: **Specific productivities of lactate and ammonia during different phases of culture.** The cell specific production of (A) lactate and (B) ammonia during the three growth phases of interest. Data represent the means $\pm$ SEM. $n = 2$.

Meanwhile, ammonia production was lower in the TCA intermediate fed reactors. Previous studies have found that pH control through lactic acid feeding reduce ammonia accumulation, and TCA intermediate feeding appears to have a similar effect [23]. The succinic acid and α-KG fed reactors had the lowest ammonia concentrations throughout the culture, while the malic acid fed reactors had ammonia concentrations between the other TCA intermediate fed reactors and the control reactor (Fig. 6.2B). Specific ammonia production was also generally lower in all TCA intermediate fed reactors compared to the control, as shown in Figure 6.3B, while ammonia production increased as culture duration increased. During the day 6-8 time period, ammonia production in the succinic acid and α-KG fed reactors was nearly zero, while malic acid fed reactors had a similar specific production rate as the control reactors. Again, during days 10-12, the malic acid fed and the control reactors had similar ammonia production while the succinic acid and α-KG fed reactors were slightly lower. Finally, during days 14-16, all three TCA intermediate fed reactors had lower ammonia production compared to the control reactors. This lower ammonia production is also likely due to increased TCA cycle flux in the TCA intermediate fed reactors, as a number of cataplerotic reactions that form amino acids from TCA intermediates

consume ammonia.

6.3.3 TCA intermediate feeding alters consumption of carbon sources

A large bolus of glucose was fed at the beginning of each labeling period to ensure that glucose would not be depleted during the labeling study. The glucose consumption rate over the time period of interest was calculated for each feeding condition using ETA [14] (Figure 6.4). Glucose consumption was similar across all conditions during the day 6-8 time period. During days 10-12, α-KG fed reactors had significantly lower glucose consumption rates compared to the control reactors, while the malic acid and succinic acid fed reactors trended towards lower glucose consumption. During days 14-16, glucose consumption in the succinic acid fed reactors was similar to that of the control reactors, while malic acid and α-KG fed reactors trended towards lower glucose consumption. This reduced glucose consumption is possibly due to the availability of the TCA cycle intermediates as additional carbon sources; the uptake of these TCA intermediates more than compensates for the reduction in glucose consumption (Figure 6.5).

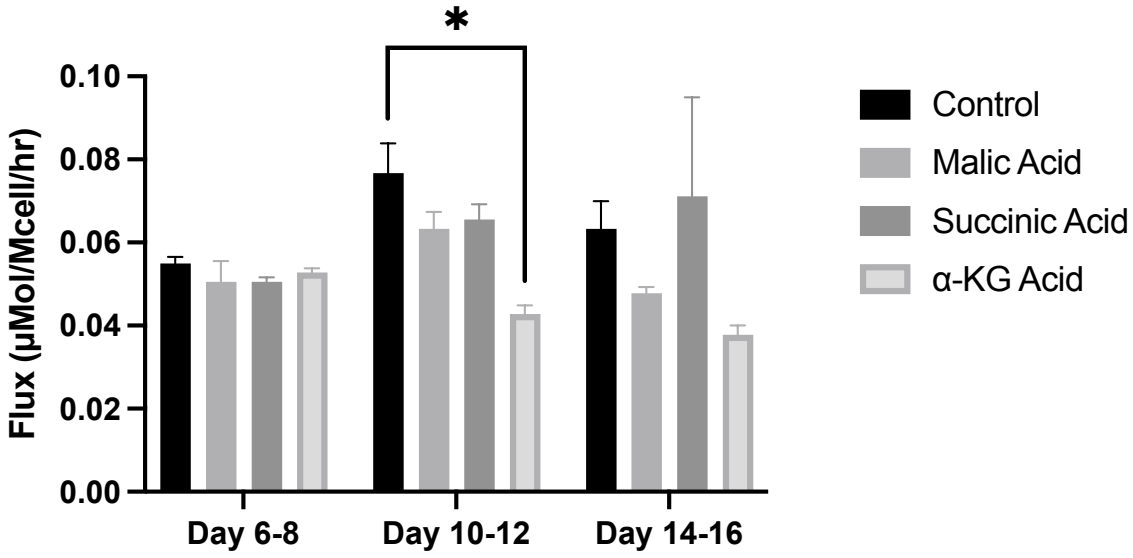

Figure 6.4: **Glucose consumption rates.** Glucose consumption rates were calculated for each feed condition during each time period of interest. Data represent the means $\pm$ SEM. $^{*}p < 0.05$.

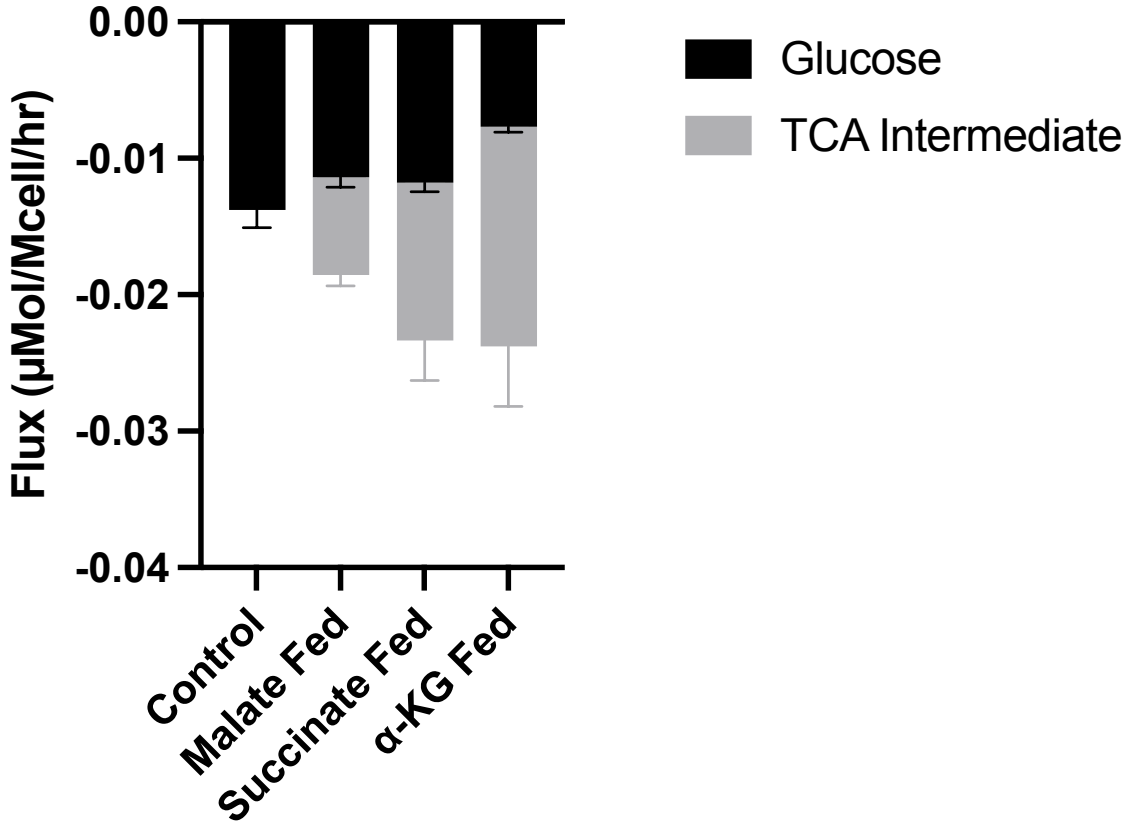

Figure 6.5: **The summation of glucose and TCA intermediates during days 10-12.** The consumption rate of glucose is shown in black while the consumption rate of the respective TCA intermediate is shown in grey. Data represent the means ± SEM.

The consumption and production rates of all twenty amino acids were also calculated using equation 6.1, since all amino acids were fed throughout the labeling study. During the day 6-8 labeling period, the only significant difference in amino acid flux was in glutamine production for the malic acid fed reactor (Figure 5.7A). For 12 of the 16 measured amino acids, succinic acid and α-KG fed reactors trended towards higher consumption rates. While not significant, α-KG fed reactors trended towards lower consumption, and possibly production, of glutamate as well as higher consumption of aspartate. Since α-KG is a precursor of glutamate, it is likely that the excess α-KG is being used to produce glutamate, leading to the reduced consumption rate. The additional consumption of aspartate, a precursor of oxaloacetate (OAA), could be due to an increased demand for TCA cycle

anaplerosis.

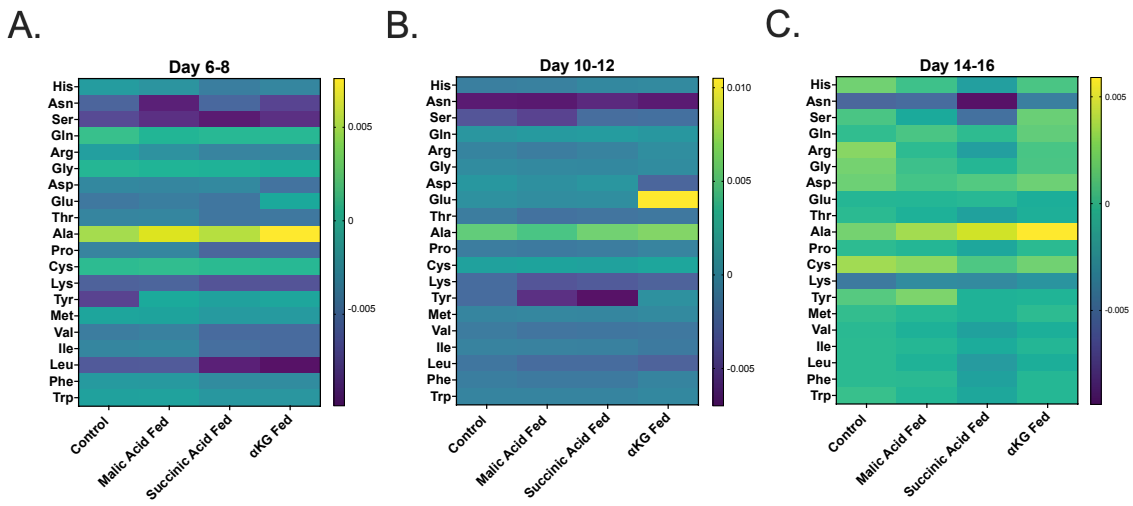

Figure 6.6: **Amino acid production and consumption rates during the labeling experiments.** Amino acid fluxes for (A) Days 6-8, (B) Days 10-12, and (C) Days 14-16. Positive values indicate production while negative values indicate consumption.

As shown in Figure 6.6B, amino acid fluxes were more similar across all feeding conditions during the day 10-12 time period. The notable exceptions are the significantly higher production of glutamate and significantly higher consumption of aspartate in the α-KG fed reactors (Figure 6.7). Similar to the reasoning described for day 6-8, glutamate production is likely higher due excess α-KG being used to produce glutamate via the glutamate dehydrogenase (GluDH) reaction. Aspartate serves as a precursor for OAA, and α-KG is consumed in the production of OAA from aspartate; therefore, increased aspartate consumption can be due to an increased demand for OAA or an additional sink for excess α-KG.

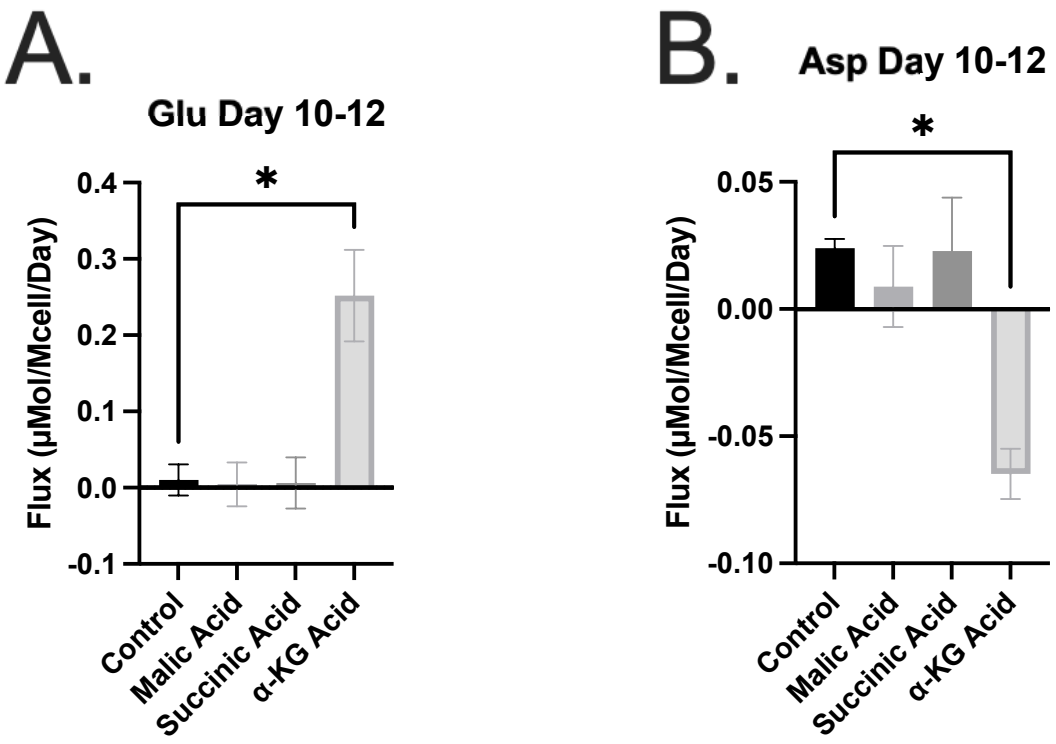

Figure 6.7: **Amino acid consumption and production rates during the day 10-12 time period.** Data represent the means $\pm$ SEM. $*p < 0.05$.

During days 14-16, most amino acid fluxes for the control reactor appeared as net production (Figure 6.6C). Due to the high cell death observed during this time, it is likely that the apparent net production is an artifact due to lysis of proteins from cell death. Amino acid fluxes were also close to zero for the malic acid and α-KG fed reactors, also likely due to high rates of cell death. The only significant difference in amino acid consumption during this time period was for lysine, where the α-KG fed reactor had significantly lower consumption compared to the control reactor. However, it is unclear why this may be the case and could be another artifact of increased cell death.

6.3.4 Volumetric titer and specific productivity trend higher in TCA intermediate fed reactors

The volumetric titer is an important cell culture characteristic. Volumetric titer can be increased in one of two ways: (i) by increasing the number of viable cells in the reactor (VCD) or (ii) by increasing the amount of product a single cell can produce (qP). The use of TCA cycle intermediates to control the pH offered a modest increase in volumetric titer after day 9 of culture (Figure 6.8A). After day 13 of culture, the titer in the control reactors began to decrease; this was likely due to the addition of water to maintain culture volumes in the control reactors similar to those in the TCA intermediate fed reactors. The TCA cycle intermediate fed reactors maintained titer until the end of culture.

Specific productivity (qP) was similar across all conditions during the day 6-8 time period. During days 10-12, the qP of the control reactors did not change significantly from the qP during days 6-8. However, qP was higher by 27%, 13%, and 6% in the succinic acid fed, malic acid fed, and α-KG fed reactors, respectively, compared to the day 10-12 control qP. Due to the decrease in volumetric titer from day 13 onwards, the qP of the control cultures was negative during the day 14-16 time period. While the qP of the TCA fed intermediate reactors was lower than in the other time periods of interest, qPs remained positive during days 14-16.

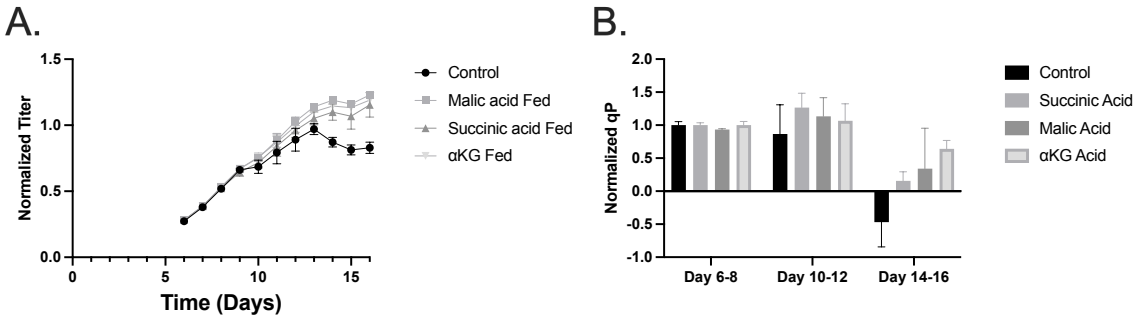

Figure 6.8: **Volumetric titer and specific productivity.** The (A) volumetric titer was normalized to the peak control titer measurement and (B) qP was normalized to the control value on day 6-8. Likely due to lysis of proteins, the titer actually declined during the day 14-16 time period, leading to a negative qP. Data represent the means $\pm$ SEM.

6.3.5 ^{13}C MFA reveals upregulated TCA cycle metabolism in TCA intermediate fed reactors

Due to the rapid decrease in viability and VCD from days 14-16, applying ^{13}C MFA to the samples collected from this time frame was not possible. It is difficult to account for the flux of amino acids and other nutrients that are produced during cell lysis, so we could not successfully resolve any fluxes for this time frame. Additionally, fluxes were difficult to resolve for the day 6-8 time period due to the fact that the automated pH control system introduces an average 1 mMol bolus of TCA intermediates, beginning on day 6 of culture, causing a shift in the metabolic state of the culture. An assumption of our model is that metabolism is at steady state; therefore, if the metabolism shifts during the labeling experiment, our model is not able to account for this shift and therefore cannot provide an adequate fit to the data. Overall, due to the likely metabolic changes occurring during days 6-8 and 14-16, only flux results for the day 10-12 labeling study are reported.

Fluxes were determined by ^{13}C MFA of isotope labeling and extracellular rate measurements using a previously established model of CHO central carbon metabolism [24] for days 10-12. As shown in Figure 6.9, fluxes throughout glycolysis were similar when comparing the control reactors to the malic acid and succinic acid fed reactors. Glycolytic fluxes in the α-KG fed reactor were lower, likely due to the lower rate of glucose uptake (Figure 6.4). Flux through pyruvate kinase (PK) was elevated in the succinic acid fed reactors (Figure 6.9A), likely due to increased flux through PEPCK (Figure 6.9D). PPP fluxes were approximately zero in all three TCA intermediate fed reactors (Figure 6.9B). Fluxes throughout the TCA cycle were slightly elevated in the three TCA intermediate fed reactors. Figure 6.10 shows flux maps generated based on the flux values reported in Figure 6.9.

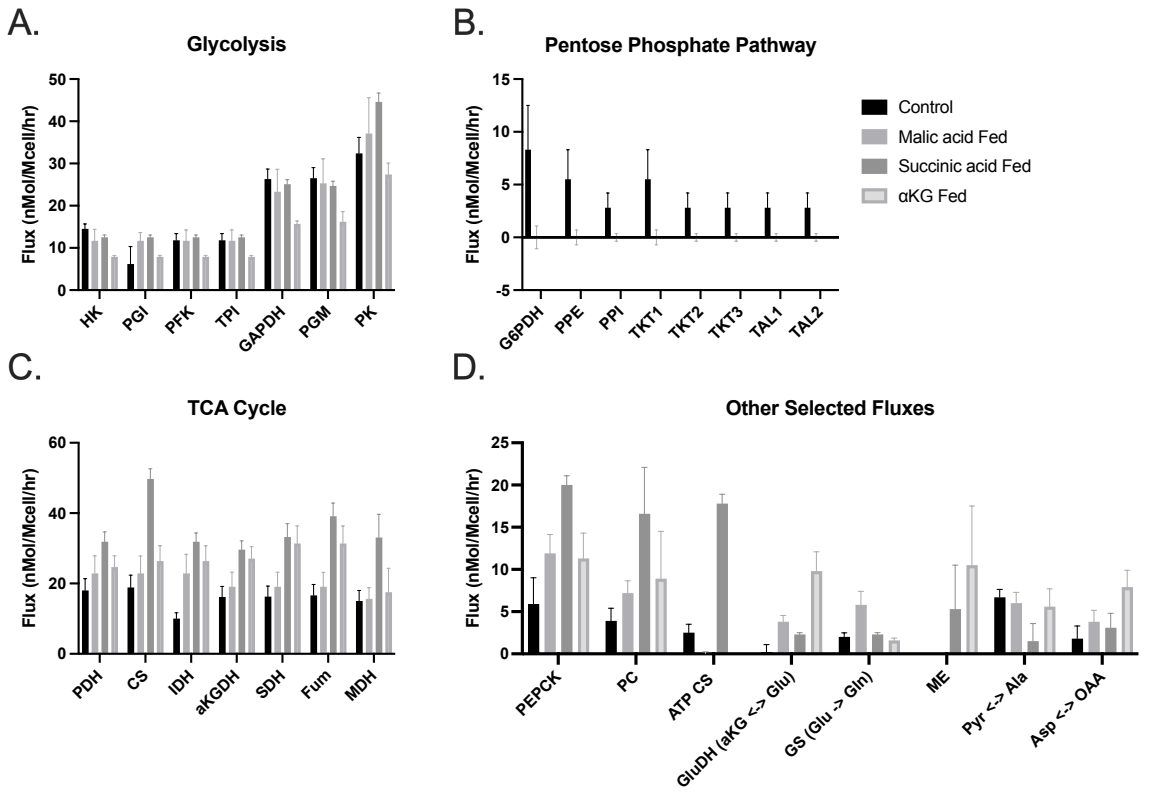

Figure 6.9: **Absolute fluxes during days 10-12.** The absolute flux rates determined by ^{13}C MFA for reactions in (A) glycolysis, (B) PPP, (C) TCA cycle, and (D) other selected fluxes are shown. Data represent the means ± SEM.

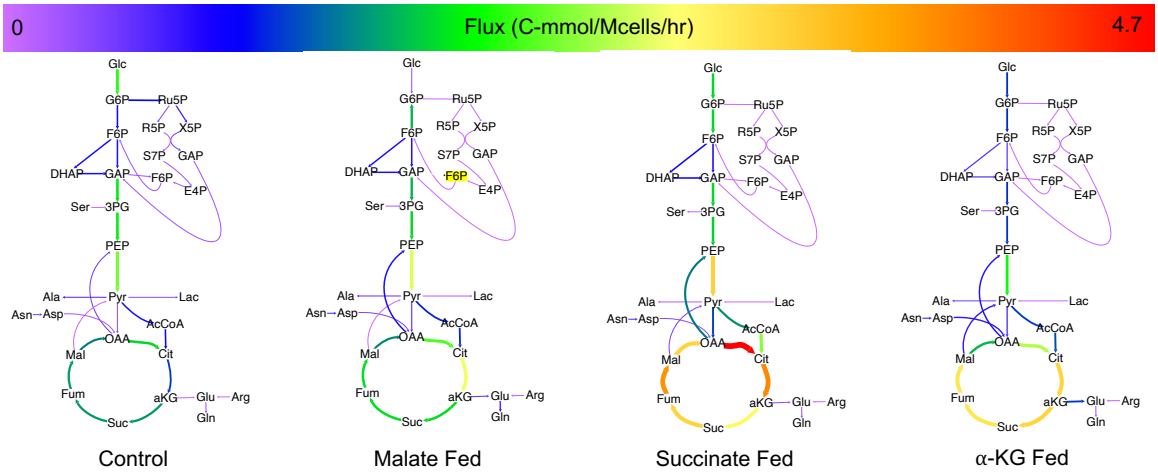

Figure 6.10: **Flux maps based on the absolute fluxes determined by ^{13}C MFA.**

Due to the differences in glucose uptake rates (Figure 6.4), the absolute fluxes shown above were normalized to glucose uptake to control for these differences. Upon normal-

ization, certain differences between the feeding conditions become more apparent. In glycolysis, all three TCA intermediate fed conditions trend towards higher PK flux (Figure 6.11A), with significant increases occurring in the succinic acid and α-KG fed reactors. The increase in PK aligns with the observed increases in PEPCK (Figure 6.11D). In the PPP, all TCA intermediate fed reactors still have approximately zero flux, while the control reactors have significantly higher fluxes through the first few reactions of the PPP. In the TCA cycle, the increases in flux become more obvious upon normalization. Fluxes throughout the TCA cycle trend higher in all TCA intermediate fed reactors, with significant increases occurring for most reactions in the succinic acid and α-KG fed reactors. The fluxes through PEPCK and PC trend higher in all three TCA intermediate fed conditions, with significant increases in PEPCK flux for the succinic acid and α-KG fed reactors and in PC for the succinic acid fed reactors. For the α-KG fed reactors, flux through GluDH was significantly higher, indicating that excess α-KG was used for glutamate production. The ME flux was also increased in the α-KG fed reactors. Malic enzyme flux has been hypothesized to have a Michaelis-Menten type correlation with qP [25]; this does not appear to be the case here, since the α-KG fed reactors had the lowest qP during this time period (Figure 6.8B). Figure 6.12 shows flux maps generated based on the flux values reported in Figure 6.11.

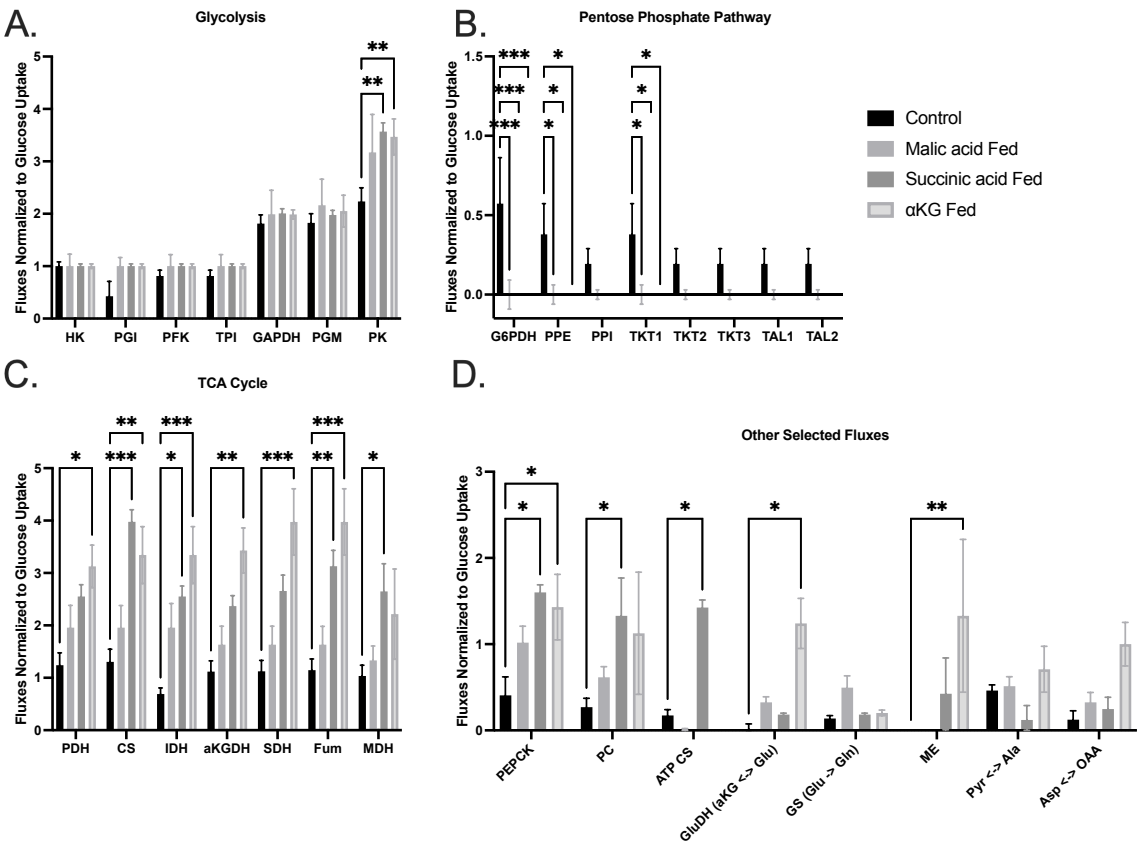

Figure 6.11: **Fluxes normalized to glucose uptake during days 10-12.** The flux rates determined by ^{13}C MFA normalized to the glucose uptake rate for reactions in (A) glycolysis, (B) PPP, (C) TCA cycle, and (D) other selected fluxes are shown. Data represent the means $\pm$ SEM. $^{*}p < 0.05, ^{**}p < 0.01, ^{***}p < 0.001$.

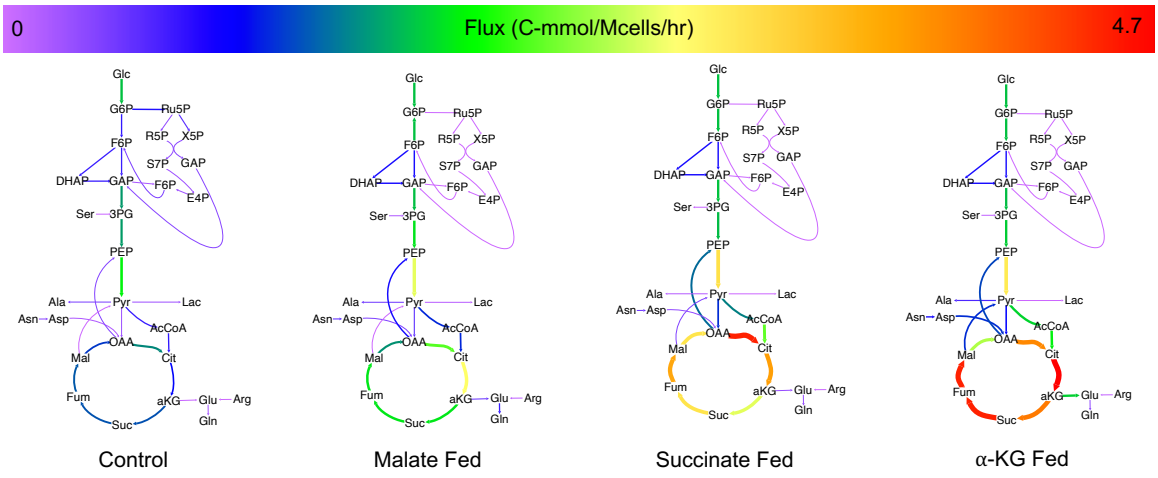

Figure 6.12: **Flux maps based on the ^{13}C MFA fluxes normalized to glucose uptake.**

While most glycolytic fluxes were not significantly different in the TCA intermediate fed reactors compared to the control, pyruvate kinase (PK) fluxes were significantly higher in the succinic acid and α-KG fed reactors. Malic acid fed reactors also trended towards higher PK fluxes. Interestingly, while malic acid fed reactors had similar glycolytic fluxes when compared to succinic acid and α-KG reactors, TCA cycle fluxes were lower. As shown in Figure 6.13A, flux through malic enzyme (ME) provides a substantial increase in pyruvate production in addition to PK flux. This increase in pyruvate production leads to increased flux of pyruvate into the TCA cycle, as shown by the increase in fluxes through PDH and PC in the succinic acid and α-KG fed reactors (Figure 6.13B). The feeding of succinic acid and α-KG appear to increase pyruvate production through ME, leading to increased TCA cycle flux.

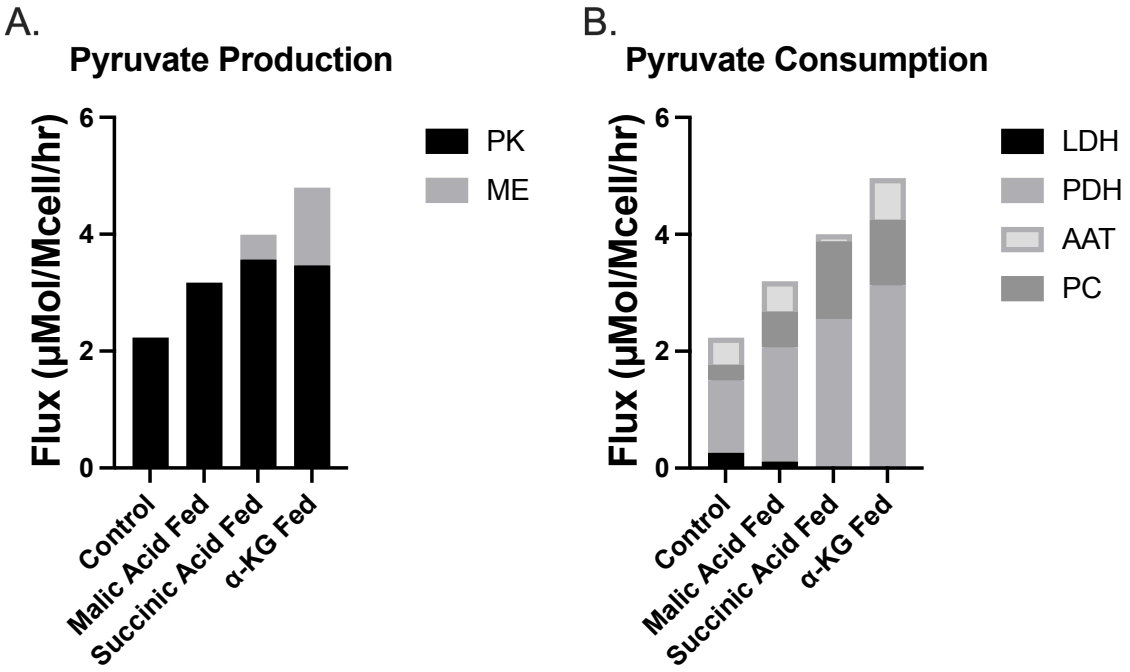

Figure 6.13: **Fluxes for reactions that produce and consume pyruvate.** Pyruvate is produced from glycolysis via pyruvate kinase (PK) or from malate via malic enzyme (ME). Pyruvate can be consumed by the production of the byproducts lactate (lactate dehydrogenase, LDH) or alanine (alanine aminotransferase, AAT) or by entering the TCA cycle via pyruvate dehydrogenase (PDH) or pyruvate carboxylase (PC).

Based on these flux results, it would appear that TCA intermediate feeding leads to

increased futile pyruvate cycling. Pyruvate can be produced from OAA via PEPCK and PK and from malate via ME. PEPCK and PK were increased in TCA intermediate fed reactors while ME fluxes were upregulated in succinic acid and α-KG fed reactors. Pyruvate consumption mainly occurred through the PDH reaction, which allows for the oxidation of pyruvate via the TCA cycle. Additionally, PC flux was increased in the TCA intermediate fed reactors. This anaplerotic reaction provides OAA for other biosynthetic precursors, but does not lead to oxidation of pyruvate. Therefore, it would appear that pyruvate consumed by the PC reaction is entering a futile cycle of pyruvate conversion to OAA, OAA conversion to PEP, and PEP conversion back to pyruvate via PC, PEPCK, and PK, respectively. Pyruvate cycling is thought to provide reducing equivalents, particularly NADPH, which could provide a reason for this futile cycling [26].

6.3.6 TCA intermediate feeding alters intracellular redox state

The redox state within the cell can control various cellular processes. In order to assess how the feeding of TCA cycle intermediates affects the redox state, we determined the ratio of NADPH to $NADP^+$ in the cytosol and the ratio of NADH to NAD^+ in the cytosol. As shown in Figure 6.14, the ratio of NADPH to $NADP^+$ in the cytosol was significantly higher in all TCA cycle fed reactors at all time points, aside from 24 and 36 hours after tracer addition for the α-KG fed reactors. The NADH to NAD^+ ratio was significantly lower in all TCA cycle fed reactors at all time points.

The PPP is one of the main producers of NADPH; however, we did not see any increase in PPP flux in the TCA intermediate fed reactors. In fact, there was a reduction of PPP flux for all three of the TCA intermediate fed reactors. Other sources of NADPH include IDH, GluDH, and ME; all of these, aside from ME in the malic acid fed reactor, were higher in the TCA intermediate fed reactors, which may explain the increase in NADPH and also the inhibition of PPP flux. The increased NADPH aligns well with the observation of pyruvate cycling, as NADPH is an expected product of the reactions involved in pyruvate cycling

[26]. One major consumer of NADH is the electron transport chain (ETC); the increase in TCA cycle fluxes in all three TCA intermediate fed conditions therefore likely explains the decrease in NADH to NAD^+ ratio.

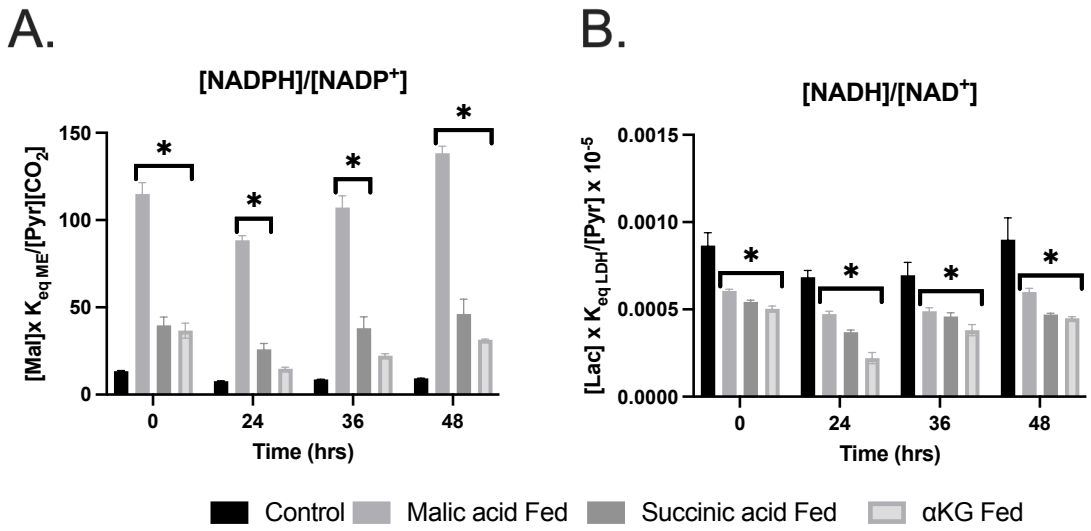

Figure 6.14: **Redox ratios over time during days 10-12.** Data represent means $\pm$ SEM. $*p < 0.05$.

6.3.7 Conclusions

TCA cycle flux has been found to peak during stationary phase, coinciding with the peak production phase [11]. Elevated TCA cycle flux has also been identified as a hallmark of high-producing CHO cell lines [27]. Identifying feeding schemes that can lead to increased TCA cycle flux can provide ways to induce the desirable high-producing phenotype in CHO cells. In this study, it was hypothesized that the feeding of TCA cycle intermediates as a form of culture pH control would lead to increased TCA cycle flux. TCA intermediate feeding was found to increase final volumetric titer and qP. While the increases in titer and qP were modest, the concentrations of lactate and ammonia were maintained at lower levels throughout the later phases of culture. ^{13}C MFA revealed altered metabolism in the three TCA intermediate fed conditions, particularly in the increased fluxes of the TCA cycle. In combination with other strategies to improve product yield, the use of TCA cycle intermediates to control pH levels can enhance the metabolism within the cell by providing

additional carbon sources while maintaining desirable culture characteristics.

Lactate and ammonia are byproducts of CHO cell growth that can have negative effects on culture growth and product quality [9]. Low-levels of lactate and ammonia in culture fed citrate and α-KG have been previously shown [28, 8]. The switch to lactate consumption has been found to be a desirable culture trait[27, 10], and was exhibited by all cultures in this study. However, control cultures eventually resumed lactate production, resulting in nearly 4-fold higher lactate concentrations in the control reactors compared to the TCA intermediate fed reactors. This is likely due to the use of CO_2 for pH control, which has been found to negatively impact lactate metabolism. Previous studies have found that high levels of pCO_2 can cause cultures to never consume lactate or even resume lactate production [21, 22]. When lactic acid is fed as a form of pH control, high levels of lactate consumption are maintained while pCO_2 levels are kept at fairly low levels [23]. TCA intermediate feeding, in place of CO_2, as a form of pH control can help to maintain lactate consumption throughout the culture duration by keeping pCO_2 relatively low.

Meanwhile, ammonia production was likely reduced in the TCA intermediate fed reactors due to increased cataplerosis. Amino acids can be used to fuel the TCA cycle via anaplerotic reactions [29, 30]; these reactions inherently produce ammonia, so increased ammonia levels are to be expected in this case. It can also be expected that when amino acids are produced via these same reactions, ammonia will be consumed. When TCA cycle intermediates are available through direct feeding, there is lower demand to produce these metabolites from amino acids via anaplerosis. Additionally, cultures with higher productivity require more amino acids to serve as building blocks for protein synthesis [31]; when TCA intermediates are available in high abundance, these amino acids can be produced via cataplerosis, further consuming ammonia.

Meanwhile, the observation of futile pyruvate cycling in the TCA intermediate fed reactors is quite interesting. TCA intermediate feeding reduces pCO_2; it has been hypothesized that the PEPCK reaction would be extremely sensitive to pCO_2, due to the production of

CO_2 by this reaction [32]. It is expected that similar regulatory mechanisms can be present in mammalian cells [21]. Therefore, it is feasible that the increased flux through PEPCK, and by extension pyruvate cycling, could be due to the lower pCO_2 levels in the TCA intermediate fed reactors compared to the control reactors. This increased PEPCK flux does appear to allow for increased oxidation of pyruvate, as shown by the increased PDH fluxes in the TCA intermediate fed reactors, while also allowing for increased PC flux (Figure 6.13). Furthermore, NADPH is a byproduct of this futile pyruvate cycling; the calculated redox ratios show significant increases in NADPH in all TCA intermediate fed reactors. The increased NADPH ratio could also be inhibiting PPP flux; since oxidative PPP flux has also been shown to increase during times of high productivity [11], the inhibition of the PPP could be limiting the qP. It should be noted that the NADPH and NADH ratios that were calculated herein are by proxy; it would be interesting to see how well these calculated ratios align with a direct measurement of intracellular NADPH and NADH ratios.

Overall, it appears that the reduced levels of pCO_2 in the TCA intermediate fed reactors could be responsible for not only the maintenance of low lactate concentrations throughout the culture duration, but also the increased PEPCK flux and pyruvate cycling. The use of another, more inert acid, such as HCl, could maintain similar pCO_2 levels between the control and TCA intermediate fed reactors, allowing for a more direct comparison of lactate and intracellular metabolism. It would also be interesting to see whether pyruvate cycling is observed at the same level in an HCl control as the TCA intermediate fed reactors.

6.4 Appendix

Condition	Sum of Squared Residuals (SSR)	95% Confidence Interval LB (SSR)	95% Confidence Interval UB (SSR)	DOF
Control	132.3	102.1	165.7	132
malic acid Fed	137.0	87.2	146.6	115
succinic acid Fed	147.3	99.5	162.3	129
α-KG Fed	106.5	79.4	136.4	106

Table 6.A1: **Sum of squared residuals (SSR) for ^{13}C MFA best-fit solutions.** Confidence intervals are based on a chi-squared distribution with the indicated degrees of freedom (DOF). If SSR is below the UB threshold, the fit is acceptable. LB = lower bound, UB = upper bound

References

[1] F M Wurm. Production of recombinant protein therapeutics in cultivated mammalian cells. *Nat Biotechnol*, 22(11):1393–1398, 2004.

[2] M. De Jesus and F. M. Wurm. Manufacturing Recombinant Proteins in kg-ton Quantities Using Animal Cells in Bioreactors. *Comprehensive Biotechnology, Second Edition*, 3(2):357–362, 2011.

[3] Natalia I. Majewska, Max L. Tejada, Michael J. Betenbaugh, and Nitin Agarwal. N-Glycosylation of IgG and IgG-like recombinant proteins: Why is it important and how can we control it? *Annual Review of Chemical and Biomolecular Engineering*, 11(13):1–28, 2020.

[4] Simon Fischer, René Handrick, and Kerstin Otte. The art of CHO cell engineering : A comprehensive retrospect and future perspectives. *Biotechnology Advances*, 33(8):1878–1896, 2015.

[5] Maria Elisa Rodrigues, Ana Rita Costa, Mariana Henriques, Philip Cunnah, David W. Melton, Joana Azeredo, and Rosário Oliveira. Advances and drawbacks of the adaptation to serum-free culture of CHO-K1 cells for monoclonal antibody production. *Applied Biochemistry and Biotechnology*, 169(4):1279–1291, 2013.

[6] Karthik P. Jayapal, Katie F. Wlaschin, Wei Shou Hu, and Miranda G.S. Yap. Recombinant protein therapeutics from CHO Cells - 20 years and counting. *Chemical Engineering Progress*, 103(10):40–47, 2007.

[7] Gargi Seth, Patrick Hossler, Joon Chong Yee, and Wei-Shou Hu. Engineering Cells for Cell Culture Bioprocessing- Physiological Fundamentals. *Adv Biochem Eng Biotechnol*, 101:119–164, 2006.

[8] Xiaolin Zhang, Rubin Jiang, Henry Lin, and Sen Xu. Feeding tricarboxylic acid cycle intermediates improves lactate consumption and antibody production in Chinese hamster ovary cell cultures. *Biotechnology Progress*, (January):1–9, 2020.

[9] Mio Sam Lao and Derek Toth. Effects of ammonium and lactate on growth and metabolism of a recombinant Chinese hamster ovary cell culture. *Biotechnology Progress*, 13(5):688–691, 1997.

[10] Fiona Hartley, Tracy Walker, Vicky Chung, and Karl Morten. Mechanisms driving the lactate switch in Chinese hamster ovary cells. *Biotechnology and Bioengineering*, 115(8):1890–1903, 2018.

[11] Neil Templeton, Jason Dean, Pranhitha Reddy, and Jamey D. Young. Peak antibody production is associated with increased oxidative metabolism in an industrially relevant fed-batch CHO cell culture. *Biotechnology and Bioengineering*, 110(7):2013–2024, 2013.

[12] Maciek R. Antoniewicz, Joanne K. Kelleher, and Gregory Stephanopoulos. Measuring deuterium enrichment of glucose hydrogen atoms by gas chromatography/mass spectrometry. *Analytical Chemistry*, 83(8):3211–3216, 2011.

[13] Sarah A Sacco, Angela M Tuckowski, Irina Trenary, Lauren Kraft, Michael J Betenbaugh, Jamey D Young, and Kevin D Smith. Attenuation of glutamine synthetase selection marker improves product titer and reduces glutamine overflow in Chinese hamster ovary cells. *Biotechnology and bioengineering*, mar 2022.

[14] Taylor A. Murphy and Jamey D. Young. ETA: Robust software for determination of cell specific rates from extracellular time courses. *Biotechnology and Bioengineering*, 110(6):1748–1758, 2013.

[15] H.A. Krebs and R.L. Veech. Equilibrium relations between pyridine nucleotides and adenin nucleotides and their roles in the regulation of metabolic processes. *Adv. Enzyme Regul.*, 7:397–413, 1969.

[16] Mohsin Rahim, Arya Y. Nakhe, Deveena R. Banerjee, Emily M. Overway, Karin J. Bosma, Jonah C. Rosch, James K. Oeser, Bo Wang, Ethan S. Lippmann, David A. Jacobson, Richard M. O'Brien, and Jamey D. Young. Glucose-6-phosphatase catalytic subunit 2 negatively regulates glucose oxidation and insulin secretion in pancreatic β-cells. *Journal of Biological Chemistry*, page 101729, 2022.

[17] Neil Templeton, Sen Xu, David J Roush, and Hao Chen. 13C metabolic flux analysis identifies limitations to increasing specific productivity in fed-batch and perfusion. *Metabolic Engineering*, 44(September):126–133, 2017.

[18] Jamey D. Young. INCA: A computational platform for isotopically non-stationary metabolic flux analysis. *Bioinformatics*, 30(9):1333–1335, 2014.

[19] Neil Templeton, Abasha Lewis, Haimanti Dorai, Elaine A. Qian, Marguerite P. Campbell, Kevin D. Smith, Steven E. Lang, Michael J. Betenbaugh, and Jamey D. Young. The impact of anti-apoptotic gene Bcl-2 expression on CHO central metabolism. *Metabolic Engineering*, 25:92–102, 2014.

[20] Yi Ern Cheah and Jamey D. Young. Isotopically nonstationary metabolic flux analysis (INST-MFA): putting theory into practice. *Current Opinion in Biotechnology*, 54:80–87, 2018.

[21] Matthias Brunner, Philipp Doppler, Tobias Klein, Christoph Herwig, and Jens Fricke. Elevated pCO2 affects the lactate metabolic shift in CHO cell culture processes. *Engineering in Life Sciences*, 18(3):204–214, 2018.

[22] Sen Xu, Rubin Jiang, Roland Mueller, Nadja Hoesli, Thomas Kretz, John Bowers, and Hao Chen. Probing lactate metabolism variations in large-scale bioreactors. *Biotechnology Progress*, 34(3):756–766, 2018.

[23] Jincai Li, Chun Loong Wong, Natarajan Vijayasankaran, Terry Hudson, and Ashraf Amanullah. Feeding lactate for CHO cell culture processes: Impact on culture metabolism and performance. *Biotechnology and Bioengineering*, 109(5):1173–1186, 2012.

[24] Sarah A. Sacco. Glutamine Synthetase promoter Attenuation Modeling Data, 2022.

[25] Lisa Junghans, Attila Teleki, Andy Wiranata Wijaya, Max Becker, Michael Schweikert, and Ralf Takors. From nutritional wealth to autophagy: In vivo metabolic dynamics in the cytosol, mitochondrion and shuttles of IgG producing CHO cells. *Metabolic Engineering*, 54(January):145–159, 2019.

[26] Sarah M. Ronnebaum, Olga Ilkayeva, Shawn C. Burgess, Jamie W. Joseph, Danhong Lu, Robert D. Stevens, Thomas C. Becker, A. Dean Sherry, Christopher B. Newgard, and Mette V. Jensen. A pyruvate cycling pathway involving cytosolic NADP-dependent isocitrate dehydrogenase regulates glucose-stimulated insulin secretion. *Journal of Biological Chemistry*, 281(41):30593–30602, 2006.

[27] Neil Templeton, Kevin D Smith, Allison G Mcatee-pereira, Haimanti Dorai, J Betenbaugh, Steven E Lang, and Jamey D Young. Application of 13C flux analysis to identify high-productivity CHO metabolic phenotypes. *Metabolic Engineering*, 43(B):218–225, 2017.

[28] Alan Gilbert, Kyle Mcelearney, Rashmi Kshirsagar, Martin S. Sinacore, and Thomas Ryll. Investigation of metabolic variability observed in extended fed batch cell culture. *Biotechnology Progress*, 29(6):1519–1527, 2013.

[29] Jason Dean and Pranhitha Reddy. Metabolic analysis of antibody producing CHO cells in fed-batch production. *Biotechnology and Bioengineering*, 110(6):1735–1747, 2013.

[30] Averina Nicolae, Judith Wahrheit, Janina Bahnemann, An Ping Zeng, and Elmar Heinzle. Non-stationary 13C metabolic flux analysis of Chinese hamster ovary cells in batch culture using extracellular labeling highlights metabolic reversibility and compartmentation. *BMC Systems Biology*, 8(1):1–15, 2014.

[31] Nuno Carinhas, Tiago M. Duarte, Laura C. Barreiro, Manuel J.T. Carrondo, Paula M. Alves, and Ana P. Teixeira. Metabolic signatures of GS-CHO cell clones associated with butyrate treatment and culture phase transition. *Biotechnology and Bioengineering*, 110(12):3244–3257, 2013.

[32] Rodney P. Jones and Paul F. Greenfield. Effect of carbon dioxide on yeast growth and fermentation. *Enzyme and Microbial Technology*, 4(4):210–223, 1982.

CHAPTER 7

Conclusions

Portions of this chapter are adapted from ^{13}C metabolic flux analysis in cell line and bioprocess development *published in* Current Opinion in Chemical Engineering *and has been reproduced with the permission of the publisher and my co-author, Jamey Young* [1]

This dissertation describes several examples which highlight the application of ^{13}C metabolic flux analysis (MFA) as a technique to increase the metabolic efficiency of Chinese hamster ovary (CHO) cells. First, the affects of attenuation of the promoter region of the glutamine synthetase (GS) selection system were quantified. We found that attenuation of the GS promoter reduced wasteful glutamine overflow and increased specific productivity, while metabolism remained largely unchanged. Next, we aimed to characterize a CHO cell line that had been engineered to overexpress PGC-1α, a global regulator of mitochondrial metabolism, which was found to have increased titer and oxidative metabolism. A range of techniques were examined to determine the mRNA and protein level expression of PGC-1α, directly or indirectly. Additionally, a metabolic model was developed to allow for the quantification of fluxes through the synthesis pathways of glycosylation precursors. This model was validated with a ^{13}C MFA study of cultures fed either glucose or galactose during stationary phase. Finally, the metabolic alterations that result from feeding TCA cycle intermediates were explored through a ^{13}C MFA study. TCA cycle intermediate feeding was found to significantly increase flux through the TCA cycle while lowering concentrations of the inhibitory byproducts, lactate and ammonia. All of these studies focused on different desirable aspects of CHO cell culture - improved productivity, decreased byproduct formation, or increased product quality - and explored the relationship between these culture traits and metabolism. These studies highlight the metabolic engineering paradigm of "design-build-test-learn"; ^{13}C MFA was used as a "test" to provide insights

for the "learn" phase, which were eventually used to guide the "design" phase.

Returning to the questions posed in the introduction to this dissertation:

- Which metabolic phenotypes correlate with high specific productivity (qP)?
- How does cellular metabolism change under different bioprocess conditions?
- Can metabolic engineering be applied to systematically generate high producing CHO cell lines?
- What tools and techniques can be developed to aid in answering these questions?

Based on previous work, it was hypothesized that high TCA cycle flux correlates with high specific productivity. In CHO cells engineered to overexpress PGC-1α, further evidence was provided that showed that the upregulation of TCA cycle flux can lead to increased qP. Interestingly, in CHO cells where the GS selection system was attenuated, increased qP was observed with no concurrent increase in TCA cycle fluxes. In this case, it appears that IgG copy number was the major determinant of qP, likely due to lower production levels that weren't yet limited by energetics.

In the two studies that focused on feeding strategies, either galactose feeding to alter glycosylation or TCA intermediates to fuel the TCA cycle, the consumption of carbon sources beyond glucose appeared to be critical to TCA cycle flux. In cultures fed galactose as the main carbon source, glycolytic fluxes were reduced but TCA cycle fluxes were similar to those in glucose fed cultures; the reduced glycolytic flux appears to be compensated for by increased lactate consumption, fueling the TCA cycle. Meanwhile, in cultures fed TCA cycle intermediates, lower glucose uptakes and glycolytic fluxes were more than compensated for by the consumption of the TCA intermediates, leading to increased TCA cycle flux.

Two studies presented herein focus on engineering cell lines. The overexpression of PGC-1α was found to increase qP nearly 4-fold over the parental cell line. Additionally,

in CHO cells that featured an attenuated GS selection system, qP was also significantly increased. Both of these studies highlight the application of metabolic engineering to systematically generate high producing CHO cell lines, based on the insights learned from previous metabolic studies.

A number of tools and techniques were also introduced in this dissertation that not only aided in the studies described herein, but can be applied in future studies. First, for the GS attenuation study described in Chapter 3, a compartmentalized model of CHO cells was developed due to the inability of a non-compartmentalized model to accurately regress fluxes from the data generated in this study. This model was applied in every other study described in this dissertation. For the galactose feeding study in Chapter 5, this compartmentalized model was expanded to include NT and NT-sugar biosynthesis reactions, the first metabolic model that attempted to do so. In addition to this expanded model, an LC-MS/MS method was developed to determine the labeling of NTs and NT-sugars. All of these tools can be applied for future studies of CHO cell metabolism.

7.1 Future Directions

The work described in this dissertation provides several questions and opportunities for future study. The cell lines that were used in the attenuated GS promoter study were non-clonal, meaning they featured genotypic diversity. It is likely that upon generation of clonal cell lines, phenotypic changes will be observed, particularly in terms of increased qP. In this study, it was particularly surprising that there was no alteration to central carbon metabolism. We have hypothesized that the qP levels observed in these non-clonal cells could be too low to cause energetics to be the limiting factor, which could explain the lack of metabolic changes. It would be interesting to see whether clonality has any effect on the characteristics that were reported in this study. In addition to modulating GS expression, it would be interesting to see how overexpression of glutamate dehydrogenase, which allows for the entry of glutamate into the TCA cycle via α-ketoglutarate, would affect the

proportion of glutamate entering the TCA cycle.

The cultures that were engineered to overexpress PGC-1α exhibited decreased viable cell density (VCD) and increased cell size compared to the parental line. One explanation for the decrease in VCD is that the metabolic burden due to constitutive PGC-1α expression could be limiting the growth of these cultures. Therefore, it could be beneficial to express PGC-1α from an inducible promoter, which would allow for PGC-1α expression to be turned on after the cells have reached maximum peak VCDs, similar to the galactose feeding strategies employed in another study in this dissertation (Chapter 5). However, the increase in cell size could present another explanation for the decreased VCD. PGC-1α has an intricate relationship with mammalian target of rapamycin (mTOR), a well-known regulator of cell growth [2, 3]. The increase in cell size could be related to cell cycle arrest, but overall represents another interesting facet of the PGC-1α overexpression phenotype.

The metabolic model that was developed to incorporate nucleotide sugar biosynthesis was validated using glucose and galactose fed cultures as model systems. Ultimately, we aim for this model to be utilized to study the relationship between central carbon metabolism and glycosylation. From the model description, it can be observed that glycosylation precursors are directly related to central carbon metabolic pathways. It could be assumed that if fluxes through central carbon metabolism are altered, the fluxes through the glycosylation precursor pathways will also be altered, possibly leading to changes in glycosylation profiles. An in-depth understanding of how varied metabolic phenotypes affect glycosylation can help to identify targets that lead to desirable glycosylation patterns. Herein, fluxes through the NT-sugar biosynthesis pathways were not well-resolved. The assessment of additional metabolites through NT-sugar biosynthesis could help to improve flux estimates; in particular, assessing the labeling of AcCoA, which contributes the NAc group to the UDP-HexNAc NT-sugars. Further constraints on NT-sugar demands, for glycans on the mAbs and host cell proteins, could also help to improve resolution through these pathways. These demands can be easily included as terms in the mAb and biomass forma-

tion reactions, with stoichiometric coefficients calculated based on glycan profile measurements and previously reported estimates for NT-sugar demands in CHO host cell proteins [4].

7.1.1 Future improvements to the ^{13}C MFA workflow

7.1.1.1 Mini bioreactors

For a rigorous ^{13}C MFA study, multiple replicates of each tested condition are necessary. However, the labeled tracers used can become prohibitively expensive when a variety of conditions are being studied in large-volume bioreactors. In the case of ^{13}C MFA studies utilizing parallel tracers, the required number of replicates increases in proportion to the number of tracers. Many prior MFA experiments were either run in smaller volumes, such as shake flasks that are not necessarily representative of industrial production conditions, or in larger, more representative bioreactors using minimal (or no) replicates. With the rising prevalence of mini bioreactors, such as the high-throughput AMBR system, industrially relevant conditions can be analyzed while maintaining a sufficient number of replicates [5]. AMBR mini bioreactors provide representative scale-down models of commercial-scale processes over 10,000L [6, 7]. The high-throughput nature of these systems has been utilized to study varying feed conditions in parallel [8, 9]. With the ability to operate a large number of mini bioreactors simultaneously, multiple conditions can be studied utilizing multiple tracers in parallel. We expect that these small-volume, high-throughput systems will allow for ^{13}C MFA to be more widely utilized to study the metabolism of industrially relevant cell lines.

7.1.1.2 Expansion of metabolic models

Eukaryotic cells are inherently compartmentalized, with important metabolic reactions occurring in both the cytosol and mitochondria, sometimes in parallel via different enzyme isoforms [10]. Metabolic models used in ^{13}C MFA are increasingly accounting for this compartmentalization to more accurately determine the intracellular flux landscape

[11, 12, 13]. In addition, methods to isolate subcellular compartments are being developed and optimized, opening the door for more robust modeling of compartmentalized metabolic fluxes [14, 15]. Lee et al. [16] employed a protocol consisting of rapid fractionation followed by quenching to study labeling of metabolites in the cytosol and mitochondria of HeLa cells. By combining the MIDs measured from the two compartments with a compartmentalized model of metabolism, they were able to identify that cytosolic isocitrate dehydrogenase was the major source of cytosolic citrate, which was previously not elucidated using whole-cell labeling patterns. While the experimental methods to support compartmentalized ^{13}C MFA models are still being optimized, the eventual inclusion of compartment-based labeling data will increase the information that can be drawn from ^{13}C MFA studies.

In addition to the inclusion of compartmentalization, the advent of genome-scale models (GSMs) broadens the possible scope of reactions that can be included in ^{13}C MFA models. With the publication of the first GSM for CHO in 2016 by Hefzi et al.[17], there has been an increase in utilization of GSMs for a variety of studies [18, 19, 20, 21]. The inclusion of ^{13}C labeling data can further increase the power of these models. In a comparison of fluxes estimated by a core model and a GSM in E. coli, it was found that while the GSM was able to better fit the experimental data, fluxes were better resolved in the core model. This is likely due to the presence of redundant reactions in the GSM and highlights the need for tracer optimization and increased experimental measurements when using GSMs [22].

7.2 Contribution

The work presented within this dissertation highlights the wide range of applicability of ^{13}C MFA. A greater understanding of CHO cell metabolism can aid in the rational engineering of high-producing cell lines. The studies presented herein provide evidence that optimizing metabolic efficiency can lead to increased qP. Additionally, this dissertation

provides examples of industrial-academic collaborations that provide industrially relevant outputs while also investigating fundamental research questions. These collaborations are unique, as many academic studies of CHO cells are in non-producing lines, due to the inaccessibility of industrial producing lines to most academic researchers. While many studies have aimed to understand cellular metabolism in CHO cell lines, the findings are not often applied to guide host cell engineering strategies. Even more rare is the ability to test these engineering strategies in industrial production CHO cell lines. A major goal of the biopharmaceutical industry is to increase qP in CHO host cell lines; this work presents evidence of the use of ^{13}C MFA to help achieve this goal.

References

[1] Sarah A Sacco and Jamey D Young. 13C metabolic flux analysis in cell line and bioprocess development. *Current Opinion in Chemical Engineering*, 34, 2021.

[2] Yaniv Lustig, Jorge L Ruas, Jennifer L Estall, James C Lo, Srikripa Devarakonda, Dina Laznik, Jang Hyun Choi, Hiraku Ono, Jesper V Olsen, and Bruce M Spiegelman. Separation of the gluconeogenic and mitochondrial functions of PGC-1a through S6 kinase. *Genes Development*, pages 1–13, 2011.

[3] Ruben Boon, Manoj Kumar, Tine Tricot, Ilaria Elia, Laura Ordovas, Frank Jacobs, Jennifer One, Jonathan De Smedt, Guy Eelen, Matthew Bird, Philip Roelandt, Ginevra Doglioni, Kim Vriens, Matteo Rossi, Marta Aguirre Vazquez, Thomas Vanwelden, François Chesnais, Adil El Taghdouini, Mustapha Najimi, Etienne Sokal, David Cassiman, Jan Snoeys, Mario Monshouwer, Wei Shou Hu, Christian Lange, Peter Carmeliet, Sarah Maria Fendt, and Catherine M. Verfaillie. Amino acid levels determine metabolism and CYP450 function of hepatocytes and hepatoma cell lines. *Nature Communications*, 11(1):1–16, 2020.

[4] Ioscani Jimenez Del Val, Karen M. Polizzi, and Cleo Kontoravdi. A theoretical estimate for nucleotide sugar demand towards Chinese Hamster Ovary cellular glycosylation. *Scientific Reports*, 6(June):1–15, 2016.

[5] Viktor Sandner, Leon P. Pybus, Graham McCreath, and Jarka Glassey. Scale-Down Model Development in ambr systems: An Industrial Perspective. *Biotechnology Journal*, 14(4):1–11, 2019.

[6] Matthew Manahan, Michael Nelson, Jonathan J. Cacciatore, Jessica Weng, Sen Xu, and Jennifer Pollard. Scale-down model qualification of ambr® 250 high-throughput mini-bioreactor system for two commercial-scale mAb processes. *Biotechnology Progress*, 35(6):1–13, 2019.

[7] Ping Xu, Colleen Clark, Todd Ryder, Colleen Sparks, Jiping Zhou, Michelle Wang, Reb Russell, and Charo Scott. Characterization of TAP Ambr 250 disposable bioreactors, as a reliable scale-down model for biologics process development. *Biotechnology Progress*, 33(2):478–489, 2017.

[8] Xiaolin Zhang, Rubin Jiang, Henry Lin, and Sen Xu. Feeding tricarboxylic acid cycle intermediates improves lactate consumption and antibody production in Chinese hamster ovary cell cultures. *Biotechnology Progress*, (January):1–9, 2020.

[9] Matjaž Brinc and Aleš Belič. Optimization of process conditions for mammalian fed-batch cell culture in automated micro-bioreactor system using genetic algorithm. *Journal of Biotechnology*, 300:40–47, 2019.

[10] Judith Wahrheit, Averina Nicolae, and Elmar Heinzle. Eukaryotic metabolism: Measuring compartment fluxes. *Biotechnology Journal*, 6(9):1071–1085, 2011.

[11] Lisa Junghans, Attila Teleki, Andy Wiranata Wijaya, Max Becker, Michael Schweikert, and Ralf Takors. From nutritional wealth to autophagy: In vivo metabolic dynamics in the cytosol, mitochondrion and shuttles of IgG producing CHO cells. *Metabolic Engineering*, 54(January):145–159, 2019.

[12] Averina Nicolae, Judith Wahrheit, Janina Bahnemann, An Ping Zeng, and Elmar Heinzle. Non-stationary 13C metabolic flux analysis of Chinese hamster ovary cells in batch culture using extracellular labeling highlights metabolic reversibility and compartmentation. *BMC Systems Biology*, 8(1):1–15, 2014.

[13] Judith Wahrheit, Jens Niklas, and Elmar Heinzle. Metabolic control at the cytosol-mitochondria interface in different growth phases of CHO cells. *Metabolic Engineering*, 23:9–21, 2014.

[14] Yannic Nonnenmacher, Roberta Palorini, and Karsten Hiller. Determining compartment-specific metabolic fluxes. *Methods in Molecular Biology*, 1862:137–149, 2019.

[15] Esther W Lim, Seth J Parker, and Christian M Metallo. Chapter 4 Deuterium Tracing to Interrogate Compartment-Specific. 2088, 2020.

[16] Won Dong Lee, Dzmitry Mukha, Elina Aizenshtein, and Tomer Shlomi. Spatial-fluxomics provides a subcellular-compartmentalized view of reductive glutamine metabolism in cancer cells. *Nature Communications*, 10(1):1–14, 2019.

[17] Hooman Hefzi, Kok Siong Ang, Michael Hanscho, Aarash Bordbar, David Ruckerbauer, Meiyappan Lakshmanan, Camila A. Orellana, Deniz Baycin-Hizal, Yingxiang Huang, Daniel Ley, Veronica S. Martinez, Sarantos Kyriakopoulos, Natalia E. Jiménez, Daniel C. Zielinski, Lake-Ee Ee Quek, Tune Wulff, Johnny Arnsdorf, Shangzhong Li, Jae Seong Lee, Giuseppe Paglia, Nicolas Loira, Philipp N. Spahn, Lasse E. Pedersen, Jahir M. Gutierrez, Zachary A. King, Anne Mathilde Lund, Harish Nagarajan, Alex Thomas, Alyaa M. Abdel-Haleem, Juergen Zanghellini, Helene F. Kildegaard, Bjørn G. Voldborg, Ziomara P. Gerdtzen, Michael J. Betenbaugh, Bernhard O. Palsson, Mikael R. Andersen, Lars K. Nielsen, Nicole Borth, Dong-Yup Yup Lee, and Nathan E. Lewis. A Consensus Genome-scale Reconstruction of Chinese Hamster Ovary Cell Metabolism. *Cell systems*, 3(5):434–443.e8, 2016.

[18] Zhuangrong Huang, Jianlin Xu, Andrew Yongky, Caitlin S. Morris, Ashli L. Polanco, Michael Reily, Michael C. Borys, Zheng Jian Li, and Seongkyu Yoon. CHO cell productivity improvement by genome-scale modeling and pathway analysis: Application to feed supplements. *Biochemical Engineering Journal*, 160(January):107638, 2020.

[19] Cyrielle Calmels, Solène Arnoult, Bassem Ben Yahia, Laetitia Malphettes, and Mikael Rørdam Andersen. Application of a genome-scale model in tandem with enzyme assays for identification of metabolic signatures of high and low CHO cell producers. *Metabolic Engineering Communications*, 9(July), 2019.

[20] Cyrielle Calmels, Andréa McCann, Laetitia Malphettes, and Mikael Rørdam Andersen. Application of a curated genome-scale metabolic model of CHO DG44 to an industrial fed-batch process. *Metabolic Engineering*, 51(September 2018):9–19, 2019.

[21] Hock Chuan Yeo, Jongkwang Hong, Meiyappan Lakshmanan, and Dong Yup Lee. Enzyme capacity-based genome scale modelling of CHO cells. *Metabolic Engineering*, 60(December 2019):138–147, 2020.

[22] Saratram Gopalakrishnan and Costas D. Maranas. 13C metabolic flux analysis at a genome-scale. *Metabolic Engineering*, 32:12–22, 2015.

.

CHAPTER 8

Appendix: Common Protocols

1. Quench and extract protocol
2. Methanol/chloroform extraction from plasma or media
3. MOX-TBDMS derivatization of intracellular or extracellular metabolites
4. Di-*O*-isopropylidene propionate derivatization of glucose
5. Protein extraction for Western blotting
6. Sample prep for electrophoresis
7. Western blot
8. qPCR
9. Immunofluorescence for suspension CHO cells

Quench Protocol

Notes:
Need 5 million cells from each culture.
Make AMBIC/water solution, quenching solution, and CaCl solution in advance.
Steps 9 and 10 must be as fast as possible.

1. Prepare an 8.5 g/L solution of ammonium bicarbonate (AMBIC) in water (or 0.85% w/v)
2. Mix AMBIC solution with MeOH (60% MeOH, 40% AMBIC) to form quenching solution (in 50 mL centrifuge tubes).
3. Pre-chill quenching solution to -40°C. (Cool extra just in case.)
    a. Make a 4.5 M CaCl solution and put it in a small cooler than holds a sample rack of 4 tubes.
    b. Fill the small cooler with CaCl to a depth that will cover the volume of quenching solution in tube(s).
    c. Place the small cooler inside another cooler (to ensure conditions as close to adiabatic as possible upon removal from freezer) and place in a -80°C freezer and wait several hours.
    d. Confirm that the temperature of the quenching solution has reached -40°C with K type thermocouple.
4. Turn centrifuge to 0°C or lower if possible.
5. Check cell density of culture.
6. If centrifuge is going to be at 0°C or lower by the time you've quenched, continue.
7. Set up vortex in the -20°C freezer for later use in the extraction protocol.
8. Move enough quench solution to new 15 mL centrifuge tubes such that there will be 5 volumes of quench solution for every 1 volume of media (based on cell density of culture and need 5 million cells).
    a. Keep 15 mL tubes in cooler with CaCl solution.
    b. Place cooler in cell culture hood (sterilizing containers with EtOH).
9. Draw cell media volume for 5 million cells with pipette in hood.
10. IMMEDIATELY eject cell media into quench solution.
11. Centrifuge cells at 1000 RCF for 1 minute.
12. Remove quenching solution/supernatant (keep 1 mL for metabolite leakage analysis.
    a. Store 1 mL supernatant sample in freezer.
    b. Keep pellet for extraction.

Extraction Protocol

1. Add 2 mL of ice cold MeOH and 4 mL chloroform to the tube with pellet remaining from step 12 of quench protocol.**Chill the night before hand; always use glass pipette for choloroform
2. Vortex this solution for 30 minutes in a 4°C freezer.
3. Add 1.5 mL DI H_2O to the tube and 6 µL of 10 mM Norvaline internal standard
4. Vortex for 5 minutes in 4°C freezer.
5. Centrifuge at 4000 RCF for 20 minutes at -4˚C
6. Collect ~2 mL of upper phase (aqueous, polar phase) in small centrifuge tube. (This is the sample of interest.) [in 2 separate tubes, combine after 1 hr. of drying]
7. Collect lower phase (organic) in different tube(s).
    a. Can keep for conservation's sake but no further steps with this phase required.
8. Evaporate aqueous phase under evaporator.
    a. Will take several hours—to be safe wait overnight.

Protocol for Methanol/Chloroform extraction from Plasma or Media

Materials:

- 10 mL Methanol (MeOH) at -20°C
- 10 mL Chloroform ($ChCl_3$) at -20°C
- 10 mL of UltraPure H_2O on ice
- Crushed ice to hold samples
- Microcentrifuge tubes
- Vortexer with access to -20°C freezer
- Centrifuge set to 0°C

Procedure:

1. Prepare 360µL mixture of MeOH/$ChCl_3$ (2:1) for every 30 µL of plasma/media
2. Add the 360µL mixture of MeOH/$ChCl_3$ (2:1) to a sample and vortex for ~30s; place the sample on ice
3. Repeat (2.) for a small number of additional samples
4. Vortex all samples simultaneously for 10min at -20°C
5. Place samples in crushed ice for 20min
6. Add 120 µL of cold $ChCl_3$ followed by 210 µL of ice cold H_2O to a sample
7. Vortex for ~1min and place on ice
8. Repeat (7.) for remaining samples
9. Centrifuge samples at 0°C for 10min at 14,000 RPM
10. Isolate the aqueous phase with a fine-tipped pipette and place in a microcentrifuge tube
11. Overnight dry samples at room temperature under gentle air flow

* Adjust volumes of reagents proportional to the plasma or tissue amount

MOX-TBDMS Derivatization of Intracellular or Extracellular Metabolites

Purpose

This protocol steps the user through the derivatization process for intracellular and extracellular metabolites for GC/MS analysis. This does not include an internal standard.

Safety Precautions

MOX and TBDMS reagents are extremely toxic. Be sure the perform the steps with open samples in the chemical hood and not to inhale the reagents or allow contact with skin.

References

1. Ahn and Antnoniewicz (2012), *Parallel labeling experiments with [1,2-13C] glucose and [U-13C] Glutamine provide new insights into CHO cell metabolism. Metabolic Engineering, Vol. 15 pp. 34-47.*
2. Previous Protocol “MOX-TBDMS derivatization of metabolite extracts” by Neil Templeton.

Materials

- MOX reagent (Thermo Scientific, Item #TS-45950)
- TBDMS: MTBSTFA + 10% TBDMCS, 1 mL ampules (Thermo Scientific, Item #TS-48927)
- 2 mL amber glass injection vial
- 150 uL insert for injection vial
- Evaporator (Pierce Reacti-Vap)
- Sonicator
- Heating block

Sample Preparation

Samples should be frozen and completely dried down.

MOX Derivatization

1. Dissolve dried sample in 50 µL MOX reagent
2. Place in sonication both for 30 minutes at RT
3. Incubated at 40˚C for 90 minutes

TBDMS Derivitization

1. Add 70 µL of MTBSTFA + 1% TBDMCS
2. Incubate at 70˚C for 30 minutes

GC/MS preparation

1. Centrifuge at 14,000 RPM for 5 minutes to remove solid debris
2. Transfer liquid to an insert inside an injection vial. Be sure to not get any solid material into the injection vial as it will clog the instrument.
3. If you don’t run the samples right away, tightly close all vials and put them in the -80˚C freezer until ready to analyze.

STANDARD OPERATING PROCEDURE

Di-O-isopropylidene propionate derivatization of glucose

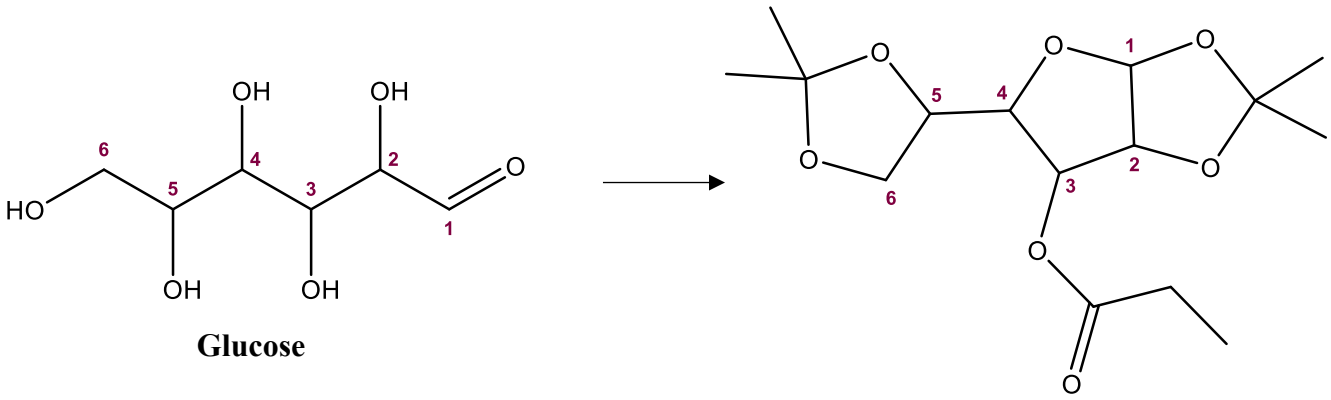

Glucose **Glucose 1,2,5,6-di-isopropylidene propionate**

I. Chemicals

a. Acetone, stored at 4°C ($(CH_3)_2CO$; Sigma-Aldrich #179124-4L)
b. 96% Sulfuric acid (H_2SO_4; EMD Millipore #SX1244-5 2.5L)
c. 0.44 M Sodium Carbonate solution (Na_2CO_3; Fisher Scientific #S495-500)
d. Saturated sodium chloride solution (Fisher Scientific #S271-1)
e. Propionic anhydride ($C_6H_{10}O_3$; Sigma-Aldrich #240311-50G)
f. Pyridine (C_5H_5N; Sigma-Aldrich #270970-100ML))
g. Ethyl acetate ($CH_3COOCH_2CH_3$; Fisher Scientific #E195-1 1L)
h. 5 mM U-^{13}C6-D7-Glucose (Cambridge Isotopes); Optional

II. Materials

a. 1.5 mL microcentrifuge tubes
b. 10 mL screw-cap culture tubes (Fisher Scientific #14-959-25A)
c. 100 mL glass vials or test tubes
d. Pipettes and tips
e. 1 mL glass Pasteur pipettes and bulb
f. 1.5 mL GC injection vial and injection caps (Agilent 5182-0716, 5182-0717)
g. 250 µL glass inserts (Agilent 5181-1270)

III. Equipment

a. Sample dryer (e.g. Pierce Reacti-Therm III and Reacti-Vap III)
b. Heating block
c. Microcentrifuge
d. Vortex

IV. Procedure

a. Sample Preparation – protein precipitation

i. Transfer 20 µL of sample or standard to a labeled microcentrifuge tube
ii. If needed, spike in 20 µL of 5 mM U-^{13}C6-D7-Glucose (I.h.) to use as an internal standard for estimating absolute glucose concentration; pipette up and down to mix

iii. Add 300 µL cold acetone (I.a.)
iv. Vortex vigorously for 10 seconds
v. Centrifuge for 5 minutes at 14,000 rpm
vi. Carefully transfer the supernatant by pipetting to a labeled 10 mL screw-top culture tube (II.b.)
vii. Evaporate samples to dryness under air flow at 60°C
    1. Drying takes approximately 20 minutes
    2. Breakpoint; dried samples can sit on bench for 1-2 hours before proceeding

b. Derivatization

i. In a glass vial or test tube (II.c.), carefully mix 1 part sulfuric acid (I.b.):46 parts acetone (I.a.) v/v; swirl to mix
    1. Must be prepared fresh
ii. Add 500 µL of acetone/sulfuric acid solution to each sample
iii. Vortex 10 seconds
iv. Incubate at room temperature for 60 minutes
v. Add 400 µL of 0.44mM sodium carbonate solution (I.c.) to stop the reaction; swirl to mix until bubbling ceases
vi. Add 1 mL of saturated sodium chloride solution (I.d.) **(1.5 mL for CHO media)**
vii. Add 1 mL of ethyl acetate (I.g.)
viii. Vortex vigorously for 15 seconds
ix. Allow tubes to incubate 2 minutes or until the two layers are fully separated
x. Using a glass Pasteur pipette, carefully transfer the top organic layer to a labeled microcentrifuge tube
    1. The top layer should be > 1 mL
xi. Evaporate to dryness under air flow at room temperature
    1. Drying takes approximately 45 minutes – 1 hour
    2. The dried samples are usually white powder
    3. Breakpoint; samples can sit on bench for 1-2 hours before proceeding
xii. In a glass vial or test tube (II.c.), prepare a 2:1 solution of propionic anhydride (I.e.):pyridine (I.f.); swirl to mix
    1. Must be prepared fresh
xiii. Add 150 µL of propionic anhydride/pyridine solution to each sample; scrape powder with tip to dissolve and pipette up and down to mix
xiv. Incubate for 30 minutes at 60°C on the heating block
xv. Centrifuge for 30 seconds at 14,000 rpm to remove condensation
xvi. Evaporate samples to dryness under air flow at 60°C. Takes around 20-30 minutes
xvii. Dissolve the samples in 100 µL ethyl acetate
xviii. Centrifuge 10 minutes at 14,000 rpm to remove solid debris
xix. Transfer supernatant to a GC injection vial containing a 150 µL glass insert
    1. Close vials tightly and store at -20°C

Protein Extraction for Western Blotting

Lysis Buffer

Make Lysis buffer according to the following concentrations. You need 100 uL/sample so determine total volume needed and go from there. RIPA buffer is in 1.5 mL aliquots already.

*Keep very cold (on ice entire time)

RIPA buffer	0.5 mL	1.0 mL	1.5 mL
PMSF	5 uL	10 uL	15 uL
OV	5 uL	10 uL	15 uL
Halt Protease/phosphatase inhibitor	5 µL	10 µL	15 µL

Protein Extraction

1. Thaw cell pellet if frozen
2. Divide cell pellet into thirds if starting from brand new pellets directly from transfection.
    a. Take 3 mL PBS and mix with pellet
    b. Remove 1 mL for extraction
    c. Remaining 2 mL freeze in -80 for future extraction if needed
    d. Centrifuge (10,000 for 5 min)
3. Make pellet ~50 uL in size
4. Suspend pellet in 100 uL Lysis buffer. When confuse about how much Lysis buffer to add, add less because you can dilute the samples later always.
    a. Pipette 10-20 times to mix well
5. Incubate on ice for 30 minutes
    a. Vortex samples ~ every 5 minutes during incubation
6. Centrifuge 13,000 RPM for 30 min. @ 4C
7. **Collect supernatant** into new epi tubes
8. Move on to protein measurement with BCA kit.
    a. After measurement, extracted samples can be stored at -20˚C for months

Sample Prep for Electrophoresis

Materials

1. dH2O
2. Sample buffer: SDS-PAGE with betamercaptoethanol (BME) added (BME breaks the disulfide bonds) [4X]
3. Purified protein sample (stored at -80C) **THAW ON ICE
4. Hot plate (94-100C)

Method

1. Add volume of dH2O (from spreadsheet calculations dependent upon protein concentrations in each sample) to each new epi-tube
2. Add 10 uL of sample buffer for each sample
3. Add the protein volume for each sample (remaining sample protein needs to be stored at -80C)
4. Boil at 94-100C for 2-5 minutes
5. Cool to room temperature
6. Load into gel (10 uL)
7. Store extra boiled sample in -20C or store until ready to use for a western blot
8. Heat at 95C for 5 minutes before loading on the gel.

Sample buffer recipe:

Should be prepared in the chem hood—the BME stinks.

1. SDS-PAGE (stored in 4C by chem hood top shelf)
2. BME (stored in 4C by chem hood top shelf)

Western Blot (with IR 2˚ ab instructions)

Running Gel

1. Get gel set up in electrophoresis contraption.
2. Make sure to fill up inner space between 2 gels with 1XTGS (Running Buffer) and also up to the level of the base of the gel in the total container. Note: if only doing one gel, put gel sized spacer and thin smaller plastic slip (faces out) on other side of clamp to keep everything together
3. Clean out wells of gel. Use 70uL of surrounding Running Buffer solution to pipette into each well and try to blow out debris. Use pipette tip to straighten out any sagging well walls.
4. Pipette Ladder and samples into wells in SPECIFIC ORDER. Write down the order that you put in samples.
5. Top off chamber between gels with more running buffer (until it spills over the sides)
6. Run gel @100V for 90 minutes. (for 4-15% gradient gel)
    a. Sometimes (dependent on gel %) this may be too long or too short. Be sure to check every 5-10 minutes if you are not sure about timing for your specific gel

Transferring to Membrane (Using iBlot 2)

**You will need to determine which type of membrane (Nitrocellulose or PVDF) is optimal

7. Prepare stack according to order below, rolling each layer to ensure no air bubbles:
    a. Bottom stack
    b. Gel
    c. Filter paper (make sure to wet with DI water)
    d. Top stack
    e. Absorbent pad
8. Place in iBlot 2, run protocol 0
    a. Protocol 0 is a generic protocol for this; while it will generally work, this is a step where optimization may be needed
9. Cut membrane as desired and place in CLEAN black WB box
    a. DO NOT TOUCH AN UNBLOCKED MEMBRANE; should only be handled with CLEAN tweezers
10. Let membrane dry completely if using IR 2˚ antibodies. (~1 hr. in closed WB box)

Blocking

11. Place container with ~5mL Blocking buffer (5% BSA in TBS, DO NOT USE DETERGENT FOR IR WB BLOCKING) on rocker at RT for ~1 hr. or overnight at 4˚C
12. DO NOT WASH after block. Also, remaking blocking buffer is easy and cheap; no need to re-use it and risk contamination.

Antibodies and Imaging

13. Dissolve 5uL Primary Antibody in 5mL (1:1000) of 5% BSA in TBS or **TBST** (ratio varies depending on antibody using)
    a. Label tube with type, initials, date, dilution factor, species-can use 4-5 times, up to 1 month after initial dilution; fresh antibody is desirable, but it's expensive.
    b. Make sure that 1:1000 dilution is appropriate (some require less, some require more)
14. Pour antibody solution over membrane; make sure membrane is floating.
15. Incubate overnight on rocker at 4˚C
    a. Make sure this is appropriate for your antibody. Ex. Actin does not need to be incubated overnight. Incubating at RT for 1 hour is sufficient.
16. Remove antibody---put back in tube & put back in 4C for later use (can store for up to 1 month)
17. Wash membrane with **TBST** @RT 3 x 10 mins.

18. Make solution of 2.5% non-fat milk in TBS or **TBST** (Add 0.01-0.02% SDS for PVDF, NO SDS FOR NC)
    a. Use anti-species secondary of whatever the species the primary antibody came from
    b. Determine an appropriate dilution for your use. For Li-Cor IR 2˚ antibodies, they recommend a starting dilution of 1:15,000, with a dilution range of 1:10,000-1:40,000.
19. Incubate on rocker @RT for 60 mins
20. Discard Secondary antibody
21. Wash x3 **TBST** (~10mL) for 10 mins each on rocker.

Imaging

22. Image final blot on Li-Cor imager. IR blots can be imaged either wet or dry.
23. To properly store an IR blot, place membrane between two pieces of filter paper and store in a dry, dark place.

qPCR

Primer Preparation

- QuickSpin the tubes in which the dry oligos were delivered
- Add the appropriate amount of water (pH around 7 according to manufacturer's instructions) to make 100 μM solution (should be on the sheet)
- Shake and quickspin again
- To make the working primer mixture, add 2.5 μL (each) of the sense and anti-sense primers to 95 μL of water.

cDNA Preparation

- Want 25 ng of cDNA/well
- Add water to appropriate cDNA so final concentration of mixture is 3.125 ng/uL
- Add 8 uL of cDNA+H20 mixture to wells

qPCR Plate Preparation

1. Calculate the number of replicates that are needed. Typically, 3 technical replicates per sample per primer are needed. Make a little bit extra to account for liquid adherence (multiply by 3.5 for 3 replicates).

2. Add to wells in the following order (per well):
   - 10 μL of 2X SYBR Green Mix
   - 8 μL of cDNA Sample
   - 2 μL of primer mixture

3. Stick film to top of plate
4. Centrifuge for 5 minutes
5. Run PCR on the instruments at the core.

Notes

1. Make sure to have some wells with just H20+SYBR Green and some with H20+primers+SYBR Green for controls

Immunofluorescence for Suspension CHO cells

Based on protocol from: Wang CC, Bajikar SS, Jamal L, Atkins KA, Janes, KA. (2014) A Time- and Matrix-dependent TGFBR3-JUND-KRT5 regulatory circuit in single breast epithelial cells and basal-like premalignancies. Nat. Cell. Biol., 16, 345-56.

**Media should always be removed with a pipette (NOT aspirated) and extreme care should be taken to not also remove any cells, especially after cells are fixed.
**Keep cells in the same microcentrifuge tube for the entirety of the protocol.
**Do not exceed centrifuge speeds. Cells will stick together and you won't be able to resuspend them.

Materials:

- Labeled microcentrifuge tubes
- PBS
- Rotoshaker
- Vortex with multi-tube attachment
- 80% Acetone/20% DI H2O at -20˚C
- Blocking solution: 5% NGS in PBS or 1% BSA in PBS
- Primary and secondary antibody
- Vectashield hard set mounting media with DAPI
- Microscope Slides
- Cover Slips
- Clear Nail Polish

1. Measure out cell culture volume to give 5X106 cells. Spin at 1000xG for 3 min. Remove media, leaving just a cell pellet.
2. Resuspend cells in 1 mL PBS. Spin at 1000xG for 3 min. Remove supernatant.
3. Resuspend cells in 800 µL of 80% acetone at -20˚C. Tubes should be placed in vortex at max speed at room temperature for 15 min.
    a. This step both fixes and permeabilizes cells; see notes for other options
    b. If the cells aren't kept on the vortex, they will fix together. Which is bad.
4. Spin down cells at 1000xG for 3 min. Remove supernatant
    a. At this point, the cells will appear whiter in color and will no longer pellet, but rather "smear" along the side of the tube. This means they have been fixed properly.
5. Wash cells once with 800 µL of PBS.
    a. If needed, cells can be stored in 800 µL of PBS at 4˚C for a few days (I've never gone above 1 week); when ready to continue, spin down and remove PBS as the "wash step"
6. Resuspend cells in blocking solution. Let incubate in the rotoshaker for 1 hour at room temp.
    a. You can use either 5% NGS in PBS or 1% BSA in PBS to block, 500 µL is sufficient volume.

7. DO NOT WASH AFTER BLOCKING
8. Spin down cells at 1000xG for 3 min. Resuspend in primary antibody solution.
    a. Use appropriate dilution of antibody in 1% BSA in PBS (regardless of blocking solution). 200µL is sufficient volume.
        a. Typically 1:250, check antibody data sheet; this can be optimized a lot
9. Let cells incubate in primary antibody overnight in the rotoshaker at 4˚C.
10. Spin down cells at 1000xG for 3 min. and remove primary antibody.
11. Wash cells twice with 800µL of PBS. Place in rotoshaker for 5 min. before spinning down at 1000xG for 3 min.
12. From here on out, everything should be done in the dark as the secondary antibody is photosensitive. Wrap things in foil as needed.
13. Resuspend cells in secondary antibody dilution. Allow to incubate in rotoshaker for 1 hr. at room temp.
    a. Use appropriate dilution of antibody in 1% BSA in PBS. 200µL is sufficient volume.
        a. Typically 1:250, check antibody data sheet; this can be optimized a lot
    b. Phalloidin should be included in the secondary antibody solution, if using.
14. Wash cells twice with 800µL of PBS. Place in rotoshaker for 5 min. before spinning down at 1000xG for 3 min.
15. Resuspend cells in 50µL of mounting media.
16. Add the resuspension to a labeled microscope slide and carefully place a coverslip on top.
        a. Carefully push out excess liquid and air bubbles as needed. Bubbles will make imaging very difficult!!
17. Allow slides to dry for at least 30 minutes in the dark. (put in foil)
    a. You can do this overnight to ensure the media is completely dry
18. Seal edges with clear nail polish and allow to air dry
    a. With hardset mounting media, this step is not necessary, but can provide extra preservation (especially if you think you may need to re-image these slides again down the road)
19. Store slides at 4˚C
20.

Troubleshooting and Optimization:
- Cell is not pelleting when it was before: you do lose cells throughout the protocol, and you need a certain “threshold density” to actually pellet them. Start with a higher cell density.
- Cells are not in a monolayer on slide: balancing a high enough density to actually pellet the cells and a low enough density to not overcrowd the slide is difficult; try diluting cells just before you mount them
- Cells are pelleting, but not breaking apart when resuspending: cells have been spun down at too high a speed.

Options for fixing/permeabilization:
1. Acetone (fixes and permeabilizes)
    a. Resuspend cells in 800 µL of 80% acetone at -20˚C for 15 min. at RT.
    b. Vortex throughout entire fixation process.

2. Methanol (fixes and permeabilizes)
    a. Resuspend cells in 800 µL of methanol at -20˚C for 15 min. at RT.
    b. Vortex throughout entire fixation process
3. Formalin (required if using Phalloidin)
    a. Resuspend cells in 10% formalin for 10 min. at RT
    b. Incubate on rotoshaker (vortexing will destroy cells)
    c. Wash 2 x 5 min. in PBS
        a. If not planning to use immediately, keep cells in 800 µL PBS at 4˚C
        b. When ready to continue, spin down and proceed to wash one more time
    d. Permeabilize with 0.25% triton X-100 in PBS for 15 min. or 1 hr. at RT on rotoshaker
    e. Wash 2 x 5 min. in PBS